

**Manganese: Minerals, Microbes, and  
the Evolution of Oxygenic  
Photosynthesis**

Thesis by  
Jena Elaine Johnson

In Partial Fulfillment of the Requirements  
for the degree of  
Doctor of Philosophy



CALIFORNIA INSTITUTE OF TECHNOLOGY

Pasadena, California

2015

(Defended May, 2015)



© 2015

Jena Elaine Johnson

All Rights Reserved

## ACKNOWLEDGEMENTS

This thesis could not have been possible without so many people. Foremost is Woody Fischer. I came to Caltech excited about anything related to the evolution of life, and Woody somehow had the ability to both focus and magnify my excitement. Woody's enthusiasm about everything geobiology (and every type of geochemical technique) is infectious and inspiring. Woody opened my eyes to primary literature through one-on-one paper discussions and his weekly Geobiology Reading group, and kept me ever-learning and ever-motivated by sending me to stimulating conferences, courses, and field work around the world. I am so grateful for his always-open door and quick email replies, the way he pushed me to meet with visiting speakers when I felt like I had nothing to say and email collaborators myself when I was feeling intimidated, and the way he treats no question as stupid – whether over coffee or in Geobiology Reading Group. I feel truly lucky to have had an advisor who drops everything to look at thin section samples with you the day they arrive, who puts a positive spin on even awful data, and who sneaks you a granola bar when you're starving in a meeting. So thank you, Woody, for being my #1 advocate and mentor for the past five years.

There are many others that were essential to produce the collaborative, curious, and critical environment at Caltech that made my PhD possible. For me, one of the most important people is George Rossman. I met George Rossman the first summer I arrived at Caltech, and he has been my mineralogical sounding board ever since. It has been both incredibly fun and helpful to walk up to George's third-floor office with some crazy thin section or rock, smile at his almost-always open door, and barge in with my new bizarre question. I will truly miss the way George's face will go from glum at my awful mineral mixture (sorry, never a pure gemstone!) to cheerful and beaming, fired up by teaching me a new spectroscopic technique and following the clues to the mineral identification. I don't know what I would have done without you, George.

I also need to thank the members of my thesis committee: Alex Sessions, Victoria Orphan, Sam Webb, and Dianne Newman. Dianne always drives the hardest to find the holes in whatever I say, and I am a better scientist because of her. Alex has been my reliable rock: whether I'm looking for candidacy requirements, photography help on a field trip, arranging a dinner date with a future advisor, or simply some amusing wit (whether in Wyoming, New Zealand, or North Mudd hall), Alex is the one I turn to. I'm so grateful for Victoria's sweet presence and gentle encouragement, as well as her periodic check-ins and ever-present hallway smiles. TAing for Victoria was

probably my most challenging and time-consuming assignment, but also the one where I learned the most and gained the most confidence - and I thank Victoria for treating me as a partner in teaching. And Sam! Truly my second advisor, Sam was indispensable to this PhD. Sam taught me everything I know about X-rays and their incredible power to understand the intersection of chemistry, geology, and biology. He has also been a source of countless ideas presented in this thesis about how manganese oxidizes and reduces, as well as a source of constant excitement about all things X-ray, not to mention wine knowledge (yes, I'm now the family wine snob because of you, Sam). So thank you to my fellow nerding-out partner - whether it's checking out giant pyrite and iron formations in South Africa or discussing manganese reactions over wine or fiendishly analyzing data pouring in at the beam line - you have gotten me hooked on X-rays for life and I look forward to many more collaborations!

A few other professors deserve wholehearted acknowledgement. Jess Adkins taught an aquatic chemistry class my first fall at Caltech that changed how I saw the world, and altered the course of my PhD because now every reaction I see is linked back to Morel and Hering. I return to those class notes and my Post-it-filled aquatic chemistry book over and over again, and I think that will be true for the rest of my scientific career. Dianne Newman then taught me how I can see every microbial reaction through the lens of aquatic chemistry, and for that I thank her once more. Dianne's 'Microbial Diversity' class was like most interactions with her: incredibly challenging and at a pace near-impossible to follow, and because of that, totally stimulating and completely rewarding. I also need to thank Sebastian Kopf for his excellent (and patient!) discussion sections because those really cemented the class for me. Ken Farley and John Eiler's isotope geochemistry class was mind-blowing. I entered not knowing what a harmonic oscillator was and I finished by enriching uranium for a nuclear reactor (well, in writing) and being able to join discussions on mantle overturn in Petrology Reading Group. I also want to thank John for always being eager and willing to hear about my latest science; it's been great to know I can always pop by his office and ask a question about the SIMS, metamorphism, carbonates, or anything! Mike Lamb has been both a fun collaborator (who knew a coffee consultation could turn into a cool paper?) and a dependable source of calculus, teasing, and scientific encouragement and for that I thank him. I am grateful to Ken Nealson for his ever-positive attitude and contagious joy in all things manganese - I always leave discussions with Ken feeling on top of the world (as well as full of exciting ideas!). And finally I want to extend my gratitude to John Grotzinger, who has amazingly enabled me to see the wonderful and wacky stromatolites of Oman, awesome

evaporites, cements, and fossils in Texas, magnificent iron formations and carbonates in western Australia, and the modern carbonate platform of the Turks and Caicos. I am so very lucky to have been in the field with John, because it is inspiring to see rocks through his laser-eye focus on details which he can then fold into understanding the broader geology. He is one of the few people who you discuss science with and it becomes poetry.

I would also like to thank a few professors from Brown University, where I received my undergraduate degree: Jan Tullis, Jessica Whiteside, and Tim Herbert. Jan has been the epitome of a perfect advisor since my first day at Brown. She always cared so much about which classes I took and what I thought of them, helped me obtain research positions and teaching assistant jobs, had written notes on my goals and did everything she could to help me accomplish them, and has remained in touch since I graduated. Jessica took me to Scotland, where I realized I loved field work, and pushed me both to perform high-level research and apply to Caltech, and for that I am grateful. And Tim I must thank for teaching such wonderful earth systems history classes.

Several grad students were pivotal in my time here at Caltech. Kristin Bergmann, Anne Dekas, June Wicks, and Lauren Edgar were role models for me as smart, successful female scientists who also led balanced and happy lives, and they were also close friends. I am so glad to have overlapped with each of you. And Kristin I thank doubly, triply, and more! for many scientific insights and for encouraging me to explore detrital grains, for teaching me carbonate sedimentology, for career and life advice, and for being my fellow Arabic pupil learning from Younis, my general-venting buddy, and my dancing and drinking and pumpkin-carving friend.

I also want to thank my pit cohort: Stephen Cox, Jeff Prancevic, Elizabeth Trembath-Reichert, David Case, Sarah Slotznick, and Morgan Raven. From working through problem sets together to practice quals to help after bike accidents, it's been great having you all in my life. Alison Piasecki, thank you for the swimming and venting and keeping me sane at the end. I thank Lizzy Stefurak, Ted Present, Max Lloyd, and Guillaume Paris for all our science discussions and also our fun breaks from science. And I'm grateful to monthly wine tasting nights with Jessica Ricci, which have been great releases from lab frustrations. Pratixa Savalia taught me all the microbiology I know, and being partners with her on the hunt for the products of manganese reduction was one of the highlights of my dissertation. I also want to thank my housemate Lizzy Wilbanks for putting up with my weird thesis hours and intensive stress baking, and making me

take rollerblading and drinking and venting breaks. Chi Ma and Yunbin Guan have provided so much technical support on the SEM, electron microprobe, and the SIMS, and I thank them both for this. I am also very grateful to Liz Boyd, Alice Oh, and Kathy Lima for all their support over the years, and I'd like to extend particular thanks to Marcia Hudson, who has been a terrific help for all things administrative as well as times when I just need a smile and chocolate.

My labmates, past and present, have been both formative and supportive and I'm very grateful to them for scientific feedback, sitting through practice talks, and general support. And my officemates have been amazing for a crazy array of things – from drinking breaks to computer help to baked goods to fun science discussions. So thank you for everything to Jim Hemp, Lewis Ward, Jon Wilson, Renata Cummins, Itay Halevy, Sean Mullin, and a special thanks to Grayson Chadwick for all the Matlab and math help and Shawn McGlynn for all the evenings in the non-science world of music and cooking. And my non-Caltech friends, Ellie Wen and Tala Toufanian and Alex Smith, thanks to you all for helping me stay balanced through my thesis.

I also need to thank my family. Aunt Cheryl and Uncle Tim have let me escape to their seaside home several times during my thesis for sanity breaks, and have given me the perfect amount of encouragement and support. My parents have listened to me talk about manganese for far too long but listened and gave me feedback anyway. I especially want to thank my mom. Whether it was taking me to natural history museums growing up or letting me watch her biology documentaries with the wild heat-loving Archaea that awed me, my mom has continually fostered and supported my interest in biology, geology and the natural world. I'm so grateful that I can call my mom for help on any problem, from major life decisions to trivial complaints, and she's been my pillar of support for the last five years (and my whole life).

My last thanks goes to Wendy Van Norden, at Harvard-Westlake School. During my senior year of high school, I took an independent study in geology, and this class changed my life. Mrs. Van Norden presented all the evidence available at 1965 and let me re-discover the theory of plate tectonics; she took me to the field and showed me how to take a strike and dip and I figured out we were in a giant syncline; she taught me about the fossil and chemical clues recorded in rocks and I realized that I could study ancient rocks and help tell the story of life's origins and its complex journey to form the incredible diversity we know today. So really I'm here getting my PhD in Geobiology because of Wendy Van Norden. Thank you.

## ABSTRACT

Oxygenic photosynthesis fundamentally transformed our planet by releasing molecular oxygen and altering major biogeochemical cycles, and this exceptional metabolism relies on a redox-active cubane cluster of four manganese atoms. Not only is manganese essential for producing oxygen, but manganese is also only oxidized by oxygen and oxygen-derived species. Thus the history of manganese oxidation provides a valuable perspective on our planet's environmental past, the ancient availability of oxygen, and the evolution of oxygenic photosynthesis. Broadly, the general trends of the geologic record of manganese deposition is a chronicle of ancient manganese oxidation: manganese is introduced into the fluid Earth as Mn(II) and it will remain only a trace component in sedimentary rocks until it is oxidized, forming Mn(III,IV) insoluble precipitates that are concentrated in the rock record. Because these manganese oxides are highly favorable electron acceptors, they often undergo reduction in sediments through anaerobic respiration and abiotic reaction pathways.

The following dissertation presents five chapters investigating manganese cycling both by examining ancient examples of manganese enrichments in the geologic record and exploring the mineralogical products of various pathways of manganese oxide reduction that may occur in sediments. The first chapter explores the mineralogical record of manganese and reports abundant manganese reduction recorded in six representative manganese-enriched sedimentary sequences. This is followed by a second chapter that further analyzes the earliest significant manganese deposit 2.4 billion years ago, and determines that it predated the origin of oxygenic photosynthesis and thus is supporting evidence for manganese-oxidizing photosynthesis as an evolutionary precursor prior to oxygenic photosynthesis. The lack of oxygen during this early manganese deposition was partially established using oxygen-sensitive detrital grains, and so a third chapter delves into what these grains mean for oxygen constraints using a mathematical model. The fourth chapter returns to processes affecting manganese post-deposition, and explores the relationships between manganese mineral products and (bio)geochemical reduction processes to understand how various manganese minerals can reveal ancient environmental conditions and biological metabolisms. Finally, a fifth chapter considers whether manganese can be mobilized and enriched in sedimentary rocks and determines that manganese was concentrated secondarily in a 2.5 billion-year-old example from South Africa. Overall, this thesis demonstrates how microbial processes, namely photosynthesis and metal oxide-reducing metabolisms, are linked to and recorded in the rich complexity of the manganese mineralogical record.

## TABLE OF CONTENTS

Acknowledgements .....	iii
Abstract.....	vii
Table of Contents .....	viii
List of Figures and Tables.....	x
Introduction .....	1
 Chapter I: Manganese mineralogy and diagenesis in the sedimentary rock record .....	6
Introduction .....	7
Methods .....	22
Results.....	30
Discussion.....	49
Conclusions .....	58
Figures .....	61
Tables.....	79
References .....	80
Supplemental Figures and Tables .....	91
 Chapter II: Manganese-oxidizing photosynthesis before the rise of cyanobacteria ....	94
Introduction .....	95
Results.....	101
Discussion.....	107
Figures .....	112
References .....	116
Supporting Information.....	121
Supporting Figures and Tables.....	136
Supporting References .....	152
 Chapter III: O <sub>2</sub> Constraints from Paleoproterozoic detrital pyrite and uraninite .....	155
Introduction .....	156
Observations from the Transvaal Supergroup, South Africa .....	160
Combining Physical and Chemical Weathering Processes to Constrain Ancient O <sub>2</sub> Levels.....	170
Discussion and Conclusions.....	188
Figures and Tables.....	194
References .....	204
 Chapter IV: Real-time manganese phase dynamics during abiotic and biological manganese oxide reduction.....	215
Introduction .....	216
Materials and Methods.....	219
Results.....	223
Discussion.....	226
Figures .....	234
References .....	243

Supporting Figures .....	247
Chapter V: Manganese mobility during metamorphism: An example from the 2.5 Ga Kuruman-Penge Formation.....	249
Introduction .....	250
Geologic Setting .....	254
Materials and Methods .....	256
Results.....	260
Discussion.....	267
Figures and Tables.....	271
Supporting Tables.....	286
References .....	292
Concluding Remarks and Future Directions .....	296
Appendix A: Supergene manganese deposits: An example from South Africa.....	304
Tables and Figures .....	304
Appendix B: Pongola-Witwatersrand examples of Mn enrichments .....	306
Figures .....	310
References .....	314
Appendix C: Changing redox states in iron formations across the GOE .....	315
Figures .....	317
References .....	326



## LIST OF FIGURES AND TABLES

	<i>Page</i>
I. Introduction	
I.1 Redox tower with photosystems.....	2
I.2 Schematic of manganese cycle .....	3
1. Manganese mineralogy and diagenesis in the sedimentary rock record	
1.1 Manganese ore deposits through time.....	61
1.2 Mn K-edge X-ray absorption spectra of known manganese minerals .....	62
1.3 Light and electron microscopy of a seafloor manganese nodule.....	63
1.4 Seafloor manganese nodule XAS images and spectra.....	64
1.5 Japan Sea Miocene sediments light and electron microscopy.....	65
1.6 Japan Sea Pliocene-Miocene sediments XAS images and spectra.....	65
1.7 Jurassic-age Molango deposit light and electron microscopy .....	66
1.8 Jurassic-age Molango deposit XAS images and spectra .....	67
1.9 Santa Cruz Formation light and electron microscopy .....	69
1.10 Santa Cruz Formation XAS images and spectra.....	70
1.11 Hotazel Formation light and electron microscopy.....	71
1.12 Hotazel Formation XAS mapping and spectra .....	72
1.13 Koegas Subgroup light and electron microscopy .....	73
1.14 Koegas Subgroup XAS imaging and spectra.....	74
1.15 Light and electron microscopy of weathered Koegas Subgroup in outcrop ...	75
1.16 XAS imaging and spectra of weathered Koegas Subgroup in outcrop .....	75
1.17 Paleoproterozoic-age Kungarra Formation light and electron microscopy ....	76
1.18 Paleoproterozoic-age Kungarra Formation XAS imaging and spectra.....	77
1.19 Paragenetic model for the diagenetic stabilization of Mn deposits .....	77
1.SI.1 EBSD patterns and identifications.....	90
1.SI.2 Raman identification of caryopilite .....	91
1.SI.Table1 Survey of manganese ore deposits through geologic time .....	92
2. Manganese-oxidizing photosynthesis before the rise of cyanobacteria	
2.1 Stratigraphic columns of drill cores GEC01 and GTF01 .....	112

2.2 Light, Mn concentration, and Mn redox maps from Koegas Subgroup.....	113
2.3 Elemental maps and $\delta^{13}\text{C}$ of Mn-bearing carbonates.....	114
2.4 Multiple sulfur isotope ratio data from GTF01 and GEC01 samples .....	115
2.SI.1 Geologic map of Transvaal Supergroup in Griqualand West.....	136
2.SI.2 Lack of manganese oxidation in powdered samples.....	137
2.SI.3 Koegas Mn X-ray spectra compared with known minerals .....	138
2.SI.4 XRF maps and EDS mineral identification in Hotazel Formation .....	139
2.SI.5 Lack of manganese in mineralized cracks and vein-fill pyrite .....	140
2.SI.6 SEM images and elemental identifications of Mn in samples.....	141
2.SI.7 SEM images of detrital pyrite grains in sandstone from GTF01 .....	142
2.SI.8 Photomicrographs showing late pyrite textures .....	143
S.SI.9 Photomicrographs showing domains of chalcopyrite and galena .....	144
S.SI.10 Sulfur isotopic measurements <i>in situ</i> on a pyrite fracture.....	145
S.SI.11 GEC01 sulfur and carbon isotopic data plotted against depth.....	146
S.SI.12 GTF01 sulfur and carbon isotopic data plotted against depth .....	147
S.SI.Table1 Bulk Mn concentrations from both cores.....	148
S.SI.Table2 $\delta^{13}\text{C}$ and $\delta^{18}\text{O}$ measurements from both cores.....	150
 3. $\text{O}_2$ constraints from Paleoproterozoic detrital pyrite and uraninite	
3.1 Geologic map of Kaapvaal craton and map of Griqualand West study area..	194
3.2 Stratigraphic cross section of the Transvaal Supergroup .....	195
3.3 GTF01 stratigraphic section with locations of pyrite and uraninite grains....	196
3.4 Electron microscopy of sandstone textures .....	197
3.5 Pyrite distributions along ripple foreset laminae.....	198
3.6 Electron photomicrographs of detrital pyrite and uraninite examples.....	199
3.7 Chemical weathering as function of distance traveled and grain size .....	200
3.8 Calculated constraints on environmental $\text{O}_2$ levels .....	201
3.Table1 Reported occurrences of redox-sensitive detrital grains .....	203
3.Table2 Estimates of various detrital grain abundances .....	203
 4. Real-time manganese phase dynamics during abiotic and biological manganese oxide reduction	
4.1 Schematic of flow-through system .....	234

4.2 Representative microbial reduction experiments induced by <i>S. oneidensis</i> ...	235
4.3 Representative abiotic reduction experiments.....	239
4.4 Kinetic model of manganese reduction pathways.....	242
4.SI.1 Control experiment.....	247
4.SI.2 XRD of manganese standards and experiment product .....	248
 5. Manganese mobility during metamorphism: An example from the 2.5 Ga Kuruman-Penge Formation	
5.1 Core locations and core stratigraphic sections .....	271
5.2 Photographs of core samples and lithologies .....	272
5.3 X-ray fluorescence imaging of iron, calcium and manganese.....	273
5.4 Microscopic photographs of representative thin sections .....	275
5.5 X-ray spectroscopic imaging and electron microscopy of PA 2014m .....	276
5.6 X-ray spectroscopic imaging and electron microscopy of MF 402m.....	278
5.7 X-ray spectroscopic imaging and electron microscopy of PA 1470m .....	279
5.8 X-ray spectroscopic imaging and electron microscopy of MF 493m.....	280
5.9 X-ray spectroscopic imaging and electron microscopy of DI 218m .....	281
5.10 X-ray spectroscopic imaging and electron microscopy of WB 830m.....	282
5.11 X-ray spectroscopic imaging and electron microscopy of GKF 338.....	283
5.12 X-ray spectroscopic imaging and electron microscopy of GKP 242.....	284
5.Table1 Bulk Mn concentrations from selected samples .....	285
5.SI.Table1 Point elemental abundance measurements .....	286
 A. Appendix A: Supergene manganese preliminary results	
A.Table1 Comparing supergene deposit and underlying carbonate .....	304
A.1 X-ray absorption spectra of Mn deposit .....	305
 B. Appendix B: Pongola-Witwatersrand examples of Mn enrichments	
B.1 Mn- and Fe- enriched sandstone from DDN-1 core analyses .....	310
B.2 Manganese-enriched concretion from DBK-1 core analyses.....	311
B.3 Manganese-enriched sample from PNG-3 core analyses.....	313

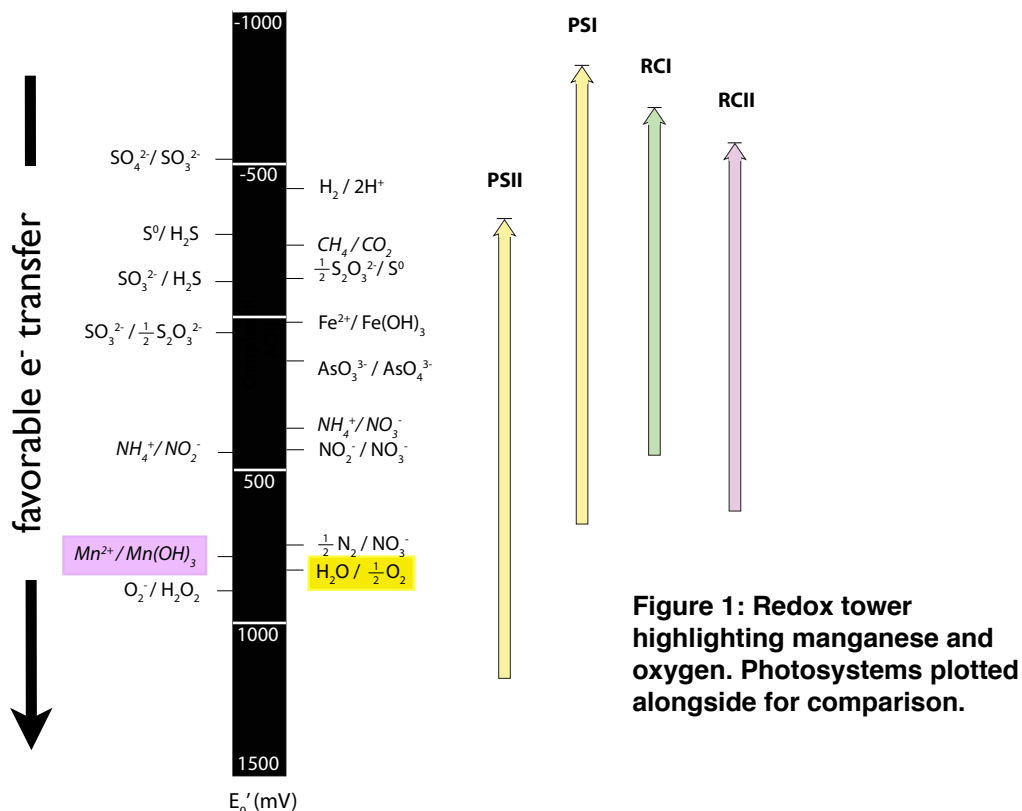
C. Appendix C: Changing redox states in iron formations across the GOE	
C.1 Representative samples from the Moodies Group.....	317
C.2 Representative sample from the Kuruman Formation.....	318
C.3 Representative regions from the Mt. Sylvia Formation .....	319
C.4 Representative area from the Koegas Subgroup.....	321
C.5 Representative area from the Hotazel Formation .....	322
C.6 Representative sample from the Gunflint Formation .....	323
C.7 Representative sample from the Rapitan Group .....	324
C.8 Representative sample from the Santa Cruz Formation, Brazil .....	325

## *Introduction*

The invention of oxygenic photosynthesis was difficult – it only occurred once relatively late in Earth history – and yet the oxygen this metabolism released fundamentally and forever changed our planet. The emergence of oxygen altered the biogeochemical cycles of iron, sulfur, carbon, nitrogen, and manganese, and transformed the fitness landscape for life - laying the foundations for the evolution of complex multicellularity. Manganese is critically important for the functioning of oxygenic photosynthesis, and thus the history of manganese is linked to one of the most pivotal evolutionary innovations on ancient Earth. Manganese oxides are also uniquely sensitive as proxies for ancient oxygen, and thus the geologic record of manganese offers compelling insights into both the history of environmental oxygen and oxygenic photosynthesis.

The use of manganese in oxygenic photosynthesis and its specific reactivity with oxygen stem from the thermodynamic properties of manganese. Manganese has a very high reduction-oxidation (or redox) potential, and consequently the only common environmental oxidants that can oxidize manganese are oxygen and oxygen-derived products like superoxide (Figure 1). Its redox potential and multiple stable redox states also make it an ideal cofactor for oxygenic photosynthesis: four manganese atoms in the water-oxidizing complex each donate an electron to Photosystem II, building oxidizing potential until they can split water and generate an O-O bond to form O<sub>2</sub>. The integral

role of manganese in water oxidation forms the basis of an evolutionary hypothesis that manganese-oxidizing photosynthesis was a transitional step between anoxygenic photosynthesis (PSI, RCI, RCII in Figure 1) and high-potential oxygenic photosynthesis (PSII in Figure 1).



Manganese has a further advantage: the dominant way for manganese to become concentrated in the sedimentary record is through oxidation, which requires oxygen or a high-potential photosystem to be present. So the presence of manganese oxides in the rock record can be understood as proxies for either oxygen or high-potential phototrophy using a photosystem oxidizing manganese (Figure 2). Without either of these two oxidation sources, manganese enters the fluid Earth from weathering of igneous rocks or

hydrothermal sources as  $\text{Mn}^{2+}$  and remains as an aqueous cation. The main sink for reduced manganese is substitution for calcium in carbonates, and this does not form a significant manganese enrichment (Figure 2).

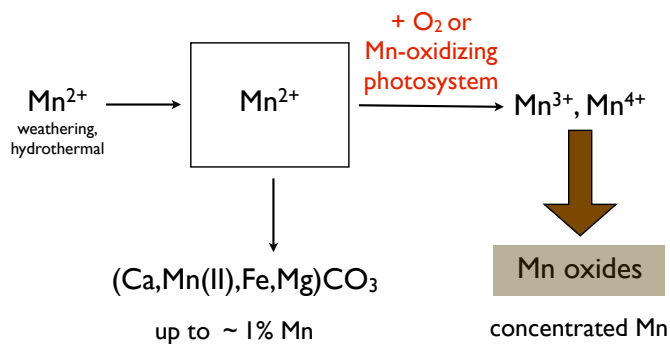


**Figure 2: Schematic representation of manganese redox cycle, including how manganese enters the sedimentary record.**

There are several potential problems with this simplified manganese model. Post-depositional processes (diagenesis) often affect the chemistry of sediments as they become lithified into a sedimentary rock, and the high redox potential of manganese makes manganese oxides an especially susceptible phase for diagenesis. Manganese oxides are highly favorable and reactive electron acceptors for a variety of organic carbon species, sulfur species, and iron species (Figure 1). Studying the geologic record of manganese therefore first requires an understanding of how diagenesis affects original deposits of manganese precipitates. Another potential complexity, especially important in very ancient sedimentary rocks, is that inferring manganese oxidation from manganese concentrates in the rock record only is accurate if manganese cannot enter the rocks another way. Secondary introduction of manganese needs to be always considered as an alternative hypothesis, and careful analysis is required to resolve whether manganese is

from original sedimentary processes or later introduction via metamorphic and metasomatic processes.

To study manganese in ancient, complicated rocks, we developed a multi-faceted approach applied throughout this dissertation. Inductively-coupled plasma mass spectrometry assessed bulk manganese concentrations. Synchrotron X-ray spectroscopic imaging and X-ray absorption spectroscopy were used to measure and map Mn redox and mineralogical state on a micron-scale. Textural relationships between mineral phases were established to understand relative timing of different manganese-bearing minerals using optical and electron microscopy, secondary ion mass spectrometry, and Raman spectroscopy. These whole-rock and *in-situ* techniques were all highly complimentary and proved essential to understanding the diagenetic history of the manganese minerals in ancient sediments.

The following dissertation focuses on how manganese minerals in the rock record can be proxies for diverse microbial processes, including photosynthesis and microbially-mediated manganese oxide reduction during diagenesis. Chapter 1 reviews the current literature on the various ways manganese can be oxidized and reduced, and presents a compilation of manganese-enriched sedimentary rock deposits ('manganese deposits') through geologic time. Selected manganese deposits were interrogated for manganese mineralogy and redox state, and these results led to a model proposing the mineralogical



changes induced during the diagenesis of manganese oxides. Chapter 2 employs South African drill cores obtained by the Agouron Drilling Project to investigate a hypothesis from evolutionary biology that Mn-oxidizing photosynthesis was a precursor to oxygenic photosynthesis. The cores had evidence of primary manganese oxides but two lines of evidence indicated oxygen was not present, and thus this manganese deposit is geologic evidence for a transitional Mn metabolism predicted by modern biology. One key observation to constrain oxygen levels here was redox-sensitive detrital pyrite, and so in Chapter 3 we expanded upon our findings and added the presence of a second oxygen-sensitive mineral, uraninite, and constructed a mathematical model to quantify the oxygen levels implied by these grains. Results from six ancient manganese deposits, presented in Chapter 1 and Chapter 2, all indicated that manganese is reduced during diagenesis, potentially via microbially-mediated mechanisms. These results inspired Chapter 4, in which a flow-through system at the synchrotron was developed to measure the phase transitions and mineralogical products during bacterial and abiotic manganese reduction. Chapter 5 returns to scrutinize the assumptions made in Figure 2 and uses a natural laboratory of correlated strata throughout South Africa that have seen dramatically different levels of heat, pressure, and hydrothermal fluids (i.e., metamorphism). Manganese concentrations increased and mineral speciation changed with increasing metamorphism, suggesting manganese can be mobilized and enriched by post-depositional processes but this can be understood using texture-specific techniques.

*Chapter 1***Manganese mineralogy and diagenesis in the sedimentary rock record**

Jena E. Johnson<sup>1\*</sup>, Samuel M. Webb<sup>2</sup>, Chi Ma<sup>1</sup>, Woodward W. Fischer<sup>1</sup>

<sup>1</sup>Division of Geological and Planetary Sciences, California Institute of Technology,  
Pasadena, CA 91125

<sup>2</sup>Stanford Synchrotron Radiation Lightsource, Stanford University, Menlo Park,  
CA 94025

**ABSTRACT**

**Oxidation of manganese(II) to manganese (III,IV) demands oxidants with very high redox potentials; consequently, manganese oxides are both excellent proxies for molecular oxygen and highly favorable electron acceptors when oxygen is absent. The first of these features results in manganese-enriched sedimentary rocks (manganese deposits, commonly Mn ore deposits), which generally correspond to the availability of molecular oxygen in Earth surface environments. And yet because manganese reduction is energetically favorable by a variety of chemical species, these ancient manganese deposits are often significantly more reduced than modern environmental manganese-rich sediments. We document the impacts of manganese reduction and the mineral phases that form stable manganese deposits from seven sedimentary examples spanning from the modern surface environments to rocks over 2 billion years old. Integrating redox and coordination information from**

synchrotron X-ray absorption spectroscopy and X-ray microprobe imaging with scanning electron microscopy and energy and wavelength-dispersive spectroscopy, we find that unlike the Mn(IV)-dominated modern manganese deposits, three manganese minerals dominate these representative ancient deposits: kutnohorite ( $\text{Mn}_{0.5}\text{Ca}_{0.5}\text{CO}_3$ ), rhodochrosite ( $\text{MnCO}_3$ ), and braunite ( $\text{Mn(III)}_6\text{Mn(II)O}_8\text{SiO}_4$ ). Pairing these mineral and textural observations with previous studies of manganese geochemistry, we develop a paragenetic model of post-depositional manganese mineralization with kutnohorite as the earliest diagenetic mineral phase and rhodochrosite and braunite forming secondarily.

## 1. INTRODUCTION

Manganese oxides are critical environmental reactants as powerful oxidants, scavengers of important trace elements and reactive oxygen species, and as electron acceptors for anaerobic respiration (C. R. Myers and Nealson, 1988; Tebo et al., 2005). Manganese is the third most abundant transition metal in Earth's crust and has the largest number of oxidation states of 3d row elements (Armstrong, 2008), and so consequently the manganese cycle involves multiple redox conversions.

Mn is present exclusively in divalent forms in a wide range of igneous minerals where it substitutes for iron (Post, 1999). It averages at 980 ppm or about 0.1% in ultrabasic, basaltic, granitic, and syenitic igneous rocks (Turekian and Wedepohl, 1961). However, in siliceous pegmatites, manganese can be more concentrated in garnets and phosphate

minerals, in addition to more obscure minerals like zirconosilicates, titanium silicates, and niobium and tantalum ore minerals (Iddings, 2009). Yet in bulk, pegmatites are still low in Mn, reaching up to approximately 0.23% Mn (Norton, 1970; Stilling, 1998; Akintola et al., 2012). Thus silicate weathering provides a substantial source of  $\text{Mn}^{2+}$  to surface and ground waters (Gross, 1965; Post, 1999).  $\text{Mn}^{2+}$  is also sourced from seafloor hydrothermal vents, at high but variable concentrations ranging from hundreds to thousands of micromoles per kilogram (Von Damm, 1990).

Manganese(II) is highly soluble, even more so than iron (Gross, 1965; Post, 1999). Strongly evaporative basins such as the Red Sea and Mediterranean Sea show no enrichment of manganese, but anoxic basins like the Black Sea can become enriched in soluble manganese(II) (Nicholson, 1997). To concentrate Mn into significant sedimentary deposits, manganese needs to be oxidized to  $\text{Mn}^{3+}$  or  $\text{Mn}^{4+}$  as these ions form insoluble oxyhydroxide minerals that are deposited in sediments (Calvert and Pedersen, 1996; Armstrong, 2008). Like iron, manganese is insoluble in its oxidized form, but unlike iron, manganese does not readily form sulfides (Van Cappellen et al., 1998; Maynard, 2010). Thus, the presence of significant manganese deposition in the sedimentary record should reflect the history of manganese oxidation.

However, there are a couple exceptions to this general pattern of manganese enrichment in the sediments signifying manganese oxidation. When there are high levels of soluble  $\text{Mn}^{2+}$ , this divalent ion can substitute for  $\text{Ca}^{2+}$  in carbonates and precipitate as Mn-

enriched carbonates. These carbonates are the main sink for  $\text{Mn}^{2+}$ : while other cations such as  $\text{Na}^+$  are removed from seawater by pore water burial and reverse weathering reactions (Berner and Berner, 2012), measurements of pore water today indicate that carbonate precipitation and dissolution seem to primarily control dissolved manganese(II) concentrations (Wallmann et al., 2008). Mn levels in carbonates are often used as a characteristic marker for secondary alteration (Brand and Veizer, 1980) since pore-water fluids are often enriched in manganese: this is due to sedimentary pore waters becoming enriched in  $\text{Mn}^{2+}$  due to the reduction and dissolution of Mn(IV) oxides (Calvert and Pedersen, 1996; Van Cappellen et al., 1998) and the elevated Mn concentrations in hydrothermal fluids (Von Damm, 1990). Despite Mn usually signifying alteration, primary well-preserved carbonates from the Archean Eon (4 Ga to 2.5 Ga) have elevated Mn levels—up to 1% Mn rather than typical Phanerozoic carbonates of 10-50 ppm in well-preserved carbonates (Veizer, 1978; Brand and Veizer, 1980; Holland, 1984; Beukes, 1987; Komiya et al., 2008; Fischer and Knoll, 2009). These anomalous Mn-enriched carbonate platforms probably occur because the oceans during this time were anoxic and able to concentrate soluble  $\text{Mn}^{2+}$  to relatively high levels (estimated at 3 to 7 micromolar, (Holland, 1984)). Karst weathering, the near-surface dissolution of carbonates from interaction with meteoritic waters, of Mn-bearing carbonates after the rise of oxygen can lead to supergene concentration of Mn as the carbonate is dissolved and  $\text{Mn}^{2+}$  is oxidized; this process can produce small but economically meaningful Mn ores such as the Postmasburg and Woodie Woodie Mn deposits (Gutzmer, 1996; Jones et al., 2013).

The high Mn levels in Archean seawater are directly related to the lack of Mn oxidation before the rise of oxygen, approximately 2.3 billion years ago. There is a very limited set of processes and oxidants able to oxidize manganese due to its high redox potential (Tebo et al., 2004). Low levels of manganese oxidation are possible, in principle, from reactions with UV light, but this is suppressed in the presence of  $\text{Fe}^{2+}$  or other reductants (Anbar and Holland, 1992). Manganese is oxidized phototrophically during the biosynthesis of the water-oxidizing complex of Photosystem II in Cyanobacteria, plants, and algae (Tamura and Cheniae, 1987; Büchel et al., 1999), but this is not thought to produce environmentally-significant manganese oxides (Madison et al., 2013) and no solely manganese-oxidizing photosystem has been documented in modern phototrophs (Johnson et al., 2013). With a notable exception (Johnson et al., 2013), Mn(II) is only oxidized at meaningful rates by molecular oxygen or  $\text{O}_2$ -derived species like superoxide (Calvert and Pedersen, 1996; Post, 1999; Tebo et al., 2004; Morgan, 2005; Dick et al., 2009; Hansel et al., 2012), so the presence of manganese(III,IV) oxides in sedimentary rocks can indicate that free oxygen was once present in the environment.

Due to the unique high-potential redox chemistry of Mn, the geologic record of manganese deposits should reflect ancient oxygen availability and the paleo-environmental chemistry (Maynard, 2010). In Fig. 1, we present an updated compilation of Mn deposits through geologic time, and also plot size estimates of each terrestrial deposit (Fig. 1, Table 1). The lack of significant Archean Mn deposits is striking, as is the

massive Hotazel deposit at around 2.22 billion years ago (Ga). Several previous compilations have included small Archean manganese deposits (Roy, 2006; Maynard, 2010), but these appear to be derived from later weathering of Archean carbonate strata (which contain elevated Mn(II)), and thus we do not include them as the timing of the weathering is unknown (Roy, 2006). Since oxygen was introduced into the atmosphere and oceans around 2.3 billion years ago (Ga) (commonly known as the ‘Great Oxidation Event’, or rise of oxygen) (Bekker et al., 2004; Hoffman, 2013), it is interesting that the world’s largest terrestrial manganese deposit—estimated to be 13,500 million metric tons (Taljaart, 1982)—was deposited soon after this dramatic environmental change occurred (Kirschvink et al., 2000). Manganese deposition appears to be associated with the presence of environmental oxygen, since manganese deposits post-2.3 Ga are common (Fig.1). Thus, Mn deposits provide insight into redox processes operating in surface environments on Earth.

To understand the genesis of Mn deposits in greater mechanistic detail, we chose to carefully investigate representative samples from seven globally-distributed manganese deposits spanning from the modern to 2.41 billion years ago. We coupled petrography and sedimentary geology using optical and electron microscopy with microscale X-ray absorption spectroscopy (XAS) imaging to better understand the manganese minerals present and the processes that produced them. From previous surveys of geologic manganese deposits, it is clear that there are significant variations in which manganese minerals are present in ancient manganese deposits (Okita et al., 1988; Roy, 2006;

Maynard, 2010); notably, the redox state of manganese varies in these minerals from Mn(II) to Mn(III) to Mn(IV). Maynard (2010) summarized the major minerals in manganese deposits as being braunite, a mixed valence Mn(III/II) oxide, and rhodochrosite, a Mn carbonate salt. He found that rhodochrosite dominated in sedimentary environments, braunite in volcanic deposits, and other Mn oxides in karstic and supergene environments (Maynard, 2010). Within sedimentary deposits, he proposed that rhodochrosite was a primary or early diagenetic (secondary) Mn mineral and that other Mn silicates and oxides (like braunite) arose during late diagenesis, metamorphism, or supergene alteration, but the only evidence for this hypothesis arose from  $^{13}\text{C}$ -depleted rhodochrosite in the major Mn deposits (Maynard, 2010). We tested this theory of manganese mineral paragenesis using classic sedimentological and petrographic observations at the scale of textures and mineral grains. We applied our microscale analyses to a range of sedimentary deposits to identify the sequence of mineralogical changes that occur to manganese deposits from deposition through early diagenesis, and metamorphism to near-surface oxidative weathering. These observations of manganese mineralization enable us to infer the likely primary precipitates that concentrated Mn in ancient sediments and the post-depositional processes that subsequently altered the manganese mineralogy and stabilized it in the rock record.

We begin by introducing the relevant environmental chemistry and biological influences on the modern manganese cycle, describe our observations of manganese deposits across



geologic time and paleo-environment, and then discuss how to connect biogeochemical processes to the rock record of manganese deposits.

### **1.1 Modern Manganese oxidation**

Several natural processes that oxidize Mn(II) to Mn oxides are currently known: all are either caused by O<sub>2</sub> or species derived from O<sub>2</sub> (like reactive oxygen species) or related to the photosynthetic production of O<sub>2</sub>. Prior to water-splitting and the production of molecular oxygen, Mn(II) is oxidized to Mn(III) and Mn(IV) in the high-valent tetra-manganese water-oxidizing complex of photosystem II (Tamura and Chéniaie, 1987; Büchel et al., 1999). To date, this is the only phototrophic mechanism known to oxidize Mn(II), with all currently known anoxygenic photosystems unable to generate the necessary high redox potential necessary for Mn oxidation. Abiotic photochemical oxidation of Mn(II) is slow and further hampered by the presence of other reductants such as Fe(II) (Anbar and Holland, 1992). Consequently, the presence of manganese oxides is generally associated with oxygen availability.

Today effectively all aquatic Mn-oxidation is controlled by biology (Tebo et al., 2004; Geszvain et al., 2012). Manganese oxidation by aerobic microorganisms occurs in diverse groups of bacteria (Firmicutes, Actinobacteria, Alphaproteobacteria, Gammaproteobacteria, and Betaproteobacteria) as well as in several types of fungi (in the Basidiomycota and Ascomycota phyla) (Hansel et al., 2012; Geszvain et al., 2012). The adaptive function of this physiology remains unclear, and none of these organisms are

known to conserve energy through this process. The pervasive distribution of Mn-oxidizing capabilities throughout such a diversity of organisms suggests that there may be multiple advantages to performing this reaction. A variety of potential functions for Mn oxidation has been proposed, including protection from UV light, predation, viruses, toxins, and reactive oxygen species, or the breakdown of refractory organic polymers into more readily usable compounds, the storage of an electron acceptor for future anaerobic respiration, or the scavenging of trace metals for micronutrient requirements (Tebo et al., 2004).

The mechanisms of microbial manganese oxidation are somewhat better understood than the biological purposes of the reaction. Some bacteria, like *Bacillus* species, use outer membrane multicopper oxidase enzymes to oxidize Mn(II) to Mn(III) and then to Mn(IV) in two sequential enzymatic oxidation steps (Samuel M. Webb et al., 2005), where the final released product is a Mn(IV)-dominated oxide like birnessite (a manganese(IV) oxide with variable amounts of Mn(III) due to substitution by Na, K, and Ca) (Bargar et al., 2000; John R Bargar et al., 2005; S. M. Webb et al., 2005; Butterfield et al., 2013). Other bacteria, like the alphaproteobacteria *Aurantimonas manganoxydans* and an *Erythrobacter* strain, appear to use an animal heme peroxidase enzyme to oxidize Mn(II) to Mn(III), which may represent an independent Mn-oxidizing mechanism in bacteria using H<sub>2</sub>O<sub>2</sub> or which may work in concert with multicopper oxidases (Anderson et al., 2009). Certain fungi, like the Basidiomycete fungi, also use manganese peroxidase to oxidize Mn(II) to Mn(III) via H<sub>2</sub>O<sub>2</sub> (Wariishi et al., 1992). In this better-studied fungal

system, the Mn(III) produced by these peroxidases is used to form reactive complexes with organic molecules, which then can be utilized to degrade lignin and become catalytically re-reduced to Mn(II) (Hammel et al., 1989; Perez and Jeffries, 1992). If not properly ligated, the Mn(III) disproportionates to Mn(II) and Mn(IV) oxide phases (Perez and Jeffries, 1992) and the ultimate manganese product from fungal Mn oxidation appears to be birnessite-like Mn(IV) oxide phases (Santelli et al., 2011). Recently, manganese oxidation via superoxide production has been discovered in both bacteria and fungi (Learman et al., 2011; Hansel et al., 2012). This superoxide-stimulated oxidation appears to proceed through an Mn(III) intermediate, with some loss to Mn(III) ligands but eventually producing a final Mn(IV) oxide precipitate that is poorly crystalline, similar to other biologically produced Mn-oxides (Learman et al., 2011; Hansel et al., 2012). While it is difficult to tie environmental data to a specific molecular oxidation mechanism, rates of microbial manganese oxidation in the environment have been measured up to 50 nM per hr (Clement et al., 2009), yielding an oxidation rate constant of up to  $\sim 10 \text{ hr}^{-1}$  (Morgan, 2005). These rates are much more rapid than abiotic oxidation mechanisms and indicate that microbial manganese oxidation is a key feature in the oxidation of Mn(II) in marine waters, and potentially in a wide variety of environments.

Mn(II) oxidation will also occur abiotically from reaction with environmental  $\text{O}_2$ , but the oxidation is thermodynamically inhibited by the first electron transfer step (Diem and Stumm, 1984; Morgan, 2005; Luther, 2010). For homogenous oxidation (without any surface catalyst), Morgan (2005) estimated the oxidation rate constant to be  $10^{-4} \text{ hr}^{-1}$

under modern atmospheric conditions, pH 8 and 7.5  $\mu\text{M}$  Mn(II). This implies a Mn(II) half-life of 200 to 300 days, and measurements suggest similar rates in sterile seawater (von Langen et al., 1997; Morgan, 2005). Experimental results indicate that Mn(II) is first oxidized by  $\text{O}_2$  to either the Mn(II,III) oxide hausmannite ( $\text{Mn}_3\text{O}_4$ ) or the Mn(III) oxyhydroxide feitknechtite ( $\beta\text{-MnOOH}$ ) (Hem and Lind, 1983). While these phases can be stable for months, eventually disproportionation reactions will yield the more stable phases and species of  $\text{MnO}_2$  and  $\text{Mn}^{2+}$ , respectively (Hem and Lind, 1983; Murray et al., 1985). Metal oxide surfaces can hasten this abiotic oxidation reaction due to adsorption-oxidation processes, with an oxidation rate about an order of magnitude greater under modern  $\text{O}_2$  levels ( $10^{-3} \text{ hr}^{-1}$ , (Davies and Morgan, 1989; Morgan, 2005). Laboratory experiments have measured feitknechtite ( $\beta\text{-MnOOH}$ ) as the primary precipitate from these surface-stimulated (or heterogeneous) Mn oxidation reactions (Junta and Hochella Jr., 1994). Junta and Hochella measured manganite (a more stable form of Mn(III) oxyhydroxide,  $\gamma\text{-MnOOH}$ ) as a secondary product. These experiments also suggested that the modeled abiotic oxidation rates may be underestimating the amount of oxidation occurring, as micro-scale techniques revealed Mn oxide formation within minutes (Junta and Hochella Jr., 1994; Junta-Rosso and Hochella Jr., 1996). While these abiotic Mn(III) oxyhydroxides were quite stable, the authors hypothesized that the Mn(III) oxyhydroxides would disproportionate to form  $\text{Mn}^{2+}$  and pyrolusite ( $\beta\text{-MnO}_2$ ) or birnessite.

Another way Mn(III) phases form is by redox reactions between  $\text{Mn}^{2+}$  and Mn(IV) oxides, known as comproportionation reactions. Bargar et al (2005) demonstrated that in abiotic experiments, Mn(IV) and aqueous Mn(II) reacted to form feitknechtite ( $\beta$ - $\text{MnOOH}$ ); this Mn(III) product was stable for days (John R. Bargar et al., 2005). Mandernack et al (1995) had calculated that feitknechtite-sodium birnessite equilibrium occurred at approximately 500  $\mu\text{M}$  Mn(II), implying that birnessite will be stable at Mn(II) concentrations below 500  $\mu\text{M}$  but for Mn(II) levels higher than 500  $\mu\text{M}$ , feitknechtite will be stable. The comproportionation process to form the Mn(III) in feitknechtite involves electron transfer from adsorbed  $\text{Mn}^{2+}$  to Mn(IV) atoms in birnessite; feitknechtite was later replaced by manganite ( $\text{MnOOH}$ ), a more stable Mn(III) oxyhydroxide (Elzinga, 2011).

Recent studies observed abundant Mn(III) in suboxic water and sediments, stabilized by organic complexes (Trouwborst et al., 2006; Madison et al., 2013). This Mn(III) was determined to be dominantly formed during Mn(II) oxidation by  $\text{O}_2$ , but may also be produced during biotic and abiotic Mn(IV) reduction and by photosynthetic Mn(II) oxidation during oxygenic photosynthesis to a lesser extent (Madison et al., 2013). At low oxygen levels (3 to 25  $\mu\text{M}$ ), up to 90% of the Mn was in soluble Mn(III) complexes, likely stabilized by organic ligands (Madison et al., 2013). This Mn(III) can participate in redox reactions in the suboxic zone, but would be reduced to Mn(II) or oxidized to Mn(IV) if exposed to different redox conditions (Madison et al., 2013). As reactive intermediates, these Mn(III) complexes can participate in both reduction and oxidation

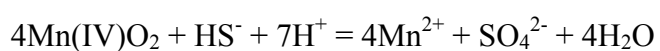
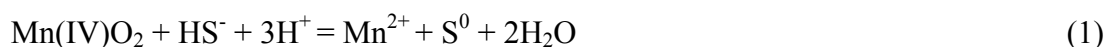
reactions and thus be a powerful addition to the redox cycling that occurs in suboxic zones (Madison et al., 2013).

Regardless of whether the oxidation mechanism is abiotic or biologically-mediated, the final products of manganese oxidation seem to be Mn(IV) oxides such as birnessite and pyrolusite. When observed in the environment, Mn(IV)-dominated, poorly crystalline, layered oxides are the ultimate product of Mn(II) oxidation in the Saanich Inlet, the Black Sea, desert varnish, lake sediments, and Pacific ocean sediments (Murray et al., 1985; Wehrli et al., 1995; McKeown and Post, 2001; Tebo et al., 2004).

## **1.2 Modern manganese reduction**

From comparing the reduction-oxidation (redox) potentials of Mn and other redox-active ions and molecules, the thermodynamics of manganese oxide reduction is highly favorable when coupled to common environmental reductants. Furthermore, the kinetics of Mn(IV)-oxide reduction, unlike Mn(II) oxidation, are rapid (Stone and Morgan, 1984; Dollhopf et al., 2000). Manganese oxide reduction has been documented in many experiments, from more common species such as sulfide and ferrous iron (Burdige and Nealson, 1986; C.R. Myers and Nealson, 1988; Thamdrup et al., 1993) to less common As- and U-bearing compounds (Fredrickson et al., 2008; Ying et al., 2011). More complex aromatic organic molecules related to humic substances have also been shown to reduce manganese oxides (mainly Mn(III)), while simpler aromatic substrates like carboxylic acids were unreactive (Stone and Morgan, 1984). The electron donor in these

reactions is important: for example, in sulfide-coupled manganese(IV) reduction that produces both elemental sulfur (Burdige and Nealson, 1986) and/or sulfate (Aller and Rude, 1988; Thamdrup et al., 1993), protons are required and thus these reactions are a source of alkalinity:



The alkalinity that this reaction produces (4 to 7 units/ mole  $\text{MnO}_2$ ) contrasts with another common mechanism to reduce manganese, coupling Mn(IV) reduction to iron oxidation:



When reduced by iron, manganese reduction actually produces protons and decreases alkalinity. More studies are needed to understand how prevalent these abiotic Mn(IV) reduction reactions are in nature.

Another mechanism of manganese oxide reduction occurs when dissimilatory metal-reducing microbes respire manganese oxides, depositing electrons on Mn(III,IV) oxides and generating Mn(II) while oxidizing organic carbon. Using a generic form for organic

carbon, this reaction produces alkalinity (2 units/ mole  $\text{MnO}_2$ ), although not as much as sulfide-induced Mn reduction:



Using lactate or pyruvate (more complex and realistic organic substrates), the reaction produces roughly the same amount of alkalinity (2.2 units/ mole  $\text{MnO}_2$ ; the alkalinity yield will only change substantially with more reduced C substrates). This type of anaerobic respiration was discovered in the 1980s in *Shewanella oneidensis* and *Geobacter* (Lovley and Phillips, 1988; C. R. Myers and Nealson, 1988) and has been widely documented in modern environments (e.g., Aller, 1990; Van Cappellen et al., 1998; Thamdrup et al., 2000). It can be difficult to diagnose what reductant or type of reduction, abiotic or biotic, results in the disappearance of Mn oxides and  $\text{Mn}^{2+}$  release (e.g., Canfield et al., 1993). However, the prevalence of Mn-reducing bacteria (for example, the well-studied metal-reducing *Shewanella* species have been found in marine, freshwater, soil, and sedimentary environments) suggests that a large portion of manganese reduction is microbially mediated.

Environmentally, evidence for manganese oxide reduction in soils and sediments is abundant (Aller, 1990; Canfield et al., 1993; Calvert and Pedersen, 1996; Van Cappellen et al., 1998; Thamdrup et al., 2000). When manganese oxides are deposited in marine sediments and subsequent manganese reduction (biotic or abiotic) occurs in sedimentary



pore waters, the Mn(II) concentrations increase dramatically—from the nanomolar Mn(II) concentrations in seawater to tens of micromolar in porewaters (Calvert and Pedersen, 1996). If there is sufficient dissolved inorganic carbon, especially if organic carbon is being respired using Mn(IV) oxides, Fe(III) oxides, or sulfate to produce additional CO<sub>2</sub>, then Mn(II) and CO<sub>3</sub><sup>2-</sup> can become supersaturated and manganese-bearing carbonates will precipitate (Calvert and Pedersen, 1996; Bergmann et al., 2013):



Because of the alkalinity produced (Reaction 3), Mn-carbonate precipitation is directly promoted by Mn oxide reduction without any need for other types of respiration.

Indeed, manganese carbonate precipitation from microbial manganese oxide reduction has been widely observed in laboratory experiments (Fischer et al., 2008; Ying et al., 2011; Lee et al., 2011). Ancient manganese carbonates have also been interpreted as products from Mn(IV) oxide reduction by heterotrophic organisms (e.g., Coleman et al., 1982; Okita et al., 1988; Matsumoto, 1992; Okita and Shanks, 1992; Johnson et al., 2013). A key line of evidence for this hypothesis is in the carbon isotopes of the manganese carbonates from these deposits: they are variably but strongly <sup>13</sup>C-depleted, suggesting that their carbon is derived from mixtures of dissolved inorganic carbon from seawater and CO<sub>2</sub> originating from <sup>13</sup>C-depleted sedimentary organic matter. Manganese oxides reduced stoichiometrically with organic compounds would produce <sup>13</sup>C-depleted

CO<sub>2</sub>, reduced Mn(II), and alkalinity (see Reaction 3), and these factors would promote the precipitation of Mn(II) carbonates and explain the unusual isotopic signatures of typical Mn-bearing carbonates in certain manganese deposits. Thus, not only does manganese reduction appear to be ubiquitous in modern environments, but this process appears to have ancient origins.

## 2. METHODS

Understanding the mineralogy, geochemistry, and petrogenesis of manganese-rich sedimentary rocks presents several challenges: the deposits are large but the materials are complex at fine scales, and thus require both microscale observations and basin-scale integration. The ideal way to determine redox state and mineral host at multiple scales is X-ray absorption spectroscopy coupled to light and electron microscopy techniques. Occasionally, more information is required, demanding the use of other methods.

One approach to assess the redox properties of manganese in a sample has focused on electron paramagnetic resonance (EPR) spectroscopy. EPR is an extremely sensitive technique to measure molecules with unpaired electrons (including Mn(II) and Mn(IV) species), and it has been useful for understanding the electronic structure and redox states of Mn in biochemical systems (see More et al., 1999; McEvoy and Brudvig, 2006). However, when this technique is applied to geological samples, results can become more complicated and nonunique. From observations of particularly narrow EPR line widths, it was suggested that EPR could be useful for distinguishing the biogenicity of the oxides

(Kim et al., 2011). Yet in concentrated geological samples, dipole-dipole interactions between closely packed Mn atoms affect the EPR signals (Pingitore Jr. et al., 1988). Thus, when Mn is concentrated in samples, it is difficult to distinguish Mn(II) minerals like rhodochrosite ( $\text{MnCO}_3$ ) from Mn(III) or Mn(IV) minerals (Pingitore Jr. et al., 1988). Furthermore, EPR of samples is effectively a bulk measurement that requires sample homogenization and thus does not pair redox data to mineral textures.

A more ideal technique for manganese-rich rock samples is synchrotron-based X-ray absorption spectroscopy (XAS), a powerful method that measures the chemical properties of a specific element (or elements) within a sample. The absorption K-edge, or the ionization threshold of an element, is the energy required to remove an inner shell electron from an atom of that element. The absorption spectrum is sensitive to the local electronic and bonding environment of the absorbing element, and thus the absorption spectrum indicates the absorbing atom's oxidation state and coordination environment. The XAS spectra can be measured either using a transmission detector, which can then be converted to absorption by comparing energy received as compared to incoming energy, or using a fluorescence detector binned for the appropriate element. Generally in rock samples, X-ray fluorescence is measured since the transmission signal is absorbed by the thick sample and/or glass slide.

There are other, more indirect ways to measure the redox state of manganese, but they either also operate in bulk or do not offer a definitive redox measurement. Titration

methods can give the average redox state of a bulk sample (e.g., Moore et al., 1950), but cannot distinguish mineral host or map redox state at a textural scale. X-ray diffraction (XRD) methods yield the crystal structures present in samples, which can lead to a definitive mineral identification implying redox state, but a bulk XRD measurement cannot show the small-scale relationships between minerals or detect rare and fine-grained or amorphous phases, all of which are vital for understanding the minerals' depositional history. Electron backscatter diffraction (EBSD) on the scanning electron microscope (SEM) can match smaller-scale textures to mineral diffraction patterns, but not all minerals give good diffraction patterns and EBSD is limited by the small area of focus of the SEM. Furthermore, in carbonates (an important phase in ancient manganese deposits), chemical substitution causes variety in mineral structure and ambiguous XRD identifications (Matsumoto, 1992).

Using synchrotron-based X-ray absorption spectroscopy, one can definitively identify mineral host and distinguish redox states clearly by fingerprinting, or comparison to standards (Fig. 2). Bulk powders of the rocks can be measured for overall mineralogy and redox state to extend data to larger scales, but thin sections of the rock can also be produced and analyzed using a spatially-resolved XAS microprobe to understand small-scale relationships. The microprobe can be used to measure X-ray fluorescence for a particular element on a micron scale by rastering the X-ray beam across the sample. X-ray absorption spectra for a particular element can also be obtained at targeted points, providing parallel information on the overall chemistry as well as precise redox and

mineral information. Furthermore, the microprobe can produce ‘redox images’ of a sample by measuring the X-ray fluorescence across a sample at several energies through the absorption edge of interest (Mayhew et al., 2011; Webb, 2011; Johnson et al., 2013). These multiple-energy maps are subsequently reduced by fitting to internal standards to a redox map, thereby creating an image of variations in phase and/or redox state at a  $\sim 2\ \mu\text{m}$  scale of a given element within a sample.

XRD methods and other light and electron-based microscopy can effectively be used to complement X-ray absorption spectroscopy measurements to produce a thorough understanding of a manganese deposit. Light and electron microscopy are crucial for understanding phase relationships as observations can be made on the same scale as mineralogical textures, allowing one to distinguish more primary minerals from cross-cutting or vein-filling phases. SEMs with an attached X-ray energy dispersive spectrometer (EDS) or an electron microprobe with X-ray wavelength dispersive spectrometers (WDS) measures elemental abundances via characteristic X-ray fluorescence spectra that are suggestive and/or indicative of various minerals.

## **2.1 Sample acquisition and preparation**

We produced ultrathin ( $\sim 15\ \mu\text{m}$ ) sections from rock billets cut from each of our study sites and analyzed them using a diversity of methods. Ultrathin sections were made from rock billets by High Mesa Petrographics. For most samples, we also powdered  $\sim 200\ \text{mg}$  using a microdrill or an agate mortar and pestle to make a bulk measurement. Samples

were acquired from a variety of sources. The deep-sea manganese nodule was collected from the seafloor surface of the South Pacific Gyre by the deep-sea submersible robot ‘Alvin’ during the IODP oceanic cruise Expedition 329 in 2010. Four samples from the IODP Leg 128 cores held at the Kochi Core Center in Kochi, Japan were acquired by a sample request application. J.B. Maynard, from the University of Cincinnati, graciously donated a variety of his samples from the Molango manganese deposit in Mexico. T. Piacentini, then at University of Queensland-Brisbane, kindly donated one thin section and two powdered samples from the Urucum mine in Brazil for this project. Hotazel samples examined were collected from a well-preserved open mine by T. Raub and J. Kirschvink (Caltech). Koegas samples are derived from the Agouron drilling project and a trip funded by the Lewis and Clark Astrobiology Fund. Kungarra samples were collected by J. Johnson from the Bolgeeda-Turee Creek ‘Boundary section’ described in Williford et al (2011) during the course of an Agouron-sponsored field research excursion. The relevant geological contexts for each Mn deposit are described in the Results section.

## **2.2 Analytical methods**

We examined our thin sections with transmitted and reflected light microscopy to observe petrographic textures. We used the SEM-EDS to document small-scale relationships between textures and measure elemental distributions and abundances. The Caltech Geological and Planetary Sciences Division Analytical Facility houses a Zeiss 1550VP Field Emission SEM equipped with an Oxford X-Max 80mm<sup>2</sup> SDD EDS system. We

produced high-resolution images in backscatter detector imaging mode to enhance compositional contrast, as areas with higher average atomic numbers will generate more backscattered electrons. We used EDS to produce point elemental measurements and X-ray maps of regions. Quantitative elemental analysis provides relative accuracy of better than 5%.

We measured these powder and thin section samples at the Stanford Synchrotron Radiation Lightsource (SSRL). We used two imaging beam lines: beam line 10-2 and beam line 2-3. These experimental stations cover a wide range of beam sizes (2-100 microns) and incident X-ray energies (2-20 keV). With beam line 10-2, we use the larger beam size and high photon flux to perform rapid screening of thin sections. These qualities allow us to produce coarse-scale maps of a wide range of samples across the deposit volume, and determine representative domains to target with smaller-scale analysis. Beam line 10-2 maps were generated using a Vortex SII International Silicon drift detector to collect X-ray fluorescence signals for each  $\sim 30\text{-}100\text{ }\mu\text{m} \times \sim 30\text{-}100\text{ }\mu\text{m}$  pixel. Subsequently, at beam line 2-3, we mapped chosen regions of interest at four to five energies chosen to have redox- or mineral-distinctive X-ray absorptions (6551 eV, 6557/8 eV, 6562 eV, 6573/5 eV for Mn). These higher resolution maps at  $\sim 2\text{-}5\text{ }\mu\text{m}$  were produced with a  $2\text{ }\mu\text{m}$  beam using Kirkpatrick Baez mirrors for focusing, with X-ray fluorescence signals collected on a Vortex SII International Silicon drift detector. We measured X-ray absorption near edge structure (XANES) spectra at  $2\text{ }\mu\text{m}$  points in these maps to produce internal standards and to confirm best-fit assignments. When available,

we additionally measured bulk sample powder at beam line 4-1 to obtain the spectra for average manganese redox state and mineral phase. At beam line 4-1, we collected X-ray absorption spectra in both transmission and fluorescence mode using a Lytle detector for fluorescence detection. The energy of the experiment was selected using a Si(220)  $\Phi = 90$  crystal. We used a collimating mirror to help reduce harmonics in the beam and duplicates were run on all spectra for XANES scanning from 6310 to 7108 eV. Samples were prepared as monolayers of bulk sample powder on tape. All beam lines were calibrated using the pre-edge peak of a potassium permanganate  $[\text{KMnO}_4]$  standard defined as 6543.34 eV.

After initial observations that we had two end-members in the Mn-carbonate family, we measured XANES spectra of standards of kutnohorite and rhodochrosite. Our rhodochrosite standard from the Pachapaqui District, Peru has a relatively uniform composition averaging  $\text{Mn}_{0.97}\text{Ca}_{0.02}\text{Mg}_{0.01}\text{CO}_3$ . We had two kutnohorite samples, one from a 5cm crystalline cluster from South Africa and one microdrilled from carbonate nodules with a composition  $\text{CaMn}_{0.7}\text{Mg}_{0.3}(\text{CO}_3)_2$  in the South African Hotazel formation. The kutnohorite crystal cluster had a variable Mn:Ca ratio with some pure calcite but we use a homogenized powder approximated at  $\text{Ca}_{0.63}\text{Mn}_{0.36}\text{Mg}_{0.01}\text{CO}_3$  from an average of EDS spectra (chosen from spectra that had measurable Mn since XANES of only Mn will not measure pure calcite). Previous compilations had determined that rhodochrosite was an abundant mineral in many Mn deposits (Maynard, 2010) and kutnohorite also appeared to be an important phase in several ancient deposits of manganese, including the



giant Hotazel formation and the Koegas Subgroup in South Africa (Gutzmer, 1996; Tsikos et al., 2003; Johnson et al., 2013). Our standard spectra and sample measurements highlight the subtle XAS differences between rhodochrosite and a kutnohorite or Mn-bearing calcite. These differences arise from the expansion of the hexagonal unit cell of kutnohorite and calcite (kutnohorite ideally  $a = b = 4.850$ ,  $c = 16.340$ ; calcite ideally  $a=b=4.989$ ,  $c=17.061$ , crystal cluster standard measured  $a=b=4.949$ ,  $c=17.062$ ) as compared to rhodochrosite (ideally  $a = b = 4.7680$ ,  $c = 15.6350$ ; measured  $a=b=4.779$ ,  $c=17.062$ ), resulting in slightly larger distances from the central Mn to the carbonate groups and tertiary Ca and Mn shell distances. We harnessed these slight XAS differences to map the spatial distribution of these two carbonate types in carbonate-dominated Mn deposits, which enabled us to better understand the primary vs. secondary nature of rhodochrosite and kutnohorite in these formations.

Several sections contained previously unidentified minerals in terms of Mn XAS spectra and X-ray EDS spectra. Two were small Mn(IV) oxides identified from our Hotazel representative section and one was an abundant Mn(II) mineral from our Santa Cruz section. These and other samples were further examined using SEM-based electron backscatter diffraction (EBSD) and on the electron microprobe to quantify elemental abundance. Samples for EBSD measurements were additionally polished using a vibration polisher. EBSD patterns of minerals were indexed using crystal structure databases for identification and/or confirmation of mineral phase. Quantitative measurements of points from manganese-bearing carbonates and from minerals

unidentified by XAS spectrometry were made using a JEOL JXA-8200 advanced Electron Probe Microanalyzer (EPMA). This instrument is part of the Geological and Planetary Sciences Division Analytical Facility and is equipped with five wavelength dispersive X-ray spectrometers (WDS) and a tungsten electron source. The precision for elements were as follows for carbonates: Mn (0.6%), Ca (0.69%), Mg (1.5%), and Fe (1.1%). For Hotazel oxides and the Santa Cruz formation silicate, one-sigma precision was slightly different due to the different minerals: Al (1.9%), Fe (1.7%), Mg (1.7%), Ca (1.1%), Na (5.2%), K (5.3%), Mn (0.27%), and O (0.28%). Detection limits were 0.04 or better for all five elements. The Mn(II) mineral from the Santa Cruz section was further analyzed using Raman spectroscopy, a visible light (514nm) vibrational spectroscopic technique that probes molecular symmetry, using the Raman detector in the Mineralogy lab at Caltech.

### **3. RESULTS**

We have chosen a range of manganese deposits, from a variety of paleoenvironments and geologic intervals, to capture the mineralogical and textural diversity of manganese-enriched formations (Fig. 1, arrows). While there is significantly more mineralogical richness associated with hydrothermal and metamorphic manganese deposits, we focused this study on the best-preserved samples we could acquire from each of these deposits. We note that nearly all ancient rocks have been affected by late diagenetic, metamorphic, and metasomatic processes, and our observations highlight the key changes that have taken place. With that in mind, by combining traditional sedimentology and advanced

microscale techniques, we can piece together a common paragenetic sequence of mineral formation in Mn-rich sediments.

Modern manganese deposits and manganese-enriched rocks from 3 million years ago to 2415 million years ago were probed for overall manganese redox state, and meso- and micro-scale manganese mineral relationships. In seeking to understand the processes that alter manganese minerals through time, we developed efficient strategies to understand manganese mineralogy using synchrotron-based methods and synthesized a theory of manganese stabilization in the rock record. We also made fundamental observations documenting the important reduction processes that occur in ancient manganese deposits, as all ancient deposits are significantly more reduced (Mn(II) or Mn(II/III) phases) than modern deposits (Mn(IV) phases). See Table 1 for a summary of our results.

### **3.1 Modern manganese deposits**

Our calibration point for ‘modern’ manganese deposition was a deep-sea manganese nodule collected from the ocean floor. The deep-sea manganese nodule (Fig. 3) was collected from the South Pacific Gyre, an extremely oligotrophic area of the ocean where sedimentary organic fluxes are low and pore fluid oxygen levels remain high – within 150 to 250  $\mu\text{M}$  of  $\text{O}_2$  (Ingle et al., 1990). The expedition observed abundant Mn nodules on the seafloor surface, which consisted of a thin carapace of sediments (1-100 m) on top of  $\sim 100$  Ma ocean crust (Ingle et al., 1990).

The textures of this deep-sea manganese nodule, best observed under SEM, are quite striking (Fig. 3). The manganese presents as thin layers of isopachous cements with abundant inclusions of aluminosilicate detrital minerals that together manifest in a stromatolitic morphology. Brighter manganese oxide bands alternate with mixed manganese and iron oxides, and on a micron-scale, the bands vary from finely laminated to porous (Fig. 3). The manganese oxide phases are sub-micrometer disordered material intermixed with other phases in a replacive texture, and they generate no EBSD pattern as they are either amorphous or too finely crystalline to produce a discernible diffraction pattern.

By synchrotron analyses, the entire nodule consists of solely Mn(IV) oxides. Bulk samples and thin sections of all these modern-day manganese deposits were imaged using synchrotron-based redox and mineral mapping (Fig. 4). Fig. 4 shows manganese abundance as mapped on beam line 10-2 and reduced from multiple energy maps using fitting to produce a manganese redox map (see Methods). We also mapped smaller, representative areas at beam line 2-3 at a higher resolution and measured X-ray absorption spectra of specific points. X-ray absorption spectra from points and bulk powders are shown on the right with the most similar standard spectra. For this modern manganese deposit, birnessite was the best spectral match, and both redox mapping and point spectra indicate that manganese is dominantly present as Mn(IV) oxides. Others (Bargar et al., 2000; Tebo et al., 2004; John R. Bargar et al., 2005; S. M. Webb et al.,

2005) also determined that birnessite was the dominant oxide formed by manganese oxidation, and we therefore concur that birnessite is the stable Mn oxidation product.

### **3.2 Ancient manganese deposits**

While Mn(IV) oxides appear to be the primary Mn phase entering sediments, we consistently observe that Mn is converted to other phases by diagenetic (secondary) processes. To explore how manganese ends up stabilized in the rock record and probe which processes have affected the Mn mineralogy, we examined five Mn-enriched sedimentary deposits ranging from relatively recent material in ocean drill cores (3 million years ago) to the earliest large deposit of Mn in the rock record (2.4 billion years ago). Most of these ancient deposits are significant terrestrial Mn ores and are highlighted in Fig. 1. These Mn deposits not only cover an enormous expanse of time, but they also capture a variety of both modern and ancient environments: samples were acquired from South Africa, Brazil, Mexico, and the Japan Sea, and their environments have been reconstructed as varying from shallow marine to continental rift basin to deep ocean trench. Surprisingly, this diversity of Mn deposits displays relatively few predominant minerals, suggesting the operation of common and widespread diagenetic processes in Mn-rich sediments. Beginning with the most recent deposit and proceeding back through time, we describe the geologic setting, visual and electron microscopic observations, and finally the X-ray absorption measurements for each of these deposits.

### *3.2.1 Japan Sea Drill Core*

We studied materials from an ODP Site 799 core drilled in the Japan Sea that had reported high manganese levels from intervals > 50 meters below sea floor (Matsumoto, 1992). This ODP core was drilled into the Kito-Yamato trough, an organic carbon-rich deep trench formed as a failed rift basin in the center of the Japan Sea (Matsumoto, 1992). The sediments contain a suite of unusual diagenetic carbonates, including lansfordite (a hydrated magnesium carbonate), magnesite, and rhodochrosite, as well as calcite and dolomite. Rhodochrosite was reported in Quaternary to Miocene-aged rocks, especially abundant in Pliocene and upper Miocene sediments and interpreted as diagenetic. Calcian (22.5-38.5% Ca) rhodochrosite microspherules, about 2 to 12  $\mu\text{m}$  in diameter, were described as filling interstices of the matrix (Matsumoto, 1992). This sedimentological description and the depleted carbon isotopes (-4 to -15 ‰, reflecting incorporation of organic carbon-derived  $\text{CO}_2$ ) implies that the rhodochrosite was secondary (Matsumoto, 1992). Matsumoto (1992) observed several micrometer-sized bright spots in the rhodochrosite that he was unable to identify as either iron sulfides, or manganese or iron oxides (Matsumoto, 1992).

To examine the petrogenesis of manganese in this deposit, we acquired several samples from this core. Three samples (196m, 326m, 502m, Pliocene to late Miocene in age) were unlithified, but the deepest sample at 533m (from the Late-Middle Miocene boundary, approximately 11 million years ago) was sufficiently consolidated enough to make a thin section. Our thin section of core material at 533m had tan and darker brown carbonates

with scattered opaque minerals (Fig. 5). The top of the section was dominated by darker carbonates while the bottom half had a higher abundance of lighter tan carbonates but both were patchily distributed throughout the section (Fig. 5). SEM observations indicated that the tan carbonates were coarsely crystalline ferrous magnesium carbonates, which appear yellow-orange under transmitted light and a slightly darker grey in SEM photos. These are labelled  $(\text{Mg,Fe})\text{CO}_3$  but this represents a range of EDS measurements, which were  $\text{Mg}_{0.37-0.44}\text{Fe}_{0.32-0.37}\text{Mn}_{0.1-0.17}\text{Ca}_{0.09-0.14}\text{CO}_3$ . These coarse magnesian crystals have brighter rims, which we measured to be iron-enriched, with formulas of  $\text{Fe}_{0.44-0.52}\text{Mg}_{0.22-0.25}\text{Mn}_{0.15-0.21}\text{Ca}_{0.08-0.11}\text{CO}_3$ . The top half of the sample and a spot at the bottom, which appear darker brown in transmitted light and brighter grey in SEM photos, are much more manganese-enriched, and these areas have clusters of finer-grained calcium and manganese carbonates. In the top half of the section, we observed manganoan calcium carbonate similar to kutnohorite with a formula of  $\text{Ca}_{0.38-0.52}\text{Mn}_{0.29-0.41}\text{Mg}_{0.12-0.19}\text{Fe}_{0.03-0.06}\text{CO}_3$ . These finer-grained carbonate clusters were surrounded by the coarser-grained magnesian carbonates (Fig. 5). Upon close examination, the small dark brown spot at the bottom of the section is a combination of high-backscatter and low-backscatter minerals. Indeed, we found examples of both crystalline and finer-grained kutnohorite-like carbonates similar to the top half of the section, but these display rims and crystalline masses of a calcian rhodochrosite as well. This rhodochrosite had a formula range of  $\text{Mn}_{0.68-0.74}\text{Ca}_{0.21-0.25}\text{Mg}_{0.03-0.05}\text{Fe}_{0.01-0.02}\text{CO}_3$ . Both cross-cutting relationships and the finest-grained carbonates imply that the manganoan calcium carbonate phases were produced early during sedimentary diagenesis, suggesting the precipitating fluids were

both calcium- and manganese-rich. The coarser ferrous magnesium carbonate crystals that suggest later recrystallizing fluids were magnesium and iron rich, and the bright iron-rich rims of these crystals point to an even later introduction of more iron-enriched fluids. The rhodochrosite too appears to be tied to later diagenetic processes, either from manganese-rich fluids or recrystallization and redistribution of calcium and manganese from earlier manganoan calcite precipitates.

We measured all four samples for bulk powder XAS and mapped the thin section sample at 533m for manganese mineralogy and redox information (Fig. 6). One sample, IODP 326m, had a very weak absorption signal due to very low levels of manganese, and the spectra was difficult to identify besides observing a Mn(II) peak. The other samples were more clearly associated with the Mn-rich carbonate zones previously described (Matsumoto, 1992). The sample at 196m contains a mixture of kutnohorite ( $\text{Ca}_{0.5}\text{Mn}_{0.5}\text{CO}_3$ ) and rhodochrosite ( $\text{MnCO}_3$ ), best fit by linear combination to 58% kutnohorite and 42% rhodochrosite. At 502m, the kutnohorite influence on the spectra had decreased, with the fit yielding an estimate of 54% kutnohorite and 46% rhodochrosite. By 533m, the bulk spectra was fit by 52% kutnohorite and 48% rhodochrosite. It is notable that the rhodochrosite appears to be increasing with depth, suggesting that a greater degree of burial induces rhodochrosite replacement of kutnohorite. By X-ray mapping, manganese was present exclusively as Mn(II) in different carbonate phases; the bright minerals observed previously (Matsumoto, 1992) were iron sulfides, not Mn oxides. Multiple-energy X-ray fitting showed a dominance of



kutnohorite-like carbonates from the top of the section, similar to results from the SEM (Figs. 5 and 6), and a mixture of rhodochrosite and kutnohorite from the bottom manganese-enhanced spot. This hot spot shows a similar mixed pattern of rhodochrosite and kutnohorite in both light and dark grey backscatter on the SEM and the mapped kutnohorite/rhodochrosite distribution from XAS.

### *3.2.2 Mexican Molango Deposit*

The largest manganese deposit in North America is the Upper Jurassic-age (~155 Ma) Molango deposit in Mexico. During this time, Mexico's large rift basins had become open to marine waters and had developed a carbonate platform-shelf, lying behind a trough-island arc system (Scott, 1984). The manganese enrichments are hosted by marine limestone and have been determined to be primarily in rhodochrosite and kutnohorite, with the Mn ore zone directly overlying a black calcareous shale (Okita et al., 1988; Okita and Shanks, 1992). Okita et al (1988) proposed that the stratiform, laminated manganese-bearing carbonates formed from the diagenetic reduction of manganese oxides by organic carbon—a hypothesis supported by  $^{13}\text{C}$ -depleted carbon isotopic data from the Mn-enriched carbonates. Dispersed organic matter occurs throughout the manganese ore bed, suggesting that manganese oxide reduction had occurred in pore waters (Okita et al., 1988). The isotopic composition of the Mn-carbonates reflects a mixture of seawater and dissolved inorganic carbon (DIC) produced from the respiration of organic carbon; measured rhodochrosite carbon isotopes average at -13 per mill and

kutnohorite carbon isotopes covary systematically from -7 to 1.7 per mill with decreasing Mn content (Okita et al., 1988).

We examined a variety of samples from the Molango deposit via X-ray analyses and microscopy. Looking at the microscale textures of one sample [Aco 2.4m, all rhodochrosite by XAS], we found blocky crystals of ferrous rhodochrosite ( $\text{Mn}_{0.69}\text{Fe}_{0.16}\text{Ca}_{0.1}\text{Mg}_{0.04}\text{CO}_3$ ), potential dark grey pockets of the original matrix ( $\text{Ca}_{0.55}\text{Mn}_{0.24}\text{Fe}_{0.14}\text{Mg}_{0.07}\text{CO}_3$ ), and bright white rhodochrosite cements (bright white,  $\text{Mn}_{0.93}\text{Ca}_{0.06}\text{Fe}_{0.01}\text{CO}_3$ ) (Fig. 7). Although the highly recrystallized nature of the Molango deposit makes observing consistent cross-cutting relationships challenging, the extremely high Mn (24 to 93% of cations) content of the cements suggests the secondary precipitation enriches carbonates in Mn, and that perhaps the calcian carbonates reflect the earliest sedimentary phase. We measured XAS spectra on seven samples from throughout the Molango deposit from the Tetzintla section (T1) and the Acoxcatlan section (Aco) (Okita and Shanks, 1992) (Fig. 8). These showed rhodochrosite in the 0-9m range, where the Mn ore zone is located (Okita and Shanks, 1992), transitioning to a mixture of kutnohorite (71%) and rhodochrosite (29%) at 19m and then only kutnohorite well above the ore zone. We also mapped three representative thin section samples in detail for redox state and speciation on the X-ray microprobe (Fig. 8). These samples are dominantly rhodochrosite with small patches of kutnohorite in ore zone samples (Aco 0m and 2.4m, Fig. 8), consistent with observations from the SEM-EDS. When mapping for carbonate speciation in overlying non-ore samples, we found dominantly kutnohorite (T1

26.5m, Fig. 8), similar to previous results (Okita et al., 1988; Okita and Shanks, 1992). The highly recrystallized nature of the ore zone sample (Fig. 7) indicates that the ore zone may have undergone significant hydrothermal or metamorphic alteration.

### *3.2.3 Brazilian Santa Cruz deposit*

During the extreme Neoproterozoic glaciations, significant iron-and-manganese formations were deposited on several cratons (Hoffman and Schrag, 2002; Klein, 2005). One iron-manganese deposit from Brazil was described early on as the “youngest” banded iron formation remarkably enriched in manganese, from 27% to 45% Mn by weight (Urban et al., 1992). This deposit, in the Santa Cruz Formation, has age constraints between  $889\pm44$  Ma and  $587\pm7$  Ma (Hasui and Almeida, 1970; Piacentini et al., 2013) and is associated with diamictites. It is located in the Jacadigo Basin, an ancient continental rift basin that records the transition from clastic basin fill to lacustrine or marine gulf deposits that include iron and manganese formation and carbonate deposits (Freitas et al., 2011). While most authors consider the outsized clasts in the manganese and iron deposits as dropstones from glacial retreat (e.g., Urban et al., 1992; Klein and Ladeira, 2004), these have also been interpreted as rift-related mass flow deposits (Freitas et al., 2011).

Despite the still-contentious regional tectonics of the Jacadigo Basin, the Santa Cruz formation has been better studied in terms of manganese and iron mineralogy. There are four separate Mn-rich intervals throughout the formation, with manganese occurring as

nodules, as cements around clastic detritus, and as massive sedimentary horizons, separated by ferruginous sandstones and hematite jaspelites (Urban et al., 1992). Urban et al. identified cryptomelane, a K-bearing manganese oxide  $[\text{KMn(IV)}_6\text{Mn(II)}_2\text{O}_{16}]$ , as the dominant manganese mineral, but also found braunite  $[\text{Mn(III)}_6\text{Mn(II)O}_8\text{SiO}_4]$  and noted that braunite was replaced by cryptomelane and pyrolusite, another Mn(IV) oxide mineral  $[\text{Mn(IV)O}_2]$ . They found other accessory manganese minerals like lithiophorite  $[\text{Mn(IV)(Al,Li)O}_2(\text{OH})_2]$ , manganite  $[\text{Mn(III)OOH}]$ , and fissure-associated metamorphic minerals such as Mn-rich amphiboles and nambulite  $[\text{LiMn(II)}_4\text{Si}_5\text{O}_{14}(\text{OH})]$  (Urban et al., 1992). Later, Klein and Ladeira (2004) also described another manganese-bearing mineral from this deposit as manganoan dolomite, which they found in both the iron and manganese layers.

While the best manganese ore comes from surface-weathered supergene caps or hydrothermally-altered zones along faults (Klein and Ladeira, 2004), we focused on well-preserved underground samples, since weathering horizons in this area are very deep (Vasconcelos, 1999). We obtained one thin section sample and two bulk powder samples from the Brazilian Santa Cruz Formation. The thin section sample (SD92.11) came from over 2.5 km into an underground manganese mine at Urucum, and was collected away from faults or exposed surfaces. Thus, it provides a well-preserved example of the Santa Cruz Fm mineralogy. It is derived from the second stratigraphic manganese layer (Mn 2), which is the largest of the four layers (Urban et al., 1992). Another sample, a powder

sample also from the second manganese layer (SD92.07), was collected ~1km into the Urucum underground manganese mine, but along a fault.

SEM observations of the manganese-rich strata from the Santa Cruz Formation reveals that even the best-preserved materials contain a remarkably complex (compared to other deposits) assemblage of Mn minerals. While braunite ( $\text{Mn(III)}_6\text{Mn(II)SiO}_{12}$ ), rhodochrosite, and kutnohorite are present, and confirmed via EBSD (Fig. A1), there were other Mn minerals that were more difficult to identify (Fig. 9). In bulk XAS, the sample from the fault zone best matched cryptomelane, confirming that this is a prevalent mineral in the formation and suggesting that the faults through the Santa Cruz Formation have introduced oxidizing fluids to the rock surrounding the faults. However, the subsurface sample collected away from the surface and any faults was composed of only Mn(II) and Mn(III) minerals by X-ray mapping, with four distinctive minerals identified using our point spectra (Fig. 10). The Mn(III) minerals are mainly braunite [ $\text{Mn(III)}_6\text{Mn(II)O}_8\text{SiO}_4$ ], but the Mn(II) minerals consisted of kutnohorite, rhodochrosite, and another spectra we could not identify based on our standard suite (Fig. 2). We examined this phase using EBSD but found it was amorphous or too finely grained to generate a diffraction pattern. Textural observations indicated that this is a late-stage metamorphic phase, as it had a webbed and fibrous texture and appeared to be growing on and replacing kutnohorite (Fig. 9). By electron probe, we were able to identify that this mineral had a formula of approximately  $\text{MnSiO}_3$ , with 44.8% MnO, 35.6%  $\text{SiO}_2$ , 4.9%  $\text{Al}_2\text{O}_3$ , 2.28% FeO, 2% MgO, 0.5% Ca, and either water or hydroxide groups. This

is a good fit for caryopilite, but could be either caryopilite or kellyite, which are both metamorphic manganese silicates. We further examined the mineral using Raman spectroscopy and found that the best match was caryopilite (using the online RRUFF database). Kellyite has a completely different structure and Raman spectrum (Fig. A2).

### *3.2.4 South African Hotazel Formation*

The enormous *circa* 2.2 billion-year-old manganese deposit within the Hotazel Formation in the ancient Kaapvaal Craton of South Africa is a marine sedimentary deposit consisting of interbedded manganese-rich and iron-rich rock strata (Gutzmer, 1996). The timing of its deposition—soon after the first ‘great’ rise of oxygen—has invoked the hypothesis that the deposit might be recording interactions between the newly sourced O<sub>2</sub> and the iron- and manganese-rich ocean (Kirschvink et al., 2000). The Hotazel Formation was deposited in a marine setting, either in a back-arc setting with a distant volcanic source (Beukes, 1983) or a proximal mid-ocean ridge environment (Cornell and Schütte, 1995). Jaspilitic iron formation and manganese intervals overlie the subaqueous Ongeluk basalts and then transition into the Mooidrai Formation carbonate platform, which progrades across the basin from east to west (Gutzmer, 1996; Kirschvink et al., 2000). The three manganese ore units have been well-characterized as mineralogically braunite and kutnohorite (Gutzmer, 1996; Tsikos et al., 2003), but highly altered and hydrothermal regions of the Hotazel Formation have exotic minerals and spectacular gemstones (Cairncross and Beukes, 2013).

Electron and X-ray analyses of the Hotazel samples indicate that these two minerals—braunite and kutnohorite—are pervasive, but we observed several other interesting minerals as well. From our SEM imaging of samples from the Hotazel manganese formation, it is clear that braunite crystals cross-cut kutnohorite, indicating that kutnohorite was an earlier phase as compared to the braunite (Fig. 11). There is a recrystallized Mn-calcite phase (with about 10% Mn) that too cross-cuts the kutnohorite (Fig. 11). Micron-sized iron oxides appear to have precipitated even later than the braunite, as their mineral boundaries cut into braunite (Fig. 11, matrix). Using SEM-EDS, we observed several Mn or Mn-Fe oxides that did not appear to contain silicon, but we could not determine the mineralogy of these phases.

At the synchrotron, we measured braunite and kutnohorite by XAS on micromilled (bulk) powder from the dark matrix and bright white nodules of the Hotazel, and used X-ray mapping to confirm that braunite and kutnohorite dominate the deposit. However, X-ray mapping also indicated the presence of rare Mn(IV) oxide minerals that coincided with the silicon-free oxides we had observed on the SEM. Texturally, these Hotazel Mn(IV) minerals are very different from the modern manganese nodule oxides (Fig. 12) (or the surface-weathered samples of Kungarra Formation and Koegas Subgroup discussed in section 3.3), which appear fuzzy and soft. Instead, these Hotazel Mn oxides have a hard, mineralized texture. Several of these Mn(IV) oxides appear to be fibrous and are related to cross-cutting veins, and are likely related to later oxidizing fluids (Gutzmer, 1996) (Fig. 12). However, two of the discovered Mn(IV) oxide minerals are more consistent

with an early inclusion, or unreacted residue, of original sediment. One banded manganese oxide is cross-cut by two generations of kutnohorite and by a braunite crystal, implying that it was present in the sediments earlier than all three of these phases (Fig. 11). Another is a Mn and Fe oxide which is also cut by Mn-carbonate precipitates. We examined the two Mn(IV) oxide types, one fibrous and one layered manganese oxide (not mixed Mn-Fe oxide), using electron backscatter diffraction (EBSD) on the SEM, and found that they were crystalline but poorly matched by standard spectra. E-probe measurements of these two oxide types determined that the composition of the fibrous oxide is  $\text{Mn}_{0.84}\text{Na}_{0.04}\text{Ca}_{0.03}\text{Fe}_{0.02}\text{O}_2$  and the potential early inclusion is  $\text{Mn}_{0.85}\text{Na}_{0.05}\text{K}_{0.04}\text{Fe}_{0.03}\text{Ca}_{0.03}\text{O}_2$ .

### *3.2.5 South African Koegas Subgroup*

Also on the western side of the Kaapvaal Craton, there is an older manganese-enriched suite of rocks in the Koegas Subgroup of the Transvaal Supergroup. The Koegas strata are composed of mainly deltaic and near-shore marine siliciclastics intermixed with banded and granular iron formation, with a paleoenvironmental gradient from proximal to distal (broadly east to west). Manganese enrichments occur in clastic-starved intervals of iron formation deposition (Schröder et al., 2011; Johnson et al., 2013; Johnson et al., 2014). This Koegas Subgroup manganese deposit has been shown to pre-date the rise of oxygen and thus the manganese oxidation mechanism was inferred to be a manganese-oxidizing photosystem prior water-oxidizing photosynthesis (Johnson et al., 2013). From examining two drill cores (GEC and GTF) drilled as part of the Agouron Drilling project,



the manganese in the Koegas Subgroup was determined to be hosted entirely by Mn-bearing carbonates (Johnson et al., 2013).

With a manganese-enriched core sample from the Koegas Subgroup (11.6% MnO in bulk, Johnson et al, 2013), we focused on manganese-enriched carbonate nodules with clear compositional variations to examine the relationships between the different major Mn-bearing carbonate phases in the Koegas samples. While most core samples had micron-scale mixtures of Ca-Mn carbonates and Fe-Mn carbonates, a sample from core GTF at 230m shows discrete zonation of these minerals in carbonate nodules with signs of differential compaction. We measured the two carbonate endmembers, shown in SEM photos as bright white-grey (high backscatter) and darker grey (low backscatter), on the E-probe to measure exactly what these two minerals were and determined that they were composed of a  $\text{Mn}_{0.41}\text{Fe}_{0.41}\text{Mg}_{0.14}\text{Ca}_{0.04}\text{CO}_3$  (average of white-grey carbonate) and  $\text{Ca}_{0.48}\text{Mn}_{0.20}\text{Fe}_{0.18}\text{Mg}_{0.15}\text{CO}_3$  (average of dark grey carbonate) using 18 data points from all three nodules (Fig. 13). While these minerals are not strictly rhodochrosite nor kutnohorite, they comprise a solid solution between ferroan rhodochrosite, manganoan siderite, and manganoan calcite. All the carbonate phases in this sample appear to have been “ankeritized”, with 14 to 15 cation percent magnesium (Fig. 13).

We measured manganese and calcium abundance by XRF at the synchrotron to isolate the ‘rhodochrosite-like’ and ‘kutnohorite-like’ endmembers for further measurements. The general trends of Mn and Ca concentrations obtained from synchrotron based

microprobe observations are consistent with the E-probe measurements and backscatter-highlighted compositional differences. Microprobe XAS spectra through the Ca-rich and Mn-rich portions of the nodule show dramatic changes, with kutnohorite spectra correctly corresponding to the kutnohorite-like Ca-rich portions of the nodules and rhodochrosite spectra corresponding to the rhodochrosite-like Mn-rich areas (Fig. 14). We were able to map these two carbonate endmembers to indicate their discrete geographical distribution (Fig. 14). With the extent of recrystallization present in the Koegas, it is not possible to conclusively determine whether the manganoan siderite or the manganoan calcite is more primary (Fig. 13).

### **3.3 Surface-weathered deposits**

Many manganese deposits are not studied from core or mine samples, but instead from outcrop samples. While we are primarily interested in understanding the Mn mineralogy of diagenetically stabilized deposits and how these phases reflect processes during and after lithification, we also wished to understand how surface weathering changes the redox state and mineralogy of manganese deposits. We collected samples from three outcrop sites, two of which we also have studied in drill core or mine exposures for primary mineralogy, and we will compare the chemistry of Mn here to our more pristine samples.

From the Santa Cruz Formation manganese deposit, we obtained a sample (SD11.08) from a near-surface sample of the fourth manganese layer (position shown in Piacentini

et al, 2013). This sample represents a supergene, oxidized example of a similar provenance but with different preservation conditions for the Santa Cruz Fm than for the thin section sample previously discussed. The best fit for the spectrum from this sample measured in bulk powder was cryptomelane, identical to what was obtained from the fault-associated sample. This mineralization is likely associated with supergene enrichment and oxidative weathering of the more reduced manganese minerals from this deposit (Urban et al., 1992) (Fig. 10).

We also examined a sample from the 2.415 Ga Koegas Subgroup collected from surface outcrops near Rooinekke, which can be correlated to core samples. The outcrop sample comes from the thin microbialite and grainstone interval in the Rooinekke Formation of the Koegas Subgroup, which has intraformational grains of Mn- and Fe-bearing carbonate (see GTF 63.86m in Fig. 2 of Johnson et al, 2013). High-resolution SEM imaging showed that sub-micrometer Mn oxides intermixed with other phases in a replacive texture without a diffraction pattern (Fig. 15). The surface-weathered sample similarly shows discrete, but random, Mn-enriched zones, and the XAS measurements are most similar to the Mn(IV) oxides cryptomelane or birnessite (Fig. 16). EDS measurements show peaks of potassium and calcium but no sodium—which may be more consistent with Ca-enriched cryptomelane rather than birnessite. Like the Santa Cruz Formation sample, surface weathering again seems to have oxidized Mn(II) carbonate minerals to Mn(IV) oxides and destroyed textural information.

A sample from the Paleoproterozoic-age Kungarra Formation in Australia represents the third highly weathered manganese location. This sample comes from a thin sedimentary bed with 7% Mn just above the lower contact with the Bolgeeda Iron Formation (Williford et al., 2011). The original mineralogy is unknown, and the age constraints on the Proterozoic deposit are similarly uncertain. The Kungarra Mn horizon appears to be younger than 2449  $\pm$  3 Ma (Barley et al., 1997) and older than overlying 2209  $\pm$  15 Ma Cheela Springs Basalt (Martin et al., 1998) and older than intruding mafic sills dated at 2208 Ma  $\pm$  15 Ma (Müller et al., 2005). Detrital zircons in the Kungarra Formation restrict the depositional age to younger than 2420 Ma (Takehara et al., 2010). Thus, the Kungarra deposit may be a contemporary deposit to the Koegas strata, or it may be better correlated to the 2.2 Ga South African Hotazel manganese deposit. We note that the Hotazel deposit does lie above glacial deposits similar to the Kungarra Formation (Williford et al., 2011), but the Hotazel is significantly more Mn-enriched (up to 38% in well-preserved examples) than the Kungarra deposit, which only has 7.4% Mn (Williford et al., 2011), more similar to the Koegas manganese levels.

Light and electron microscopy of the Kungarra manganese-rich bed shows textures similar to the Koegas weathered samples that indicate Mn oxide replacements, and no EBSD pattern could be generated as the crystals are likely too small (Fig. 17). X-ray absorption spectroscopy indicates that the sample is universally Mn(IV) oxides, again either fitting birnessite or cryptomelane (Fig. 18). From the potassium and calcium in EDS measurements, this mineral is potentially cryptomelane  $(\text{KMn(IV)}_7\text{Mn(III)O}_{16})$ , a

common supergene product of Mn oxidation (Urban et al., 1992). The massive, fibrous texture of the Mn(IV) oxide shown by SEM (Fig. 17) highlights that the Mn(IV) is plainly secondary, likely enriched from original Mn-bearing minerals but possibly introduced by hydrothermal or other fluids.

These three examples indicate that while the kinetics of manganese oxidation may be slow (Morgan, 2005), the exposure to oxygen during long intervals integrated by weathering is effective at oxidizing all lower valent minerals to Mn(IV) oxide phases, and at the same time alters the primary textures.

#### **4. DISCUSSION**

From our survey of the mineralogy, textures, and chemistry of manganese deposits, we can divide our observations into three categories: 1) manganese deposits composed of essentially all Mn(IV) oxides, such as the modern seafloor manganese nodules or surface-weathered manganese deposits, 2) deposits where the Mn is found exclusively in Mn(II) carbonates, such as the Koegas deposit, the Molango deposit, and the IODP deposit, and 3) deposits with subequal mixtures of Mn(II)- and Mn(III)-bearing minerals like in the manganese-rich intervals in the Hotazel deposit and the Santa Cruz Formation.

In marine and lacustrine sediments manganese oxidation processes form Mn(IV)-dominated oxides like birnessite (Fig. 3; (Murray et al., 1985; Wehrli et al., 1995;

McKeown and Post, 2001; Tebo et al., 2004) and the reduction of these oxides produces Mn-carbonates (Thamdrup et al., 1993; Calvert and Pedersen, 1996; Fischer et al., 2008; Ying et al., 2011; Lee et al., 2011). Mn oxidation does appear to yield a Mn(III) intermediate that is observable as a short-lived (but potentially important) redox player in suboxic environments (Madison et al., 2013). However, it is not common to observe substantial accumulation of Mn(III) species because they typically disproportionate to  $\text{Mn}^{2+}$  and Mn(IV) oxides or are subsequently fully oxidized to Mn(IV) oxides that are added to the sediments (Perez and Jeffries, 1992; Wariishi et al., 1992; Samuel M. Webb et al., 2005; Anderson et al., 2009; Learman et al., 2011; Hansel et al., 2012). Reduction of Mn(IV) oxides also may proceed through a short-lived Mn(III) intermediate (Lin et al., 2012), but again, the final product of manganese reduction is  $\text{Mn}^{2+}$  (Lovley and Phillips, 1988; C.R. Myers and Nealson, 1988; Aller, 1990; Van Cappellen et al., 1998; Thamdrup et al., 2000). Thus the widespread observation of non-transient but stable and abundant Mn(III) phases in the rock record, as documented by this study and others (Gutzmer, 1996; Tsikos et al., 2003; Roy, 2006; Maynard, 2010), is intriguing and indicative of post-depositional processes.

Indeed, all the manganese from well-preserved samples of ancient deposits, whether 3 million years old or 2.2 billion years old, are all more reduced than the modern Mn-rich surface sediments (with the notable exception of rare  $\text{MnO}_2$  inclusions in some early diagenetic Hotazel kutnohorite nodules). These observations illustrate that there are common and effective post-depositional reduction processes that convert the Mn(IV)

precipitates in sediments to Mn(II) and Mn(III) minerals during early and late diagenesis. Using micro-scale observations of mineralogy and chemistry tied to petrographic textures, we can ordinate these different phases and develop a general framework for how post-depositional processes impact manganese mineralogy and redox state and determine a paragenetic sequence of manganese minerals.

#### **4.1 Paragenetic model**

The first precipitates to enter and concentrate Mn in sediments are Mn(IV)-dominated oxides. The deep-sea manganese nodule from the seafloor being fully comprised of Mn(IV)-dominated oxides lends support to this, as well as other reports of Mn(IV) oxides being the dominant precipitate produced by manganese oxidation (e.g., Tebo et al., 2004). The discovery of Mn(IV) oxide inclusions, which we propose is a primary residue from the original sedimentary precipitates on the basis of petrographic textures, is an additional line of evidence suggesting that these manganese deposits began as Mn(IV)-dominated oxides. The weathered samples of Mn-bearing rocks confirm that when oxygen is present for a sufficient amount of time, manganese seems to be dominantly oxidized and stabilized as Mn(IV)-oxide phases.

The precipitation of Mn(II)-bearing carbonates from the reduction of Mn(IV) oxides by organic carbon has been inferred previously from observations of the geologic record (Okita et al., 1988; Tsikos et al., 2003). Often, the diagenetic reaction is presented similar to Reaction (4), implying that rhodochrosite, or  $\text{MnCO}_3$ , is the reaction product.

However, we document in several formations (see the Koegas, Molango, Urucum, and Hotazel deposits) the priority of kutnohorite ( $\text{Mn}_{0.5}\text{Ca}_{0.5}\text{CO}_3$ ). This calcium manganese carbonate precipitation is also promoted from similar Mn(IV) reduction reactions described in (3) but the precipitating carbonate incorporates Ca abundant in pore fluids. As discussed above, these manganese reduction reactions occur by interaction of microbes and solid Mn(IV) oxides in the absence of oxygen. While manganese reduction does take place in anoxic waters, such as the Black Sea, the Mn(II) produced is diluted into the surrounding water column, and does not sufficiently increase in concentration to form Mn-carbonates (Calvert and Pederson, 1996). Thus, the production of Mn-carbonates post-Mn(IV) reduction likely only takes place in porewater-filled cavities of anoxic sediments enriched in “trapped” manganese oxides (Calvert and Pedersen, 1996). Marine sedimentary porewater is Ca-rich at  $\sim 10.5$  mM (Wenzhöfer et al., 2001; Rao et al., 2012), and increasing the  $\text{Mn}^{2+}$  concentration of seawater promotes the precipitation of carbonates with kutnohorite-like composition. Bottcher (1998) precipitated calcium-manganese carbonates at 20, 60, and 90°C, and the carbonate precipitates had a manganese composition that was enriched but related to the Ca:Mn concentrations. Similarly, Mucci (2004) synthesized a calcian rhodochrosite by combining equal molar solutions of Ca and Mn. He demonstrated that either manganoan calcite or calcian rhodochrosite will form depending on the porewater Mn:Ca concentrations, calcite surfaces, and reaction kinetics (Mucci, 2004). Thus in the presence of high porewater Ca levels (i.e., seawater compositions), manganese oxide reduction promotes the

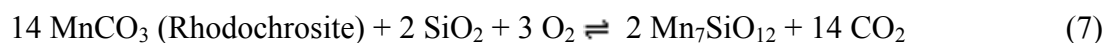
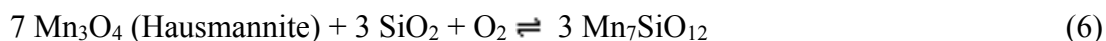
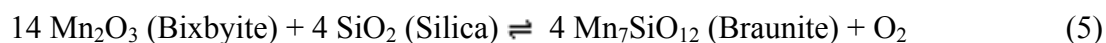


precipitation of carbonates with subequal amounts of Mn and Ca, as opposed to endmember carbonates like rhodochrosite ( $\text{MnCO}_3$ ).

Mn-bearing carbonates from a variety of unlithified sediments are invariably mixed Mn-Ca(+/-Mg) carbonates rather than endmember rhodochrosite, including sediments in the Baltic Sea, Panama Basin, Loch Fyne, among other locations (Calvert and Price, 1970; Pedersen and Price, 1982; Jakobsen and Postma, 1989; Calvert and Pedersen, 1996). Modeling the precipitation dynamics similarly results in formation of kutnohorite or calcic-rhodochrosites depending on Mn concentration, and rhodochrosite is not a stable phase in reasonable porewater compositions (Middelburg et al., 1987). Since all of our examined sedimentary deposits are marine in origin, and it is unlikely that Ca levels in the oceans have changed so substantially since Archean time (Grotzinger and Kasting, 1993; Lowenstein et al., 2001; Fischer et al., 2009), the early diagenetic carbonate precipitate of all of these deposits was likely kutnohorite. Rhodochrosite, then, either forms in Ca-depleted porewaters (which seems unlikely) or more probably as a secondary carbonate associated with dissolution and higher temperature re-precipitation of carbonate closer to endmember  $\text{MnCO}_3$ . Carbonate mineral textures from light and electron microscopy (e.g., Figs. 5, 7, 13) demonstrate substantial amounts of carbonate diagenesis—recrystallization and precipitation of secondary and tertiary cements that are commonly chemically zoned. It is also interesting, and perhaps illuminating, that the Mn(IV) oxide inclusion in the Hotazel formation occurs occluded by kutnohorite nodular

cements, not rhodochrosite. These textures imply that kutnohorite is commonly an earlier diagenetic precipitate rather than rhodochrosite.

Textural observations of the Mn(III)-rich phase braunite from the Hotazel and Santa Cruz formations indicate that it formed after kutnohorite, but still early in diagenesis as the braunite is generally fine-grained and defines sedimentary lamination. Yet the timing and formation process of braunite during diagenesis and/or metamorphism is unclear (Robie et al., 1995). The composition of braunite is related to the manganese(III) oxide bixbyite ( $\text{Mn(III)}_2\text{O}_3$ ), but with substitution of  $\text{Mn}^{2+}$  and  $\text{Si}^{4+}$  for  $2 \text{ Mn}^{3+}$ . Interestingly, the Si content of braunite appears to be relatively invariable with metamorphic grade (Abs-Wurmbach, 1980). Braunite has not been synthesized in the laboratory, but there are several proposed mechanisms for its formation (Robie et al., 1995); we highlight those with plausible initial conditions for marine sediments (e.g., rhodonite, a high-temperature metamorphic Mn(II) silicate is not a likely precursor precipitate):



We favor Reaction (5) as the most plausible mechanism for braunite formation. Both Reaction (6) and (7) require oxygen in the sediments to form braunite. When we have observed evidence of oxidizing fluids moving through discrete veins or faults, we see Mn(IV) oxides in the Hotazel and Urucum examples, not braunite enrichments. It is also difficult to envision the correct amount of oxygen being introduced post-depositionally into the whole of the Hotazel deposit to produce braunite throughout the entire formation. Thus we prefer Reaction (5), which seems the simplest explanation for a silicified Mn(III)-dominated mineral: begin with a Mn(III) oxide and add silica.

Our observations also constrain the timing of braunite formation. The euhedral braunite crystals in the Hotazel Formation cross-cut kutnohorite and are therefore definitively younger (Fig. 11). However, if manganese reduction converts Mn(IV)-oxides to  $\text{Mn}^{2+}$ , for Mn(III) production we either need secondary oxidation of the  $\text{Mn}^{2+}$  or some way to produce Mn(III) oxides from Mn(IV) oxides or Mn(II) carbonates to eventually crystallize into braunite. Experimental evidence has suggested that Mn(IV)-oxide reduction by the metal-reducing bacteria of the genus *Shewanella* may proceed through a Mn(III) step, which could be a Mn(III) oxide source (Lin et al., 2012). The difficulty here is to keep this Mn(III) from becoming fully reduced  $\text{Mn}^{2+}$ , but this could occur via more stable Mn(III)-ligand complexes (Madison et al., 2013) or the formation of Mn(III) oxyhydroxides, which can be temporarily stable (Hem and Lind, 1983; Murray et al., 1985). Another possibility is the synthesis of Mn(III)-oxyhydroxides like feitknechtite ( $\beta$ - $\text{MnOOH}$ ) from reaction of co-existing  $\text{Mn}^{2+}$  and Mn(IV) oxides (Elzinga, 2011). While

any of these alternatives are possible, we do know that some Mn(III)-dominated phase must have existed in the Hotazel and Santa Cruz sediments that was ultimately stabilized as braunite, perhaps with diagenetic addition of silica, but after the precipitation of Mn(II)-carbonate.

The Santa Cruz Formation also contains caryopilite—the Mn(II) aluminosilicate member of the kaolinite-serpentine group. This mineral appears to have formed during burial diagenesis or metamorphism from late-stage alteration and silicification of kutnohorite into caryopilite. Cross-cutting relationships show caryopilite is secondary to the Mn-carbonate, and caryopilite is known as a metamorphic mineral (Brusnitsyn, 2006); thus we regard these Mn-silicates as the result of much later post-depositional processes.

Combining knowledge of Mn redox dynamics, reduction processes, and textural, mineralogical, and redox observations, we can construct a conceptual model of manganese precipitation, diagenesis, and stabilization in the geological record (Fig. 19). Mn(IV)-oxides constitute the principal mode by which Mn enters and is concentrated in marine sediments, but these are subsequently reduced either completely or partially by sedimentary organic matter and/or related reductants (e.g., sulfide). Reduction by organic matter is commonly mediated by anaerobic microbes and promotes the precipitation of Mn-carbonates, forming first Ca-rich phases like kutnohorite, but which often undergo carbonate diagenesis to produce rhodochrosite. During reduction of Mn(IV) oxides,

Mn(III) oxides or complexes are produced, which later are crystallized in the presence of silica to the Mn(III)-dominated oxide, braunite.

Our observations display a general pattern of manganese deposits composed of either exclusively Mn(II) carbonates or a mixture of Mn(III) and Mn(II) phases, but what determines which of these two assemblages occur? We have established that Mn(II) carbonates derive from Mn(IV) oxides through reduction by organic carbon, and the Mn(III) precursor phase to braunite forms via partial reduction of Mn(IV) oxides or by Mn(IV) oxides reacting with Mn(II). We hypothesize that the kinetics of Mn(IV) reduction is critical to determining whether Mn(III) phases form since the stabilization of Mn(III)-oxides requires the presence of Mn(IV) and Mn(II). However, Mn(III) can still be reduced by metal-reducing microbes (Kostka et al., 1995), and so ultimately the assemblage redox state must be determined by the amount of reductant. If organic carbon, or another chemical species able to reduce Mn(IV) oxides, is more abundant than manganese, then all of the oxidized manganese should be reduced to Mn(II) and react to form Mn(II) carbonates or diffuse away. If organic carbon or other reductants are limiting, then the surplus of manganese should result in more oxidized phases being preserved. Theoretically, this should mean that with very little organic carbon, there is potential for preserving original manganese oxides – and while this may have happened in rare instances of the Hotazel formation, it is clear that usually manganese is reduced by available electron donors. This premise of competing manganese-electron donor dynamics allows us to infer organic carbon availability in ancient paleoenvironments –

such as, in the Molango shallow sea there was highly abundant organic carbon, but in the Urucum continental rift basin, manganese was more abundant than available organic carbon or other reductants.

Later metamorphic processes may transform the kutnohorite, rhodochrosite, and/or braunite into a variety of other minerals, such as the hydrated Mn(II) alumino silicate caryopilite found in the Santa Cruz Formation. Diagenetically stabilized Mn deposits may again be exposed to oxygen via uplift and surface weathering, and all the minerals will once again be fully oxidized to Mn(IV) oxides as in the Koegas, Urucum, and Kungarra examples. This will occur from abiotic weathering in the presence of O<sub>2</sub> (Morgan, 2005), but recent reports suggest that the oxidation of Mn-carbonates to Mn(IV) oxides may also be microbially mediated (Tang et al., 2013). Thus to achieve an accurate understanding of early Mn mineralization both unweathered core samples and lack of metamorphism are essential to determine how much Mn was delivered to the sediments and how it was transformed by diagenesis.

## **5. CONCLUSIONS**

We combined light and electron microscopy, X-ray absorption spectroscopy, and X-ray imaging techniques to examine key manganese deposits through time and understand their mineralogy and petrogenesis in detail across multiple scales. While manganese oxidation produces Mn(IV)-dominated oxides comprising the major vector for the sedimentation and concentration of Mn in sedimentary rocks, ancient manganese deposits

are composed only of Mn(II) and Mn(III) minerals (with rare exceptions of small preserved Mn(IV)-oxide inclusions). The geological record of (relatively) well-preserved manganese deposits is thus composed predominantly of kutnohorite ( $\text{Mn}_{0.5}\text{Ca}_{0.5}\text{CO}_3$ ), rhodochrosite ( $\text{MnCO}_3$ ), and braunite ( $\text{Mn(III)}_6\text{Mn(II)O}_8\text{SiO}_4$ ). A dataset of the abundances of Mn deposits throughout Earth history reveals major changes, with most deposits that only emerge after the rise of oxygen; a notable exception is found in the Paleoproterozoic-age Koegas subgroup of the Transvaal Supergroup, deposited just prior to the rise of oxygen, and potentially the age-ambiguous manganese enrichment in the Australian Kungarra formation. Constrained by texture-specific mineral analyses and sedimentological observations, we constructed a paragenetic model of manganese mineral formation beginning with deposition of Mn(IV)-dominated oxides leading to the early diagenetic production of carbonate phases such as kutnohorite, with potential for stabilization of Mn(III)-rich oxides (now marked by braunite) in sedimentary environments with relatively low fluxes of sedimentary organic matter, under deep burial the ingrowth of metamorphic mineral assemblage (recrystallization of carbonate phases and production of Mn(II)-silicates), and finally possible re-oxidation to Mn(IV)-oxides driven by post-depositional exposure to  $\text{O}_2$ -bearing fluids during near surface weathering. This framework provides logic to invert sedimentological, mineralogical, and textural observations of Mn-rich sedimentary rocks for the biogeochemical processes once operating in Earth (and Mars; (Lanza et al., 2014)) surface environments.

## **Acknowledgements**

We are grateful for manuscript comments and analytical support from George Rossman. We thank the David and Lucile Packard Foundation and a NSF-GRFP grant to J.E.J. for support. We acknowledge the Lewis and Clark Foundation for funding field work for J.E.J., the Agouron Institute for supporting both the Agouron South Africa Drilling Project, which provided core samples of the Koegas Subgroup and the Agouron Field Excursions, which allowed J.E.J. to sample the Kungarra Formation manganese; Victoria Orphan and Josh Steele for donating part of a deep-sea ferromanganese nodule, J.B. Maynard for contributing many Molango deposit samples, Joseph Kirschvink for donating a well-preserved sample of the Hotazel formation, Thiago Piacentini for samples of the Santa Cruz Formation, and Nic Beukes and Bertus Smith for assistance in the field. The Stanford Synchrotron Radiation Lightsource, SLAC National Accelerator Laboratory, is supported by the U.S. Department of Energy, Office of Science, Office of Basic Energy Sciences under Contract No. DE-AC02-76SF00515. SEM, EBSD, and EPMA analyses were carried out at the Caltech GPS Division Analytical Facility, which is supported, in part, by NSF Grants EAR-0318518 and DMR-0080065.



## FIGURES

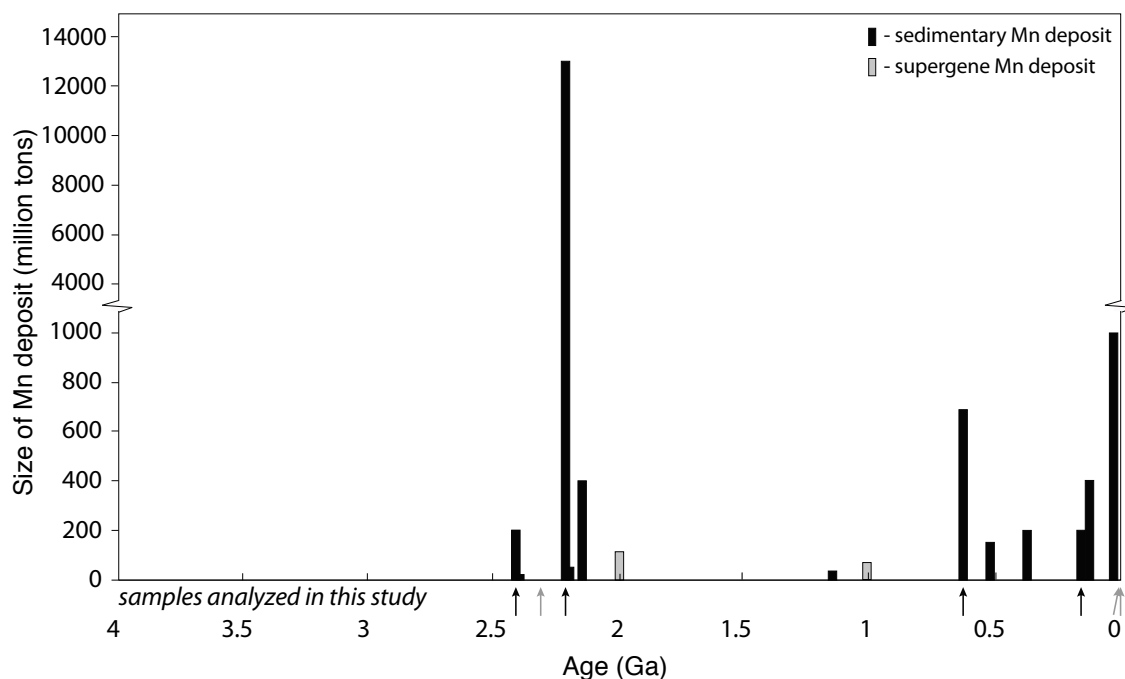
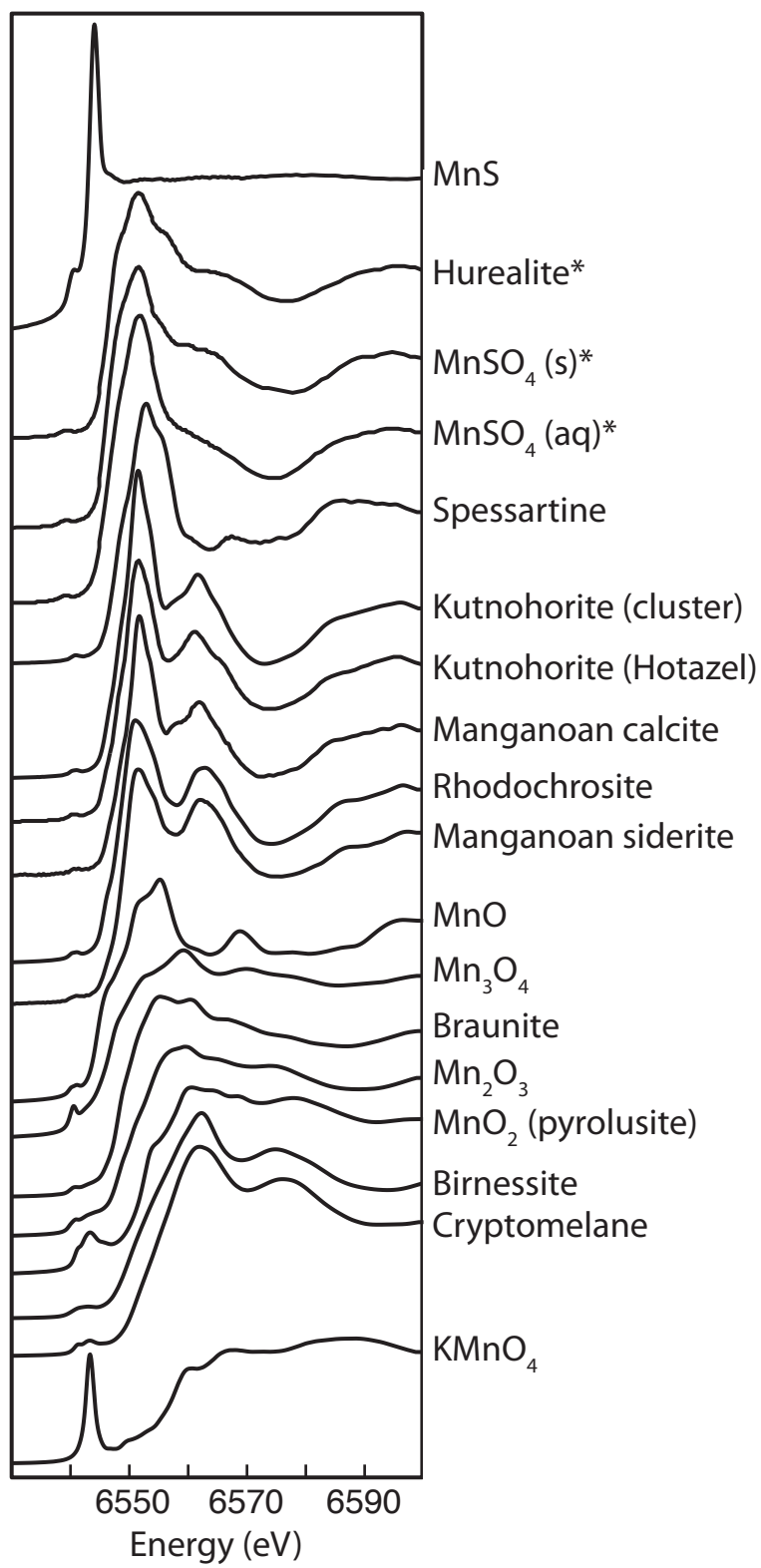


**Fig. 1: Manganese ore deposits through time**

Estimated volumes of major sedimentary manganese deposits plotted as a function of their best-constrained geologic age. Arrows mark deposits analyzed in this study, with black signifying large manganese deposits plotted and grey indicating timing of smaller deposits. Supergene deposits are shown in grey for cases where the age of mineralization is known; deposits from Archean proto-ore, primarily in India, occur but the age of mineralization is not known.

**Fig. 2 (below): Mn K-edge X-ray absorption spectra of known manganese minerals relevant to geological deposits.**

Manganese mineral standards were measured from the Caltech Mineralogical Collection, Fischer lab acquired collection. Two additional spectra for Mn(II) sulfates and a Mn(II) phosphate (marked by asterisks) are from Manceau et al (Manceau et al., 2012).



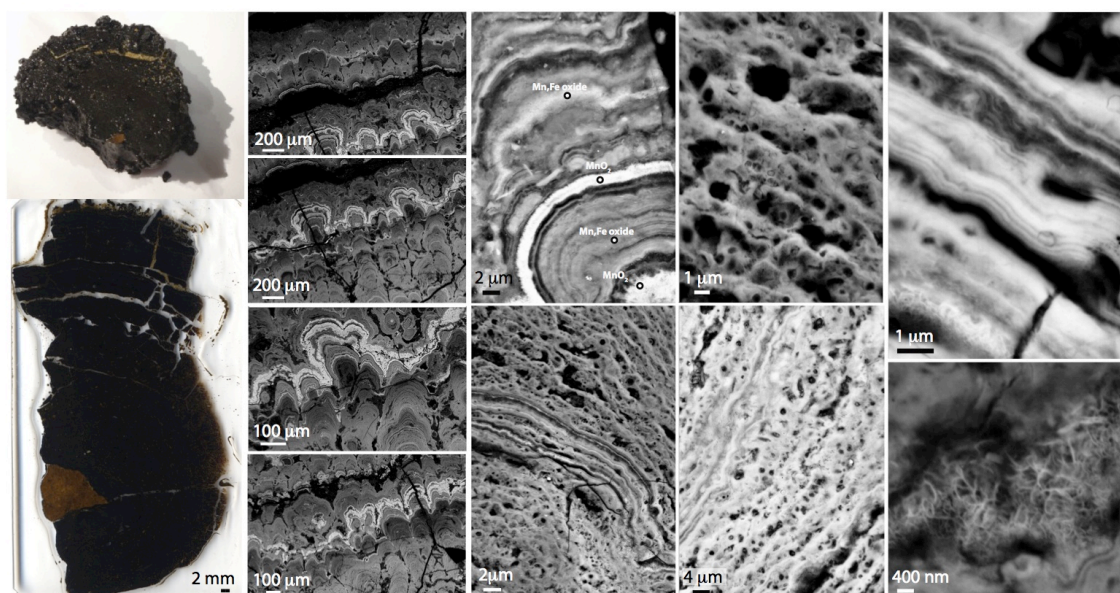


**Fig. 3: Light and electron microscopy of a seafloor manganese nodule**

Ferromanganese nodule from the South Pacific Gyre collected during IODP Expedition 329. Leftmost panel shows transmitted light images of the entire nodule (above) and thin section (below). Center and right panels contain electron photomicrographs of the nodule at different scales. Note the abundant isopachous and stromatolitic laminations.

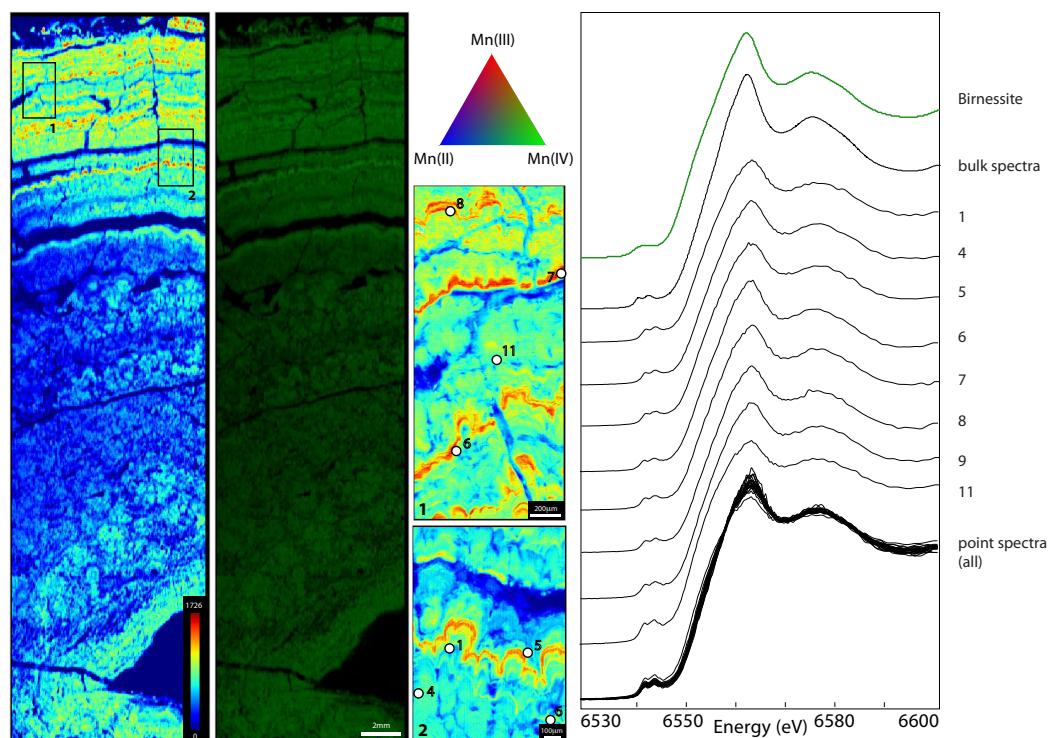


**Fig. 4: Seafloor manganese nodule XAS images and spectra**

X-ray absorption spectroscopy results from the modern ferromanganese nodule, showing microprobe maps of manganese concentration (jet colors in cps units), and a best-fit redox maps (tricolor RGB scale) indicating that only Mn(IV)-oxide phases are present (with Mn(II) in blue, Mn(III) in red, and Mn(IV) in green). This is supported by full XANES spectra from points throughout the nodule (marked by numbers), which indicate Mn(IV)-oxides most similar to birnessite.



Transmitted light (top) and scanning electron microscope (bottom A and B panels) images of a manganese-enriched sample at 533 m from ODP core 799 from the Japan Sea. Compositions derived from energy dispersive X-ray spectroscopy spot measurements are summarized in text labels. Variations in carbonate cation chemistry manifest as different backscatter contrast colors optically or varying levels of backscatter under the SEM.

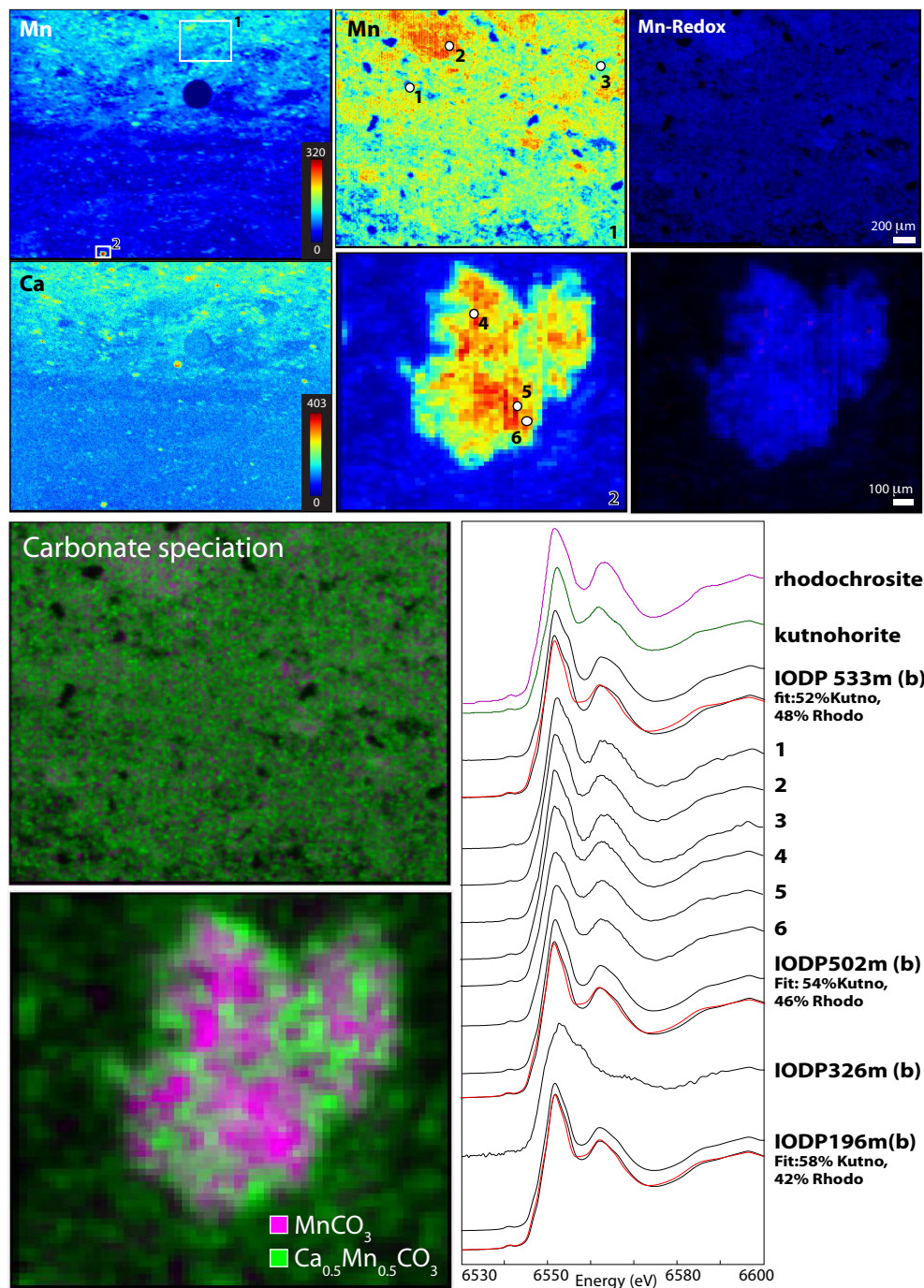


**Fig. 6: Japan Sea Pliocene-Miocene sediments XAS images and spectra**

X-ray absorption spectroscopy results from four samples of ODP core 799. Lithified sample at 533 m was mapped for manganese concentration (jet colors in cps units), manganese redox state (with Mn(II) in blue, Mn(III) in red, and Mn(IV) in green). The sample is comprised solely of Mn(II)-carbonate minerals; sample point spectra are plotted below standard spectra of rhodochrosite and kutnohorite. Bulk spectra were fit to



standards, with fit (red) plotted on top of and below the measured spectra (black). Best-fit estimates of rhodochrosite and kutnorhorite spectral contributions marked adjacent.

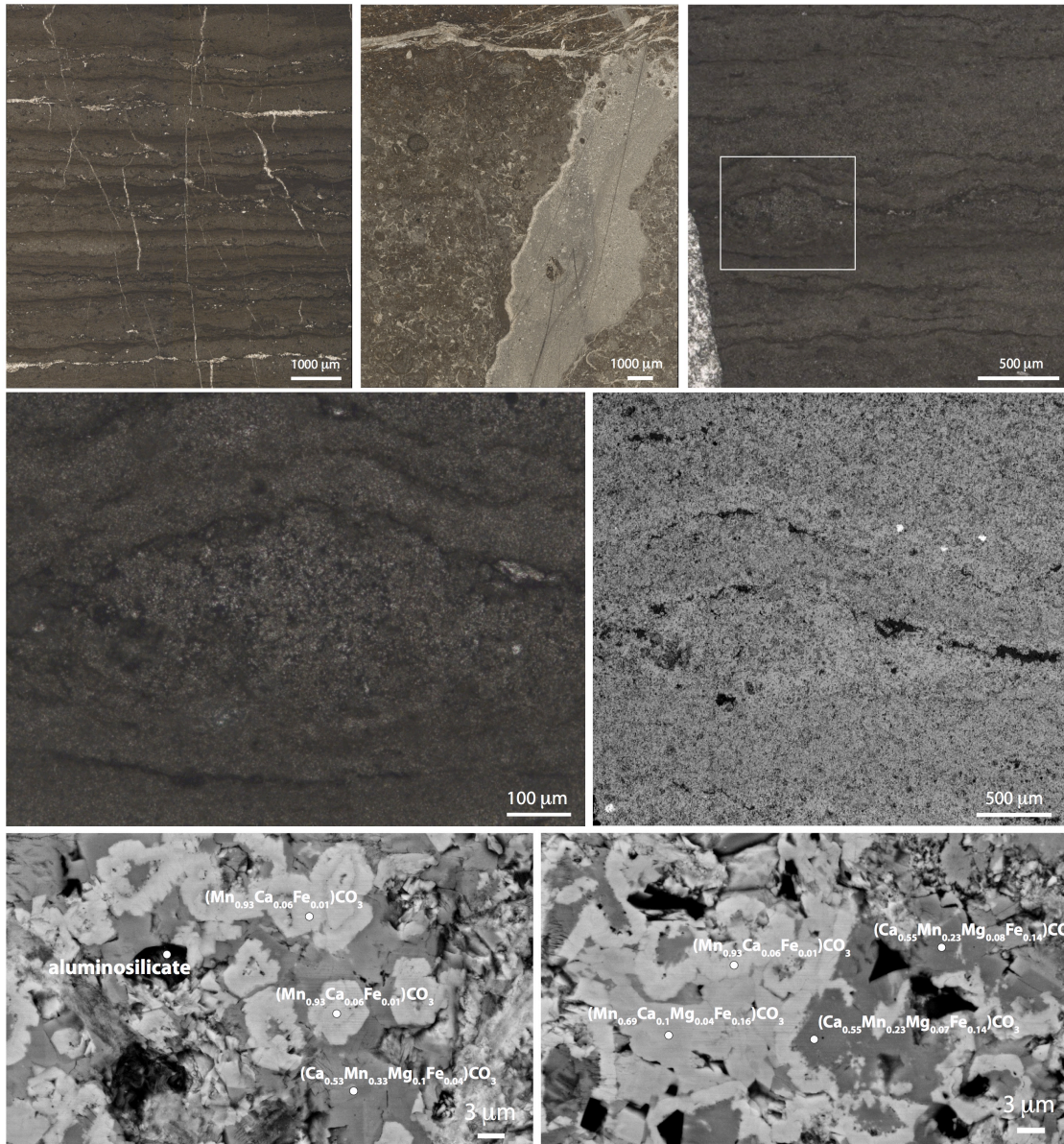


**Fig. 7: Jurassic-age Molango deposit light and electron microscopy**

Transmitted light (top and left) and scanning electron microscope (bottom right) images of manganese-enriched samples from the Molango deposit in Mexico. Compositional data from energy dispersive X-ray spectroscopy are summarized in text labels. The samples appear highly recrystallized and manganese is only present in carbonate minerals.



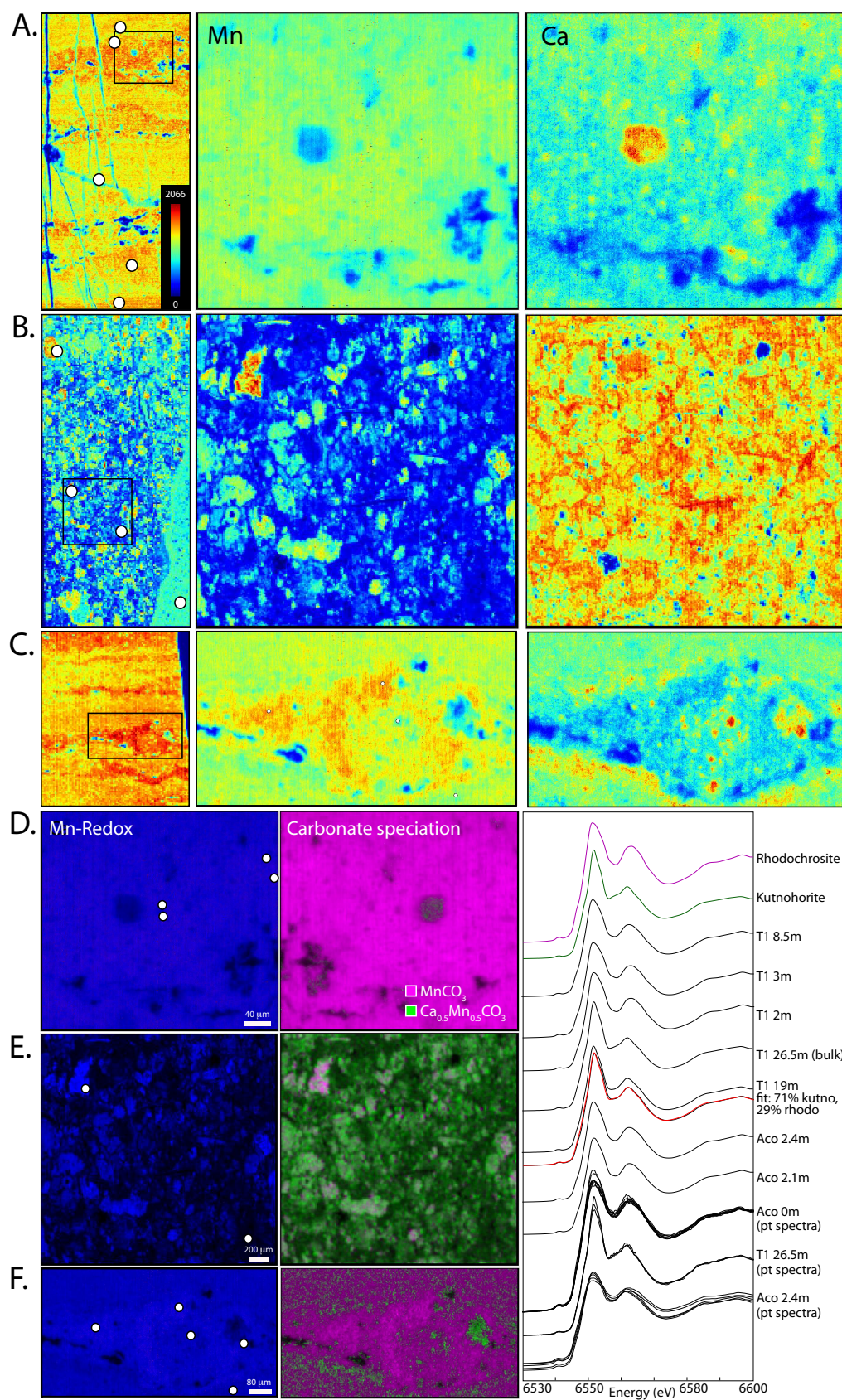


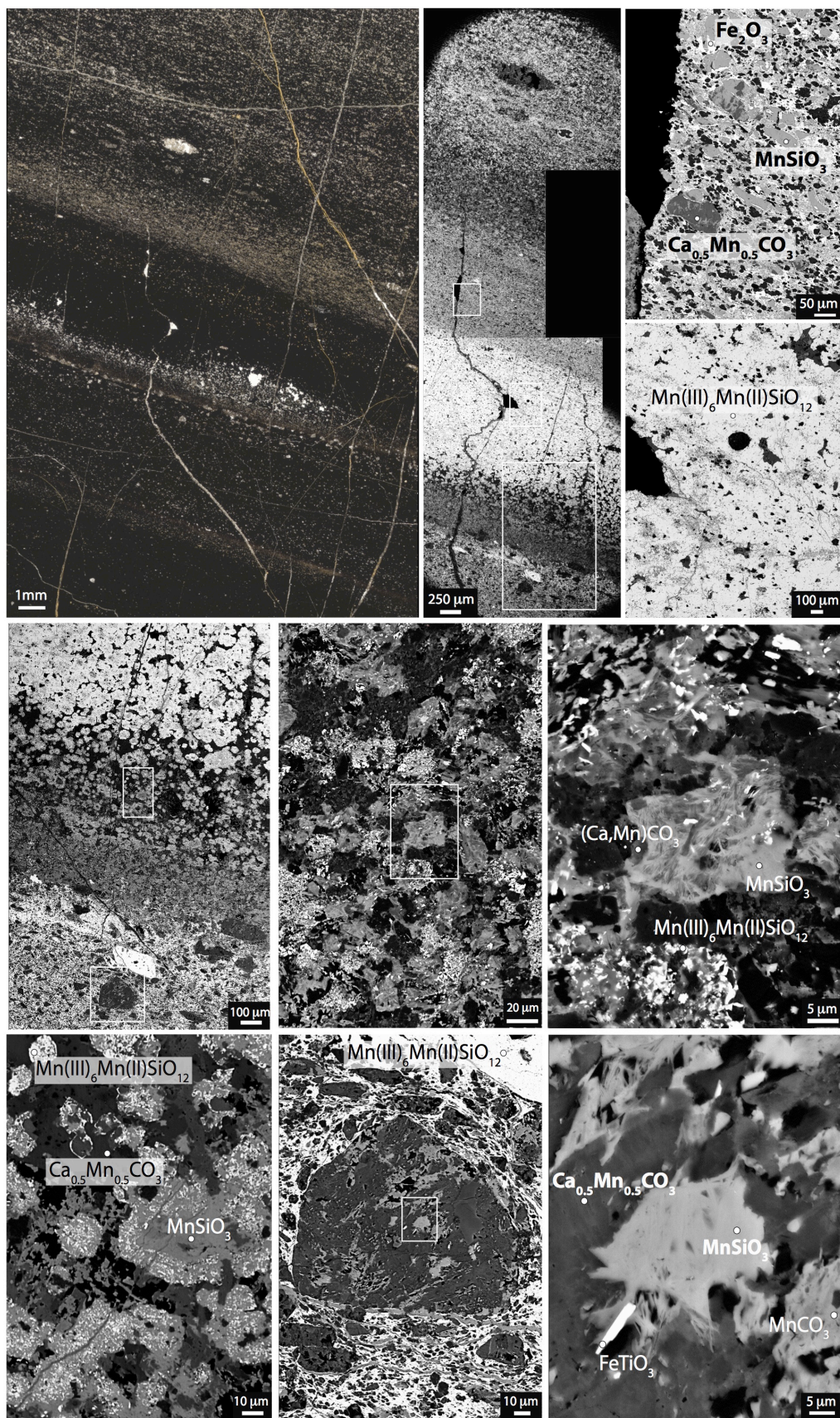


**Fig. 8: Jurassic-age Molango deposit XAS images and spectra**

Mn and Ca concentration (jet colors in cps units) of three samples from the Molango deposit are shown in A-C; Redox maps (Mn(II) in blue, Mn(III) in red, and Mn(IV) in green) shown below: A,D. Acoxcatlan section at 0 m. B,E. Tetztintla1 section at 26.5 m. C,F. Acoxcatlan section at 2.4 m. Manganese is only present as Mn(II) in rhodochrosite and kutnohorite, as confirmed by sample spectra plotted below standard spectra of these two manganese-bearing carbonates.

**Fig. 9 (below): Santa Cruz Formation light and electron microscopy**

Transmitted light (left) and scanning electron microscope (right) images of manganese-rich samples from the Neoproterozoic Santa Cruz Formation from Brazil. Compositional results from energy dispersive X-ray spectroscopy spot measurements are summarized in the text labels. The sample shows a complex mineralogy and petrographic textures at a microscale. Note the presence of Mn-silicates that appear to be replacing a manganese-calcium carbonate phase.





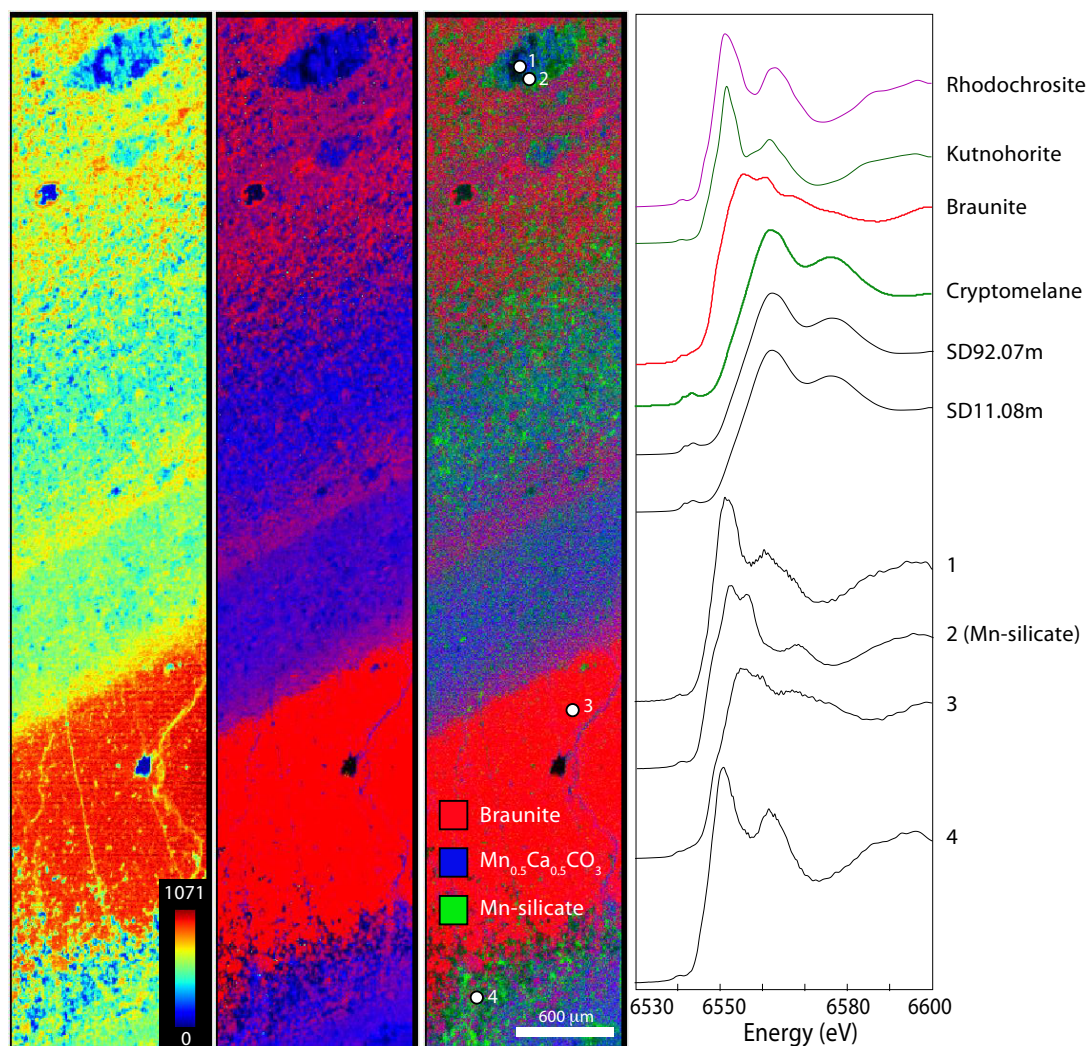


**Fig. 10: Santa Cruz Formation XAS images and spectra**

X-ray absorption spectroscopy results from three samples (two bulk powders, one thin section) of the Santa Cruz manganese formation. Samples were mapped for manganese concentration (jet colors in cps units), manganese redox state (tricolor RGB color scale with Mn(II) in blue, Mn(III) in red, and Mn(IV) in green), and manganese phase (with braunite in red,  $\text{Mn}_{0.5}\text{Ca}_{0.5}\text{CO}_3$  in blue, and Mn-silicate identified by Raman (Fig. A2) as caryopilite in green). Measured point spectra are plotted below standard spectra and confirm the presence of rhodochrosite, kutnohorite, braunite, and cryptomelane.

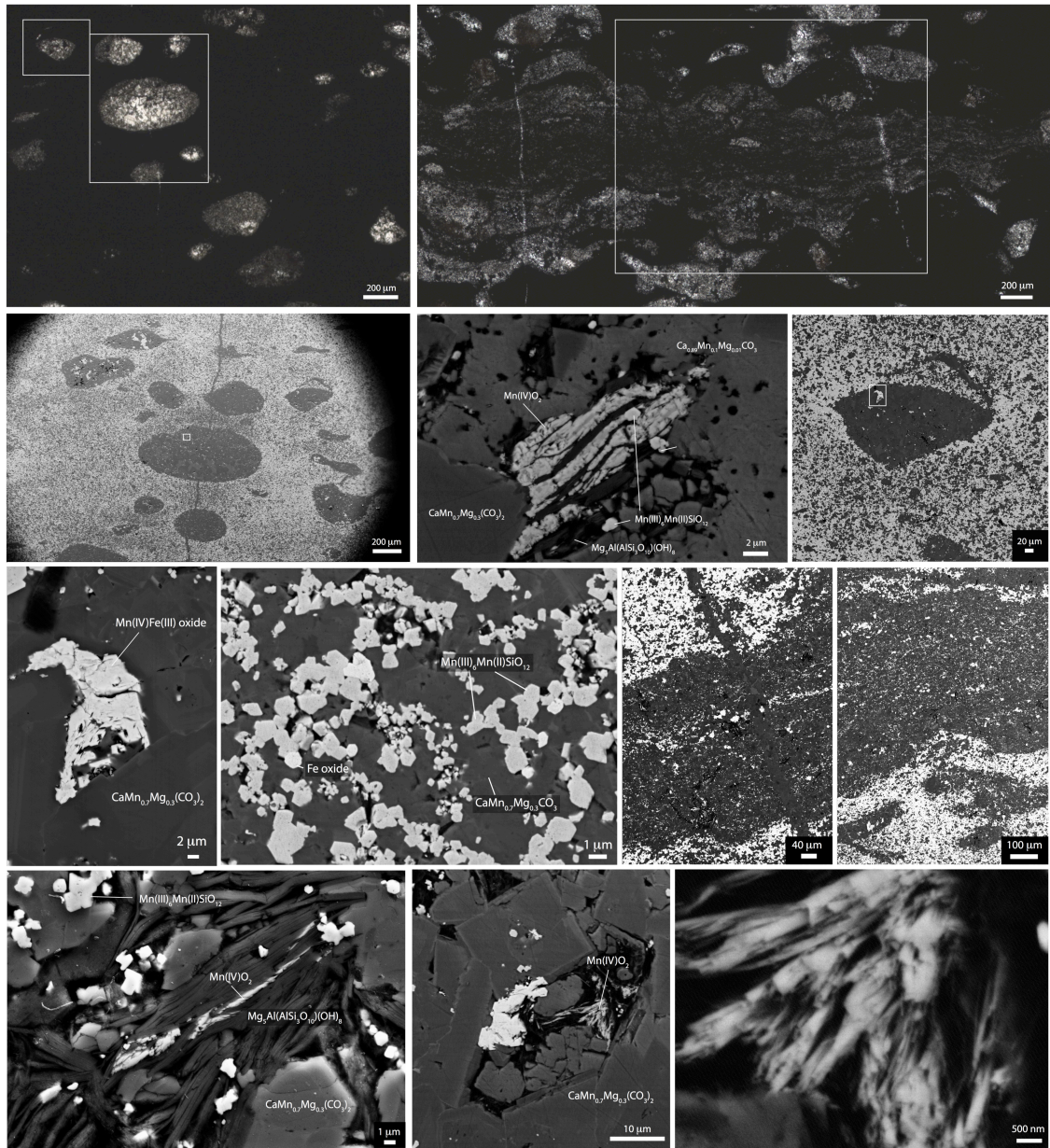


**Fig. 11: Hotazel Formation light and electron microscopy**

Transmitted light (top) and scanning electron microscope (bottom) images of samples from the Hotazel Formation of the Paleoproterozoic Kalahari Manganese Field from South Africa. Compositional information from energy dispersive X-ray spectroscopy spot measurements are provided in the text labels overlaid on the photomicrographs. Note the common early diagenetic Mn-carbonate nodules (light colors in transmitted light, dark in SEM backscatter contrast), floating in a dark (or backscatter-bright) Mn-oxide matrix.



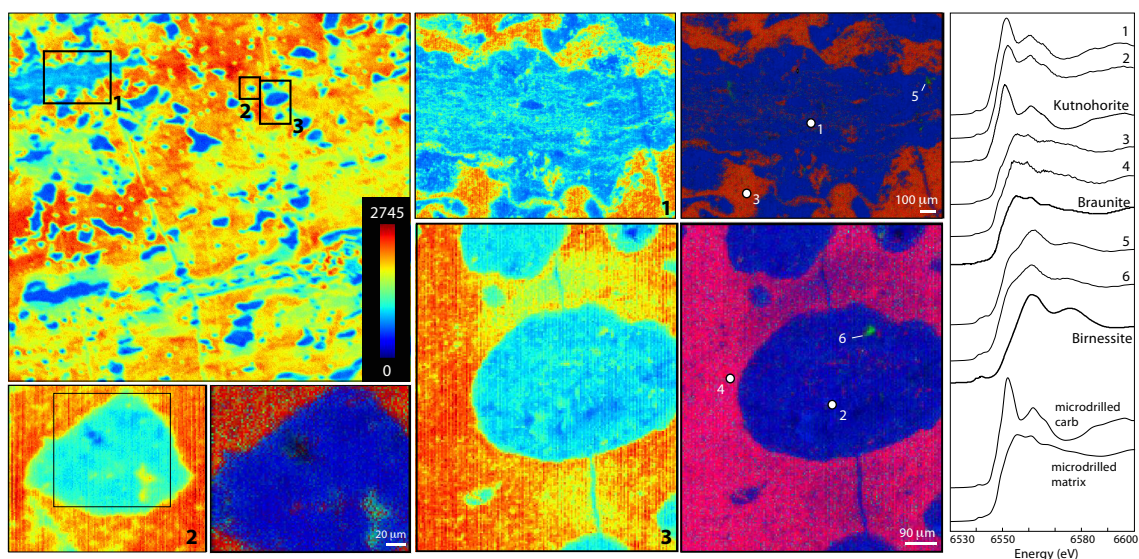


**Fig. 12: Hotazel Formation XAS mapping and spectra**

X-ray absorption spectroscopy of three regions of interest from Hotazel Formation samples. Samples were mapped for manganese concentration (jet colors in cps units) and manganese redox state (tricolor RGB scale with Mn(II) in blue, Mn(III) in red, and Mn(IV) in green). Phases containing Mn in all three redox states were observed in this unit. Sample spectra best matched standard spectra of kutnohorite, braunite, and birnessite (plotted above sample spectra). Note the presence of rare small inclusions of Mn(IV)-oxides preserved within nodules of kutnohorite.

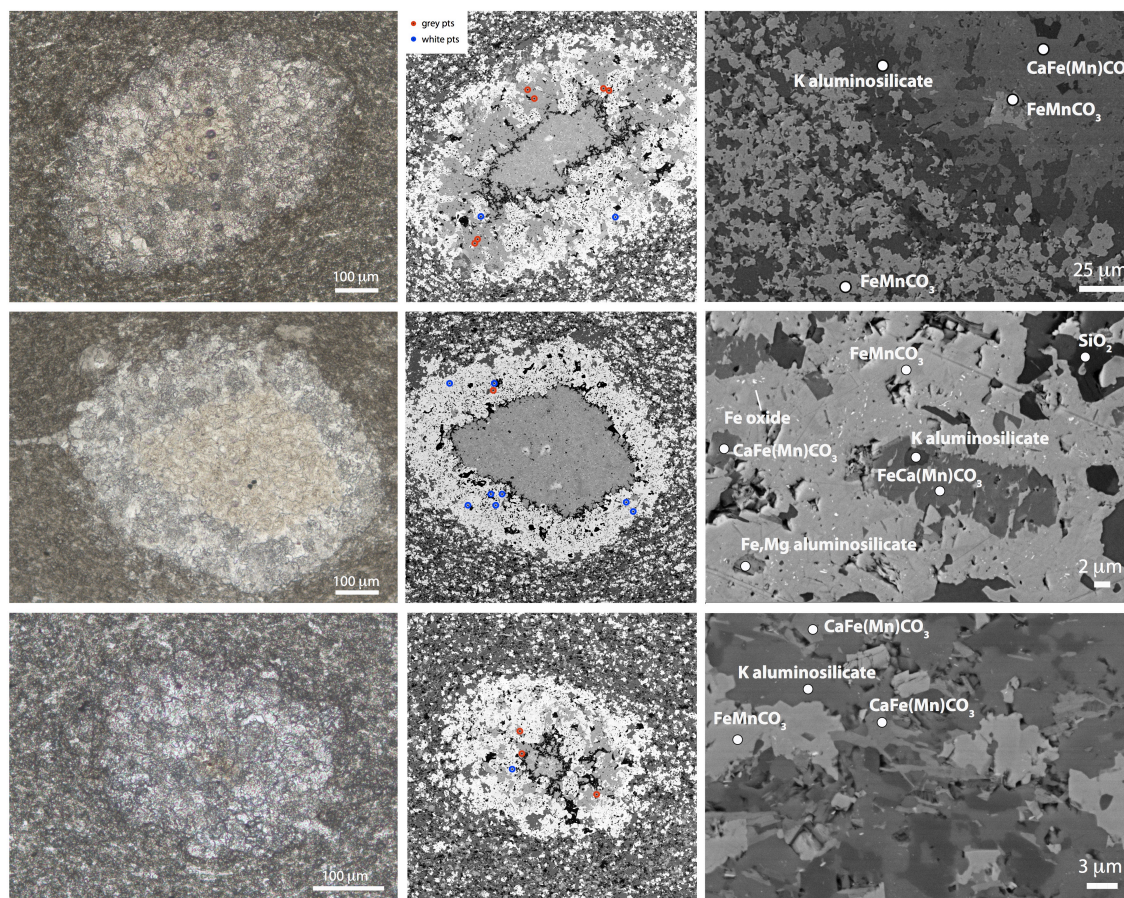


**Fig. 13: Paleoproterozoic-age Koegas Subgroup light and electron microscopy**  
 Transmitted light (left) and scanning electron microscope (right) photomicrographs of a manganese-rich sample from the ~2.415 Ga Koegas Subgroup in South Africa. Compositional data obtained from energy dispersive X-ray spectroscopy spot measurements are summarized with text labels. Phases studied by electron microprobe wavelength-dispersive spectroscopy are indicated in red (grey/low backscatter, kutnohorite endmember) and blue (white/high backscatter, ferrous rhodochrosite endmember).



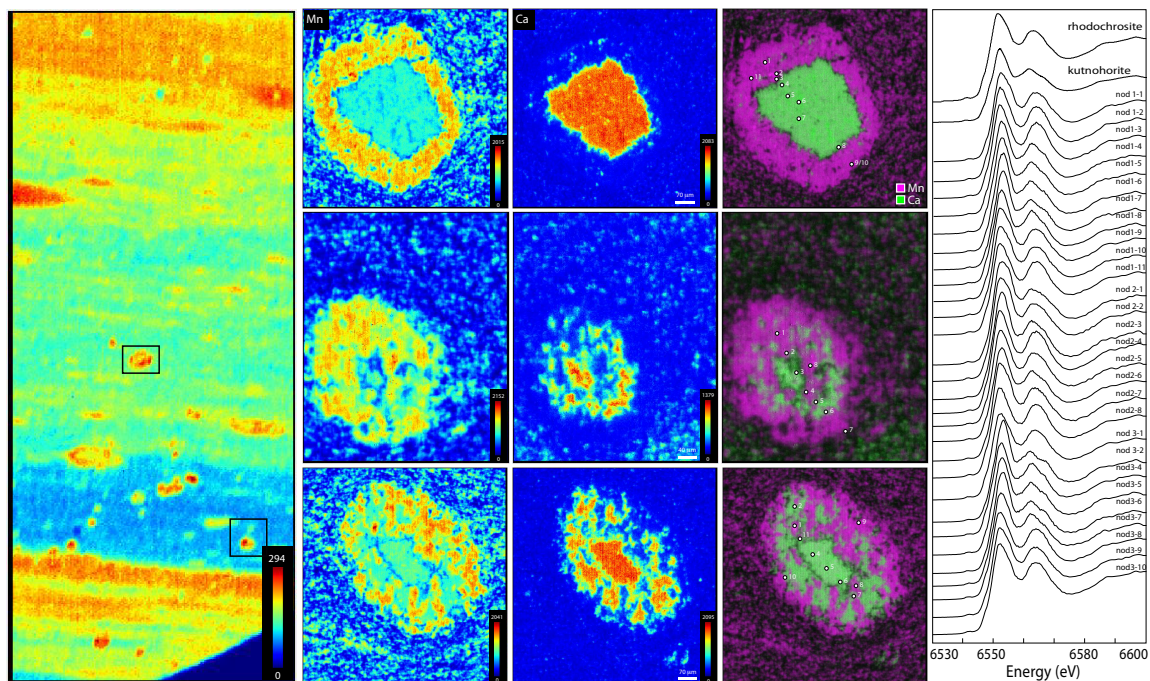


**Fig. 14: Paleoproterozoic-age Koegas Subgroup XAS imaging and spectra**

X-ray absorption spectroscopy results from three samples of the Koegas Subgroup. Manganese concentration (jet color scale in cps units), manganese redox state (with Mn(II) in blue, Mn(III) in red, and Mn(IV) in green), and carbonate speciation (with  $\text{MnCO}_3$  in purple and  $\text{Mn}_{0.5}\text{Ca}_{0.5}\text{CO}_3$  in green) are displayed. Numbered spots mark the locations of sample spectra, which are consistent with speciation maps and resemble standard spectra of rhodochrosite and kutnohorite.

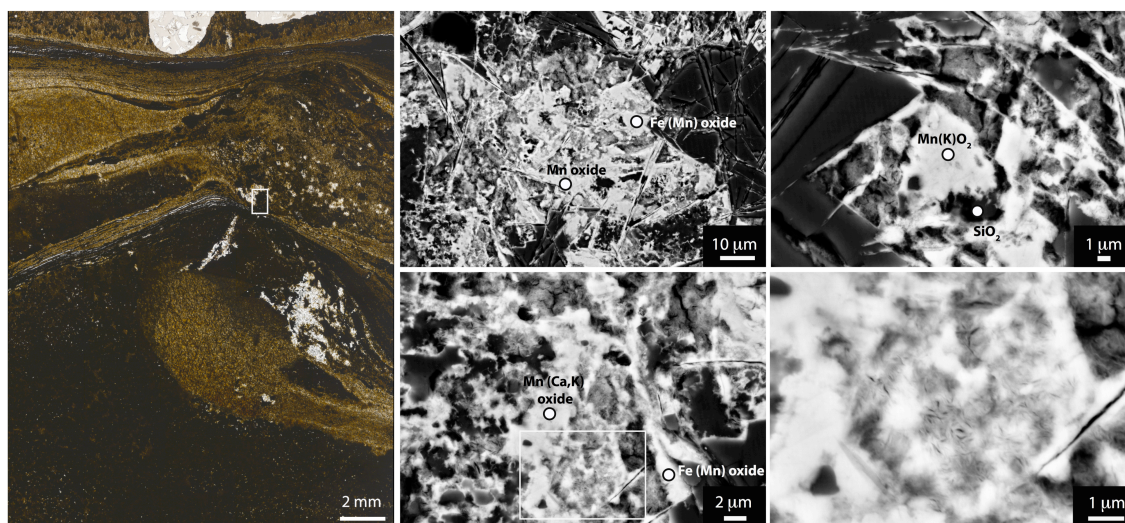


**Fig. 15: Light and electron microscopy of weathered Koegas Subgroup in outcrop**  
Transmitted light (left) and backscatter electron (right) photomicrographs of a microbially-bound grainstone from the Koegas Subgroup exposed at the surface in weathered outcrops in South Africa. Compositional constraints from energy dispersive X-ray spectroscopy measurements are summarized in text labels. In contrast to subsurface samples from drill cores (Figs. 13 and 14), manganese minerals appear to be predominantly oxides and manifest as fine-grained masses that mask petrographic textures.

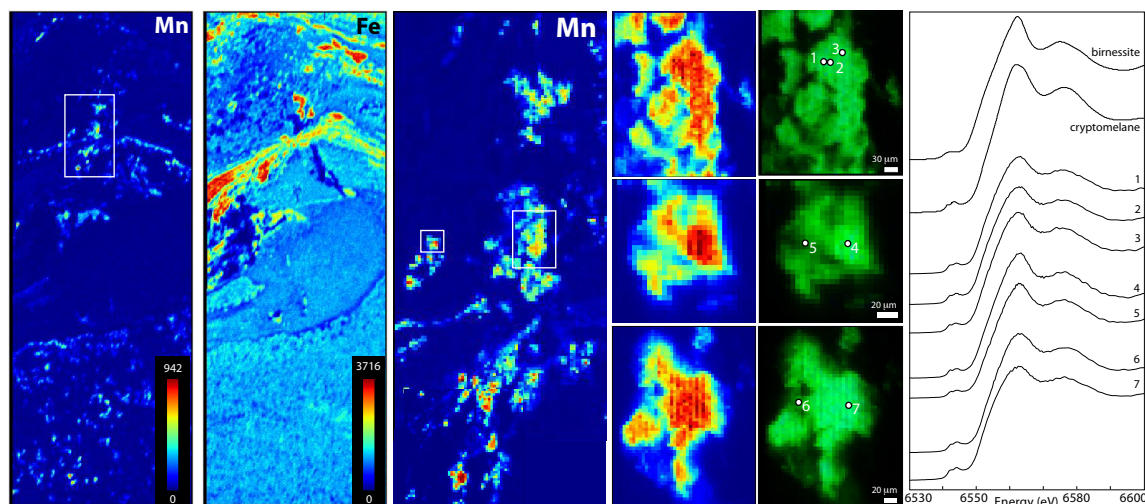


**Fig. 16: XAS imaging and spectra of weathered Koegas Subgroup in outcrop**  
Results of X-ray absorption spectroscopy from three regions of interest of sample of the Koegas Subgroup. Manganese concentration (in jet colors for cps units) and manganese redox state (tricolor RGB scale with Mn(II) in blue, Mn(III) in red, and Mn(IV) in green). Supporting the electron microscopy all pixels fit to Mn(IV) phases. Sample point spectra are marked and plotted to the right adjacent to their closest standard matches, cryptomelane and birnessite.



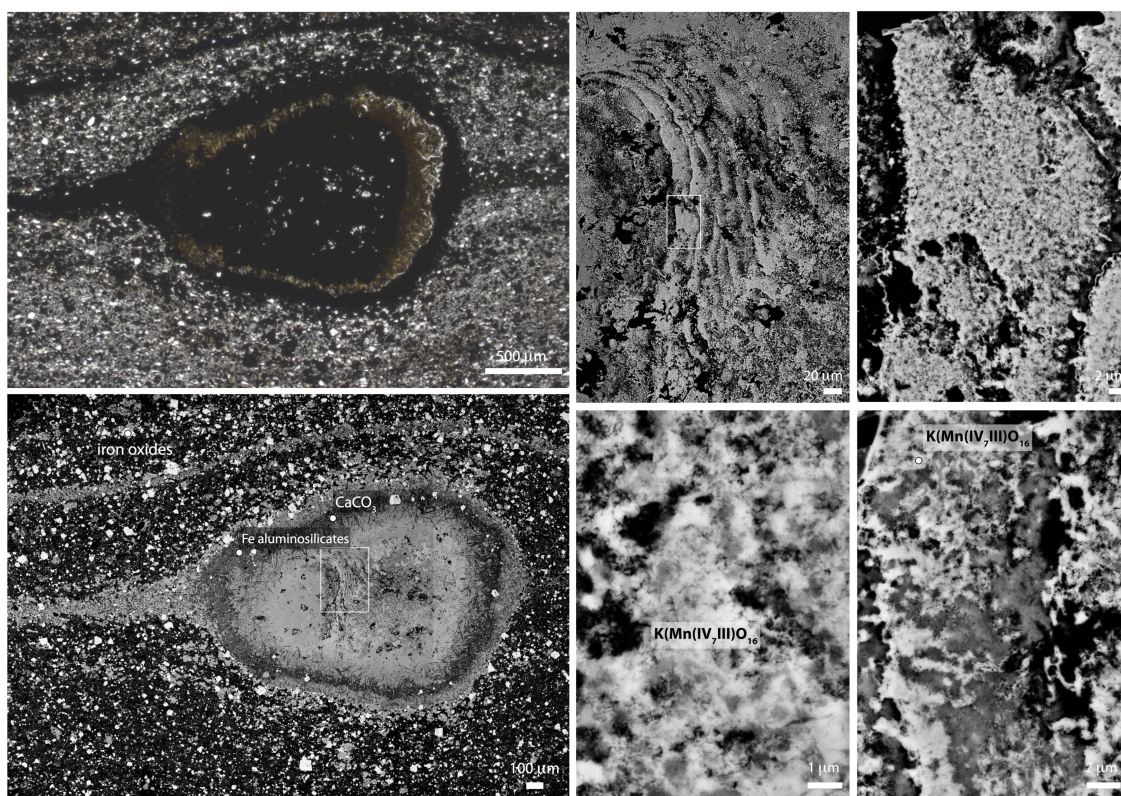


**Fig. 17: Paleoproterozoic-age Kungarra Formation light and electron microscopy**  
Optical (upper left) and scanning electron microscope photos of the Kungarra Formation from weathered outcrops in Australia. Compositional data from energy dispersive X-ray spectroscopy measurements are summarized in text labels. Manganese appears to be predominantly in oxide minerals of unknown redox state. Fine-scale textures are largely obliterated by growth of oxide phases, but at larger scales some nodular textures can still be observed. Note differential compaction of laminae of the nodule.

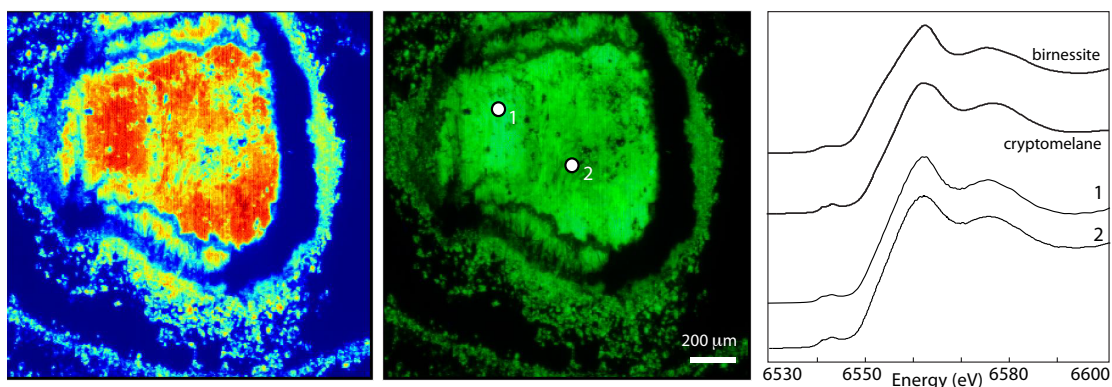


**Fig. 18: Paleoproterozoic-age Kungarra Formation XAS imaging and spectra**

X-ray absorption spectroscopy of three regions of interest from a weathered outcrop sample of the Kungarra Formation exposed in NW Australia. Regions were imaged for manganese concentration (jet colors in cps units) and manganese redox state (tricolor RGB image with Mn(II) in blue, Mn(III) in red, and Mn(IV) in green). The entire sample is composed of Mn(IV)-oxides. Point spectra are plotted alongside cryptomelane and birnessite.

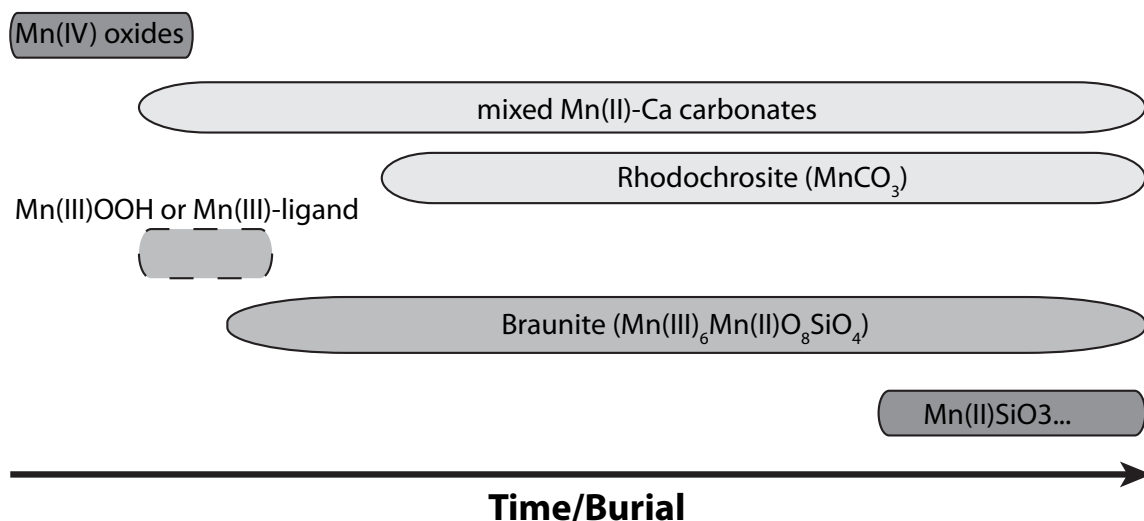


**Fig. 19: Paragenetic model for the diagenetic stabilization of Mn deposits**

Manganese is deposited and concentrated in sediments as Mn(IV) oxides, and subsequently reduced during organic diagenesis either partially to Mn(III) phases or fully to  $\text{Mn}^{2+}$ .  $\text{Mn}^{2+}$  is then precipitated as Mn-bearing carbonates. The most primary of these appears to be manganese-calcium carbonates like kutnohorite ( $\text{Mn}_{0.5}\text{Ca}_{0.5}\text{CO}_3$ ) but which can with burial diagenesis yield undergo recrystallization and yield more manganese-enriched carbonate phases like rhodochrosite ( $\text{MnCO}_3$ ). Mn(III)-oxide phases are silicified and stabilized as braunite ( $\text{Mn(III)}_6\text{Mn(II)SiO}_{12}$ ). Increasing burial diagenesis and metamorphism can greatly increase the mineralogical diversity of Mn deposits, particularly with Mn-silicate minerals, including caryopilite. See text for details.

<b>Deposit Name</b>	<b>Location</b>	<b>Age</b>	<b>Geologic Setting</b>	<b>Redox state</b>	<b>Mn minerals</b>
ferromanganese nodule	South Pacific Gyre	effectively modern	Oligotrophic ocean floor	Mn(IV)	birnessite-like
Japan Sea core	Japan Sea	Pliocene-Miocene	organic-rich failed rift basin	Mn(II)	magnesite, siderite, manganoan calcite/kutnohorite, calcian rhodochrosite
Molango deposit	Mexico	Upper Jurassic (ca. 155 Ma)	carbonate platform shelf	Mn(II)	rhodochrosite, manganoan calcite
Santa Cruz deposit	Jacadiño Basin, Brazil	Neoproterozoic	lacustrine or marine gulf continental rift basin	Mn(II,III)	braunite, rhodochrosite, kutnohorite, caryopilite
<i>weathered</i>				Mn(IV)	<i>cryptomelane (or birnessite)</i>
Hotazel Formation	South Africa	ca. 2200 Ma	marine back-arc basin or proximal mid-ocean ridge	Mn(II,III)	braunite, kutnohorite, manganoan calcite
Koegas Subgroup	South Africa	ca. 2415 Ma	deltaic near-shore marine	Mn(II)	ferrous rhodochrosite, manganoan siderite, manganoan calcite
<i>weathered</i>				Mn(IV)	<i>cryptomelane or birnessite</i>

**Table 1: A summary of the results from Mn deposits examined.**

## REFERENCES

- Akintola A. I., Ikhane P. R., Akintola G. ., Sanni O. G. and Oduneye O. A. (2012) Petrochemical Evaluations of the Pan African Pegmatites of Apomu Area, Southwestern Nigeria. *Environ. Nat. Resour. Res.* **2**, 8–17.
- Aller R. C. (1990) Bioturbation and Manganese Cycling in Hemipelagic Sediments. *Philos. Trans. R. Soc. Lond. Ser. Math. Phys. Sci.* **331**, 51–68.
- Aller R. C. and Rude P. D. (1988) Complete oxidation of solid phase sulfides by manganese and bacteria in anoxic marine sediments. *Geochim. Cosmochim. Acta* **52**, 751–765.
- Anbar A. D. and Holland H. D. (1992) The photochemistry of manganese and the origin of banded iron formations. *Geochim. Cosmochim. Acta* **56**, 2595–2603.
- Anderson C. R., Johnson H. A., Caputo N., Davis R. E., Torpey J. W. and Tebo B. M. (2009) Mn(II) oxidation is catalyzed by heme peroxidases in “*Aurantimonas manganooxydans*” strain SI85-9A1 and *Erythrobacter* sp. strain SD-21. *Appl. Environ. Microbiol.* **75**, 4130–4138.
- Armstrong F. A. (2008) Why Did Nature Choose Manganese to Make Oxygen? *Philos. Trans. R. Soc. B Biol. Sci.* **363**, 1263–1270.
- Bargar J. R., Tebo B. M., Bergmann U., Webb S. M., Glatzel P., Chiu V. Q. and Villalobos M. (2005) Biotic and abiotic products of Mn(II) oxidation by spores of the marine *Bacillus* sp. strain SG-1. *Am. Mineral.* **90**, 143–154.
- Bargar J. R., Tebo B. M. and Villinski J. E. (2000) In situ characterization of Mn(II) oxidation by spores of the marine *Bacillus* sp. strain SG-1. *Geochim. Cosmochim. Acta* **64**, 2775–2778.
- Bargar J. R., Webb S. M. and Synchrontron S. (2005) Structural Determination of Marine Bacteriogenic Manganese Oxides oxides. *Sci. York*, 1–4.
- Barley M. E., Pickard A. L. and Sylvester P. J. (1997) Emplacement of a large igneous province as a possible cause of banded iron formation 2.45 billion years ago. *Nature* **385**, 55–58.
- Bekker A., Holland H. D., Wang P.-L., Rumble D., Stein H. J., Hannah J. L., Coetzee L. L. and Beukes N. J. (2004) Dating the rise of atmospheric oxygen. *Nature* **427**, 117–120.
- Bergmann K. D., Grotzinger J. P. and Fischer W. W. (2013) Biological Influences on Seafloor Carbonate Precipitation. *PALAIOS* **28**, 99–115.

- Berner E. K. and Berner R. A. (2012) *Global Environment: Water, Air, and Geochemical Cycles*, Princeton University Press.
- Beukes N. J. (1987) Facies relations, depositional environments and diagenesis in a major early Proterozoic stromatolitic carbonate platform to basinal sequence, Campbellrand Subgroup, Transvaal Supergroup, Southern Africa. *Sediment. Geol.* **54**, 1–46.
- Beukes N. J. (1983) Palaeoenvironmental Setting of Iron-Formations in the Depositional Basin of the Transvaal Supergroup, South Africa. In *Developments in Precambrian Geology* (eds. A. F. Trendall and R. C. Morris). Elsevier, Amsterdam, The Netherlands. pp. 131–198. Available at: <http://www.sciencedirect.com/science/article/pii/S0166263508700434> [Accessed March 22, 2013].
- Brand U. and Veizer J. (1980) Chemical diagenesis of a multicomponent carbonate system; 1, Trace elements. *J. Sediment. Res.* **50**, 1219–1236.
- Brusnitsyn A. I. (2006) Mineralogy and metamorphism conditions of manganese ore at the South Faizulino deposit, the southern Urals, Russia. *Geol. Ore Depos.* **48**, 193–214.
- Büchel C., Barber J., Ananyev G., Eshaghi S., Watt R. and Dismukes C. (1999) Photoassembly of the Manganese Cluster and Oxygen Evolution from Monomeric and Dimeric CP47 Reaction Center Photosystem II Complexes. *Proc. Natl. Acad. Sci.* **96**, 14288–14293.
- Burdige D. J. and Nealson K. H. (1986) Chemical and microbiological studies of sulfide-mediated manganese reduction. *Geomicrobiol. J.* **4**, 361–387.
- Butterfield C. N., Soldatova A. V., Lee S.-W., Spiro T. G. and Tebo B. M. (2013) Mn(II,III) oxidation and MnO<sub>2</sub> mineralization by an expressed bacterial multicopper oxidase. *Proc. Natl. Acad. Sci. U. S. A.* **110**, 11731–11735.
- Cairncross B. and Beukes N. J. (2013) *The Kalahari Manganese Field, the adventure continues...*, Struik Nature, Cape Town.
- Calvert S. E. and Pedersen T. F. (1996) Sedimentary geochemistry of manganese; implications for the environment of formation of manganiferous black shales. *Econ. Geol.* **91**, 36–47.
- Calvert S. E. and Price N. B. (1970) Composition of manganese nodules and manganese carbonates from Loch Fyne, Scotland. *Contrib. Mineral. Petrol.* **29**, 215–233.

- Canfield D. E., Thamdrup B. and Hansen J. W. (1993) The anaerobic degradation of organic matter in Danish coastal sediments: Iron reduction, manganese reduction, and sulfate reduction. *Geochim. Cosmochim. Acta* **57**, 3867–3883.
- Van Cappellen P., Viollier E., Roychoudhury A., Clark L., Ingali E., Lowe K. and Dichistrina T. (1998) Cycling of iron and manganese in surface sediments; a general theory for the coupled transport and reaction of carbon, oxygen, nitrogen, sulfur, iron, and manganese. *Environ. Sci. Technol.* **32**, 2931–2939.
- Clement B. G., Luther III G. W. and Tebo B. M. (2009) Rapid, oxygen-dependent microbial Mn(II) oxidation kinetics at sub-micromolar oxygen concentrations in the Black Sea suboxic zone. *Geochim. Cosmochim. Acta* **73**, 1878–1889.
- Coleman M. L., Fleet A. and Donson P. (1982) *Preliminary studies of manganese-rich carbonate nodules from Leg 68, Site 503, eastern equatorial Pacific.*
- Cornell D. H. and Schütte S. S. (1995) A volcanic-exhalative origin for the world's largest (Kalahari) Manganese field. *Miner. Deposita* **30**, 146–151.
- Von Damm K. L. (1990) Seafloor Hydrothermal Activity: Black Smoker Chemistry and Chimneys. *Annu. Rev. Earth Planet. Sci.* **18**, 173.
- Davies S. H. R. and Morgan J. J. (1989) Manganese(II) oxidation kinetics on metal oxide surfaces. *J. Colloid Interface Sci.* **129**, 63–77.
- Dick G. J., Clement B. G., Webb S. M., Fodrie F. J., Bargar J. R. and Tebo B. M. (2009) Enzymatic microbial Mn(II) oxidation and Mn biooxide production in the Guaymas Basin deep-sea hydrothermal plume. *Geochim. Cosmochim. Acta* **73**, 6517–6530.
- Diem D. and Stumm W. (1984) Is dissolved  $Mn^{2+}$  being oxidized by  $O_2$  in absence of Mn-bacteria or surface catalysts? *Geochim. Cosmochim. Acta* **48**, 1571–1573.
- Dollhopf M. E., Nealson K. H., Simon D. M. and Luther III G. W. (2000) Kinetics of Fe(III) and Mn(IV) reduction by the Black Sea strain of *Shewanella putrefaciens* using in situ solid state voltammetric Au/Hg electrodes. *Mar. Chem.* **70**, 171–180.
- Elzinga E. J. (2011) Reductive Transformation of Birnessite by Aqueous Mn(II). *Environ. Sci. Technol.* **45**, 6366–6372.
- Fischer T. B., Heaney P. J., Jang J.-H., Ross D. E., Brantley S. L., Post J. E. and Tien M. (2008) Continuous time-resolved X-ray diffraction of the biocatalyzed reduction of Mn oxide. *Am. Mineral.* **93**, 1929–1932.

- Fischer W. W. and Knoll A. H. (2009) An Iron Shuttle for Deepwater Silica in Late Archean and Early Paleoproterozoic Iron Formation. *Geol. Soc. Am. Bull.* **121**, 222–235.
- Fischer W. W., Schroeder S., Lacassie J. P., Beukes N. J., Goldberg T., Strauss H., Horstmann U. E., Schrag D. P. and Knoll A. H. (2009) Isotopic constraints on the Late Archean carbon cycle from the Transvaal Supergroup along the western margin of the Kaapvaal Craton, South Africa. *Precambrian Res.* **169**, 15–27.
- Fredrickson J. K., Romine M. F., Beliaev A. S., Auchtung J. M., Driscoll M. E., Gardner T. S., Nealon K. H., Osterman A. L., Pinchuk G., Reed J. L., Rodionov D. A., Rodrigues J. L. M., Saffarini D. A., Serres M. H., Spormann A. M., Zhulin I. B. and Tiedje J. M. (2008) Towards environmental systems biology of *Shewanella*. *Nat. Rev. Microbiol.* **6**, 592–603.
- Freitas B. T., Warren L. V., Boggiani P. C., De Almeida R. P. and Piacentini T. (2011) Tectono-sedimentary evolution of the Neoproterozoic BIF-bearing Jacadigo Group, SW-Brazil. *Sediment. Geol.* **238**, 48–70.
- Geszvain K., Butterfield C., Davis R. E., Madison A. S., Lee S., Parker D. L., Soldatova A., Spiro T. G., Luther G. W. and Tebo B. M. (2012) The molecular biogeochemistry of manganese(II) oxidation. *Biochem. Soc. Trans.* **40**, 1244–1248.
- Gross G. A. (1965) *Geology of Iron Deposits in Canada.*, Department of Mines and Technical Surveys, Geological Survey of Canada, Ottawa.
- Grotzinger J. P. and Kasting J. F. (1993) New constraints on Precambrian ocean composition. *J. Geol.* **101**, 235–243.
- Gutzmer J. (1996) Genesis and alteration of the Kalahari and Postmasburg manganese deposits, Griqualand West, South Africa. Rand Afrikaans University.
- Hammel K. E., Tardone P. J., Moen M. A. and Price L. A. (1989) Biomimetic oxidation of nonphenolic lignin models by Mn(III): new observations on the oxidizability of guaiacyl and syringyl substructures. *Arch. Biochem. Biophys.* **270**, 404–409.
- Hansel C. M., Zeiner C. A., Santelli C. M. and Webb S. M. (2012) Mn(II) oxidation by an ascomycete fungus is linked to superoxide production during asexual reproduction. *Proc. Natl. Acad. Sci.* **109**, 12621–12625.
- Hasui Y. and Almeida F. F. M. (1970) Geocronologia do Centro-Oeste brasileiro. *Bol. Soc. Bras. Geol. Sao Paulo* **19**, 5–26.
- Hem J. D. and Lind C. J. (1983) Nonequilibrium models for predicting forms of precipitated manganese oxides. *Geochim. Cosmochim. Acta* **47**, 2037–2046.

- Hoffman P. F. (2013) The Great Oxidation and a Siderian snowball Earth: MIF-S based correlation of Paleoproterozoic glacial epochs. *Chem. Geol.* **362**, 142–156.
- Hoffman P. F. and Schrag D. P. (2002) The snowball Earth hypothesis: testing the limits of global change. *Terra Nova* **14**, 129–155.
- Holland H. D. (1984) *The Chemical Evolution of the Atmosphere and Oceans.*, Princeton University Press.
- Iddings J. P. (2009) *Igneous Rocks: Composition, Texture and Classification, Description and Occurrence.*, Univeristy of Michigan Library, Ann Arbor.
- Ingle J. C. Jr., Suyehiro K., von Breymann M. T. and et al. (1990) *Proceedings of the Ocean Drilling Program, Initial Reports.*, Ocean Drilling Program, College Station, TX.
- Jakobsen R. and Postma D. (1989) Formation and solid solution behavior of Ca-rhodochrosites in marine muds of the Baltic deeps. *Geochim. Cosmochim. Acta* **53**, 2639–2648.
- Johnson J. E., Gerpheide A., Lamb M. P. and Fischer W. W. (2014) O<sub>2</sub> constraints from Paleoproterozoic detrital pyrite and uraninite. *Geol. Soc. Am. Bull.* **126**, 813–830.
- Johnson J. E., Webb S. M., Thomas K., Ono S., Kirschvink J. L. and Fischer W. W. (2013) Manganese-oxidizing photosynthesis before the rise of cyanobacteria. *Proc. Natl. Acad. Sci.* **110**, 11238–11243.
- Jones S., McNaughton N. J. and Grguric B. (2013) Structural controls and timing of fault-hosted manganese at Woodie Woodie, East Pilbara, Western Australia. *Ore Geol. Rev.* **50**, 52–82.
- Junta J. L. and Hochella Jr. M. F. (1994) Manganese (II) oxidation at mineral surfaces: A microscopic and spectroscopic study. *Geochim. Cosmochim. Acta* **58**, 4985–4999.
- Junta-Rosso J. L. and Hochella Jr. M. F. (1996) The chemistry of hematite 001 surfaces. *Geochim. Cosmochim. Acta* **60**, 305–314.
- Kim S. S., Bargar J. R., Nealson K. H., Flood B. E., Kirschvink J. L., Raub T. D., Tebo B. M. and Villalobos M. (2011) Searching for biosignatures using electron paramagnetic resonance (EPR) analysis of manganese oxides. *Astrobiology* **11**, 775–786.
- Kirschvink J. L., Gaidos E. J., Bertani L. E., Beukes N. J., Gutzmer J., Maepa L. N. and Steinberger R. E. (2000) Paleoproterozoic snowball Earth: Extreme climatic and geochemical global change and its biological consequences. *Proc. Natl. Acad. Sci.* **97**, 1400–1405.



- Klein C. (2005) Some Precambrian Banded Iron-Formations (BIFs) from Around the World: Their Age, Geologic Setting, Mineralogy, Metamorphism, Geochemistry, and Origins. *Am. Mineral.* **90**, 1473–1499.
- Klein C. and Ladeira E. A. (2004) Geochemistry and Mineralogy of Neoproterozoic Banded Iron-Formations and Some Selected, Siliceous Manganese Formations from the Urucum District, Mato Grosso Do Sul, Brazil. *Econ. Geol.* **99**, 1233–1244.
- Komiya T., Hirata T., Kitajima K., Yamamoto S., Shibuya T., Sawaki Y., Ishikawa T., Shu D., Li Y. and Han J. (2008) Evolution of the composition of seawater through geologic time, and its influence on the evolution of life. *Gondwana Res.* **14**, 159–174.
- Kostka J. E., Luther G. W. I. and Nealson K. H. (1995) Chemical and biological reduction of Mn(III)-pyrophosphate complexes: Potential importance of dissolved Mn(III) as an environmental oxidant. *Geochim. Cosmochim. Acta* **59**, 885–894.
- Von Langen P. J., Johnson K. S., Coale K. H. and Elrod V. A. (1997) Oxidation kinetics of manganese (II) in seawater at nanomolar concentrations. *Geochim. Cosmochim. Acta* **61**, 4945–4954.
- Lanza N. L., Fischer W. W., Wiens R. C., Grotzinger J., Ollila A. M., Cousin A., Anderson R. B., Clark B. C., Gellert R., Mangold N., Maurice S., Le Mouélic S., Nachon M., Schmidt M., Berger J., Clegg S. M., Forni O., Hardgrove C., Melikechi N., Newsom H. E. and Sautter V. (2014) High manganese concentrations in rocks at Gale crater, Mars. *Geophys. Res. Lett.* **41**, 2014GL060329.
- Learman D. R., Voelker B. M., Vazquez-Rodriguez A. I. and Hansel C. M. (2011) Formation of manganese oxides by bacterially generated superoxide. *Nat. Geosci.* **4**, 95–98.
- Lee J.-H., Kennedy D. W., Dohnalkova A., Moore D. A., Nachimuthu P., Reed S. B. and Fredrickson J. K. (2011) Manganese sulfide formation via concomitant microbial manganese oxide and thiosulfate reduction. *Environ. Microbiol.* **13**, 3275–3288.
- Lin H., Szeinbaum N. H., DiChristina T. J. and Taillefert M. (2012) Microbial Mn(IV) reduction requires an initial one-electron reductive solubilization step. *Geochim. Cosmochim. Acta* **99**, 179–192.
- Lovley D. R. and Phillips E. J. P. (1988) Novel Mode of Microbial Energy Metabolism: Organic Carbon Oxidation Coupled to Dissimilatory Reduction of Iron or Manganese. *Appl. Environ. Microbiol.* **54**, 1472–1480.

- Lowenstein T. K., Timofeeff M. N., Brennan S. T., Hardie L. A. and Demicco R. V. (2001) Oscillations in Phanerozoic Seawater Chemistry: Evidence from Fluid Inclusions. *Science* **294**, 1086–1088.
- Luther G. W. I. (2010) The Role of One- and Two-Electron Transfer Reactions in Forming Thermodynamically Unstable Intermediates as Barriers in Multi-Electron Redox Reactions. *Aquat. Geochem.* **16**, 395–420.
- Madison A. S., Tebo B. M., Mucci A., Sundby B. and Luther G. W. (2013) Abundant Porewater Mn(III) Is a Major Component of the Sedimentary Redox System. *Science* **341**, 875–878.
- Manceau A., Marcus M. A. and Grangeon S. (2012) Determination of Mn valence states in mixed-valent manganates by XANES spectroscopy. *Am. Mineral.* **97**, 816–827.
- Martin D. M., Clendenin C. W., Krapez B. and McNaughton N. J. (1998) Tectonic and geochronological constraints on late Archaean and Palaeoproterozoic stratigraphic correlation within and between the Kaapvaal and Pilbara Cratons. *J. Geol. Soc. Aust.* **155**, 311–322.
- Matsumoto R. (1992) Diagenetic Dolomite, Calcite, Rhodochrosite, Magnesite, and Lansfordite from site 799, Japan Sea - Implications for depositional environments and the diagenesis of organic-rich sediments. In *Proceedings of the Ocean Drilling Program, Scientific Results* (eds. K. A. Pisciotta, J. C. Ingle Jr., M. T. von Breyman, and J. Barron). Ocean Drilling Program, College Station, TX. pp. 75–98. Available at: doi:10.2973/odp.proc.sr.127128-1.119.1992.
- Mayhew L. E., Webb S. M. and Templeton A. S. (2011) Microscale imaging and identification of Fe speciation and distribution during fluid-mineral reactions under highly reducing conditions. *Environ. Sci. Technol.* **45**, 4468–4474.
- Maynard J. B. (2010) The Chemistry of Manganese Ores through Time: A Signal of Increasing Diversity of Earth-Surface Environments. *Econ. Geol.* **105**, 535–552.
- McEvoy J. P. and Brudvig G. W. (2006) Water-Splitting Chemistry of Photosystem II. *Chem. Rev.* **106**, 4455–4483.
- McKeown D. A. and Post J. E. (2001) Characterization of manganese oxide mineralogy in rock varnish and dendrites using X-ray absorption spectroscopy. *Am. Mineral.* **86**, 701–713.
- Middelburg J. J., De Lange G. J. and van Der Weijden C. H. (1987) Manganese solubility control in marine pore waters. *Geochim. Cosmochim. Acta* **51**, 759–763.
- Moore T. E., Ellis M. and Selwood P. W. (1950) Solid Oxides and Hydroxides of Manganese. *J. Am. Chem. Soc.* **72**, 856–866.

- More C., Belle V., Asso M., Fournel A., Roger G., Guigliarelli B. and Bertrand P. (1999) EPR spectroscopy: a powerful technique for the structural and functional investigation of metalloproteins. *Biospectroscopy* **5**, S3–18.
- Morgan J. J. (2005) Kinetics of reaction between O<sub>2</sub> and Mn(II) species in aqueous solutions. *Geochim. Cosmochim. Acta* **69**, 35–48.
- Mucci A. (2004) The Behavior of Mixed Ca–Mn Carbonates in Water and Seawater: Controls of Manganese Concentrations in Marine Porewaters. *Aquat. Geochem.* **10**, 139–169.
- Müller S. G., Krapež B., Barley M. E. and Fletcher I. R. (2005) Giant iron-ore deposits of the Hamersley province related to the breakup of Paleoproterozoic Australia: New insights from in situ SHRIMP dating of baddeleyite from mafic intrusions. *Geology* **33**, 577–580.
- Murray J. W., Dillard J. G., Giovanoli R., Moers H. and Stumm W. (1985) Oxidation of Mn(II): Initial mineralogy, oxidation state and ageing. *Geochim. Cosmochim. Acta* **49**, 463–470.
- Myers C. R. and Nealson K. H. (1988) Bacterial manganese reduction and growth with manganese oxide as the sole electron acceptor. *Science* **240**, 1319–1321.
- Myers C. R. and Nealson K. H. (1988) Microbial reduction of manganese oxides: Interactions with iron and sulfur. *Geochim. Cosmochim. Acta* **52**, 2727–2732.
- Nicholson K. (1997) *Manganese Mineralization: Geochemistry And Mineralogy of Terrestrial And Marine Deposits.*, Geological Society.
- Norton J. J. (1970) Composition of a Pegmatite, Keystone, South Dakota. *Am. Mineral.* **55**, 981–1002.
- Okita P. M., Maynard J. B., Spiker E. C. and Force E. R. (1988) Isotopic evidence for organic matter oxidation by manganese reduction in the formation of stratiform manganese carbonate ore. *Geochim. Cosmochim. Acta* **52**, 2679–2685.
- Okita P. M. and Shanks W. C. (1992) Origin of stratiform sediment-hosted manganese carbonate ore deposits: Examples from Molango, Mexico, and TaoJiang, China. *Chem. Geol.* **99**, 139–163.
- Pedersen T. F. and Price N. B. (1982) The geochemistry of manganese carbonate in Panama Basin sediments. *Geochim. Cosmochim. Acta* **46**, 59–68.
- Perez J. and Jeffries T. W. (1992) Roles of manganese and organic acid chelators in regulating lignin degradation and biosynthesis of peroxidases by *Phanerochaete chrysosporium*. *Appl. Environ. Microbiol.* **58**, 2402–2409.

- Piacentini T., Vasconcelos P. M. and Farley K. A. (2013)  $^{40}\text{Ar}/^{39}\text{Ar}$  constraints on the age and thermal history of the Urucum Neoproterozoic banded iron-formation, Brazil. *Precambrian Res.* **228**, 48–62.
- Pingitore Jr. N. E., Eastman M. P., Sandidge M., Oden K. and Freiha B. (1988) The coprecipitation of manganese(II) with calcite: an experimental study. *Mar. Chem.* **25**, 107–120.
- Post J. E. (1999) Manganese oxide minerals: Crystal structures and economic and environmental significance. *Proc. Natl. Acad. Sci.* **96**, 3447–3454.
- Rao A. M. F., Polerecky L., Ionescu D., Meysman F. J. R. and de Beer D. (2012) The influence of pore-water advection, benthic photosynthesis, and respiration on calcium carbonate dynamics in reef sands. *Limnol. Oceanogr.* **57**, 809–825.
- Robie R. A., Huebner J. S. and Hemingway B. S. (1995) Heat capacities and thermodynamic properties of braunite ( $\text{Mn}_7\text{SiO}_{12}$ ) and rhodonite ( $\text{MnSiO}_3$ ). *Am. Mineral.* **80**, 560–575.
- Roy S. (2006) Sedimentary manganese metallogenesis in response to the evolution of the Earth system. *Earth-Sci. Rev.* **77**, 273–305.
- Santelli C. M., Webb S. M., Dohnalkova A. C. and Hansel C. M. (2011) Diversity of Mn oxides produced by Mn(II)-oxidizing fungi. *Geochim. Cosmochim. Acta* **75**, 2762–2776.
- Schröder S., Bedorf D., Beukes N. J. and Gutzmer J. (2011) From BIF to red beds: Sedimentology and sequence stratigraphy of the Paleoproterozoic Koegas Subgroup (South Africa). *Sediment. Geol.* **236**, 25–44.
- Scott R. W. (1984) Mesozoic Biota and Depositional Systems of the Gulf of Mexico-Caribbean Region. In *Jurassic-Cretaceous Biochronology and Paleogeography of North America* (ed. G. E. G. Westermann). Geological Association of Canada. University of Toronto Press, St. John's, Newfoundland.
- Stilling A. (1998) Bulk composition of the Tanco Pegmatite at Bernic Lake, Manitoba, Canada. Masters, University of Manitoba.
- Stone A. T. and Morgan J. J. (1984) Reduction and dissolution of manganese(III) and manganese(IV) oxides by organics: 2. Survey of the reactivity of organics. *Environ. Sci. Technol.* **18**, 617–624.
- Takehara M., Komure M., Kiyokawa S., Horie K. and Yokohama K. (2010) Detrital zircon SHRIMP U-Pb age of the 2.3 Ga diamictites of the Meteorite Bore Member in the South Pilbara, Western Australia. In *Fifth International Archean*

- Symposium Abstracts: Geological Survey of Western Australia* (eds. I. M. Tyler and C. M. Knox-Robinson). Record 2010/18. pp. 223–224.
- Tamura N. and Cheniae G. (1987) Photoactivation of the water-oxidizing complex in Photosystem II membranes depleted of Mn and extrinsic proteins. I. Biochemical and kinetic characterization. *Biochim. Biophys. Acta BBA - Bioenerg.* **890**, 179–194.
- Tang Y., Zeiner C. A., Santelli C. M. and Hansel C. M. (2013) Fungal oxidative dissolution of the Mn(II)-bearing mineral rhodochrosite and the role of metabolites in manganese oxide formation. *Environ. Microbiol.* **15**, 1063–1077.
- Tebo B. M., Bargar J. R., Clement B. G., Dick G. J., Murray K. J., Parker D., Verity R. and Webb S. M. (2004) BIOGENIC MANGANESE OXIDES: Properties and Mechanisms of Formation. *Annu. Rev. Earth Planet. Sci.* **32**, 287–328.
- Tebo B. M., Johnson H. A., McCarthy J. K. and Templeton A. S. (2005) Geomicrobiology of manganese(II) oxidation. *Trends Microbiol.* **13**, 421–428.
- Thamdrup B., Finster K., Hansen J. W. and Bak F. (1993) Bacterial Disproportionation of Elemental Sulfur Coupled to Chemical Reduction of Iron or Manganese. *Appl. Environ. Microbiol.* **59**, 101–108.
- Thamdrup B., Rosselló-Mora R. and Amann R. (2000) Microbial Manganese and Sulfate Reduction in Black Sea Shelf Sediments. *Appl. Environ. Microbiol.* **66**, 2888–2897.
- Trouwborst R. E., Clement B. G., Tebo B. M., Glazer B. T. and Luther G. W. (2006) Soluble Mn(III) in Suboxic Zones. *Science* **313**, 1955–1957.
- Tsikos H., Beukes N. J., Moore J. M. and Harris C. (2003) Deposition, Diagenesis, and Secondary Enrichment of Metals in the Paleoproterozoic Hotazel Iron Formation, Kalahari Manganese Field, South Africa. *Econ. Geol.* **98**, 1449–1462.
- Turekian K. K. and Wedepohl K. H. (1961) Distribution of the Elements in Some Major Units of the Earth's Crust. *Geol. Soc. Am. Bull.* **72**, 175–192.
- Urban H., Stribny B. and Lippolt H. J. (1992) Iron and manganese deposits of the Urucum District, Mato Grosso do Sul, Brazil. *Econ. Geol.* **87**, 1375–1392.
- Vasconcelos P. M. (1999) K-Ar AND  $^{40}\text{Ar}/^{39}\text{Ar}$  GEOCHRONOLOGY OF WEATHERING PROCESSES. *Annu. Rev. Earth Planet. Sci.* **27**, 183–229.
- Veizer J. (1978) Secular variations in the composition of sedimentary carbonate rocks, II. Fe, Mn, Ca, Mg, Si and minor constituents. *Precambrian Res.* **6**, 381–413.

- Wallmann K., Aloisi G., Haeckel M., Tishchenko P., Pavlova G., Greinert J., Kutterolf S. and Eisenhauer A. (2008) Silicate weathering in anoxic marine sediments. *Geochim. Cosmochim. Acta* **72**, 3067–3090.
- Wariishi H., Valli K. and Gold M. H. (1992) Manganese(II) oxidation by manganese peroxidase from the basidiomycete *Phanerochaete chrysosporium*. Kinetic mechanism and role of chelators. *J. Biol. Chem.* **267**, 23688–23695.
- Webb S. M. (2011) The MicroAnalysis Toolkit: X-ray Fluorescence Image Processing Software. *AIP Conf. Proc.* **1365**, 196–199.
- Webb S. M., Dick G. J., Bargar J. R. and Tebo B. M. (2005) Evidence for the presence of Mn(III) intermediates in the bacterial oxidation of Mn(II). *Proc. Natl. Acad. Sci. U. S. A.* **102**, 5558–5563.
- Webb S. M., Tebo B. M. and Bargar J. R. (2005) Structural characterization of biogenic Mn oxides produced in seawater by the marine bacillus sp. strain SG-1. *Am. Mineral.* **90**, 1342–1357.
- Wehrli B., Friedl G. and Manceau A. (1995) Reaction Rates and Products of Manganese Oxidation at the Sediment-Water Interface. In *Aquatic Chemistry Advances in Chemistry*. American Chemical Society. pp. 111–134. Available at: <http://dx.doi.org/10.1021/ba-1995-0244.ch005> [Accessed November 9, 2014].
- Wenzhöfer F., Adler M., Kohls O., Hensen C., Strotmann B., Boehme S. and Schulz H. D. (2001) Calcite dissolution driven by benthic mineralization in the deep-sea: in situ measurements of Ca<sup>2+</sup>, pH, pCO<sub>2</sub> and O<sub>2</sub>. *Geochim. Cosmochim. Acta* **65**, 2677–2690.
- Williford K. H., Van Kranendonk M. J., Ushikubo T., Kozdon R. and Valley J. W. (2011) Constraining atmospheric oxygen and seawater sulfate concentrations during Paleoproterozoic glaciation: In situ sulfur three-isotope microanalysis of pyrite from the Turee Creek Group, Western Australia. *Geochim. Cosmochim. Acta* **75**, 5686–5705.
- Abs-Wurmbach I. (1980) Miscibility and compatibility of braunite, Mn<sup>2+</sup>+Mn<sup>6 3+</sup> O<sub>8</sub>/SiO<sub>4</sub>, in the system Mn-Si-O at 1 atm in air. *Contrib. Mineral. Petrol.* **71**, 393–399.
- Ying S. C., Kocar B. D., Griffis S. D. and Fendorf S. (2011) Competitive Microbially and Mn Oxide Mediated Redox Processes Controlling Arsenic Speciation and Partitioning. *Environ. Sci. Technol.* **45**, 5572–5579.

## SUPPLEMENTAL FIGURES AND TABLES

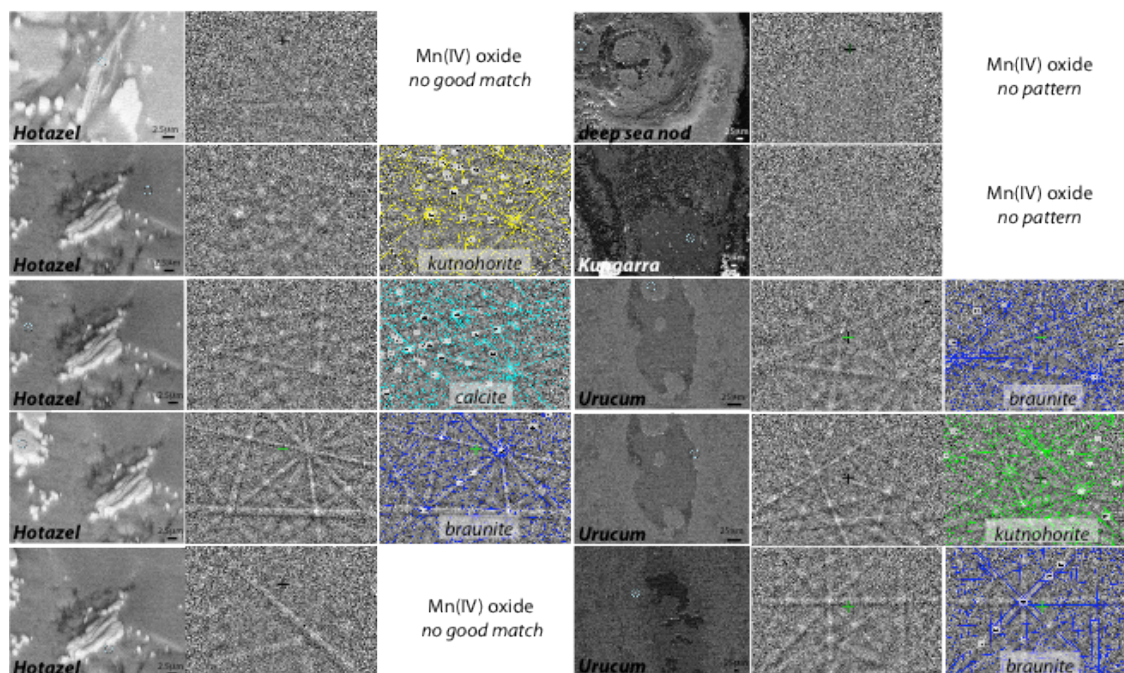
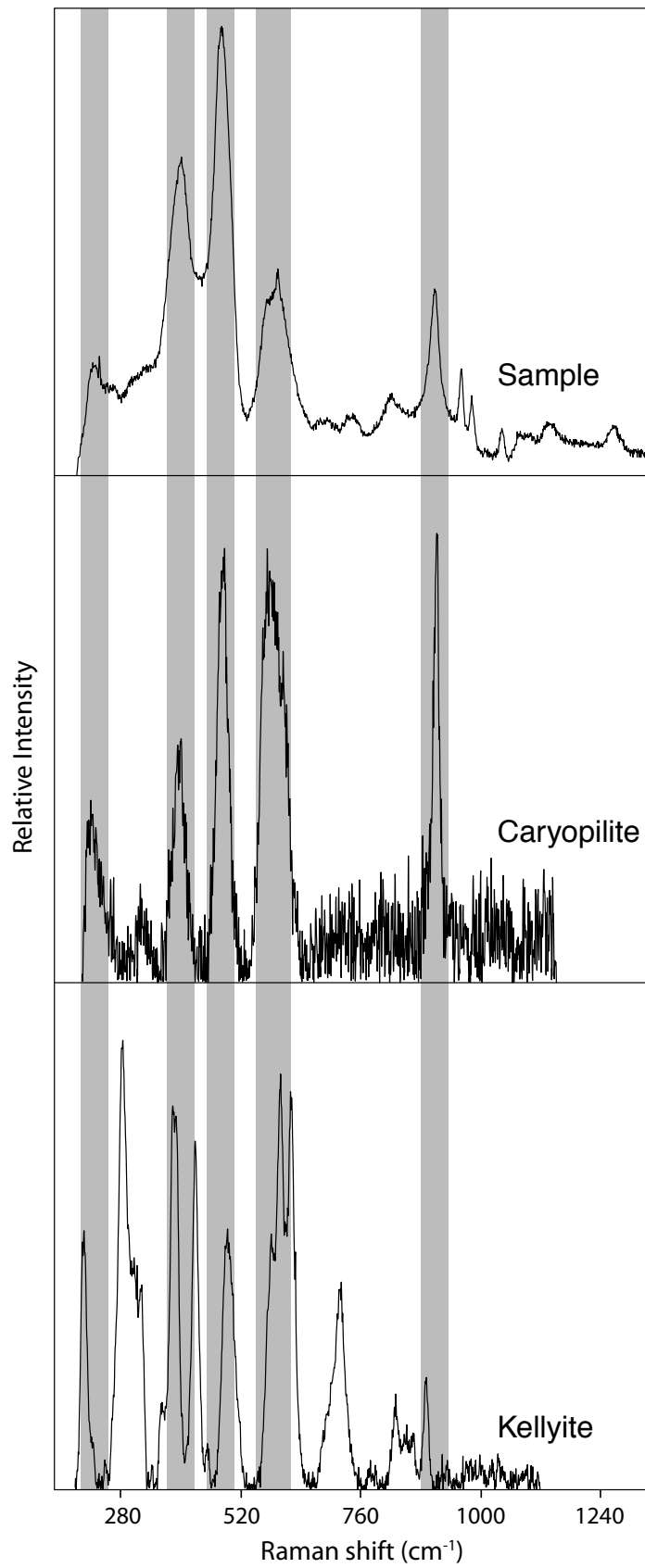


**Fig. A1: EBSD patterns and identifications**

Electron backscatter diffraction patterns measured on microscale phases within various samples to help assess mineralogy. These confirm phase identifications made from XANES, electron microscopy, and electron microprobe. These results also highlight that Mn(IV) oxides do not typically produce good diffraction patterns, in both ancient and modern samples.

**Fig. A2 (below): Raman identification of caryopilite**

Raman spectra helped constrain the identity of an unknown but common Mn-silicate observed in the Santa Cruz Formation. Two possible options from other data for this mineral were caryopilite and kellyite, but Raman shifts indicate that only caryopilite has same peaks as the sample while kellyite is a poor match for the sample.





Ore Name/Location	Volume (million tons)	Estimated Age (million years ago)	Reference
Nikopol, Ukraine, Georgia	1000	28	Varentsov and Grasselly, 1976
Groote Eylandt, Australia	400	123	Pracejus and Bolton, 1992
Molango, Mexico	200	155	Martino, 1986
Xialei, China + Atasu, Kazakhstan	200	370	Varentsov and Grasselly, 1976; Fan and Yang, 1999
Usinsk, Siberia + others	150	520	Varentsov and Grasselly, 1976
Corumbá, Brazil + small Baltic deps	686	625	Urban et al, 1992
Woodie-Woodie, Australia	65	1100-950	Jones et al, 2013
Wafangzi, China	38	1200	Rodionov et al, 2004
Sausar Group, India + Postmasburg Group	115	2000	Dasgupta et al, 1991; Gutzmer, 1996; Cairncross and Beukes, 2013
Moanda, Gabon	400	2150	National Materials Advisory Board, 1981; Gauthier-Lafaye et al, 1996
Birimian Supergroup, West Africa	49	2200	National Materials Advisory Board, 1981; Davis et al, 1994
Hotazel Formation/ Kalahari Mn field	1350	2220	Gutzmer, 1996
Minas Gerais, Brazil	20	2400	Maxwell, 1972; Babinski et al., 1995
Koegas Subgroup, S Africa	200	2420	Cairncross and Beukes, 2013

**Supplementary Table 1:** Survey of manganese ore deposits through geologic time, accompanying Figure 1.

## Chapter 2

### Manganese-oxidizing photosynthesis before the rise of cyanobacteria

Jena E. Johnson<sup>a</sup>, Samuel M. Webb<sup>b</sup>, Katherine Thomas<sup>c</sup>, Shuhei Ono<sup>c</sup>, Joseph L. Kirschvink<sup>a</sup>, Woodward W. Fischer<sup>a</sup>

<sup>a</sup>Division of Geological and Planetary Sciences, California Institute of Technology, Pasadena, CA 91125. <sup>b</sup>Stanford Synchrotron Radiation Lightsource, Menlo Park, CA 94025. <sup>c</sup>Department of Earth, Atmospheric and Planetary Sciences, Massachusetts Institute of Technology, Cambridge, MA 02139.

*Originally published in the Proceedings of the National Academy of Sciences, Volume 108, p. 11238-11243*

#### ABSTRACT

The emergence of oxygen-producing (oxygenic) photosynthesis fundamentally transformed our planet; however, the processes that led to the evolution of biological water splitting have remained largely unknown. To illuminate this history, we examined the behavior of the ancient Mn cycle using newly-obtained scientific drill cores through an early Paleoproterozoic succession (2.415 Ga) preserved in South Africa. These strata contain substantial Mn-enrichments (up to ~17 wt. %) well before those associated with the rise of oxygen like the ~2.2 Ga Kalahari Mn deposit. Utilizing new microscale X-ray spectroscopic techniques coupled to optical and electron microscopy and carbon isotope ratios, we demonstrate that the Mn is hosted exclusively in carbonate mineral phases derived

**from reduction of Mn-oxides during diagenesis of primary sediments. Additional observations of independent proxies for O<sub>2</sub>—multiple S isotopes (measured by IRMS and SIMS) and redox-sensitive detrital grains—reveals that the original Mn-oxide phases were not produced by reactions with O<sub>2</sub>, pointing to a different high potential oxidant. These results show that the oxidative branch of the Mn cycle predates the rise of oxygen, and provide strong support for the hypothesis that the water-oxidizing complex of photosystem II evolved from a former transitional photosystem capable of single electron oxidation reactions of Mn.**

## **INTRODUCTION**

The rise of atmospheric oxygen ~2.4 billion years ago (1, 2) is the most marked environmental change in Earth history, and this transition ultimately stems from a major biological innovation—the evolution of oxygenic photosynthesis (3, 4). Several biochemical attributes were invented to facilitate this metabolism, including a core photosystem pigment with a higher redox potential than other photosynthetic reaction centers (to enable the oxidation of water) and coupled photosystems. The critical photochemical invention, however, was the water oxidizing complex (WOC) of photosystem II (PSII)—a cubane cluster of four redox-active Mn atoms and a Ca atom, bound by oxo bridges (5, 6)—which acts as a capacitor to store oxidizing equivalents and link the single electron photochemistry of the reaction center to the four electron oxidation of two water molecules to molecular oxygen (7).

Several hypotheses for the origin and evolution of the remarkable water-oxidizing machinery have been proposed. Early ideas suggested that a Mn-bearing protein was evolutionarily co-opted to become the WOC. In 1970, Olson recognized the need for transitional electron donors with intermediate redox potentials, proposing a series of nitrogen-bearing compounds such as NO and  $\text{NO}_2^-$  (8). He hypothesized that a Mn(III)-porphyrin cytochrome replaced a Fe-bearing cytochrome as the first step to evolving a Mn-based WOC (8). This idea has become less plausible as the availability of these transitional N compounds is questionable in a pre-oxygenated world (9), and as our current understanding is that Mn is not bound in a cytochrome but rather a  $\text{Mn}_4\text{CaO}_5$  cluster (6). Looking to other Mn-bearing proteins as transitional WOCs, Blankenship and Hartman postulated that a Mn-containing catalase transferring electrons from an  $\text{H}_2\text{O}_2$  donor might have been an intermediate step in the evolution of oxygenic photosynthesis (10). However, there are no significant sequence or structural similarities between the core protein of PSII and Mn catalase, and no evidence for a significant amount of hydrogen peroxide in Archean oceans (10, 11).

A different class of hypotheses suggested that the WOC was derived from the integration of external manganese oxide phases, building on short-range structural similarities between the WOC and certain tunnel-structured Mn-oxide phases like hollandite (11, 12). This hypothesis, however, is at odds with the general dearth of environmental Mn-oxide phases prior to the rise of oxygen (13, 14). Furthermore, this process is not recapitulated during formation of the WOC today, which only requires soluble Mn(II) and light (15).

During modern assembly of the WOC, no  $O_2$  is evolved, but rather electrons are donated from divalent Mn to the photosystem to arrive at the basal oxidation state ( $S_0$ ) of the water-oxidizing  $Mn(III)_3Mn(IV)$  cluster (4, 7). This mechanism of photoassembly offers a potential clue to the evolution of the WOC.

**A transitional Mn-oxidizing photosystem prior to oxygenic photosynthesis.** From an evolutionary perspective, it is notable that modern biological water-splitting begins with Mn oxidation, and this observation forms the basis for a final class of evolutionary scenarios wherein Mn(II) played an important role as an electron donor for photosynthesis prior to oxygenic photosynthesis. Zubay proposed that anoxygenic Fe-based phototrophs developed the capacity for Mn oxidation, which subsequently evolved into a tetramanganese WOC able to store oxidizing equivalents and perform water oxidation (16). Dismukes and coworkers later hypothesized that  $Mn(II)(HCO_3)_x$  complexes offered lower potential donors to a transitional photosystem, which then evolved to contain a tetramanganese cluster via a ‘bicarbonate oxidase’ intermediate that produced  $O_2$  prior to water splitting (17). Allen and Martin (2007) envisioned a protocyanobacterium which started to receive electrons from soluble Mn(II) oxidized by UV radiation (18). These hypotheses differ in their evolutionary mechanics, but all broadly invoke photooxidation of Mn(II)-bearing compounds prior to the evolution of photochemical water splitting. The high concentrations of Mn(II) in Archean surface seawater (19, 20) would have presented an evolutionary opportunity and electron source for direct Mn(II) oxidation by an early photosystem able to perform one-electron

photochemical reactions. In order to exploit this resource, a primitive reaction center would have needed to produce a higher potential oxidant to strip electrons from Mn—higher than required for other electron donors but closer to that required for water oxidation. Considering these redox potential constraints, Mn oxidation is an attractive photosynthetic donor on a trajectory to oxidizing water (16–18). An initial manganese-oxidizing photosystem also explains both why the only known biological system that can oxidize water originally procures electrons from Mn and why WOC assembly begins with Mn oxidation. This hypothesis makes a clear prediction: were Mn-based photosynthesis ever realized as a transitional state, it should predate the evolution of oxygenic cyanobacteria. This would leave a distinctive mark in the geological record, with the byproduct of photosynthesis (Mn oxides) forming before the rise of cyanobacteria and in the absence of molecular oxygen.

The timing of cyanobacterial origins remains controversial because of the absence of a robust Archean fossil record. The use of molecular fossils was explored with much apparent potential (21). 2.7 Ga biomarkers associated with cyanobacteria, 2-methyl hopanoids, suggested the early rise of cyanobacteria, but the syngeneity of these compounds (22) and their connection to cyanobacteria (23, 24) has since been questioned. A separate, widely applied approach to date the evolution of cyanobacteria centers on proxies for their metabolic product:  $O_2$ . A variety of geochemical tracers, such as Mo, Re, steranes, and iron speciation, have been used to argue for very low (~ nanomolar) levels of dissolved  $O_2$ , implying that the evolution of cyanobacteria greatly

predates the rise of oxygen (see review by Farquhar *et al.*, 2011 (25)). Fundamentally, however, using O<sub>2</sub> as a proxy for cyanobacteria at such low levels is imperfect and will lead to false-positives, as there are additional sources of O<sub>2</sub> (both biotic and abiotic) that can be important at these concentrations (26–28). Further, many of these elemental proxies have non-unique interpretations and their geochemical cycles are not well understood mechanistically on both short and long timescales (29–31). These proxies can also be impacted by diagenetic and metamorphic processes and studies performed on ancient samples with complex postdepositional histories should be viewed with appropriate caution (e.g., see 29, 32, 33). Sulfur isotope systematics are perhaps the most thoroughly studied, and while the origin of minor isotope mass-anomalous fractionations are not fully understood, the preservation of these effects requires a pO<sub>2</sub> < 10<sup>-5.7</sup> atm, perhaps closer to 10<sup>-13</sup> atm (34). Currently, sulfur isotope measurements have constrained the rise of oxygen and minimum age for the origin of cyanobacteria as having occurred between 2.45 and 2.32 Ga (1, 2)—an interval supported by a broad range of geologic evidence (19, 25, 33).

To test these Mn-phototrophy hypotheses, we examined the earliest authigenic Mn deposits paired with several proxies for oxygen to probe the geologic record for evidence of these transitional phototrophs. The behavior of the ancient Mn cycle is useful because it is uniquely sensitive to high redox potential oxidants like O<sub>2</sub>: unlike other redox proxies, Mn can only be oxidized by molecular oxygen (or O<sub>2</sub>-derived species like superoxide and hydrogen peroxide) or a high potential photosystem (35, 36). Notably,

while Fe was removed from shallow water via oxidation processes in Archean marine environments, the same was not true for Mn (20, 37). In an anoxic Archean world, Mn(II) derived from weathering would have been transported and concentrated in seawater, and, in the absence of high potential oxidants and because Mn does not readily form sulfides, its primary sink would have been as a trace cation constituent of carbonates. Archean (3.5Ga – 2.5Ga) carbonates consequently have much higher Mn contents, up to 1.3% (38) as opposed to Phanerozoic carbonates averaging 30ppm (19). Mn can be further enriched in Archean carbonate host rocks by post-depositional carbonate dissolution and oxidation by oxygenated groundwater and hydrothermal fluids after the rise of oxygen (14, 39). Several small Archean-age manganese ore deposits in Brazil, India, and South Africa developed from carbonate protoliths reflect these processes (14). Conversely, chemical precipitates from seawater like iron formation from Archean deposits typically contain Mn <0.5% (40). Oxidation of aqueous Mn(II) to Mn(III/IV) solids is required to concentrate Mn in iron formation (14). Major Paleoproterozoic Mn deposits, including the ~2.22 Ga Kalahari Manganese Field in South Africa, developed in response to the rise in environmental O<sub>2</sub> (41, 42). Here we report the study of a sedimentary succession underlying and substantially older than the Kalahari deposit but also bearing strong authigenic Mn enrichments. We employ a suite of microscopic and spectroscopic techniques to determine the petrogenesis of Mn-bearing phases, and then turn to several independent redox-sensitive proxies to ascertain the possible paleoenvironmental role of O<sub>2</sub> in generating these deposits. Examining proxies from a micro- to basin-scale improves the identification of post-depositional alteration, and the use of multiple techniques in the



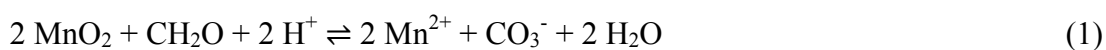
same strata provides an opportunity to address the non-uniqueness common to individual elemental and isotopic proxies.

## RESULTS

**Manganese oxidation at 2.415 Ga.** Two new scientific drill cores through the  $2415 \pm 6$  Ma Koegas Subgroup (conservatively constrained to be  $<2.43$  Ga and  $>2.22$  Ga, see *SI Text*, (43)) were retrieved as a part of the Agouron Drilling Project in Griqualand West, South Africa (Fig. 1, Fig. S1). The Koegas Subgroup contains marine shelf and deltaic sediments deposited on the western margin of the Kaapvaal craton. Observed lithologies include interbedded siliclastics, iron formation with abundant current and wave ripple cross-stratification, and minor carbonates (43). The two cores are aligned across the strike of the basin and capture proximal (GTF01) and distal (GEC01) paleoenvironments, with a higher proportion of iron formation corresponding to the loss of clastic input basinward (Fig. 1). The inboard sections (GTF01) remain flat-lying and are sub-greenschist in metamorphic grade (44), whereas GEC01 is located on the margin of a younger Paleoproterozoic fold-and-thrust belt (Fig. S1), and was more deeply buried to lower greenschist facies with discrete zones of chlorite formation (44). Well captured by the cores, the Koegas strata contain horizons in iron formation with anomalous Mn concentrations (43, 45), ranging from 1 to 16.6% (weight percent) in bulk (Fig. 1), which is extremely enriched compared to average Archean iron formation concentrations of  $<0.5\%$  (40). We observed elevated sedimentary Mn concentrations repeatedly throughout both cores in condensed sequence stratigraphic intervals (Fig. 1). This illustrates that

sedimentary Mn concentrations were high in all environments and interpreted as having low relative sedimentation rates (e.g., maximum flooding intervals and delta lobe-switches) regardless of position on the shelf or paleowater depth.

The Mn phases responsible for the enrichments in these rocks are very fine-grained and intimately associated with mixed valence iron-bearing minerals, making their analysis by standard methods challenging. Because textural context is critical to understanding the origin of these phases, we employed a new set of X-ray absorption spectroscopy techniques that provide insight into redox states and coordination environment of Mn across a large range of length scales. In addition to X-ray absorption near edge spectroscopy (XANES) of the Mn K-edge of bulk powders, we used a microprobe technique with 2 $\mu$ m resolution to obtain XANES spectra on small sample domains and construct micro-scale redox maps of ultrathin sections (46, 47, *SI Text*). We tested these methods on the well-characterized Kalahari Mn Field of the Hotazel Fm, in which Mn is hosted by two phases, braunite (Mn(III)<sub>6</sub>Mn(II)(SiO<sub>4</sub>)O<sub>8</sub>) and kutnohorite (CaMn(II)<sub>0.7</sub>Mg<sub>0.3</sub>)(CO<sub>3</sub>)<sub>2</sub> (48) (Fig. S3, Fig. S4). The kutnohorite yields a low  $\delta^{13}\text{C}$  signature (-8.1 to -12.5‰), is found in abundant concretions and laminae, and is interpreted to be secondary and diagenetic in origin from the coupled oxidation of organic carbon and reduction of manganese oxides in sedimentary pore fluids (48, 49), leading to the precipitation of Mn-carbonates:



We acquired XANES spectra of these carbonate concretions and their braunite matrix at a 2 $\mu$ m resolution (Fig. S3). We then used spectral differences between these endmembers to distinguish Mn redox states for each pixel and construct a redox map. A redox map from the Kalahari Mn deposit cleanly differentiates Mn(II) carbonate concretions from the Mn(III+II) braunite matrix (Fig. 2; Fig. S4).

In contrast to the Kalahari Hotazel Formation, XAS measurements and multiple energy redox maps of 2.415 Ga Mn enrichments throughout both cores, which occur in granular and banded iron formation, reveal that the Mn enrichments are spatially heterogeneous and exclusively in a Mn(II) valence state (Fig. 2; Fig. S3B). Bulk and point spectra best match kutnohorite and rule out the presence of Mn-oxides [Mn(III) or Mn(IV)] at the ~ 5% abundance level (at any scale) (Fig. S3). We confirmed the localization and heterogeneity of Mn in carbonate phases by energy-dispersive spectroscopy (Fig. 3 A and B).

Several independent observations reveal that these Mn carbonates in the Koegas subgroup have a secondary, diagenetic origin from reduction of sedimentary Mn oxide phases, described in Eqns. (1) and (2). The Mn mineralization is not associated with post-depositional leaching of carbonate beds or more permeable lithologies like sandstones (Fig. 1). We tested whether later metasomatic fluids (potentially derived from hydrothermal systems in the younger Kalahari Hotazel Formation that occurs ~150km to

the north; Fig. S1) could have introduced the Mn by measuring concentrations in veins and found they had no Mn enrichments (Fig. S5). Rather, the Mn enrichments are stratigraphically restricted to condensed horizons of iron formation, concentrated in authigenic 10-40 $\mu$ m Mn-carbonate crystals that display diagenetic textures (Fig. 3 *A* and *B*; Fig. S6). The C isotopic composition of these Mn-carbonate phases is highly variable and strongly  $^{13}\text{C}$ -depleted from values of seawater dissolved inorganic carbon (Fig. 3C; Fig. S11, S12). These observations imply that the carbonates were precipitated from pore fluids influenced by the microbial respiration of organic carbon (e.g., Eqn. 1). The Mn and Fe contents of these carbonates, their diagenetic textures, and their carbon isotopic values indicate that these secondary carbonates were formed from reduction of Mn and Fe oxides, a process widely recognized from Archean and Paleoproterozoic iron formations (20, 48) and Mn ore deposits (48). Examples of diagenetic Mn-bearing carbonates produced from reduction of Mn-oxides are well known from Mesozoic and Neogene deep-sea sediments, driven by reactions with Mn oxide phases with sedimentary organic matter, and show very similar isotopic characteristics (49, 50). Together these results indicate the sediments accumulated solid Mn-oxide phases, resulting in precursor sediments enriched with Mn-oxides at the time of deposition, which were subsequently reduced to Mn-carbonate during early diagenesis.

**Environmental O<sub>2</sub> levels were very low during Koegas deposition.** The oxidation of Mn to form these precursor Mn oxides points to the existence of high potential oxidants in the environment prior to 2.415 Ga. It is notable that although marine

paleoenvironments throughout this basin were capable of producing Mn-oxides, the sedimentary environment was not able to stabilize them, suggesting the lack of O<sub>2</sub> in this environment; were O<sub>2</sub> present in surface sediments, then Mn-oxides could persist because O<sub>2</sub> is a more favorable electron acceptor (51). To further ascertain whether the Mn oxidant was provided by O<sub>2</sub> or a Mn-oxidizing photosystem, we examined the behavior of several independent redox-sensitive proxies. We investigated whether O<sub>2</sub>-sensitive detrital grains were present in intercalated Koegas sandstones and whether early diagenetic pyrite in shale lithologies bears mass independent S isotope signals.

We observed detrital pyrite grains in subarkosic sandstone beds throughout the GTF01 core (Fig. 1). These redox-sensitive grains offer a simple and straightforward proxy for environmental O<sub>2</sub> because, in the presence of O<sub>2</sub>, pyrite is unstable and undergoes rapid oxidative chemical weathering. Consequently, redox-sensitive detrital grains are common in fluvial and nearshore marine sediments prior to the rise of oxygen (19, 52), and extremely scarce thereafter (19). Physically rounded pyrite grains in these marine sediments (Fig. S7) indicate the lack of O<sub>2</sub> during their weathering, transport, and sedimentation. The detrital origin of these pyrite grains is identified by their rounded, irregular shape, proximity to other dense mineral grains such as zircons and monazites, and in some cases observations of grain-boundary truncations (Fig S7). We confirmed that these grains had a provenance distinct from authigenic pyrite (53) by measuring multiple sulfur isotope ratios from two thin sections using SIMS, finding distinct mass-anomalous fractionations (mean  $\Delta^{33}\text{S}$ : -1.12‰; Table S1) that differ from authigenic

pyrite with mainly zero or positive  $\Delta^{33}\text{S}$  (discussed below). Redox-sensitive detrital pyrite is thought to be sensitive to environmental  $\text{O}_2$  concentrations of approximately  $10^{-5.7}$  atm (54).

Multiple sulfur isotope ratios ( $\delta^{34}\text{S}$  and  $\Delta^{33}\text{S}$ ) provide another independent proxy sensitive to very low levels of atmospheric  $\text{O}_2$  ( $< 10^{-5.7}$  atm (34)), and currently constitute the most established geochemical standard for marking the rise of oxygen (1, 2, 55). In addition to detrital pyrite in the sandstones, Koegas strata contain shale horizons with authigenic sulfide-bearing minerals. However, it is also clear from petrography that these phases record multiple episodes of sulfide mineralization, including euhedral ingrowths and overgrowths, fracture-filling cements, and replacements (Fig. S8, Fig. S9)—requiring careful analysis and interpretation of isotope ratio data. To untangle this history we complimented our bulk  $\text{SF}_6$  gas source mass spectrometry analyses with secondary ion mass spectrometry (SIMS), which enabled us to connect multiple sulfur isotope measurements to texture and insight gained from petrography and cross-cutting relationships. The  $\text{SF}_6$  and SIMS data overlap and record the same systematics (Fig. 4; Fig. S11, Fig. S12). Altogether the multiple sulfur isotope data reveal two discordant isotopic trends. Pyrites with late textures show a  $\Delta^{33}\text{S}$  near zero and highly variable and positive  $\delta^{34}\text{S}$  values, whereas pyrites that lack these late textures show  $\Delta^{33}\text{S}$  values with clear mass anomalous fractionations and muted  $\delta^{34}\text{S}$  values—two features characteristic of strata deposited prior to the rise of oxygen (55). These multiple S isotope data imply environmental  $\text{O}_2$  concentrations at this time were far less than  $10^{-5.7}$  atm (34).

## DISCUSSION

The extensive accumulation of manganese-rich deposits ca. 2.415 Ga indicates prevalent Mn oxidation, but independent redox-sensitive proxies (detrital pyrite and anomalous multiple S isotope fractionations) suggest that environmental O<sub>2</sub> concentrations remained very low. The sedimentary Mn concentrations we observe are too high for abiological mechanisms (*SI Text*) and therefore require a biological oxidation mechanism. This is consistent with the idea of transitional Mn-oxidizing phototrophy prior to the rise of cyanobacteria and oxygenic photosynthesis. However, to examine the possibility that O<sub>2</sub> production by cyanobacteria was responsible for our Mn deposits, we considered scenarios wherein the Mn oxides might have been created by reacting with O<sub>2</sub>.

Some have postulated the existence of ‘oxygen oases’ adjacent to cyanobacterial mats prior to the rise of oxygen, in which oxygen production could exceed the vanishingly low global O<sub>2</sub> average (56). The observations of Mn, redox-sensitive detrital grains, and anomalous multiple sulfur isotope fractionations within Koegas Subgroup facies model do not support the existence of such oases in this sedimentary basin. The Mn-enrichments are not uniquely tied to microbial mat lithofacies or a restricted paleoenvironment, but rather are found across the basin, both up and down depositional dip, implying a continuity of process over > 50km of the ocean basin that separates our two cores (Fig. S1). This includes deep-water iron formation facies that accumulated chemical sediment from suspension. Moreover, Mn deposits occur in formations spanning the entire Koegas

Subgroup, over ~230m of stratigraphy in GEC01 and ~210m in GTF01. This repeated sequence stratigraphic occurrence indicates Mn deposition across a broad range of space and time and is not consistent with a transient, restricted mat environment producing O<sub>2</sub>. Rather, independent of Mn, all of our observations instead point to its paucity. Shallow water environments with cross-stratified sandstones have repeated occurrences of redox-sensitive detrital grains in every bed examined throughout the stratigraphy. Shales throughout the stratigraphy have pyrite nodules bearing anomalous sulfur isotope fractionations. These proxies are sensitive to O<sub>2</sub> both locally and globally, and strongly suggest that oxygen oases were not responsible for creating the Mn enrichments in the Koegas Subgroup.

It is also important to consider whether the very low levels of O<sub>2</sub> permissible from the different redox proxies might have been sufficient to oxidize Mn, concentrating oxides in Koegas sediments. It was hypothesized that O<sub>2</sub> cycled as a trace gas prior to the rise of oxygen (57), and from a thermodynamic perspective, Mn is sensitive to low levels of oxygen ( $\sim 10^{-10}$  atm). However it is widely recognized that the abiotic kinetics of Mn<sup>2+</sup> oxidation by O<sub>2</sub> are extremely slow (58). Biological oxidation using O<sub>2</sub> is notably faster (35, 58), but occurs at rates too slow to explain the enrichments observed here. Calculations of Mn oxidation rates at O<sub>2</sub> concentrations of 2.6 nM—the maximum value allowed by multiple sulfur isotope constraints—yield 0.073 g of oxidized Mn per liter per kyr, or between 0.02% to 0.2% of the total sediment mass depending on sedimentation rate estimations. These calculations use the maximal biological rates, highest possible



dissolved O<sub>2</sub> concentrations, assume conservatively that all Mn-oxides reduced were converted to carbonate phases with no return loss to seawater, and still are insufficient to produce these Mn deposits (*SI Text*). For these reasons we do not favor O<sub>2</sub> as the oxidant responsible for creating the sedimentary Mn-enrichments we observe. Oxidation rates catalyzed by a photosystem are much faster (59), and consequently we postulate that these Mn deposits were derived from a manganese-based photosynthetic process. Similar to photoferrotrophy proposed for the accumulation of iron in Archean iron formations (60), we interpret the original manganese oxides as products of anoxygenic photobiology, with Mn(II) donating electrons directly to an ancestral reaction center.

The integrated results presented here indicate that the oxidative branch of the manganese cycle was operating prior to 2.415 Ga, but reveal that Mn was not oxidized by O<sub>2</sub>. These observations suggest that a transitional photosystem lent the biochemical capability of using Mn as an electron donor, and support a distinct class of hypotheses for the origin of the WOC of PSII that describe single electron photooxidation reactions involving manganese as an evolutionary intermediate in the development of one of biology's greatest achievements—light-driven water oxidation.

## **METHODS**

Bulk element geochemistry was measured using X-ray fluorescence and inductively coupled plasma mass spectrometer (ICP-MS). XAS analyses were generated from monolayer powders or ultra thin sections at SSRL. Thin section samples were examined

by SEM using EDS for elemental mapping. Values of  $\delta^{13}\text{C}$  and  $\delta^{18}\text{O}$  for carbonates were measured on a MAT 253 isotope ratio mass spectrometer. Pyrite  $\delta^{34}\text{S}$  and  $\Delta^{33}\text{S}$  were measured in bulk at the MIT Stable Isotope Laboratory and *in situ* on a Cameca 7f-GEO. See *SI Text* for additional details on materials and methods.

## FOOTNOTES

Abbreviations:

$$\delta^{34}\text{S} = ([^{34}\text{S}/^{32}\text{S}_{\text{samp}}]/[^{34}\text{S}/^{32}\text{S}_{\text{std}}]) - 1)1000$$

$$\delta^{33}\text{S} = ([^{33}\text{S}/^{32}\text{S}_{\text{samp}}]/[^{33}\text{S}/^{32}\text{S}_{\text{std}}]) - 1)1000$$

$$\Delta^{33}\text{S} = 1000(\ln(1+(\delta^{33}\text{S}/1000)) - 0.515(\ln(1+(\delta^{34}\text{S}/1000)))$$

## ACKNOWLEDGEMENTS

We thank James Hemp for useful discussions and valuable manuscript feedback, Yunbin Guan for assistance with the ion microprobe data collection and reduction, Kristin Bergmann for discussions and assistance with sample preparation and analyses, Nic Beukes for helpful comments and assistance in the field, Chi Ma for assistance with SEM and e-probe analyses, Benjamin Kocar and John Bargar for additional help at the synchrotron, and George Rossman, John Eiler, Tim Raub, and John Abelson for helpful discussions and laboratory assistance. We also thank the valuable insights of four anonymous reviewers. Support for this work was provided by the Agouron Institute, NASA Exobiology (W.W.F.), the David and Lucile Packard Foundation (W.W.F.), and the NSF Graduate Research Fellowship program (J.E.J.). Data are available in

supplementary tables. Portions of this research were carried out at the Stanford Synchrotron Radiation Lightsource, a Directorate of SLAC National Accelerator Laboratory and an Office of Science User Facility operated for the U.S. Department of Energy Office of Science by Stanford University. The SSRL Structural Molecular Biology Program is supported by the DOE Office of Biological and Environmental Research, and by the National Institutes of Health, National Institute of General Medical Sciences (including P41GM103393), and the National Center for Research Resources (P41RR001209). The contents of this publication are solely the responsibility of the authors and do not necessarily represent the official views of NIGMS, NCRR, or NIH.

## FIGURES

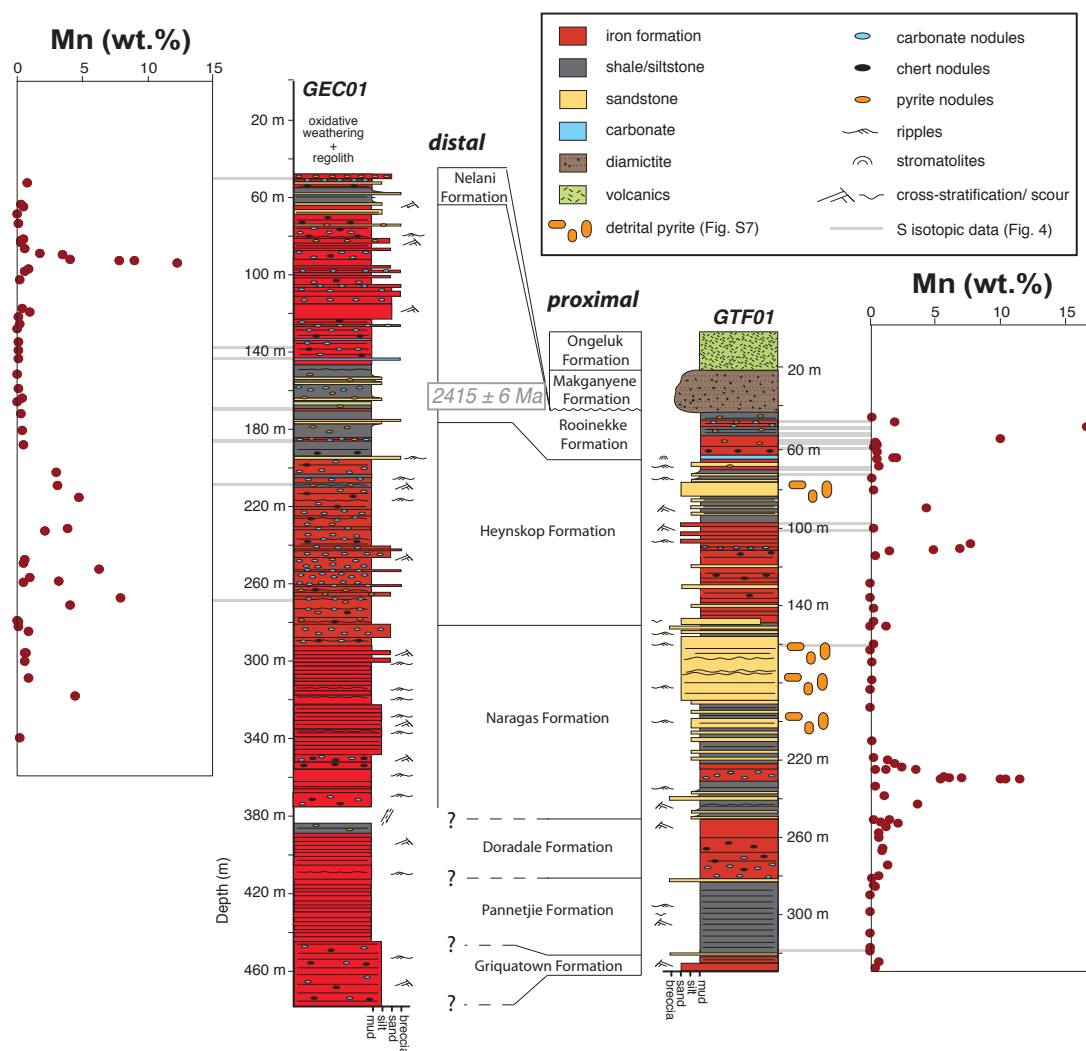


**Figure 1.** Stratigraphic columns of drill cores GEC01 and GTF01 showing horizons of Mn-enrichments in Agouron drill cores GEC01 and GTF01. Mn abundances were determined by X-ray fluorescence and inductively coupled plasma mass spectrometry. Note the locations of clastic subunits rich in detrital pyrite grains in GTF01 (Fig. S7) and measurements of multiple sulfur isotopes (Fig. 4, Fig. S11, Fig. S12).

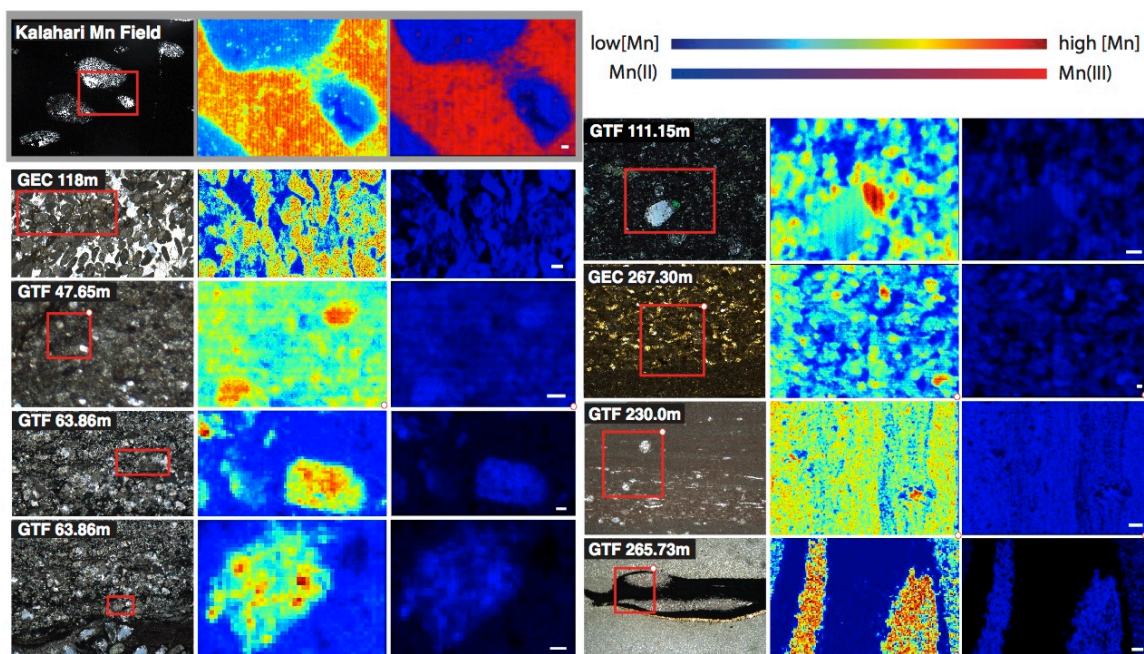


**Figure 2.** Transmitted light photomicrographs (left panel), Mn concentration maps (middle panel), and Mn redox maps (right panel). Red box inset with small white corner circle highlights the location and orientation of the concentration and redox maps. The X-ray microprobe technique is illustrated on a sample of the ~2.2 Ga Kalahari Mn Field (grey shading), containing braunite and kutnohorite (Fig. S3, Fig. S4). The remaining samples capture the Mn-rich samples from carbonate-rich granular and banded iron formation of the Rooinekke, Heynskoop, and Naragas Formations, and reveal exclusively Mn(II)-bearing phases. Scale bars are 20 $\mu$ m except GEC 118m and GTF 230m where they are 100 $\mu$ m. Manganese concentration is in  $\mu$ g/cm<sup>2</sup> and on individual scales to highlight within sample heterogeneity: Kalahari (0 to 1500); GEC 118 (0 to 50); GTF 47.65 (0 to 400); GTF 63.86 (0 to 200); GTF 111.15 (0 to 1000); GEC 267.30 (0 to 1000); GTF 230 (0 to 500); GTF 265.73 (0 to 50).

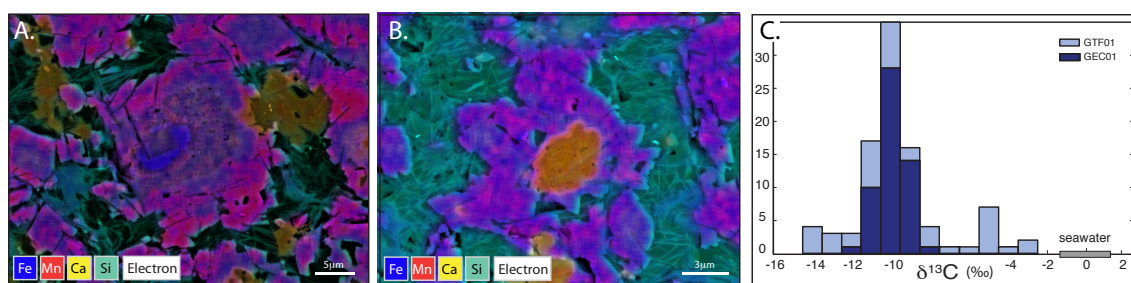


**Figure 3.** (A) and (B) Backscatter electron images with overlying electron dispersive spectroscopy elemental maps show the variable compositions and diagenetic textures of the Mn-bearing carbonates with Mn shown in red, Fe shown in blue, Ca shown in yellow, and Si shown in teal. (C) Histogram of  $\delta^{13}\text{C}$  values (in permill VPDB) from Mn-rich carbonates in GTF01 and GEC01 cores. Grey bar denotes estimated (61, 62) seawater dissolved inorganic carbon  $\delta^{13}\text{C}$ .

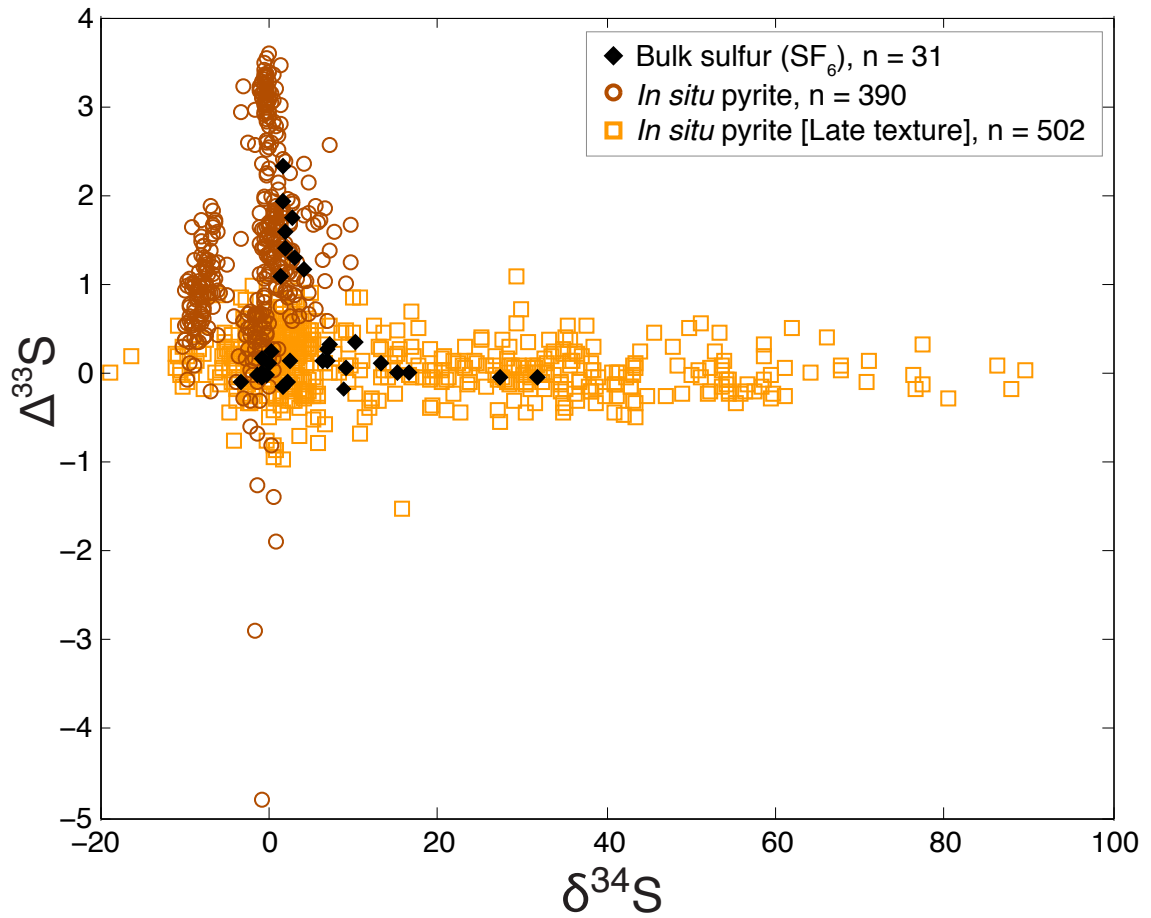


**Figure 4.** Multiple sulfur isotope ratio data from GTF01 and GEC01 samples (in permil VCDT). SIMS isotope data is further categorized based on petrographic texture (e.g., Fig. S8, Fig. S10). Late pyrites (orange squares) form an array with enriched  $\delta^{34}\text{S}$  values and  $\Delta^{33}\text{S}$  near zero and record significant closed system fractionations and perhaps thermochemical sulfate reduction from late fluids during burial metamorphism and late diagenesis. The  $2\sigma$  uncertainties for the  $\text{SF}_6$  data are 0.26‰ or better and better than 0.4‰ for SIMS data. The large deviations of  $\Delta^{33}\text{S}$  from zero for the *in situ* pyrite (brown circles) is characteristic of Archean and early Paleoproterozoic-age rocks and is indicative of an anoxic atmosphere.

## REFERENCES CITED

1. Bekker A et al. (2004) Dating the rise of atmospheric oxygen. *Nature* 427:117–120.
2. Guo Q et al. (2009) Reconstructing Earth's Surface Oxidation Across the Archean-Proterozoic Transition. *Geology* 37:399–402.
3. Xiong J, Fischer WM, Inoue K, Nakahara M, Bauer CE (2000) Molecular Evidence for the Early Evolution of Photosynthesis. *Science* 289:1724–1730.
4. Williamson A, Conlan B, Hillier W, Wydrzynski T (2011) The evolution of Photosystem II: insights into the past and future. *Photosyn Res* 107:71–86.
5. Ferreira KN, Iverson TM, Maghlaoui K, Barber J, Iwata S (2004) Architecture of the photosynthetic oxygen-evolving center. *Science* 303:1831–1838.
6. Umena Y, Kawakami K, Shen J-R, Kamiya N (2011) Crystal structure of oxygen-evolving photosystem II at a resolution of 1.9Å. *Nature* 473:55–60.
7. McEvoy JP, Brudvig GW (2006) Water-Splitting Chemistry of Photosystem II. *Chem Rev* 106:4455–4483.
8. Olson JM (1970) The Evolution of Photosynthesis. *Science* 168:438–446.
9. Navarro-González R, McKay CP, Mvondo DN (2001) A possible nitrogen crisis for Archaean life due to reduced nitrogen fixation by lightning. *Nature* 412:61–64.
10. Blankenship RE, Hartman H (1998) The origin and evolution of oxygenic photosynthesis. *Trends in Biochemical Sciences* 23:94–97.
11. Sauer K, Yachandra VK (2002) A possible evolutionary origin for the Mn<sub>4</sub> cluster of the photosynthetic water oxidation complex from natural MnO<sub>2</sub> precipitates in the early ocean. *Proc Natl Acad Sci U S A* 99:8631–8636.
12. Russell M, Allen J, James M-W (2008) in *Photosynthesis. Energy from the Sun*, eds Allen J, Gantt E, Golbeck J, Osmond B (Springer Netherlands), pp 1187–1192. Available at: [http://dx.doi.org/10.1007/978-1-4020-6709-9\\_259](http://dx.doi.org/10.1007/978-1-4020-6709-9_259).
13. Roy S (1997) in *Manganese Mineralization: Geochemistry and Mineralogy of Terrestrial and Marine Deposits*, Geological Society Special Publication., eds Nicholson K, Hein JR, Buhn B, Dasgupta S, pp 5–27.
14. Roy S (2006) Sedimentary manganese metallogenesis in response to the evolution of the Earth system. *Earth-Science Reviews* 77:273–305.



15. Tamura N, Chéniaie G (1987) Photoactivation of the water-oxidizing complex in Photosystem II membranes depleted of Mn and extrinsic proteins. I. Biochemical and kinetic characterization. *Biochimica et Biophysica Acta (BBA) - Bioenergetics* 890:179–194.
16. Zubay G (1996) *Origins of Life on the Earth and in the Cosmos* (Academic Press, San Diego). 2nd Ed.
17. Dismukes GC et al. (2001) The origin of atmospheric oxygen on Earth: The innovation of oxygenic photosynthesis. *PNAS* 98:2170–2175.
18. Allen JF, Martin W (2007) Evolutionary biology: Out of thin air. *Nature* 445:610–612.
19. Holland HD (1984) *The Chemical Evolution of the Atmosphere and Oceans* (Princeton University Press).
20. Fischer WW, Knoll AH (2009) An Iron Shuttle for Deepwater Silica in Late Archean and Early Paleoproterozoic Iron Formation. *Geological Society of America Bulletin* 121:222–235.
21. Brocks JJ, Logan GA, Buick R, Summons RE (1999) Archean Molecular Fossils and the Early Rise of Eukaryotes. *Science* 285:1033–1036.
22. Rasmussen B, Fletcher IR, Brocks JJ, Kilburn MR (2008) Reassessing the first appearance of eukaryotes and cyanobacteria. *Nature* 455:1101–1104.
23. Welander PV, Coleman ML, Sessions AL, Summons RE, Newman DK (2010) Identification of a methylase required for 2-methylhopanoid production and implications for the interpretation of sedimentary hopanes. *PNAS* 107:8537–8542.
24. Rashby SE, Sessions AL, Summons RE, Newman DK (2007) Biosynthesis of 2-methylbacteriohopanepolyols by an anoxygenic phototroph. *PNAS* 104:15099–15104.
25. Farquhar J, Zerkle AL, Bekker A (2011) Geological constraints on the origin of oxygenic photosynthesis. *Photosyn Res* 107:11–36.
26. Haqq-Misra J, Kasting JF, Lee S (2011) Availability of O<sub>2</sub> and H<sub>2</sub>O<sub>2</sub> on Pre-Photosynthetic Earth. *Astrobiology* 11:293–302.
27. Liang M-C, Hartman H, Kopp RE, Kirschvink JL, Yung YL (2006) Production of hydrogen peroxide in the atmosphere of a Snowball Earth and the origin of oxygenic photosynthesis. *Proc Natl Acad Sci USA* 103:18896–18899.

28. Ettwig KF et al. (2010) Nitrite-driven anaerobic methane oxidation by oxygenic bacteria. *Nature* 464:543–548.
29. Morford JL, Martin WR, Carney CM (2012) Rhenium geochemical cycling: Insights from continental margins. *Chemical Geology* 324–325:73–86.
30. Helz GR, Bura-Nakić E, Mikac N, Ciglencčki I (2011) New model for molybdenum behavior in euxinic waters. *Chemical Geology* 284:323–332.
31. Nägler TF, Neubert N, Böttcher ME, Dellwig O, Schnetger B (2011) Molybdenum isotope fractionation in pelagic euxinia: Evidence from the modern Black and Baltic Seas. *Chemical Geology* 289:1–11.
32. Scheiderich K, Zerkle AL, Helz GR, Farquhar J, Walker RJ (2010) Molybdenum isotope, multiple sulfur isotope, and redox-sensitive element behavior in early Pleistocene Mediterranean sapropels. *Chemical Geology* 279:134–144.
33. Pufahl PK, Hiatt EE (2012) Oxygenation of the Earth's atmosphere–ocean system: A review of physical and chemical sedimentologic responses. *Marine and Petroleum Geology* 32:1–20.
34. Pavlov AA, Kasting JF (2002) Mass-Independent Fractionation of Sulfur Isotopes in Archean Sediments: Strong Evidence for an Anoxic Archean Atmosphere. *Astrobiology* 2:27–41.
35. Clement BG, Luther III GW, Tebo BM (2009) Rapid, oxygen-dependent microbial Mn(II) oxidation kinetics at sub-micromolar oxygen concentrations in the Black Sea suboxic zone. *Geochimica et Cosmochimica Acta* 73:1878–1889.
36. Kopp RE, Kirschvink JL, Hilburn IA, Nash CZ (2005) The Paleoproterozoic snowball Earth: A climate disaster triggered by the evolution of oxygenic photosynthesis. *Proceedings of the National Academy of Sciences* 102:11131–11136.
37. Beukes N, Klein C (1992) in *The Proterozoic Biosphere: A Multidisciplinary Study*, eds Schopf JW, Klein C (Cambridge University Press).
38. Komiya T et al. (2008) Evolution of the composition of seawater through geologic time, and its influence on the evolution of life. *Gondwana Research* 14:159–174.
39. Varentsov IM (1996) *Manganese Ores of Supergene Zone: Geochemistry of Formation* (Kluwer Academic Publishers, Dordrecht, The Netherlands).
40. Klein C (2005) Some Precambrian Banded Iron-Formations (BIFs) from Around the World: Their Age, Geologic Setting, Mineralogy, Metamorphism, Geochemistry, and Origins. *American Mineralogist* 90:1473–1499.

41. Kirschvink JL et al. (2000) Paleoproterozoic snowball Earth: Extreme climatic and geochemical global change and its biological consequences. *PNAS* 97:1400–1405.
42. Schissel D, Aro P (1992) The Major Early Proterozoic Sedimentary Iron and Manganese Deposits and Their Tectonic Setting. *Economic Geology* 87:1367–1374.
43. Schröder S, Bedorf D, Beukes NJ, Gutzmer J (2011) From BIF to red beds: Sedimentology and sequence stratigraphy of the Paleoproterozoic Koegas Subgroup (South Africa). *Sedimentary Geology* 236:25–44.
44. Miyano T, Beukes NJ (1984) Phase relations of stilpnomelane, ferri-annite, and riebeckite in very low-grade metamorphosed iron-formations. *South African Journal of Geology* 87:111–124.
45. Beukes NJ, Gutzmer J (2008) in *Banded Iron Formation-Related High-Grade Ore*, eds Hagemann S, Rosiere C, Gutzmer J, Beukes N, pp 5–47.
46. Webb SM (2011) The MicroAnalysis Toolkit: X-ray Fluorescence Image Processing Software. *AIP Conference Proceedings* 1365:196–199.
47. Mayhew LE, Webb SM, Templeton AS (2011) Microscale imaging and identification of Fe speciation and distribution during fluid-mineral reactions under highly reducing conditions. *Environ Sci Technol* 45:4468–4474.
48. Tsikos H, Beukes NJ, Moore JM, Harris C (2003) Deposition, Diagenesis, and Secondary Enrichment of Metals in the Paleoproterozoic Hotazel Iron Formation, Kalahari Manganese Field, South Africa. *Economic Geology* 98:1449–1462.
49. Okita PM, Maynard JB, Spiker EC, Force ER (1988) Isotopic evidence for organic matter oxidation by manganese reduction in the formation of stratiform manganese carbonate ore. *Geochimica et Cosmochimica Acta* 52:2679–2685.
50. Matsumoto R (1992) in *Proceedings of the Ocean Drilling Program, Scientific Results*, eds Pisciotto KA, Ingle JC Jr, von Breymann MT, Barron J (Ocean Drilling Program, College Station, TX), pp 75–98. Available at: doi:10.2973/odp.proc.sr.127128-1.119.1992.
51. Froelich PN et al. (1979) Early oxidation of organic matter in pelagic sediments of the eastern equatorial Atlantic: suboxic diagenesis. *Geochimica et Cosmochimica Acta* 43:1075–1090.
52. Rasmussen B, Buick R (1999) Redox State of the Archean Atmosphere: Evidence from Detrital Heavy Minerals in Ca. 3250–2750 Ma Sandstones from the Pilbara Craton, Australia. *Geology* 27:115–118.

53. Hofmann A, Bekker A, Rouxel O, Rumble D, Master S (2009) Multiple sulphur and iron isotope composition of detrital pyrite in Archaean sedimentary rocks: A new tool for provenance analysis. *Earth and Planetary Science Letters* 286:436–445.
54. Anbar AD et al. (2007) A Whiff of Oxygen Before the Great Oxidation Event? *Science* 317:1903–1906.
55. Farquhar J, Bao H, Thiemens M (2000) Atmospheric Influence of Earth's Earliest Sulfur Cycle. *Science* 289:756–758.
56. Kasting JF, Holland HD, Kump LR (1992) in *The Proterozoic Biosphere: A Multidisciplinary Study*, eds Schopf WJ, Klein C (Cambridge University Press, Cambridge, UK), pp 1185–1188.
57. Waldbauer JR, Newman DK, Summons RE (2011) Microaerobic steroid biosynthesis and the molecular fossil record of Archean life. *PNAS* 108:13409–13414.
58. Morgan JJ (2005) Kinetics of reaction between O<sub>2</sub> and Mn(II) species in aqueous solutions. *Geochimica et Cosmochimica Acta* 69:35–48.
59. Büchel C et al. (1999) Photoassembly of the Manganese Cluster and Oxygen Evolution from Monomeric and Dimeric CP47 Reaction Center Photosystem II Complexes. *PNAS* 96:14288–14293.
60. Konhauser KO et al. (2002) Could bacteria have formed the Precambrian banded iron formations? *Geology* 30:1079–1082.
61. Bekker A et al. (2001) Chemostratigraphy of the Paleoproterozoic Duitschland Formation, South Africa: Implications for Coupled Climate Change and Carbon Cycling. *Am J Sci* 301:261–285.
62. Fischer WW et al. (2009) Isotopic constraints on the Late Archean carbon cycle from the Transvaal Supergroup along the western margin of the Kaapvaal Craton, South Africa. *Precambrian Research* 169:15–27.

## SUPPORTING INFORMATION

**Sample collection.** GEC01 and GTF01 cores were drilled in the Northern Cape Province of South Africa as part of a second phase of the South African Agouron Drilling Project. These two cores capture the Koegas Subgroup of the Ghaap Group and a portion of the overlying Postmasburg Group (Fig. S1). The Koegas Subgroup overlies the Asbestos Hills Subgroup, composed of the Kuruman and Griquatown formations. The upper Kuruman formation has ash beds dated by U-Pb SHRIMP on zircons to  $2460 \pm 5$  Ma (1) and the Griquatown Formation has zircons dated by U-Pb SHRIMP to  $2431 \pm 31$  Ma from published conference proceedings (2, 3). Overlying the Koegas Subgroup is the Makganyene Formation (a glaciogenic unit deposited on top of a substantial regional unconformity, (4–6)) and the Ongeluk Formation, which has been dated by whole-rock Pb-Pb isochron to  $2238 \pm 90$  Ma (7, 8) and refined in a later study by whole-rock Pb-Pb to  $2222 \pm 12$  Ma (9). Zircons from an ash bed in the Rooinekke Formation of the Koegas Subgroup were dated by SHRIMP U-Pb to  $2415 \pm 6$  Ma in a technical report (5, 10), which currently constitutes the best age constraint for the Koegas Subgroup (5, 6, 11–13). Cores were slabbed and logged and half were sent to the California Institute of Technology with the other half archived at the Council for Geoscience in South Africa. Details of the sedimentary geology and bulk geochemistry can be found in Schröder et al (5). Subsamples for petrographic and geochemical analysis were collected from the cores using non-magnetic blades and bit on a trim saw and drill press, respectively.

**Sample preparation and bulk element geochemistry.** A preliminary dataset for the major, minor, and trace element geochemistry was acquired at the SPECTRAU analytical facility at the University of Johannesburg (5). Wavelength-dispersive X-ray fluorescence analyses (XRF) were used on the lithium borate ( $\text{Li}_2\text{B}_4\text{O}_7\text{-LiBO}_2$ ) fused glass beads on a Philips Magix Pro Spectrometer. Elemental composition was determined with precision better than 0.5% and accuracy better than  $\pm 5\%$  for most elements except iron, which was better than  $\pm 10\%$ . A second set of core subsamples was analyzed for bulk chemistry in the Activation Laboratories, Ancaster, Ontario. Chips of core (0.5 g each) were pulverized and digested in aqua regia in a microprocessor controlled digestion block at  $90^\circ\text{C}$  for 2 hours. After diluting the resultant solution, 28 elements were analyzed by ICP/MS using a Perkin Elmer SCIEX ELAN 6000, 6100, or 9000 ICP/MS. Digestion duplicates were analyzed every 15 samples. An in-house control was run every 33 samples and blank and digested standards were run every 68 samples and instrument was recalibrated. Each batch of samples is bracketed by international reference materials, and a duplicate and internal control standards are analyzed every 10 samples. Some silicates, oxides, and resistant materials such as zircon and monazite were not totally dissolved. For more precision on highly Mn-concentrated samples, a lithium metaborate/tetraborate fusion-ICP method was used. These samples were run with replicates, a method reagent blank, and certified reference material. Samples were fused in an induction furnace after mixing with lithium metaborate and lithium tetraborate. The molten melt was added to a 5% nitric acid solution with an internal standard, and mixed  $\sim 30$  minutes until completely dissolved. The samples were then run for manganese concentration on a combination

simultaneous Thermo Jarrell-Ash ENVIRO II ICP or a sequential Varian Vista 735 ICP. The instrument is calibrated using seven certified reference materials. Data are available in Table S1.

Small samples for bulk XAS were chosen from Mn-rich intervals of both cores as well as several samples from strata with conspicuous but lower Mn concentrations (see Table S1). A micro-rotary drill with a 1mm bit was employed to produce coarse powders of all visible textures, producing ~100-200mg of powder. These samples were loaded into small glass vials and then transferred to an anaerobic chamber. In this chamber, a ceramic mortar and pestle was used to further grind this powder into a very fine, homogenous mixture. The powder was then spread evenly onto monolayers of *Scotch* tape to produce approximately 6 to 14 layers, depending on Mn concentration. These monolayer tape samples were then stored in heat-sealed mylar bags, except for one duplicate which was prepared and stored in air. The use of anaerobic glove box and vacuum bags were used to prevent any oxidation of reduced Mn in the samples. However, these extra steps were unnecessary, as the XAS spectra of the same sample prepared both anaerobically and aerobically are identical (Fig. S2). This result is consistent with theory and measurements of abiotic Mn oxidation by O<sub>2</sub>—a process that is strongly kinetically limited and proceeds very slowly in solution (14) and essentially does not occur in dry air.

Carbonate nodules and ankerite-dominated intervals were targeted for carbonate sampling using a micro-rotary drill with a 1mm bit. These microsampled powders were stored in glass vials.

Slabs and rounds were prepared from desired strata for analyses on the Scanning Electron Microscope (SEM), the Electron Microprobe (E-probe), on beam line (BL) 10-2 and 2-3 at Stanford Synchrotron Radiation Lightsource, and on the Secondary Ion Mass Spectrometry instrument (SIMS). Slabs were cut using a rock saw and rounds were made using a 1-inch drill press, targeting desired sections. Billets and rounds of approximately 5mm were made into thin sections by High Mesa Petrographics or Spectrum Petrographics, and carefully polished to obtain a microprobe quality surface. For use on the SEM and E-probe, returned thin sections were subsequently carbon coated with 7-15 nm of graphite using a Cressington Carbon Coater. Before analysis using the SIMS, thin sections were sputter coated with gold (30 nm) using a Cressington Sputter Coater. Ultrathin sections (~10µm) were made for XAS to minimize the amount of sample volume felt by the X-ray beam. The Mn concentration of the thin section glass is below the detection limit of our analyses.

Samples adjacent to sections prepared for *in situ* (SIMS) analyses were targeted for bulk sulfur measurements. These were removed from the core and cubed using a rock saw. They were then powdered using an SPEX 8510 Shatterbox to yield approximately 2 to 5g of sample. Extremely  $^{34}\text{S}$ -enriched pyrite cements (as shown by *in situ* measurements,



Fig. 4, Fig. S10, Table S3) from fracture filling cements were also sampled using a micro-rotary drill for comparison to *in situ* measurements (yielding 1.2 to 2.1 mg, Table S3 labeled with '^'). Additionally, an in-house pyrite standard used for *in situ* measurements was sub-sampled for analyses to assay standard homogeneity.

**Bulk powder X-ray absorption spectroscopy.** Beam line 4-1 at SSRL was used to analyze 16 samples for bulk manganese oxidation state and coordination environment. A Silicon 220  $\Phi = 90$  crystal was used and X-ray absorption spectra (XAS) was collected on a Lytle detector for fluorescence and on an absorption detector for transmission spectra. A collimating mirror was used to help reduce harmonics in the beam, and a potassium permanganate ( $\text{KMn(VII)O}_4$ ) standard was used for calibration. Duplicates were run on all spectra collected for X-ray Absorption Near Edge Spectroscopy (XANES) scanning from 6310 eV to 7108 eV. Representative samples were targeted for X-ray Absorption Fine Structure (XAFS) with ~4 repeats for higher Mn concentrations and ~10 repeats for lower Mn-bearing samples scanning from 6310 eV to 7223 eV.

**XAS Mapping.** Beam line 10-2 at SSRL was used to analyze 12 samples for coarse resolution mapping. Polished thin sections (rounds or rectangular) were analyzed at three energies determined to distinguish redox states: 6551 eV, 6562 eV, and 6572 eV. Maps were generated by collecting the X-ray fluorescence using a Vortex FII International Silicon drift detector on  $\sim 80\mu\text{m} \times 80\mu\text{m}$  pixels (focused by capillary optics), which were rastered over the sections. Regions of interest were subsequently mapped in higher

resolution on BL 2-3 at SSRL at  $\sim 10\mu\text{m}$  resolution (with a  $2\mu\text{m}$  beam using Kirkpatrick Baez mirrors for focusing) on a Vortex FII International Silicon drift detector using 4 redox-distinctive energies determined from braunite and kutnohorite from the Kalahari Manganese Field (Fig. S3, Fig. S4), using the maximal normalized fluorescence differences between these endmembers as targets for redox-distinguishing energies (Fig. S4). The braunite spectra were chosen as a representative end member, as they capture the most oxidized (though still mixed valence) phase found in Mn-rich sedimentary rocks of similar diagenetic and metamorphic grade like nearby Kalahari Manganese Field. We chose kutnohorite as the reduced endmember for our multiple energy maps, as our bulk XAS spectra best matched the Kalahari kutnohorite (Fig. S3). The redox-distinguishing energies chosen for high-resolution maps were 6542 eV, 6551 eV, 6560-62 eV, 6572-73 eV, and sometimes 6546 eV, 6548 eV, 6558 eV, and 6568 eV (Fig. S3). To rule out the presence of even small domains of Mn oxide-bearing phases a multiple energy map at  $\sim 2\mu\text{m}$  resolution was also generated for most of the samples (Fig. 2).

Multiple energy maps were analyzed using the MicroAnalysis Toolkit software (15). Maps of each energy were imported into one master file, thereby having a set of distinctive absorptions at several energies for every map pixel (i.e., a “mini-XANES spectrum” (15)). These pixels were then analyzed using a non-negative linear-least squares fit of the data to the two end member spectra, an Mn(II)-bearing carbonate and an oxidized Mn(III)-bearing braunite from the Kalahari Mn field using the MicroAnalysis Toolkit fitting function. Normalized intensity of the absorption spectra of the two end

members was determined for the energies measured, and then each pixel was fit to the composition of each standard. Subsequent confirmation of the fit is found by measuring XANES spectra at pixels identified as distinct by a principal component analysis of the multiple energies (15, 16). Fitted pixels were all set to the same scale, 0 to 1500 counts for kutnohorite (Mn-bearing carbonate) and 0 to 4000 counts for braunite. Fitted results agree within 5 percent (15) and all full XANES spectra collected at specific 2x2 $\mu$ m points support the fitted-pixel redox maps.

To quantify Mn concentration, the highest energy map was used (6572 eV or 6573 eV). The manganese abundance was collected in counts, which were converted to units of  $\mu\text{g}/\text{cm}^2$  using a map made at the same energy and under the same conditions (incident monochromator energy and detector distance) of an Mn foil, made from Mn deposited on a mylar film at a concentration of 47.1  $\mu\text{g}/\text{cm}^2$ . After removing edge effects of the standard map, a QuantFile of the standard was created to calibrate against the data files. Scales were then adjusted to the closest multiple of 50 for comparative purposes (scales range from 50 to 1500 in order to best show small-scale variations of Mn).

**SEM/E-probe.** A Zeiss 1550VP Field Emission Scanning Electron Microscope equipped with an Oxford INCA Energy 300 X-ray Energy Dispersive Spectrometer (EDS) system housed in the Geological and Planetary Sciences (GPS) Division Analytical Facility was used for all analyses. High-resolution images were taken in backscatter electron imaging mode to enhance compositional contrast. EDS measurements of x-ray fluorescence were

made mainly on points (see Fig. S3) but also as x-ray fluorescence maps (Fig. 3). Quantitative elemental analysis provides relative accuracy of better than 5%. These capabilities were used to identify detrital minerals such as pyrite and zircon, in order to examine pyrite nodules and fracture fills examined on the SIMS, and to investigate the textural complexity of samples from GTF01, GEC01, and from the Kalahari Mn field.

Other measurements were made on a JEOL JXA-8200 Advanced Electron Probe Micro-analyzer (E-probe) equipped with five wavelength dispersive X-ray spectrometers (WDS), tungsten and LaB<sub>6</sub> electron sources, and a detection limit of several hundred ppm. It has an accuracy as good as 1-2% and the precision on pyrite is 0.2% (S) and 0.4% (Fe). The detection limit for manganese was 300ppm, and all samples identified as pyrite phase (FeS<sub>2</sub>) were below the Mn detection limit. A late-stage fracture with discontinuous pyrite mineralization (characterized by heavy  $\delta^{34}\text{S}$  values) was examined on the E-probe and the concentration of manganese was measured from spots throughout the mineralized fracture. The Mn concentration was below detection limit for 40 measurements and below 0.1% of the total concentration for the remaining measurements, discounting 3 outliers (Fig. S5). These outliers were measurements made on non-pyrite but instead captured (partially or totally) some of the Mn-bearing matrix. Even including the outliers, the total Mn percentage is less than 0.5% in all points measured, highlighting the lack of Mn delivery from metasomatic fluids.

**Carbonate C and O isotopic analysis.** Carbonate samples were measured for their carbon isotopic distribution at the University of Michigan Stable Isotope Laboratory. Samples are heated to 200°C for one hour, removing any volatile contaminants and water. Samples are then reacted at  $77 \pm 1^\circ\text{C}$  with anhydrous phosphoric acid for 22 minutes in individual borosilicate reaction vessels in a Finnigan MAT Kiel IV preparation device. This is directly coupled to the inlet of a Finnigan MAT 253 triple collector isotope ratio mass spectrometer, which measures isotopic measurements calibrated against NBS 18 and NBS 19. Data are reported in delta notation (‰) relative to VPDB and measured precision is better than 0.1‰ as assessed by multiple analyses of a variety of carbonate standards. The data is available in Table S2. Estimates for the carbon isotopic composition of dissolved inorganic carbonate (DIC) during this time period were derived from Bekker et al. (17) and Fischer et al. (18) (Fig. 3).

**Bulk S isotope analysis by SF<sub>6</sub> gas source mass spectrometry.** At the MIT Stable Isotope Laboratory, pyrite sulfur was extracted from powdered rock samples by chromium chloride reduction following a method modified from (61). A 1M CrCl<sub>3</sub> solution was reduced using zinc metal (4g zinc/40mL of CrCl<sub>2</sub>). Sample powders (1.5g to 5g) were added to a round bottom flask connected to a condenser with a sidearm to allow N<sub>2</sub> to flow through. The condenser was connected to a water trap filled with 60-70 mL of DI H<sub>2</sub>O for condensed phases and a trap containing ~50 mL of zinc acetate. Approximately 30 mL of chromium chloride solution was added to the sample powders after flushing and then heated to boiling for 2-3 hours to drive off H<sub>2</sub>S and ultimately

precipitate ZnS. Once the reaction has completed, silver nitrate was added (5mL) to react with the zinc sulfide and form precipitated silver sulfide ( $\text{Ag}_2\text{S}$ ). The precipitates were washed with  $\text{NH}_4\text{OH}$  (to remove any silver hydride) and ultrapure DI water and dried. The silver sulfide was then reacted with  $\text{F}_2$  at  $300^\circ\text{C}$ . Reacted  $\text{SF}_6$  was transferred via liquid nitrogen cold traps, removing any extraneous  $\text{F}_2$ , and purified by means of a gas chromatograph. The  $\text{SF}_6$  was then fed into a Thermo 253 dual-inlet mass spectrometer, where the isotopes ratios sulfur isotopes ( $^{32}\text{S}$   $^{33}\text{S}$   $^{34}\text{S}$   $^{36}\text{S}$ ) were measured against in-house standards. This method offers a precision of 0.26, 0.014 and 0.19 ‰ ( $2\sigma$ ) for  $\delta^{34}\text{S}$ ,  $\Delta^{33}\text{S}$  and  $\Delta^{36}\text{S}$  values based on multiple measurements of reference materials (IAEA S-1:  $\delta^{34}\text{S}$   $-1.34 \pm 0.13$ ,  $\Delta^{33}\text{S}$   $0.10 \pm 0.007$  and  $\Delta^{36}\text{S}$   $-0.57 \pm 0.10$ , IAEA S-2:  $\delta^{34}\text{S}$   $21.18 \pm 0.13$ ,  $\Delta^{33}\text{S}$   $0.043 \pm 0.005$  and  $\Delta^{36}\text{S}$   $-0.16 \pm 0.05$ , IAEA S-3:  $\delta^{34}\text{S}$   $-33.54 \pm 0.13$ ,  $\Delta^{33}\text{S}$   $0.091 \pm 0.020$  and  $\Delta^{36}\text{S}$   $-0.58 \pm 0.11$ ). The data are reported in delta notation (‰) with respect to VCDT, and are reported in Table S3.

***In situ* S isotope analysis by secondary ion mass spectrometry.** We employed a Cameca 7f-GEO, a pseudo multi-collector SIMS instrument with three separate collectors that measure different ions in rapid succession by dynamic peak hopping, housed within the Center for Microanalysis at the California Institute of Technology. The instrument was operated at a primary beam current of  $\sim 3\text{nA}$  with a spot size of  $\sim 25\mu\text{m}$ . We measured  $^{32}\text{S}$ ,  $^{33}\text{S}$ , and  $^{34}\text{S}$  with a MRP of  $\sim 4000$  to separate  $^{33}\text{S}$  from  $^{32}\text{SH}$ , and typically achieve  $\sim 10^9$  counts  $\text{s}^{-1}$  of  $^{32}\text{S}$ , and  $\sim 10^8$  and  $\sim 10^7$  counts  $\text{s}^{-1}$  for  $^{34}\text{S}$  and  $^{33}\text{S}$ , respectively. Sample unknowns were bracketed by measurements of an inhouse pyrite

standard ( $\delta^{34}\text{S}$  1.024‰,  $\delta^{33}\text{S}$  0.608‰), co-mounted in epoxy close to the regions of the sample of interest and polished to obtain the same flat analytical surface. Data was corrected for Faraday cup yield differences ( $^{32}\text{S}$  was collected on Faraday cup 1 and  $^{33}\text{S}$  and  $^{34}\text{S}$  are collected on Faraday cup 2) and instrumental mass fractionation of isotopes. External precision (defined as the standard deviation of multiple adjacent measurements of standards) is typically better than  $\delta^{34}\text{S} = 0.4\text{‰}$ ,  $\delta^{33}\text{S} = 0.3\text{‰}$ , and  $\Delta^{33}\text{S} = 0.15\text{‰}$ . (For measurements on detrital pyrite grains, precision is similar for  $\Delta^{33}\text{S}$  but is up to 1.3‰ for  $\delta^{34}\text{S}$ , as standards were not on same mount adjacent to pyrite.) The data are reported in delta notation in permill with respect to VCDT, and is available in Table S3.

**Kinetics of manganese oxidation by  $\text{O}_2$ .** Mn(II) oxidation by the low levels of molecular oxygen allowable by our independent redox proxies does not explain the enrichments observed in Koegas strata. While thermodynamics dictate that molecular oxygen will oxidize Mn(II) at far less than  $10^{-10}$  atm, oxidation reactions by  $\text{O}_2$  are strongly kinetically limited (14, 19). Even at modern oxygen levels, abiological manganese oxidation is exceedingly slow—kinetic limitations result in an Mn(II) half life of 30 days for oxide-stimulated oxidation and 400 days for a homogenous solution with  $\text{Mn}^{2+}_{(\text{aq})}$  and  $\text{O}_2$  (under a 0.21 atm  $\text{pO}_2$  atmosphere) (14). Considering that molecular oxygen produced in the surface ocean will reside for an average of approximately 17 days before escaping to the atmosphere (20), abiological mechanisms are not rapid enough to produce the volume of manganese we observe.

Biological manganese oxidation (using O<sub>2</sub>) proceeds more rapidly and is thought to be the main mechanism for Mn oxidation in modern environments — under today's atmosphere, Mn(II) has a half life of 10 hours (14). This process is most efficient at enzyme saturation, at a range of 0.87 to 11 μM of dissolved O<sub>2</sub> (the Michaelis-Menton constant K<sub>M</sub> (21)). Oxygen levels during Koegas deposition were likely around 10<sup>-13</sup> atm (22) (the predicted O<sub>2</sub> levels for the atmosphere before the rise of cyanobacteria (23), dissolved O<sub>2</sub> would be 1.26\*10<sup>-7</sup> nM), but constrained by multiple sulfur isotope data to be at most lower than 10<sup>-5.7</sup> atm (dissolved O<sub>2</sub> would be 2.6 nM) (22). We used these two estimates of atmospheric oxygen to determine the amount of manganese that could be oxidized at these low O<sub>2</sub> levels. Using the lowest reported value for measured biological Michaelis-Menton constants (K<sub>M</sub> = 0.87 μM (21)), the highest values for maximum Mn(II)-oxidation rates at infinite O<sub>2</sub> (V<sub>Max</sub> = 50 nM per hr (21)), we estimated a maximum rate of Mn oxide production using saturation kinetics calculations (21):

$$\text{Oxidation rate of Mn(II)} = (s * V_{\text{Max}}) / (K_{\text{M}} + s)$$

At the likely pre-cyanobacteria levels of 10<sup>-13</sup> atm of O<sub>2</sub>, the Mn oxidation rate is 7.24 \* 10<sup>-9</sup> nM per hr, or 3.48 \* 10<sup>-9</sup> g per L per kyr. At the highest permitted O<sub>2</sub> concentrations of 10<sup>-5.7</sup> atm, the Mn oxidation rate is 0.151 nM per hr, or 0.073 g per L per kyr.

These rates can be considered in the context of the processes delivering sediment to this basin. Koegas Subgroup lithologies describe a mixed clastic-chemical sedimentary basin



with intercalated sequences of wave-modified deltaic siliciclastic sediments and iron formation (4, 5, 24). Iron formations here are often cross-bedded and granular, implying high wave action, and contain admixtures of sand, silt, and detrital aluminosilicate minerals, further indicating competing terrigenous detrital influxes and chemical sedimentation (5) (Fig. 3*A* and *B*). We estimate a seawater depth of approximately 10m for the GTF01 core, where sandstone intervals better constrain the water depth. Sedimentation rates can be approximated using measured rates for similar sedimentary basins and processes, with the assumption of uniform physical processes of sediment transport. Sadler (1981) constructed a vast compilation of ~25,000 rate measurements and determined that sedimentation rates vary depending on integration time span (25). With delta lobe switching occurring at approximately 3 to 1500 year intervals (26), terrigenous shelf delta and shelf seas sedimentation rates vary from ~300m per kyr to ~2m per kyr (27). We conservatively use 1m per kyr as the lowest background sediment accumulation rate during Mn deposition. Alternatively, Barley et al. (1997) estimated sedimentation rates for the deposition of banded iron formations in the Hamersley basin, a shallow marine platform of slightly older age in Western Australia, suggesting rates between 0.1 and 1 m per kyr using U-Pb zircon dating (interpolated from rates in m per myr). These rates have been used in other geobiological calculations for iron formation deposition (see (28)), and though it is an imperfect process and geodynamic basinal analog for the deposits examined here (as the Hamersley basin was a siliciclastic-starved marine platform without significant river detrital flux (29)), we also use these rates for comparison.

We converted our Mn oxidation rate calculations for different oxygen concentration scenarios into the mass of Mn deposited per thousand years and divided by the sediments accumulated in that time. A 10m-water column overlying a 1cm x 1cm square of sea floor is equal to 1 L of water in which Mn could be oxidized by O<sub>2</sub>. For the same area, continental shelf sedimentation rates would predict 100cm<sup>3</sup> deposited in 1000 years (25), while the starved marine platform rates would estimate 10 to 100cm<sup>3</sup> per kyr (30). Mass of the sedimentary column can be determined using an average density of iron formations, 3.45 g cm<sup>-3</sup>, from (31). Applying these calculations to the Mn rates determined above, at 10<sup>-13</sup> atm, the percent Mn in the sediments is insignificant: the Mn oxides produced by O<sub>2</sub> are 1.01 \* 10<sup>-9</sup> % of the sediments using shelf seas and delta sedimentation rates and 1.01 \* 10<sup>-8</sup> % of the sediments using the lowest starved marine platform sedimentation rates. At the highest O<sub>2</sub> levels allowed by our proxies, Mn oxides are 0.02% of the sediments using the higher shelf rates and 0.2% of the sediments using the lower starved platform rates. Thus the nM dissolved oxygen concentrations maximally allowed by multiple sulfur isotopes are not sufficient for producing the Mn enrichments observed throughout our cores in both shallow and deep-water paleoenvironments. These calculations do not account for any Mn loss back to the water column from pore fluids during reduction. Including a fraction of recycled Mn in these kinetic calculations would just further highlight the discordance between the required rates and the exceedingly low O<sub>2</sub> concentrations indicated by the detrital pyrite and

anomalous sulfur isotope fractionations. Simply put, Mn oxidation by  $O_2$ —either abiologically or biologically—is too slow to account for our observed enrichments.

There are few other mechanisms to potentially oxidize manganese. Biological Mn oxidation using nitrate is thermodynamically feasible but does not appear to occur in nature (21, 32). Hydrogen peroxide can oxidize manganese, but production of a large volume of  $H_2O_2$  would require a local source (33) and these deposits accumulated in a tropical paleolatitude (34). Photo-oxidation of manganese occurs at insignificant levels when dissolved iron is present (35). This points to photobiology as the process of Mn oxidation and concentration in the sediments.

## SUPPORTING FIGURES

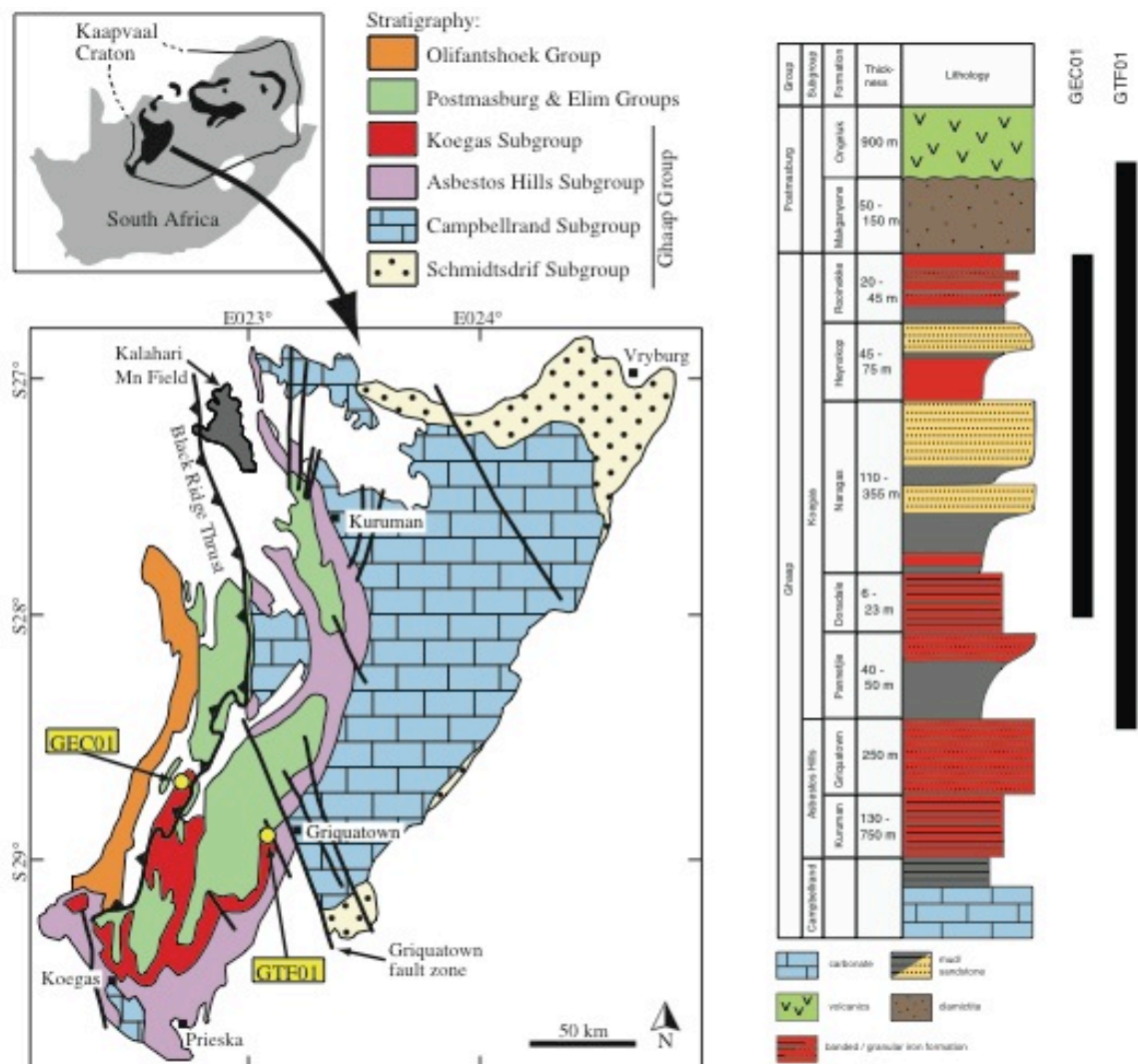


Figure S1: Geologic map of Archean and Paleoproterozoic-age strata exposed in Griqualand West sub basin of the Transvaal Supergroup, South Africa, modified from Schroder et al. (2011). Note the location of drill cores GTF01 and GEC01. To the right is a generalized stratigraphic column with lithologic information showing the stratigraphic breadth of the two drill cores.

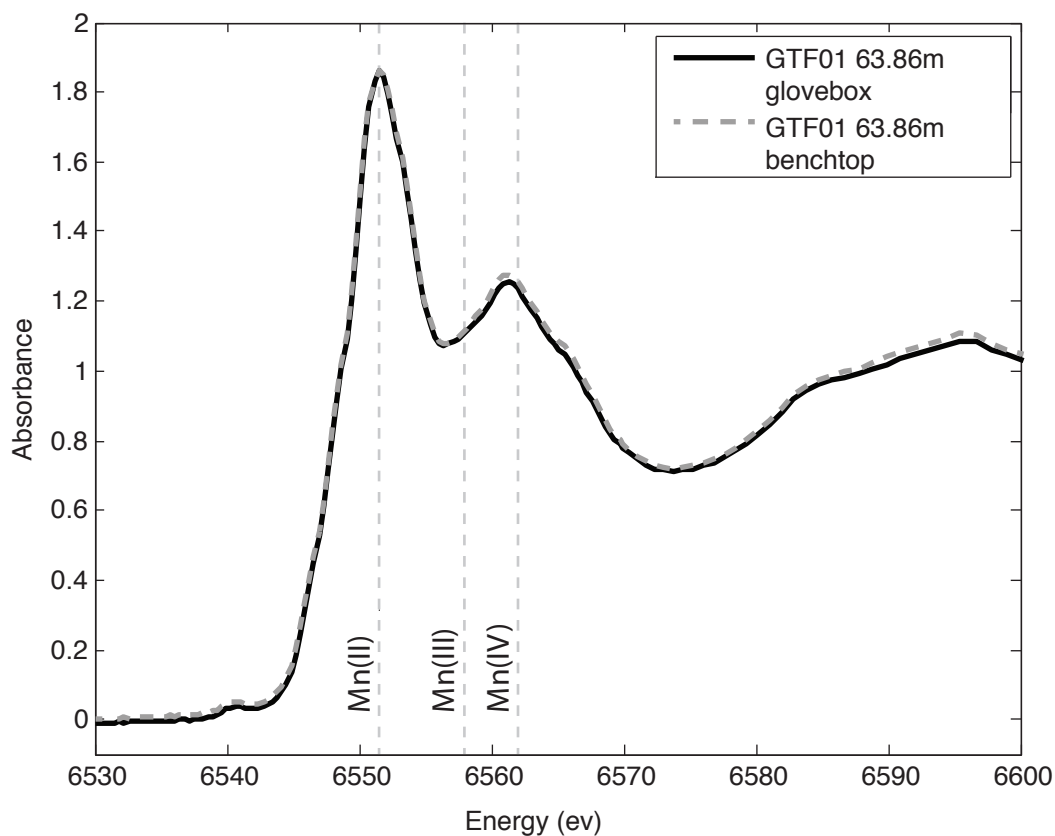


Figure S2: Bulk X-ray absorption spectra of one sample (GTF01 at 63.86m) prepared both in an anaerobic glovebox and on an aerobic benchtop and measured on beamline 4-3 at SSRL. Maximal absorptions for Mn(II), Mn(III), and Mn(IV) are shown for reference. Spectra are indistinguishable, indicating lack of Mn oxidation from exposure to oxygen over a timescale of  $\sim 1$  week.

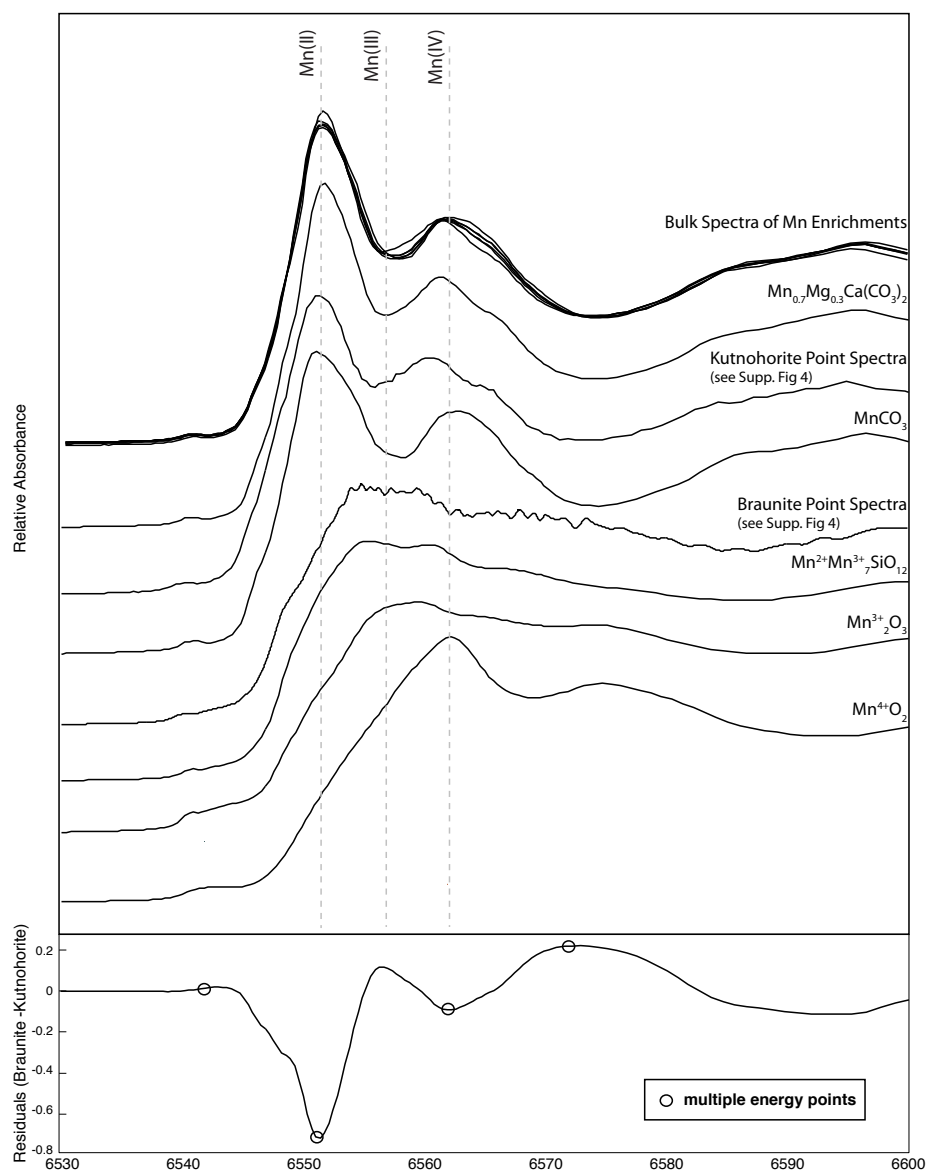


Figure S3: X-ray absorption spectra of known Mn-bearing minerals: well-characterized kutnohorite and braunitite from the Kalahari Mn Field, rhodochrosite, and Mn(III) and Mn(IV) oxides. Mn(II) in carbonate phases show XANES spectra easily distinguishable from mixed valence manganese (II and III) in braunitite  $[\text{Mn(II)Mn(III)}_4(\text{SiO}_4)_8\text{O}_8]$  and other species with oxidized Mn. Compare these to bulk spectra of all Koegas Mn enrichments from GECO1 and GTFO1 ( $n=16$ ) and point spectra from carbonate concretions and oxide matrix of the Kalahari. Bulk Koegas spectra and carbonate concretions from the Kalahari best match kutnohorite spectra. Also shown by vertical lines are maximal absorption energies of Mn(II), Mn(III), and Mn(IV). Lower panel plots residuals

when subtracting Kalahari kutnohorite from braunite. Black circles indicate the X-ray energies commonly used to distinguish Mn redox states.

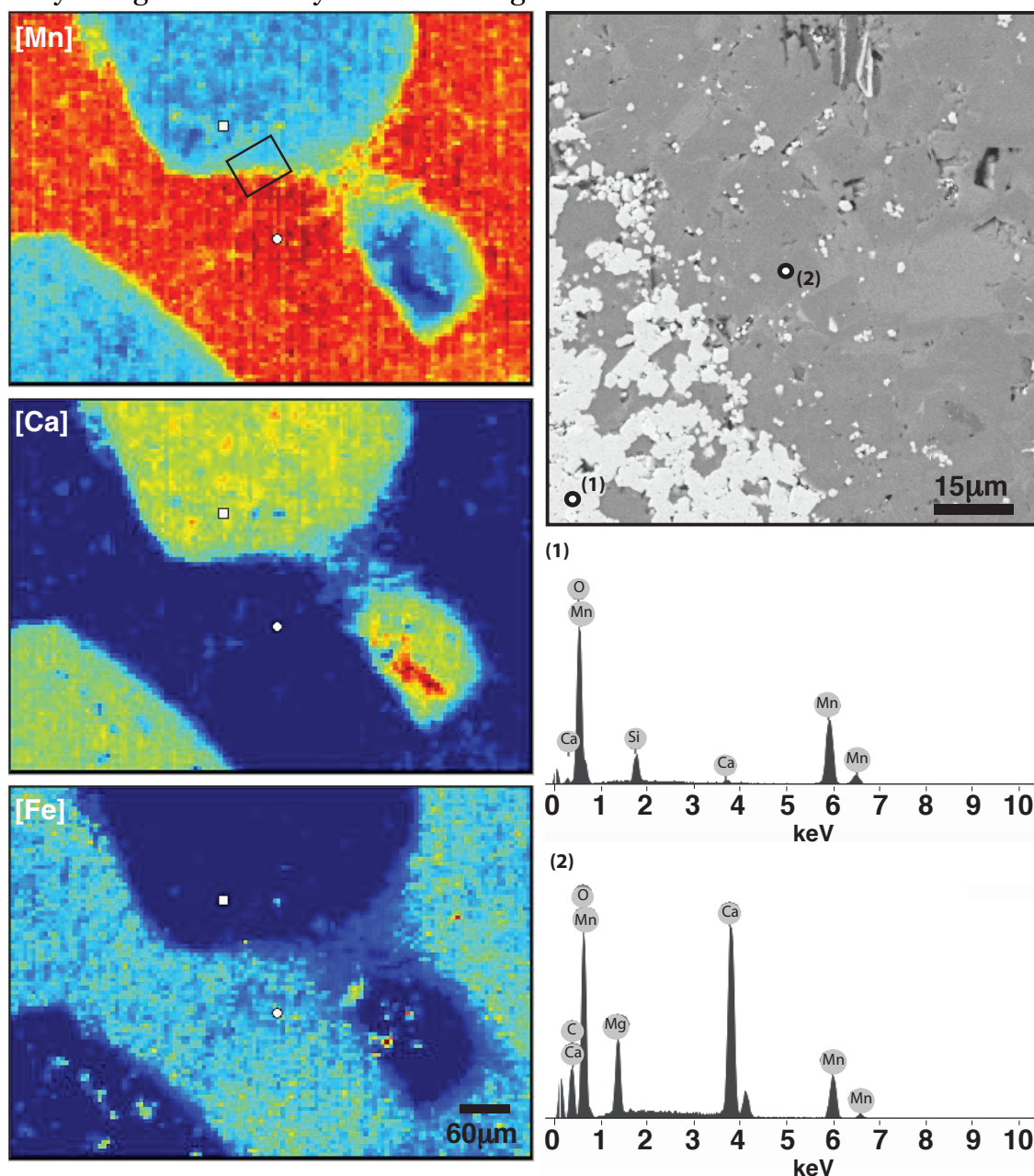


Figure S4: Left, X-ray fluorescence (XRF) maps of Mn, Ca, and Fe abundance on a sample from the Kalahari Manganese Field. Small white squares mark positions of spots where kutnohorite and braunite spectra were measured to obtain endmember spectra (Figure S3A) for multiple energy redox maps presented in Fig. 2. On the right, a SEM backscatter image of the domain highlighted in the black box on the left. EDS spectra on the first and second marked circles highlight the composition of braunite and kutnohorite, respectively.



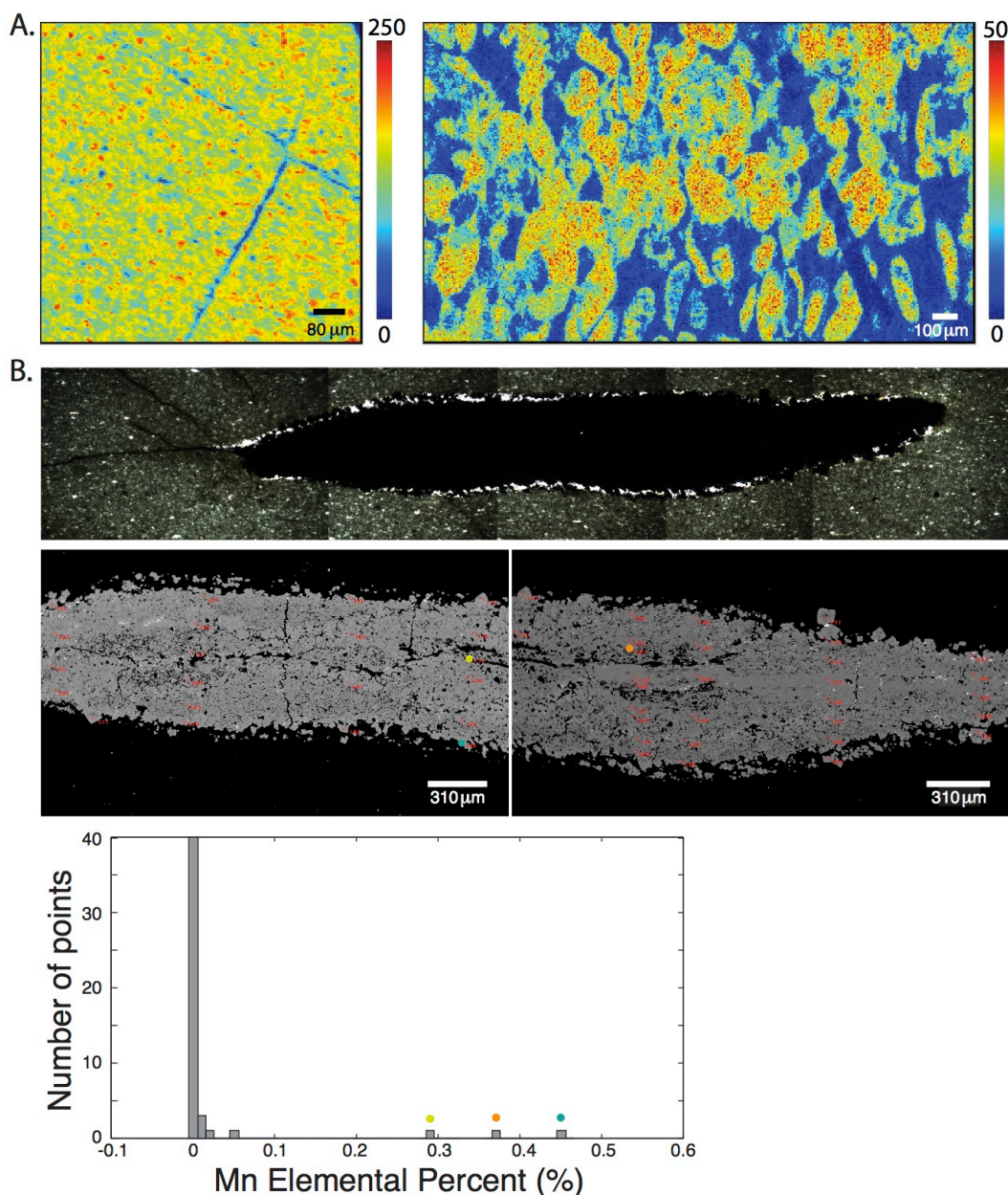


Figure S5: (A) Manganese concentration in  $\mu\text{g}/\text{cm}^2$  measured by X-ray fluorescence at SSRL. Mn concentrations are much lower in mineralized late cracks and fractures, indicating that Mn enrichments did not originate from late fluids. (B) Transmitted light photomicrograph (above) and backscatter SEM image (below) of GECO1 169.83m showing discontinuous pyrite mineralization along a fracture. Bottom is a histogram of Mn concentration from electron probe measurements. Outliers with higher Mn abundance are shown as yellow, orange and blue dots. Note that the positions of these anomalous spot analyses occur in regions that incorporate more matrix and are not solely pyrite.



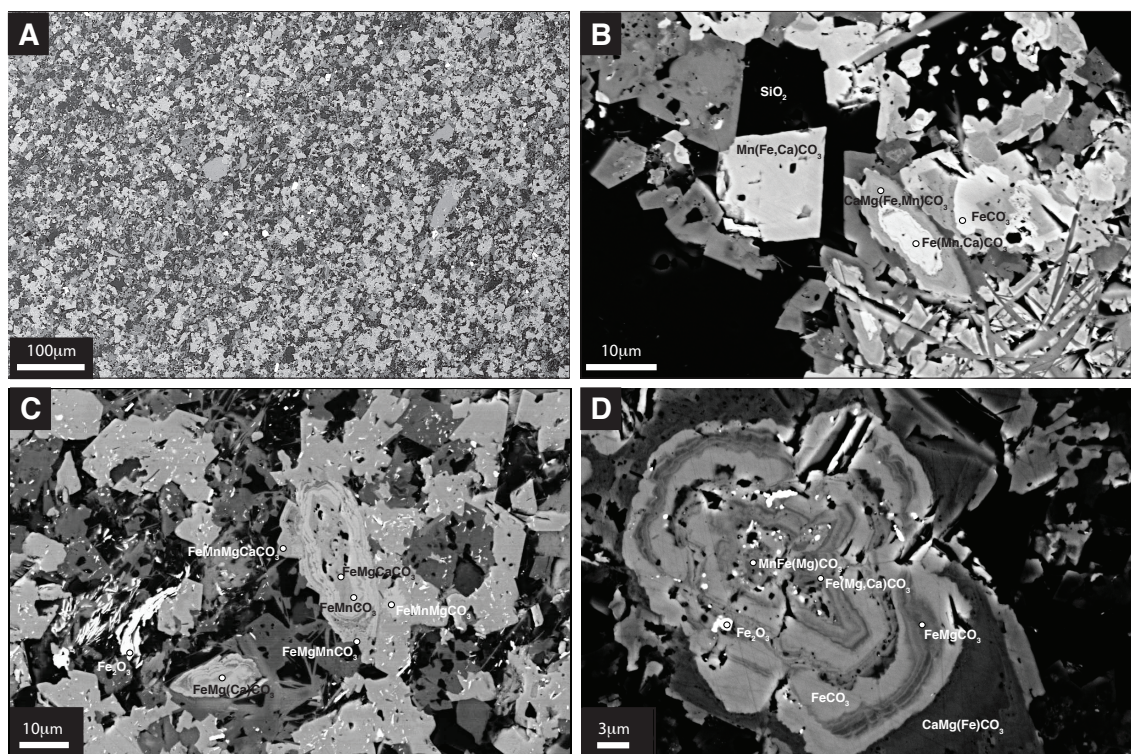


Figure S6: SEM backscatter images of samples enriched in Mn reveal very fine-grained mixtures of oxide, silicate, and carbonate phases with diagenetic textures. (A) and (C) from GTF 111.15m; (B) and (D) from GTF 54.10m.



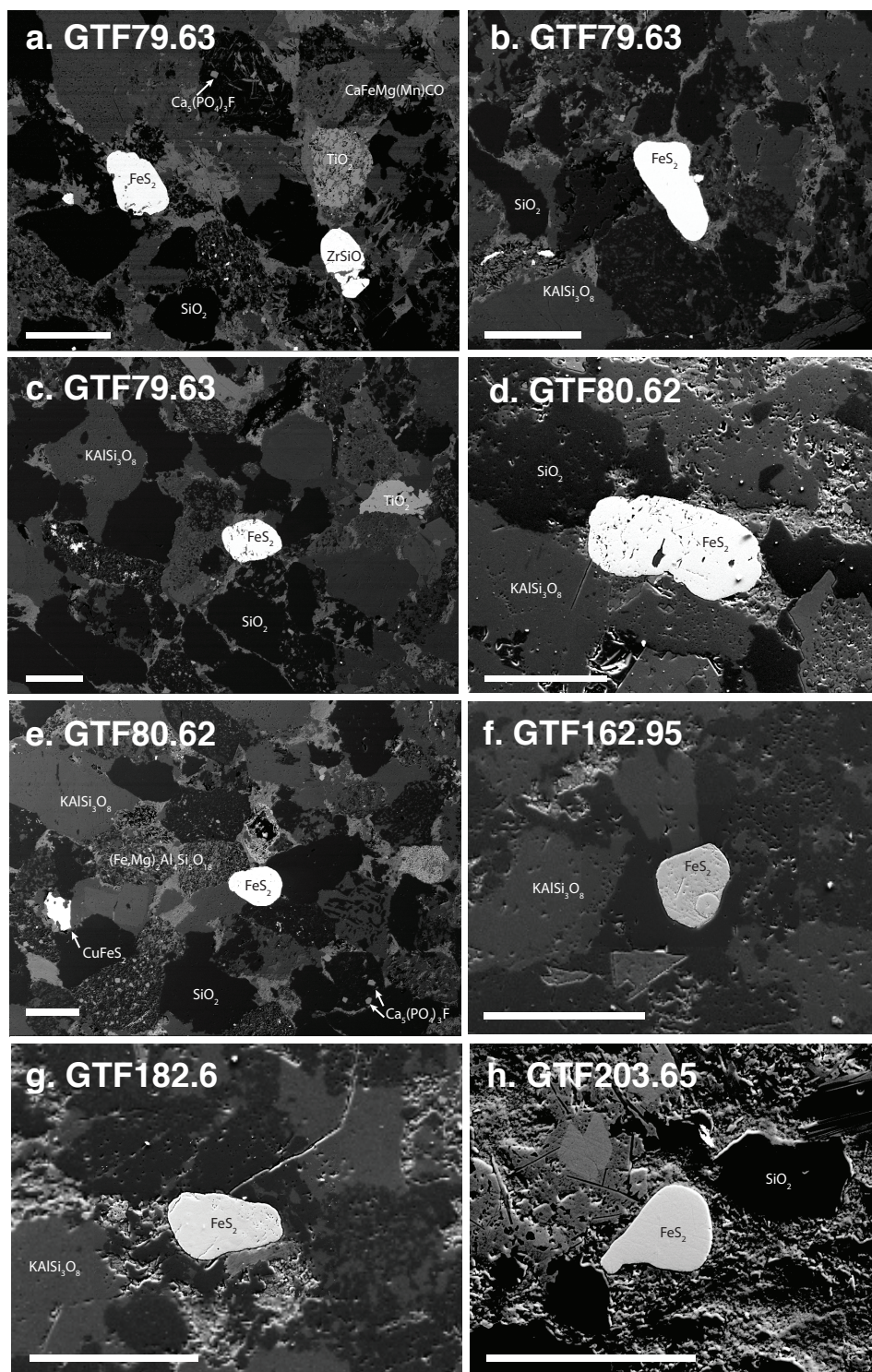


Figure S7: SEM backscatter images of detrital pyrite grains from sandstone subunits in GTF01. Note size, correlation with other heavy minerals, and rounding. Scale bars are 100 $\mu$ m.



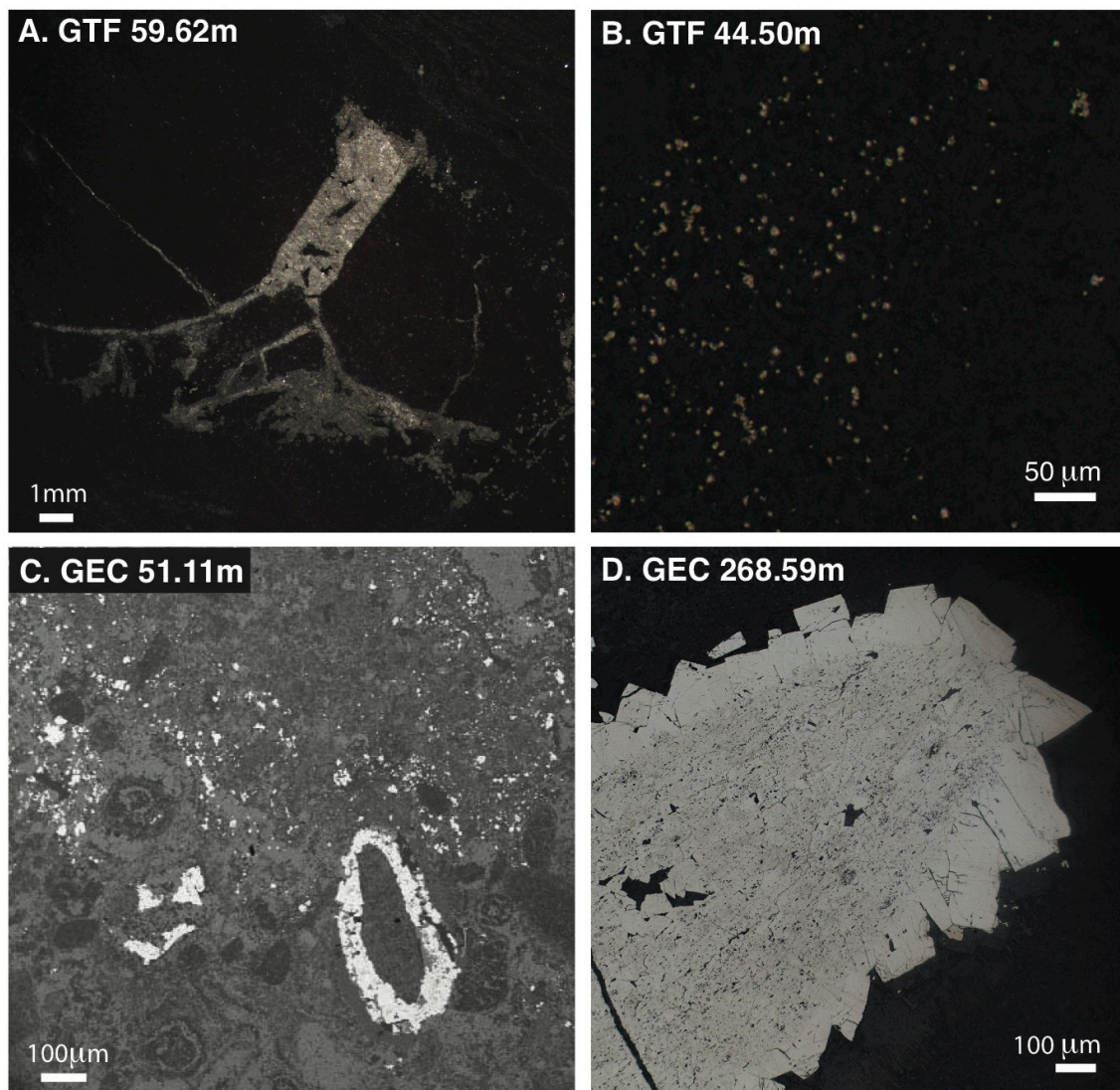


Figure S8: Photomicrographs from light and scanning electron microscopy highlighting examples of late pyrite textures. (A) GTF01 at 59.62m a fractured chert nodule hosting pyrite, (B) GTF01 at 44.50m shows finely disseminated but sharply euhedral grains, (C) GEC01 at 51.11m shows replacement of iron silicate and iron carbonate oolitic grains by pyrite, (D) GEC01 at 268.59m shows a nodule with a coarse euhedral rim.

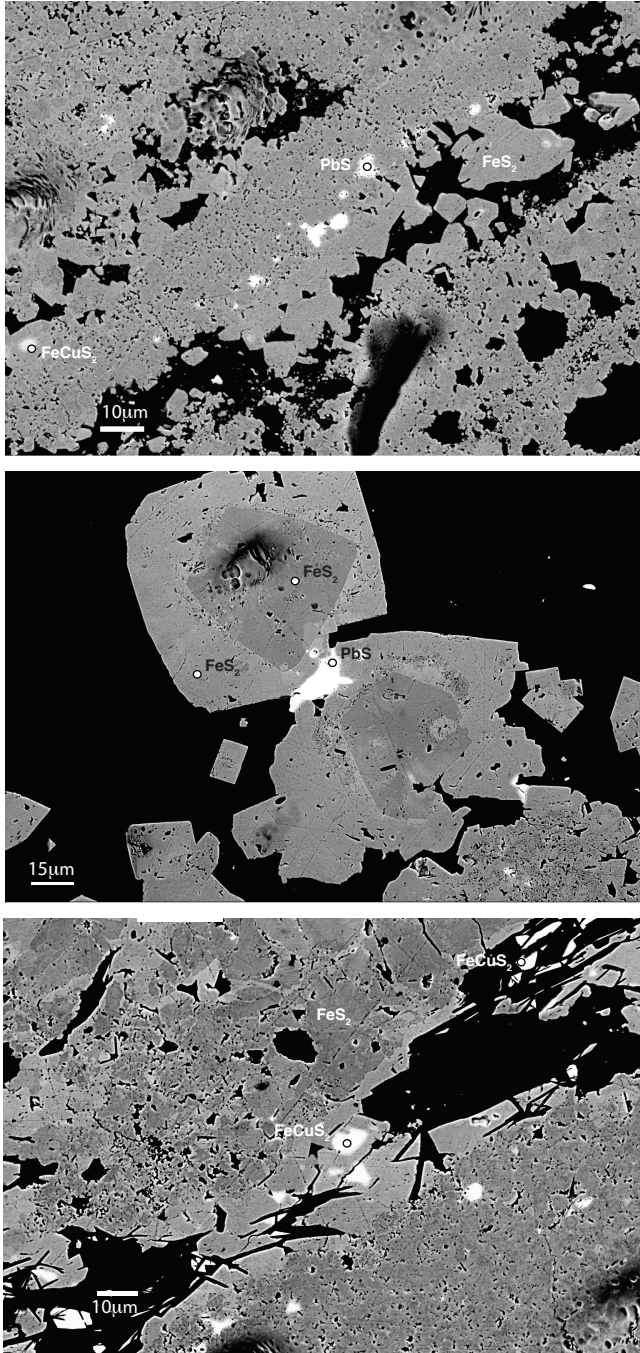


Figure S9: Backscatter electron photomicrographs of pyrites with late diagenetic textures and domains of chalcopyrite ( $\text{FeCuS}_2$ ) and galena ( $\text{PbS}$ ), highlighting several episodes of sulfide mineralization in these strata.



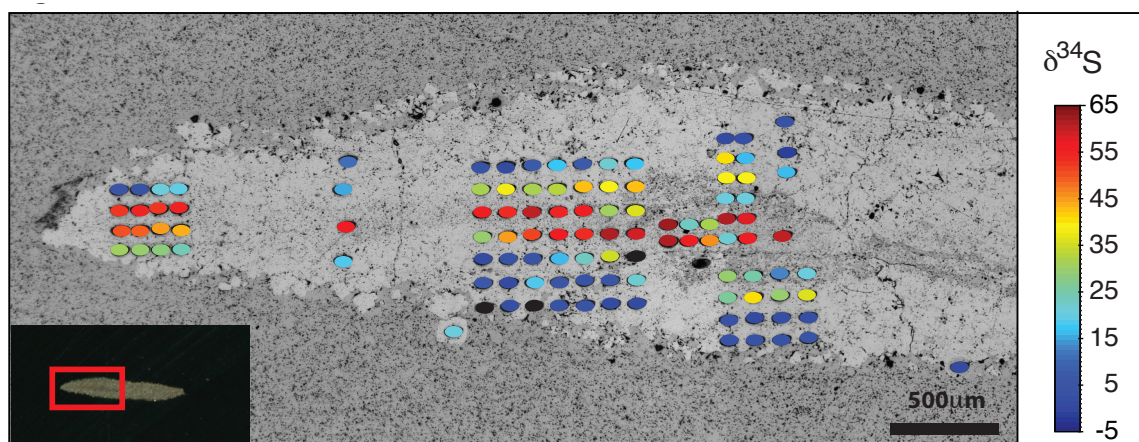


Figure S10: Example of *in situ* sulfur isotopic measurements from GECO1 at 169.83m on top of a backscatter electron image. This pyrite “nodule” is composed of aggregates of euhedral domains that grew from a through-going fracture. Color bar corresponds to  $\delta^{34}\text{S}$  isotopic values (in permil VCDT), ranging from -5 to 65‰.

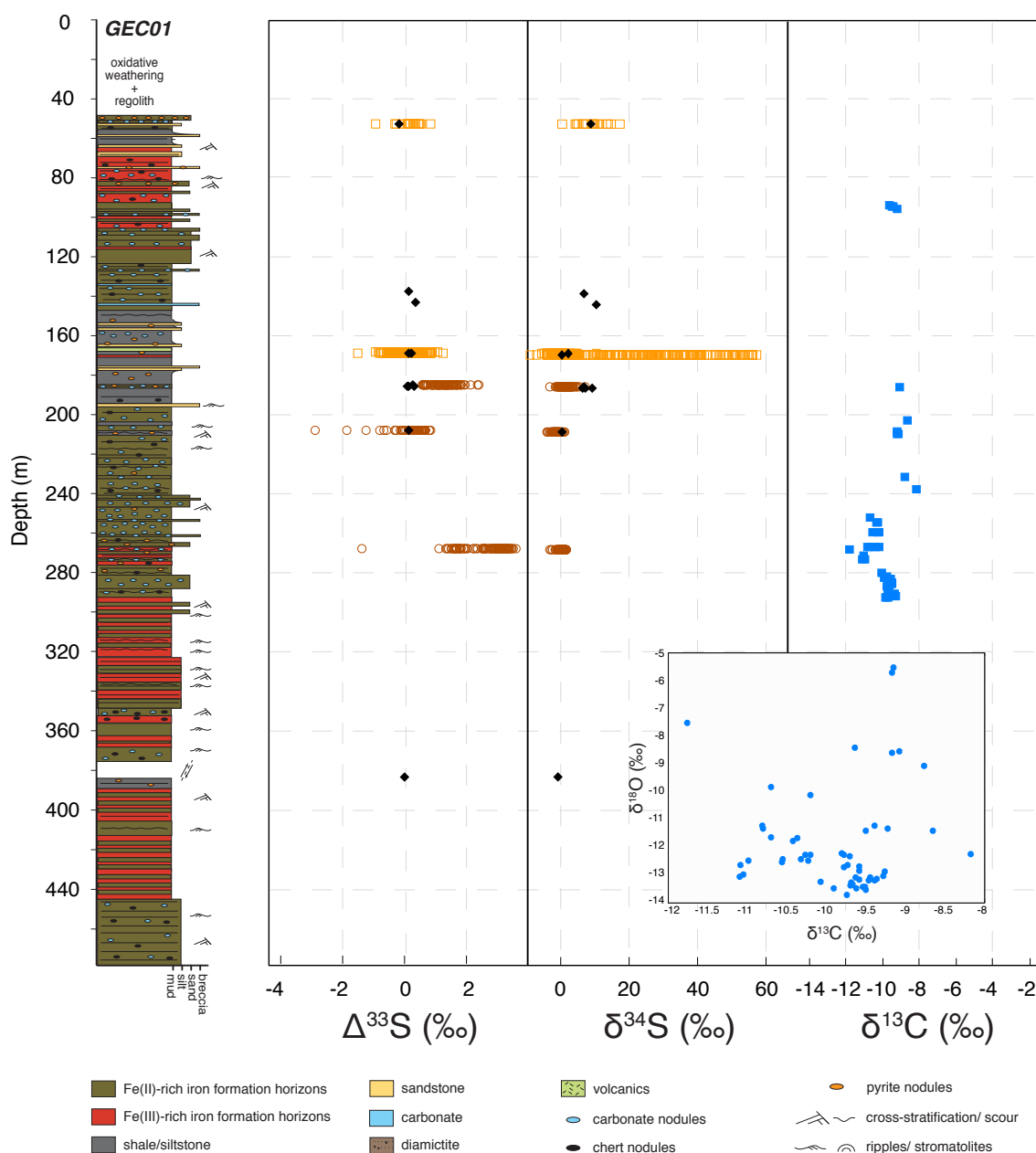


Figure S11: GEC01 core with sulfur isotopic data ( $\Delta^{33}\text{S}$  and  $\delta^{34}\text{S}$ ) and carbon isotopic data ( $\delta^{13}\text{C}$ ; blue) plotted with depth. Maroon circles mark *in situ* primary pyrite, orange squares signify *in situ* measurements of late pyrite, and black diamonds designate bulk  $\text{SF}_6$  measurements.

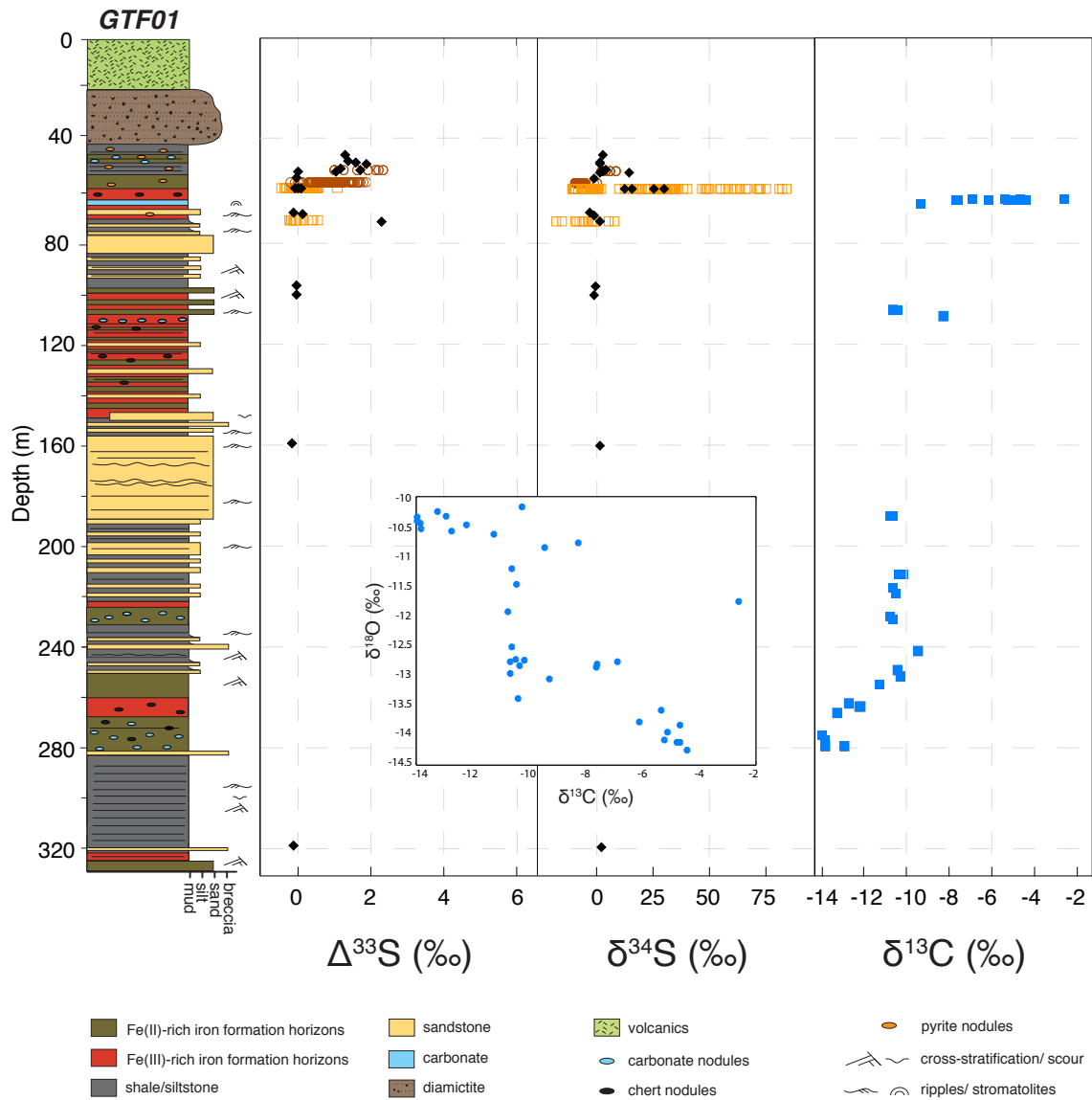


Figure S12: GTF01 core with sulfur isotopic data ( $\Delta^{33}\text{S}$  and  $\delta^{34}\text{S}$ ) and carbon isotopic data ( $\delta^{13}\text{C}$ ; blue) plotted with depth. Maroon circles mark *in situ* primary pyrite, orange squares signify *in situ* measurements of late pyrite, and black diamonds designate bulk  $\text{SF}_6$  measurements.

Table S1: Bulk Mn concentrations in weight percent at various depths from both cores (plotted in Fig. 1).

Core*	depth (m)	Mn (wt. %)		Core	depth (m)	Mn (wt. %)
GTF	42.65	0.2		GEC	41.15	0.4
GTF	45.53	1.9		GEC	53.2	0.82
GTF	47.65	16.6		GEC	64.3	0.31
GTF	54.1	10.1		GEC	65.9	0.51
GTF	55.9	0.5		GEC	69.15	0.04
GTF	57.35	0.6		GEC	74.09	0.147
GTF	58.45	0.3		GEC	82.2	0.52
GTF	60.73	0.6		GEC	82.8	0.37
GTF	63.8	1.8		GEC	84	0.32
GTF	64.12	2.1		GEC	87.5	0.66
GTF	64.45	0.6		GEC	89.6	1.8
GTF	68.2	0.7		GEC	90.4	3.57
GTF	74.18	0.2		GEC	92.96	4.14
GTF	80.62	0.3		GEC	93.5	9.04
GTF	90.12	4.4		GEC	93.6	7.92
GTF	100.15	0.4		GEC	94.5	12.3
GTF	108.4	7.8		GEC	97.71	0.915
GTF	110.7	7		GEC	99	0.583
GTF	111.15	4.9		GEC	103.38	0.246
GTF	111.75	1.5		GEC	118	0.45
GTF	114.68	0.5		GEC	120	1.01
GTF	128.47	0.1		GEC	122.5	0.17
GTF	136.16	0.1		GEC	126.5	0.28
GTF	141.8	0.3		GEC	128.5	0.05
GTF	148.3	0.3		GEC	135.5	0.15
GTF	151.22	0.1		GEC	140	0.18
GTF	151.22	1.3		GEC	144.3	0.18
GTF	160.4	0.3		GEC	152	0.07
GTF	163.1	0.1		GEC	159.83	0.16
GTF	169.54	0.2		GEC	164.5	0.39
GTF	178.45	0.2		GEC	166.5	0.04
GTF	183.92	0.1		GEC	172.5	0.3
GTF	193.06	0.1		GEC	181.1	0.45
GTF	210.08	0.2		GEC	188.4	0.49
GTF	218.76	0.3		GEC	202.5	3.04
GTF	220	1.4		GEC	209.4	3.16
GTF	221.75	2		GEC	216	4.76



GTF	223.5	2.5		GEC	231.7	3.94
GTF	224.7	3.6		GEC	233.3	2.16
GTF	225.1	1.3		GEC	247.9	0.645
GTF	225.2	0.5		GEC	249.82	0.54
GTF	228.9	5.8		GEC	253	6.3
GTF	229.25	6.2		GEC	257	1.01
GTF	229.6	7.1		GEC	259	3.2
GTF	229.8	10		GEC	259.87	0.569
GTF	229.92	10.4		GEC	267.4	7.95
GTF	230	11.6		GEC	271	4.16
GTF	230.05	5.5		GEC	279.6	0.04
GTF	233.7	0.5		GEC	280.19	0.179
GTF	238.7	1.1		GEC	282.45	0.173
GTF	243	3.7		GEC	284.7	0.94
GTF	251.06	1.5		GEC	296.22	0.596
GTF	251.06	0.4		GEC	296.27	0.758
GTF	251.88	0.9		GEC	300	0.64
GTF	253	2.2		GEC	308.84	0.879
GTF	254.8	1.3		GEC	318.18	4.52
GTF	257.65	0.7		GEC	339.59	0.24
GTF	260.08	0.7		GEC	363.1	0.59
GTF	265.62	1				
GTF	267	1				
GTF	274.24	1.4				
GTF	279.8	0.7				
GTF	281.4	0.2				
GTF	284.65	0.3				
GTF	285.5	0.5				
GTF	289.61	0.1				
GTF	298.65	0.1				
GTF	309.74	0.1				
GTF	316.8	0.1				
GTF	318.56	0.1				
GTF	324.6	0.7				
GTF	327.22	0.5				

\*some GTF data from Ref (9).

Table S2:  $\delta^{13}\text{C}$  and  $\delta^{18}\text{O}$  data at various depths from both cores (plotted in Fig. 3C and Fig. S11 and S12).

Core	depth	$\delta^{13}\text{C}$	$\delta^{18}\text{O}$		Core	depth	$\delta^{13}\text{C}$	$\delta^{18}\text{O}$
GTF	63.95	-5.33	-13.59		GEC	92.98	-9.64	-8.42
GTF	63.96	-6.88	-12.78		GEC	93.5	-9.5	-11.41
GTF	63.97	-4.68	-13.84		GEC	93.6	-9.39	-11.24
GTF	64.02	-2.58	-11.85		GEC	94.49	-9.22	-11.34
GTF	64.02	-2.6	-11.68		GEC	185.58	-9.07	-8.56
GTF	64.14	-5.12	-14.02		GEC	202.5	-8.65	-11.41
GTF	64.14	-5.12	-13.89		GEC	208.48	-9.17	-8.6
GTF	64.15	-4.42	-14.26		GEC	209.4	-9.15	-5.55
GTF	64.2	-5.21	-14.09		GEC	209.4	-9.17	-5.73
GTF	64.22	-6.11	-13.79		GEC	231.7	-8.76	-9.08
GTF	64.25	-7.62	-12.87		GEC	238.13	-8.17	-12.25
GTF	64.3	-4.68	-14.12		GEC	252.52	-10.7	-11.64
GTF	64.35pink	-7.61	-12.81		GEC	253.01	-11.02	-11.71
GTF	64.35white	-4.78	-14.13		GEC	254.49	-10.32	-12.45
GTF	65.82pink	-9.29	-13.06		GEC	254.49	-10.26	-12.28
GTF	107.86	-10.67	-12.78		GEC	259.75	-10.23	-12.48
GTF	107.92	-10.4	-13.39		GEC	259.75	-10.2	-12.28
GTF	110.22	-8.25	-10.78		GEC	259.75	-10.56	-12.55
GTF	189.66	-10.74	-12.92		GEC	259.75	-10.55	-12.44
GTF	189.66	-10.63	-13.03		GEC	267.31	-10.42	-11.79
GTF	212.45	-10.35	-12.84		GEC	267.31	-10.36	-11.67
GTF	212.57	-10.18	-12.74		GEC	267.4	-10.8	-11.34
GTF	212.57	-10.16	-12.76		GEC	267.4	-10.81	-11.23
GTF	217.52	-10.61	-12.52		GEC	267.43	-10.2	-10.13

GTF	219.99	-10.48	-12.74		GEC	267.49	-10.7	-9.83
GTF	228.8	-10.75	-11.94		GEC	268.59	-11.76	-7.52
GTF	230.1	-10.62	-11.22		GEC	271.65	-11.05	-13
GTF	243	-9.45	-10.86		GEC	273.38	-10.98	-12.48
GTF	250.27	-10.45	-11.47		GEC	273.38	-11.08	-12.66
GTF	253	-10.26	-10.18		GEC	273.38	-11.09	-13.07
GTF	255.94	-11.25	-10.63		GEC	280.66	-10.07	-13.25
GTF	263.53	-12.73	-10.59		GEC	282.64	-9.74	-13.73
GTF	265.17	-12.24	-10.55		GEC	283.38	-9.9	-13.5
GTF	265.17	-12.18	-10.41		GEC	283.99	-9.62	-13.48
GTF	267.47	-13.25	-10.26		GEC	283.99	-9.53	-13.44
GTF	276.27	-13.95	-10.35		GEC	283.99	-9.51	-13.43
GTF	276.27	-13.95	-10.41		GEC	285.81	-9.58	-13.18
GTF	278	-13.84	-10.45		GEC	285.81	-9.46	-13.19
GTF	280.28	-12.94	-10.34		GEC	285.81	-9.44	-13.09
GTF	280.38	-13.81	-10.55		GEC	286.05	-9.5	-13.53
					GEC	286.55	-9.58	-12.86
					GEC	286.55	-9.58	-12.71
					GEC	287.71	-9.77	-12.73
					GEC	287.71	-9.73	-12.64
					GEC	291.04	-9.68	-13.28
					GEC	291.04	-9.63	-13.1
					GEC	291.04	-9.66	-13.35
					GEC	291.04	-9.69	-13.39
					GEC	291.09	-9.36	-13.16
					GEC	292.2	-9.39	-13.21
					GEC	292.2	-9.28	-13.03

					GEC	292.2	-9.26	-12.88
					GEC	292.88	-9.77	-12.29
					GEC	292.88	-9.8	-12.24
					GEC	292.88	-9.7	-12.34

## SUPPORTING REFERENCES

1. Pickard A. (2003) SHRIMP U–Pb zircon ages for the Palaeoproterozoic Kuruman Iron Formation, Northern Cape Province, South Africa: evidence for simultaneous BIF deposition on Kaapvaal and Pilbara Cratons. *Precambrian Research* 125:275–315.
2. Trendall AF et al. (1990) in *Proceedings of the Third International Archaean Symposium* (Geological Society of Australia, Perth), pp 81–83.
3. Nelson DR, Trendall AF, Altermann W (1999) Chronological correlations between the Pilbara and Kaapvaal cratons. *Precambrian Research* 97:165–189.
4. Beukes NJ (1983) in *Developments in Precambrian Geology*, eds Trendall AF, Morris RC (Elsevier), pp 131–198. Available at: <http://www.sciencedirect.com/science/article/pii/S0166263508700434> [Accessed March 22, 2013].
5. Schröder S, Bedorf D, Beukes NJ, Gutzmer J (2011) From BIF to red beds: Sedimentology and sequence stratigraphy of the Paleoproterozoic Koegas Subgroup (South Africa). *Sedimentary Geology* 236:25–44.
6. Kirschvink JL et al. (2000) Paleoproterozoic snowball Earth: Extreme climatic and geochemical global change and its biological consequences. *PNAS* 97:1400–1405.
7. Walraven F, Armstrong R., Kruger F. (1990) A chronostratigraphic framework for the north-central Kaapvaal craton, the Bushveld Complex and the Vredefort structure. *Tectonophysics* 171:23–48.
8. Armstrong RA (1987) Geochronological Studies on Archean and Proterozoic Formations of the Namaqua Front and Possible Correlates on the Kaapvaal Craton [Ph.D. Thesis].
9. Cornell DH, Schütte SS, Eglington BL (1996) The Ongeluk basaltic andesite formation in Griqualand West, South Africa: submarine alteration in a 2222 Ma proterozoic sea. *Precambrian Research* 79:101–123.
10. Gutzmer, Jens, Beukes, Nicolas (1998) *High-grade manganese ores in the Kalahari manganese field: characterisation and dating of ore forming events* (Rand Afrikaans University, Johannesburg).
11. Beukes NJ, Gutzmer J (2008) in *Banded Iron Formation-Related High-Grade Ore*, eds Hagemann S, Rosiere C, Gutzmer J, Beukes N, pp 5–47.

12. Polteau S, Moore JM, Tsikos H (2006) The geology and geochemistry of the Palaeoproterozoic Makganyene diamictite. *Precambrian Research* 148:257–274.
13. Hoffman PF (2013) The Great Oxidation Event and a Siderian Snowball Earth: MIF based correlation of Paleoproterozoic glaciations. *Chemical Geology* in press.
14. Morgan JJ (2005) Kinetics of reaction between O<sub>2</sub> and Mn(II) species in aqueous solutions. *Geochimica et Cosmochimica Acta* 69:35–48.
15. Webb SM (2011) The MicroAnalysis Toolkit: X-ray Fluorescence Image Processing Software. *AIP Conference Proceedings* 1365:196–199.
16. Mayhew LE, Webb SM, Templeton AS (2011) Microscale imaging and identification of Fe speciation and distribution during fluid-mineral reactions under highly reducing conditions. *Environ Sci Technol* 45:4468–4474.
17. Bekker A et al. (2001) Chemostratigraphy of the Paleoproterozoic Duitschland Formation, South Africa: Implications for Coupled Climate Change and Carbon Cycling. *Am J Sci* 301:261–285.
18. Fischer WW et al. (2009) Isotopic constraints on the Late Archean carbon cycle from the Transvaal Supergroup along the western margin of the Kaapvaal Craton, South Africa. *Precambrian Research* 169:15–27.
19. Luther GWI (2010) The Role of One- and Two-Electron Transfer Reactions in Forming Thermodynamically Unstable Intermediates as Barriers in Multi-Electron Redox Reactions. *Aquatic Geochemistry* 16:395–420.
20. Broecker WS, Peng T-H (1982) *Tracers in the Sea* (Eldigio Pr, Columbia University, Palisades, New York).
21. Clement BG, Luther III GW, Tebo BM (2009) Rapid, oxygen-dependent microbial Mn(II) oxidation kinetics at sub-micromolar oxygen concentrations in the Black Sea suboxic zone. *Geochimica et Cosmochimica Acta* 73:1878–1889.
22. Pavlov AA, Kasting JF (2002) Mass-Independent Fractionation of Sulfur Isotopes in Archean Sediments: Strong Evidence for an Anoxic Archean Atmosphere. *Astrobiology* 2:27–41.
23. Kasting JF (1993) Earth's early atmosphere. *Science* 259:920–926.
24. Beukes NJ (1978) Die karbonaatgesteentes en ysterformasies van die Ghaap-Groep van die Transvaal-Supergroep in Noord-Kaapland.
25. Sadler P (1981) Sediment Accumulation Rates and the Completeness of Stratigraphic Sections. *Journal of Geology* 89:569–584.

26. Jerolmack DJ, Mohrig D (2007) Conditions for branching in depositional rivers. *Geology* 35:463–466.
27. Sadler PM, Hass HC (1999) in *On the determination of sediment accumulation rates*, ed Bruns P (Trans Tech Publications, Switzerland), pp 15–40.
28. Konhauser KO et al. (2002) Could bacteria have formed the Precambrian banded iron formations? *Geology* 30:1079–1082.
29. Blake TS, Barley ME (1992) Tectonic evolution of the Late Archaean to Early Proterozoic Mount Bruce Megasequence Set, western Australia. *Tectonics* 11:1415–1425.
30. Barley ME, Pickard AL, Sylvester PJ (1997) Emplacement of a large igneous province as a possible cause of banded iron formation 2.45 billion years ago. *Nature* 385:55–58.
31. Ewers WE, Morris RC (1981) Studies of the Dales Gorge Member of the Brockman Iron Formation, Western Australia. *Economic Geology* 76:1929–1953.
32. Schippers A, Neretin LN, Lavik G, Leipe T, Pollehne F (2005) Manganese(II) oxidation driven by lateral oxygen intrusions in the western Black Sea. *Geochimica et Cosmochimica Acta* 69:2241–2252.
33. Liang M-C, Hartman H, Kopp RE, Kirschvink JL, Yung YL (2006) Production of hydrogen peroxide in the atmosphere of a Snowball Earth and the origin of oxygenic photosynthesis. *Proc Natl Acad Sci USA* 103:18896–18899.
34. Evans DA, Beukes NJ, Kirschvink JL (1997) Low-latitude glaciation in the Palaeoproterozoic era, *Published online: 20 March 1997*; | doi:10.1038/386262a0 386:262–266.
35. Anbar AD, Holland HD (1992) The photochemistry of manganese and the origin of banded iron formations. *Geochimica et Cosmochimica Acta* 56:2595–2603.

*Chapter 3***O<sub>2</sub> constraints from Paleoproterozoic detrital pyrite and uraninite**

Jena E. Johnson<sup>a</sup>, Aya Gerpheidea<sup>a,b</sup>, Michael P. Lamb<sup>a</sup>, Woodward W. Fischer<sup>a</sup>

<sup>a</sup>Division of Geological and Planetary Sciences, California Institute of Technology, Pasadena, CA 91125, USA. <sup>b</sup>Department of Geology, Occidental College, Los Angeles, CA 90041

*Originally published in the Geological Society of America Bulletin, Volume 126, Issue no. 5-6, p. 813-830.*

**ABSTRACT**

**Redox-sensitive detrital grains such as pyrite and uraninite in sedimentary successions provide one of the most conspicuous geological clues to a different composition of the Archean and early Paleoproterozoic atmosphere. Today these minerals are rapidly chemically weathered within short transport distances. Prior to the rise of oxygen, low O<sub>2</sub> concentrations allowed for their survival in siliciclastic deposits with grain erosion tied only to physical transport processes. After the rise of oxygen, redox-sensitive detrital grains effectively vanish from the sedimentary record. To get a better understanding of the timing of this transition, we examined sandstones recorded in a scientific drill core from the South African 2.415 Ga Koegas Subgroup, a mixed siliciclastic and iron formation-bearing unit deposited on the western deltaic margin of the Kaapvaal Craton in early Paleoproterozoic time.**

We observed detrital pyrite and uraninite grains throughout all investigated sandstone beds in the section, indicating that the rise of oxygen is younger than 2.415 Ga. To better understand how observations of detrital pyrite and uraninite in sedimentary rocks can quantitatively constrain Earth surface redox conditions, we constructed a model of grain erosion from chemical weathering and physical abrasion to place an upper limit on ancient environmental O<sub>2</sub> concentrations. Even conservative model calculations for deltaic depositional systems with sufficient transport distances (ca. hundreds of kilometers) show that redox-sensitive detrital grains are remarkably sensitive to environmental O<sub>2</sub> concentrations, and constrain the Archean and early Paleoproterozoic atmosphere to have  $< 3.2 \times 10^{-5}$  atm of molecular O<sub>2</sub>. These levels are lower than previously hypothesized for redox-sensitive detrital grains, but are consistent with estimates made from other redox proxy data, including the anomalous fractionation of sulfur isotopes. The binary loss of detrital pyrite and uraninite from the sedimentary record coincident with the rise of oxygen indicates that atmospheric O<sub>2</sub> concentrations rose substantially at this time and were never again sufficiently low ( $< 0.01$  atm) to enable survival and preservation of these grains in short transport systems.

## INTRODUCTION

As early as the 1950s, geologists observed striking differences between the composition of grains found in conglomerates and sandstones from early Precambrian (ca. 2.4 Ga to



>3.25 Ga) sedimentary successions compared to modern deposits: the ancient sedimentary rocks contained grains of pyrite and uraninite (and occasionally siderite) in addition to the quartz, feldspar, lithic fragments, and heavy mineral grains (such as zircon, garnet, and monazite) commonly found in sediments of all age. The paleoenvironmental significance of these grains lies in their preservation during weathering and sediment transport. Both pyrite and uraninite minerals are prone to rapid oxidative chemical weathering (Grandstaff, 1976; Williamson and Rimstidt, 1994), and thus their relative abundance and preservation in siliciclastic successions implies that the Earth surface environments of weathering and sediment transport once contained less molecular oxygen ( $O_2$ ) than today (Grandstaff, 1980; Holland, 1984; Prasad and Roscoe, 1996; Rasmussen and Buick, 1999).

The preservation of redox-sensitive detrital grains are one of several basic and fundamental geologic observations, including the secular distribution of banded iron formations, red beds, and the behavior of iron in paleosols, that indicate there was significantly less oxygen on the early Earth (Cloud, 1968, 1972; Holland, 1984). Redox-sensitive detrital grains have been documented in many studies, highlighting the global prevalence and magnitude of these deposits, albeit limited in time. To illustrate this secular distribution, we compiled a list of occurrences of redox-sensitive grains throughout the geologic record (Table 1). These grains are common in Archean strata, with the most recent occurrences documented in earliest Paleoproterozoic successions. It is likely that more occurrences exist waiting to be discovered, but a general pattern

emerges pointing to loss of redox-sensitive detrital grains from the sedimentary record sometime after 2.415 billion years ago (Johnson et al., 2013). Early Paleoproterozoic sedimentary deposits dated between 2.1 and 2.3 Ga (Kozhevnikov et al., 2010) appear to lack redox-sensitive detrital grains (the Jatulian Conglomerates; Clemmey and Badham, 1982). It is important to note that the presence of detrital pyrite and uraninite suggests the rise of atmospheric oxygen occurred sometime between 2.415 and ~2.1 Ga—timing consistent with the loss of multiple sulfur isotope anomalous fractionation and a range of other geological and geochemical proxies for oxygen, including the appearance of fluvial and nearshore marine red beds and gypsum deposits marking the onset of oxidative weathering in terrestrial environments (Roscoe, 1973; Cameron, 1982; Holland, 1984; Prasad and Roscoe, 1996; Rye and Holland, 1998; Tabakh et al., 1999; Beukes et al., 2002; Utsunomiya et al., 2003; Bekker et al., 2004; Papineau et al., 2007; Guo et al., 2009; Pufahl and Hiatt, 2012).

Compared to many other proposed proxies for O<sub>2</sub>—which involve subtle and complex geochemical systems that remain poorly understood in both modern environments and geological materials—redox-sensitive detrital grains present a simple and straightforward redox proxy because they are easy to observe using light and electron microscopy and the mechanics behind the proxy are well understood. This notwithstanding, two broad challenges remain. 1) We still have a limited understanding of the secular distribution of these deposits (Table 1). Despite the relative ease of identifying these grains, many Archean and early Paleoproterozoic siliciclastic rocks have not been studied in detail for

the presence of redox sensitive detrital grains. Furthermore, few geochronological constraints, particularly in deposits surrounding the rise of O<sub>2</sub> (Hoffman, 2013), make it challenging to compare and contrast occurrences between basins with confidence. 2) While it is clear that lower O<sub>2</sub> concentrations are required to preserve redox-sensitive detrital grains through weathering and transport, the intertwined processes of chemical and physical weathering responsible for the destruction of these grains make it challenging to derive a quantitative constraint about environmental O<sub>2</sub> levels that allows for their preservation.

We recently reported detrital pyrite in a ~2.415 Ga sedimentary deposit from the western margin of the Kaapvaal Craton in South Africa (Johnson et al., 2013). Here we build on that report and address both of these challenges, beginning with a more detailed description and analysis of redox-sensitive detrital grains (including uraninite) throughout this early Paleoproterozoic deposit. Then, guided by these observations, but with broad applicability to all occurrences in the sedimentary record (Table 1), we describe the construction and results of a model combining a classic physical abrasion framework with previously determined chemical weathering rate laws to study grain erosion processes under different transport scenarios and environmental O<sub>2</sub> levels. This approach offers novel constraints and an upper limit on ancient oxygen concentrations for grain preservation across a range of different transport scenarios and depositional environments.

## **OBSERVATIONS FROM THE TRANSVAAL SUPERGROUP, SOUTH AFRICA**

The South African Kaapvaal craton (Fig. 1A) harbors the first discovered and most well-known deposit with redox-sensitive detrital grains, the ~2.85 Ga Witwatersrand Supergroup placer deposits in the Central Rand Group (Liebenberg, 1955; Ramdohr, 1958), but also possesses several other key sedimentary successions of different ages that contain detrital pyrite and uraninite. The earlier ~3.08 Rhenosterspruit Formation bears detrital pyrite grains in a quartz-dominated conglomerate (Hiemstra, 1968; Simpson and Bowles, 1977; Hofmann et al., 2009), and the Mozaan Group has a granular quartz conglomerate at ~2.95 Ga with abundant pyrite pebbles (Hegner et al., 1994; Hofmann et al., 2009; Orberger et al., 2011). The ~2.7 Ga Ventersdorp Supergroup overlying the Witwatersrand is an unconformity-bound mixed volcanic and sedimentary succession with a basal unit of interbedded conglomerate and sandstone (Krapez, 1985). This unit has been well-characterized and has uraninite and pyrite grains in the sandy matrix of channel body conglomerates (Krapez, 1985). Heating and crustal thinning during Ventersdorp deposition created thermal subsidence, eventually allowing a marine platform to cover the craton (Schmitz and Bowring, 2003; Sumner and Beukes, 2006). Overlying the Ventersdorp is the Transvaal Supergroup, which begins with the Wolkberg Group in the eastern Transvaal basin and the Schmidtsdrif Subgroup in the western Griqualand West basin (Sumner and Beukes, 2006). The Wolkberg Group is unconformably overlain by the Black Reef Quartzite Formation, a thin conglomerate and quartzite unit with abundant pyrite and uraninite grains dated by basinal correlation to ~2.64 but constrained by an ash bed 100 m above to slightly older than or ~2.59 Ga

(Walraven and Martini, 1995; Martin et al., 1998; England et al., 2002; Hofmann et al., 2009).

The Kaapvaal Craton was subsequently flooded by a shallow epicratonic sea, resulting in a long-lived carbonate platform (the Campbellrand-Malmani Platform, Fig. 2) originally deposited over the entire craton, an area  $>600,000 \text{ km}^2$  (Beukes, 1987; Sumner and Beukes, 2006). At  $\sim 2.521$  to  $2.46 \text{ Ga}$ , the carbonate platform gradually drowned and transitioned into deeper water deposition of iron formation, which is found in both the Transvaal basin (Penge Iron Formation) and Griqualand West (Kuruman Iron Formation) structural basins (Beukes, 1987; Simonson and Hassler, 1996; Sumner and Bowring, 1996; Sumner and Beukes, 2006). In the Griqualand basin, the Griquatown Iron Formation overlying the Kuruman records the filling of accommodation space on the western margin of the craton, from banded into shallower water granular iron formation (Beukes and Klein, 1992). The sequence continues to shoal into the  $\sim 2.415 \text{ Ga}$  Koegas Subgroup which contains key intervals of siliciclastics. While the Black Reef Quartzite is the youngest unit underlying the Campbellrand-Malmani Platform to have facies appropriate for bearing redox-sensitive detrital grains, the Koegas Subgroup marks the first deposits overlying the carbonate platform with the appropriate lithologies to examine for redox-sensitive detrital grains (Fig. 2).

The Koegas Subgroup from Griqualand West, South Africa, is composed of early Paleoproterozoic-age mixed siliciclastic and iron formation strata from a marine deltaic

system on the western margin of the Kaapvaal craton (Beukes 1978, Schroeder et al. 2011; Fig. 1). Strata of the Koegas Subgroup are composed of interbedded deltaic tongues of siliciclastic deposits and granular and banded iron formation, with current and wave-ripple cross-stratification and lower plane bed laminations, respectively. The siliciclastic sediments were fed by a river system that reflects the uplift and erosion of much of the pre-Koegas strata across the Kaapvaal Craton, and ended a 100-million year interval of deposition of largely chemical sediments (carbonates and iron formation) across the craton (Schröder et al., 2011). The abundance of potassium feldspar, monazite and zircons (e.g., Fig. 4) suggest a felsic igneous source for the Koegas sediments, and paleocurrent and sequence stratigraphic data indicate a sediment source to the east, as the deltaic strata prograde to the west and northwest (Schröder et al., 2011). Taken together, these observations suggest either the removal of a substantial thickness ( $>2$  km) of flat-lying sedimentary cover (iron formation and carbonate; see Fig. 2 and previous text) from the central platform to expose Ventersdorp or older bedrock or, perhaps more likely, materials were sourced from a magmatic arc to the east of the Kaapvaal Craton (Schröder et al., 2011). Geological constraints on the sediment provenance thus suggest transport from at least the central Kaapvaal craton ( $>300$  km) or across the entire craton ( $>1000$  km), with either possibility recording a substantial craton-scale river system delivering materials to the Koegas sedimentary basin. Iron formation facies developed during intervals and in areas with low relative siliclastic input. The iron formations are diverse mineralogically, with laminations composed of intimate and gradational mixtures now composed of microcrystalline hematite, siderite, magnetite, and iron silicates. Zircons

from an ash bed in the Rooinekke Formation of the Koegas Subgroup were dated to  $2415 \pm 6$  Ma (Gutzmer, Jens and Beukes, Nicolas, 1998). Other known ages are consistent with this date (Fig. 2), with the underlying Kuruman and Griquatown formations dated at  $2460 \pm 5$  Ma and  $2432 \pm 31$  Ma, respectively (Pickard, 2003; Trendall et al., 1990; Nelson et al., 1999), and with the overlying Ongeluk Formation constrained to  $2222 \pm 12$  Ma (Cornell et al., 1996).

Drill cores capturing Koegas Subgroup strata were retrieved by the South African Agouron Drilling Project in 2006 (Fig. 3; (Schröder et al., 2011; Johnson et al., 2013). Drill core materials are important here because the surface of southern Africa has not been glaciated since Permian time and is deeply weathered by oxidative chemical weathering processes that have impacted sandstones as well as iron formations. One core (GTF-01) was drilled in a proximal location in the Koegas basin, while a second core (GEC-01) was collected downdip in more distal facies that lack siliciclastic units of sufficient grain size that can be examined for redox-sensitive detrital grains, such as sandstones and conglomerates. A previous report described the stratigraphy and sedimentology of the Koegas Subgroup, including the lithostratigraphy of GTF-01 (Schröder et al., 2011). We present a similar stratigraphic column, slightly revised to reflect our petrographic work that re-described several intervals originally marked as sandstones as cross-stratified granular iron formation (Fig. 3). The general stratigraphy captured by the drill core records a dynamic interplay between iron formation and terrigenous siliciclastic deposition (Fig. 3). The contact between the lowermost unit

Koegas Subgroup, the Pannetjie Formation, and the underlying Griquatown Iron Formation is sharp and associated with a thin, 10 cm-thick conglomerate of iron formation clasts (Beukes and Gutzmer, 2008). The Pannetjie Formation marks the onset of widespread delivery of siliciclastic sediments to the basin, and is composed of shale to very fine-grained sandstones. The thin, overlying Doradale Formation begins with a coarse bed of granular iron formation, and then is mainly finely laminated mixtures of ferrous and ferric-rich iron formation with abundant diagenetic chert and carbonate nodules. The Naragas Formation, starting around 250m depth, begins with another influx of siliclastic deposits corresponding to the progradation and lobe switching of an ancient delta. We observed a thin (<10 m) unit of deeper iron formation in the thick ~100 m Naragas Formation, but as Schröder et al. (2011) noted, this formation is mainly comprised of cross-stratified detrital deltaic sandstones. The abundance of fine to medium-coarse sandstones, with common quartz and feldspar grains and occasional detrital zircon and monazite and interbedded with shales, presented ideal targets for redox-sensitive grain investigation. The overlying Heynskoop Formation begins as mainly mixed ferric and ferrous iron formation with chert nodules and thin sandstone beds. The Heynskoop then shallows in the upper half, first with beds of granular iron formation, then shale, and finally ~5 m of sandstone beds. Above the sandstones, there is a rapid deepening, including a brief ~1 m-thick microbially-textured carbonate-rich bed before banded iron formation deposition resumes in the Rooinekke Formation. From point count data of thin sections, Schröder et al. (2011) characterized the Heynskoop and Naragas sandstones as subarkosic.



In a previous study, we noted the presence of detrital pyrite and confirmed its detrital and distinct origin from authigenic pyrite using *in situ* measurements of multiple sulfur isotopes (Johnson et al., 2013). Here we explore in depth the sandstone intervals from the Koegas Subgroup using the GTF-01 core and report the discovery of detrital uraninite and a characterization of the detrital pyrite abundance in representative petrographic thin sections of sandstone beds throughout the drill core.

## Methods

Sandstone units from throughout the Koegas Subgroup were investigated for oxygen-sensitive pyrite and uraninite grains using light and electron microscopy of microprobe-quality polished thin sections. We focused on the thickest sandstone interval, which was deposited in the upper Naragas Formation, with several smaller intervals in the lower Naragas and in the Heynskop formations (Fig. 3). Twenty billets approximately 27 x 46 x 5 mm in size were cut from the core using a rock saw, sampling sandstones at 76-84 m (10 billets), 158-190 m (6), 203 m (2), and 243 m (2). These were then made into 30  $\mu$ m-thick thin sections and polished to obtain a microprobe quality surface. Thin sections were subsequently examined and mapped on a Leica polarizing microscope using reflected and transmitted light microscopy. Samples containing abundant well-rounded pyrite grains identified using reflected light microscopy were then carbon coated with 7-15 nm using a Cressington Carbon Coater in preparation for study on the scanning electron microscope (SEM) and electron microprobe (E-probe).

Pyrite and uraninite were identified and imaged on a Zeiss 1550 VP Field Emission Scanning Electron Microscope (SEM) using an attached Oxford INCA Energy 300 X-ray Energy Dispersive Spectrometer (EDS) system. Coated samples were set at a working distance of 8 mm and probed with a 15 keV electron current.  $K\alpha$  X-ray fluorescence measurements used energy-dispersive spectroscopy to confirm phase identification, with quantitative elemental analyses providing relative accuracy of 5% or better. Grains were photographed on the SEM using the backscatter electron detector mode to enhance compositional contrast. For cathodoluminescence (CL) imaging, the detector was set on Variable Pressure Secondary Electron at a working distance of 10mm, and photographs were taken to assess grain shape and abrasion by truncation of internal zonation in feldspar and quartz grains.

To measure the abundance of detrital pyrite, elemental maps of four representative sections were produced using a JEOL JXA-8200 Advanced Electron Probe Micro-analyzer (E-probe) equipped with tungsten and LaB6 electron sources and five wavelength dispersive X-ray spectrometers (WDS). Intensity maps of sulfur, zirconium, and phosphorus abundance were measured over approximately 90% of the thin section area to determine heavy mineral compositions of the sandstones (relative abundance of pyrite, zircon, and apatite+monazite, respectively). The data matrices were reduced using a scaling function to select significant concentrations of S, P, and Zr. The abundance of pyrite, zircon, and apatite+monazite were determined by calculating the fraction of area

they occupied and adjusting for porosity (estimated visually to be 20%, within a normal range for sandstones; Boggs, 2006) (Table 2). These estimates are subject to similar logical uncertainties as classic point counting, but our use of E-probe produced elemental maps should eliminate human counting and identification errors and biases.

## Results

Redox-sensitive detrital grains were definitively identified in every sandstone bed we examined from the Koegas Subgroup (Fig. 3). The most common grains, quartz and feldspar, varied from sub-angular to well-rounded (Folk, 1957) and were fine to medium sand in size (after Wentworth, 1922). Both quartz and feldspar show compositional zonations highlighted by cathodoluminescence, with abundant evidence of truncation by physical abrasion (Fig. 4). Detrital pyrite grains were also common (Fig. 4, 5, 6). These can be distinguished from authigenic pyrite using a series of qualification standards (Rasmussen and Buick, 1999). Detrital grains occur as clear sedimentary grains in grain-supported sandstones. The grains themselves have rounded profiles, distinct grain boundaries, and inclusions of other mineral phases, and are commonly hydrodynamically concentrated with other heavy (i.e., dense) mineral grains such as zircon and apatite (Fig. 5, 6). Quantification of the relative abundances showed that the amount of pyrite generally scales with zircon and apatite+monazite, with the exception of an especially pyrite-rich sandstone sample at 77 m (Table 2). Some detrital pyrite grains show grain-boundary truncations (Fig. 6) and frequently the pyrite is concentrated on heavy mineral bands associated with cross-bed foresets (Fig. 5). Because of density differences (quartz

= 2.66 g/cm<sup>3</sup>, potassium feldspar/orthoclase = 2.56 g/cm<sup>3</sup>, pyrite = 5 g/cm<sup>3</sup>) pyrite grains in hydraulic equilibrium are smaller (very coarse silt to very fine sand, when converted from 2D spherical segments to 3D spherical diameters; Kong et al., 2005) and more rounded (rounded to well-rounded; Folk, 1957) than surrounding quartz and feldspar sand grains. These detrital pyrite grains are easily differentiated from authigenic pyrite derived from post-depositional fluids, which precipitate as euhedral to subhedral crystals or in overgrowth, pore-filling, and replacement textures. The detrital grains show no signs of weathering rinds or reaction rims, which might occur if chemical erosion occurred (from dissolved oxygen) in addition to physical abrasion. This implies that physical abrasion was the dominant (and perhaps only) component of grain erosion.

Detrital uraninite is far more rare and was only detected from a thin section at 203.65m in GTF-01 (Fig. 6j). The uraninite has since undergone radioactive decay and been altered to uraninite-uranothorite (UO<sub>2</sub>-U,ThSiO<sub>4</sub>) with galena and bitumen inclusions. This mineralogy and auto-brecciation is expected from an original uraninite grain as radioactive decay of uranium yields helium, thorium, and lead as daughter products. The addition of helium causes structural strain, and its release along grain boundaries causes crack development and produces a paths for interaction with later fluids (Ono, 2001). Later, sulfur-bearing fluids reacted with radiogenic lead to produce the galena inclusions observed (Ono, 2001). Because galena has a larger molar volume than uraninite (31.5 cm<sup>3</sup>/mol vs. ~24.6 cm<sup>3</sup>/mol), this also promotes fragmentation of uraninite (Finch and Murakami, 1999; Ono, 2001). Coffinization of uraninite, or diagenetic replacement of

uraninite with coffinite ( $\text{USiO}_4$ ), is a common reaction when reducing fluids with high silica activity are present (Janeczek and Ewing, 1992). Additionally, mobile hydrocarbons are known to solidify from radiation-induced polymerization as bitumen solids (i.e., radiobitumen) in and around the uraninite, which subsequently enhances the dissolution and fragmentation of the uraninite grain (Janeczek and Ewing, 1992; England et al., 2001). The presence of each of these features in the Koegas Subgroup allows the confident identification of detrital uraninite in addition to detrital pyrite.

We did not observe any clear examples of detrital carbonate grains, including siderite. Two examples from the literature of detrital siderite grains (Table 1, (Rasmussen and Buick, 1999)) likely underwent less weathering. With the longer transport distance of the Koegas sediments, any softer siderite grains (Moh's hardness = 3.5 to 4.5)—which are also substantially more susceptible to chemical dissolution from meteoric waters—eroded while the sturdier pyrite and uraninite grains survived (Moh's hardness = 6.5 and 5 - 6, respectively).

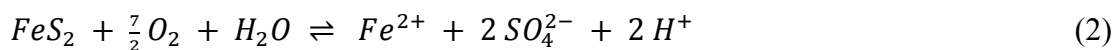
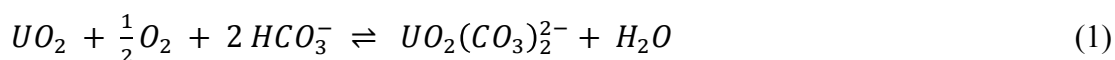
The discovery of uraninite and pyrite detrital grains in the Koegas Subgroup is interesting in light of the overall geologic context of the Transvaal Supergroup and constraints on the timing of the rise of oxygen. With the pyrite- and uraninite-bearing Black Reef Quartzite Formation at the base of the Transvaal Supergroup, the discovery of redox-sensitive detrital grains throughout the overlying Koegas subgroup neatly brackets the long-lived Campbellrand-Malmani carbonate platform between two siliciclastic successions

deposited under low O<sub>2</sub> conditions (Fig. 2). Our observations of (abundant) detrital pyrite and (more rare) detrital uraninite further suggest that at 2.415 Ga, the O<sub>2</sub> levels were not sufficiently high to oxidize these minerals during weathering and transport and remove them from the record. The presence of detrital pyrite and uraninite at 2.415 Ga marks the youngest redox-sensitive detrital grains currently known with geochronological constraints, setting an upper age for the Great Oxidation Event.

### **COMBINING PHYSICAL AND CHEMICAL WEATHERING PROCESSES TO CONSTRAIN ANCIENT O<sub>2</sub> LEVELS**

Redox-sensitive detrital grains present a simple and attractive proxy for O<sub>2</sub> in Earth surface environments. They are easily observed and the mechanics behind their preservation in fluvial and nearshore marine conglomerates and sandstones are known. A remaining challenge concerns how observations of detrital pyrite and uraninite in a given sedimentary context translate into quantitative constraints of the amount of O<sub>2</sub> present in the environment. The presence of these grains during weathering and physical transport indicates low O<sub>2</sub> levels, but how low is low? Very few sedimentary redox proxies (many of which are marine in concept) exist that can be directly inverted for O<sub>2</sub> concentrations. To provide new insight into this problem we developed a mathematical framework that captures the processes that destroy detrital pyrite and uraninite grains by coupling chemical weathering rates to physical processes that abrade grains with insight from process sedimentology (e.g., Sternberg, 1875; Sklar et al., 2006; Le Bouteiller et al., 2011).

The rates of chemical weathering of pyrite and uraninite and their sensitivity to oxygen levels have been studied (Grandstaff, 1976, 1980; Williamson and Rimstidt, 1994; Ono, 2001), with O<sub>2</sub> estimates derived solely from the chemical dissolution rate laws of these redox-sensitive minerals. In principal, both the chemical weathering of uraninite and pyrite are sensitive to oxygen (Holland, 1984; Stumm and Morgan, 1996), as shown at pH ≥ 6 as:



Laboratory rate laws have been constructed for both O<sub>2</sub>-dependent dissolution reactions. Grandstaff (1976) produced a chemical oxidation rate law for uraninite based on experiments oxidizing insoluble uraninite to soluble uranyl ions, with dissolution dependent on surface area, pH, organic compounds, the amount of non-uranium cations, the total dissolved carbonate, the temperature, and the dissolved oxygen content. From the rate law, estimates were applied to riverine conditions of organic content, cation content, CO<sub>2</sub>, temperature, alkalinity, residence time, and grain specific surface area for the Witwatersrand and Elliot Lake deposits (Grandstaff, 1980). Surface areas were chosen using the average grain diameters found in these deposits (75 μm) and Precambrian atmospheric estimates of 5 to 100 times the present levels of carbon dioxide or 0.0016 to 0.032 atm CO<sub>2</sub>. An average temperature of 15°C and travel distance of 10 to

500 km from earlier estimates of these deposits were used (McDowell, 1957; Hallbauer and Utter, 1977). Noting that the average sediment transport velocities of the Mississippi and Columbia rivers were on the order of  $1 \text{ km yr}^{-1}$ , Grandstaff (1980) decided the Witwatersrand and Elliot Lake deposits had higher velocities of  $1.5\text{-}7.5 \text{ km yr}^{-1}$  based on their larger average grain size. Yet since sediments often reside temporarily in alluvial deposits, drastically increasing their residence time by tens of thousands of years, they could also be potentially exposed to oxygen for thousands of years or more before removal from the source rock and after deposition. These varying time intervals of sediment storage were accounted for by inputting variable amounts of residence times for soil, river, and depositional time periods, from 600 to 110,000 years. Together, these estimates allowed Grandstaff to use his chemical dissolution rate law to invert for paleo-oxygen levels (Grandstaff, 1980).

Grandstaff deduced that for uraninite to be present in Archean and Paleoproterozoic siliciclastic deposits, ancient  $\text{O}_2$  concentrations must have been less than  $\sim 2.1 \times 10^{-3}$  to  $2.1 \times 10^{-6} \text{ atm}$  (Grandstaff, 1980). At the lowest  $\text{CO}_2$  levels he considered, ancient  $\text{O}_2$  constraints were higher, from around 0.001 atm to 0.0001 atm, while higher carbon dioxide levels (100 times our preindustrial atmosphere) decreased the  $\text{O}_2$  constraints to closer to  $1 \times 10^{-5}$  and  $1 \times 10^{-6} \text{ atm}$ . Though the  $\text{CO}_2$  levels of the early atmosphere remain somewhat poorly constrained and a topic of substantial debate (e.g., Rye et al., 1995; Sheldon, 2006), more recent estimates suggest an early atmosphere with even higher  $\text{CO}_2$  levels of approximately 0.03 to 5 atm, with an upper bound of 0.3 atm by early



Proterozoic time (Grotzinger and Kasting, 1993; Halevy et al., 2009). Furthermore, these previous calculations assumed physical erosion processes consumed half the mass of a detrital uraninite grain without incorporating rules for physical abrasion. Grandstaff was also careful to point out that these estimates are upper bounds as they do not take the potential impacts of uraninite-oxidizing microbes into account, as biologically driven catalysis of this reaction would occur at faster rates for a given  $O_2$  concentration (Grandstaff, 1980).

A rate law was similarly produced for the chemical weathering, or oxidation at neutral pH, of pyrite by  $O_2$  using a compilation of measured (defect-free) pyrite oxidation rates (Williamson and Rimstidt, 1994), with the dissolution solely dependent on pH and dissolved oxygen. Estimates of  $O_2$  following this pyrite oxidation rate law have suggested a constraint of approximately  $2.1 \times 10^{-6}$  atm when detrital pyrite is found (Anbar et al., 2007; Reinhard et al., 2009). As these rates are for pyrite free of defects, using this law provides an upper boundary for  $O_2$  estimates, as natural pyrite samples would likely oxidize at higher rates (Anbar et al., 2007; Reinhard et al., 2009). One study applied this rate law to a very fine sand-sized (side length = 100  $\mu\text{m}$ ) cubic pyrite crystal under a range of pH and oxygen levels and found that oxidation was extremely slow at  $O_2 \sim 1 \times 10^{-14}$  atm, taking 100 million years or more to dissolve the crystal (Reinhard et al., 2009). However, at  $O_2$  levels near the upper constraints from multiple sulfur isotopes,  $\sim 2.1 \times 10^{-6}$  atm (e.g., Pavlov and Kasting, 2002), dissolution was much more rapid, taking only tens of thousands of years (Reinhard et al., 2009). In a similar application, Anbar et al. (2007)

used Williamson's rate law to determine that a similarly-sized pyrite crystal would dissolve at  $\sim 2.1 \times 10^{-6}$  atm in less than 20,000 years (Anbar et al., 2007). Both of these calculations aimed to demonstrate how oxidative pyrite weathering might occur at ca. 2.5 Ga even at exceedingly low oxygen concentrations, and they highlight the sensitivity of pyrite to very low  $O_2$  levels, albeit at small initial grain diameters.

No previous work has combined these chemical weathering rate laws with models of physical erosion to assess the conditions required for preservation of redox-sensitive detrital grains in the geological record. It is certain that physical abrasion of sediment particles occurred during sediment transport, as evidenced by the rounding of particles and their occurrence in sedimentary structures that indicate transport (at least regionally) in bedload (Fig. 5, Fig. 6). It is crucial, therefore, to incorporate physical erosion into models of grain survival to arrive at higher quality constraints on paleoenvironmental  $O_2$  concentrations.

The presence of redox-sensitive detrital grains will be sensitive to the amount of physical abrasion, which relates in the simplest sense to the distance the grain has traveled, as well as the amount of chemical weathering, which reflects the total time of exposure and the amount of oxygen. We treat sedimentary grains as spheres and rewrite the previously derived chemical oxidation rate law for uraninite (Ono, 2001; Grandstaff, 1980) to produce an expression in terms of radial erosion rate ( $R_{uran}$ ) in meters per year:

$$R_{uran} = 6.29 \times 10^{21} (RF^{-1}) (10^{-10.8NOC}) (\Sigma CO_2) (H^+) (pO_2) \exp\left(\frac{-7045}{T}\right) MW_u \rho^{-1}, \quad (3)$$

where  $RF$  is the organic retardation factor,  $NOC$  is the mole fraction of non-uranium cations in uraninite,  $\Sigma CO_2$  is the total dissolved carbonate,  $pO_2$  is atmospheric oxygen in PAL,  $T$  is the absolute temperature,  $MW_u$  is the molecular weight of uraninite, and  $\rho$  is the uraninite density,  $11 \text{ g cm}^{-3}$ . We set  $RF = 20$  for a mid-range organic retardation factor,  $NOC = 0.17$  for a mid-range cation mole fraction, and  $T = 298 \text{ K}$  or  $25^\circ\text{C}$  (Grandstaff, 1980). We used  $0.1 \text{ atm}$  as a mid-range value of ancient  $CO_2$  estimates for the early Proterozoic atmosphere (Grotzinger and Kasting, 1993).

Similarly, for pyrite dissolution, the equation of Williamson and Rimstidt (1994) can be rewritten in terms of radial erosion rate ( $R_{pyr}$ ) in meters per year:

$$R_{pyr} = 0.135 (DO^{0.5}) MW_p \rho^{-1} (H^+)^{-0.11}, \quad (4)$$

where  $\rho = 5.01 \times 10^6 \text{ g m}^{-3}$ ,  $MW_p = 119.98 \text{ g mol}^{-1}$ , and  $DO$  is the dissolved oxygen content in  $\text{mol L}^{-1}$ .

To incorporate physical weathering, we applied Sternberg's Law, which describes the widely observed exponential reduction of particle diameter with transport distance due to abrasion of particles (Sternberg, 1875):

$$D = D_0 \exp(-x/x_0) , \quad (5)$$

where  $D$  is particle diameter at distance  $x$ ,  $D_0$  is the initial diameter,  $x$  is the distance grain has traveled, and  $x_0$  is a material specific length scale of erodability (Sternberg, 1875). The term  $x/x_0$  describes the transport distance relative to the characteristic distance to radially erode a grain by a factor of  $e$ . This model for physical abrasion of grains is widely used (Lewin and Brewer, 2002; Sklar et al., 2006; Le Bouteiller et al., 2011).

Combining both physical abrasion and chemical weathering yields an equation for grain-size evolution, with physical erosion as a function of transport distance and chemical weathering as a function of time ( $t$ ):

$$D = D_0 \exp(-x/x_0) - R t , \quad (6)$$

where  $R$  denotes the chemical weathering rate for either grain designated. We note that this model implicitly assumes that physical and chemical erosion rates are independent and additive, which may not be true. Several recent studies have shown that physical abrasion exposing new surfaces is an important control on chemical weathering rates, revealing these two processes are tightly coupled (Riebe et al., 2003; Ferrier and Kirchner, 2008). Thus  $O_2$  estimates from our approach should be treated as conservative constraints, because in more realistic scenarios physical and chemical erosion would feedback on and amplify each other. Nevertheless, this model determines an upper bound on ancient  $O_2$  concentrations and a lends stepping-stone for future modeling efforts once

the feedbacks between chemical and physical weathering are quantitatively realized for different redox-sensitive detrital minerals.

We seek to obtain this upper bound on oxygen levels using redox-sensitive grain survival; therefore, we are interested in the time it takes for a given grain of pyrite or uraninite to become effectively undetectable in the sedimentary record as a function of  $O_2$  concentrations. We assign a critical grain diameter ( $D_{cr}$ ) set at 10  $\mu m$ —a size below which grains are too small to uniquely and routinely distinguish detrital from authigenic phases in a siltstone or shale. Setting  $D$  equal to  $D_{cr}$  in equation (6), dividing the equation by  $D_{cr}$  and rearranging results in:

$$R t / D_{cr} = \left( D_0 / D_{cr} \right) \exp(-x/x_0) - 1 \quad (7)$$

Equation (7) contains three important dimensionless parameters. The term on the left hand side of the equation represents the total amount of chemical weathering relative to the critical grain diameter, which we rename for convenience as:

$$r_c = R t / D_{cr} \quad (8)$$

The second dimensionless parameter is the initial sediment diameter as compared to the critical ‘undetectable’ size ( $D_o/D_{cr}$ ), and the third parameter is the total transport distance relative to a material-specific erodibility length constant ( $x/x_o$ ).

The erodibility length coefficient,  $x_o$ , is not well-known for pyrite and uraninite. Measurements of  $x_o$  have produced variable results depending on experimental design. One study found that for 0-128 mm sieved river sediments, the erodibility coefficient varied from 50 to 333 km using abrasion experiments (Mikoš, 1995). Another experimental investigation using slightly weathered chert grains measured a larger range of erodibility coefficients, from 8 km to 794 km (Kodama, 1994). However, a study of rivers in Canada determined that many laboratory abrasion experiments underestimate the erodibility coefficient, finding that quartzite, limestone, and granitic sediments varied from 333 km to 925 km (Shaw and Kellerhals, 1982). These workers suggested that because coarse grains are often “at rest”, the estimates of abrasion from laboratory abrasion mills predict too small  $x_o$  (Shaw and Kellerhals, 1982). Earlier laboratory studies using less vigorous abrasion techniques determined erodibility coefficients for chert of ~1000 km to 10,000 km (see Kodama, 1994 for a compilation). Indeed, sediments at the deltas of long continental-scale rivers such as the 6650 km Nile River would indicate that the erodibility coefficient of these sediments is greater than a few hundred kilometers, or that fluxes of new large grains enter the river to replenish the comminuted sediment (e.g., Sklar et al., 2006). In addition to material properties,  $x_o$  might also depend on the mode of transport (e.g., bedload versus suspended load) and particle size. For example, particle-

bed impacts are viscously damped for small particles with low impact velocities. Using a Stokes number threshold of 30 for viscously damped impacts (Schmeeckle et al., 2001; Joseph and Hunt, 2004), we find that particle-bed impacts from dense pyrite and uraninite grains can be damped for diameters finer than fine- to very-fine sand when falling in still water, thereby effectively increasing  $x_0$ . However, particle velocities can increase substantially in turbulent flow due to suspension (e.g., (Lamb et al., 2008)), so that even silt-sized grains still erode depending on the transport mode. No estimates of the erodibility coefficient of pyrite or uraninite have been measured, but the relatively similar Moh's hardness for quartz (7), uraninite (5-6), and pyrite (6.5) suggests similar erodibility coefficients. To keep our analysis tractable for analyzing ancient rocks, we employ a constant  $x_0$  of 1000 km for both pyrite and uraninite for comparison when dimensionalizing equation (7). Note that while we will discuss the dimensionless parameter  $x/x_0$  as increasing by distance traveled, the term can also be thought of as increasing with more erodible material or more energetic grain-to-bed impacts (i.e., smaller  $x_0$ ).

To determine a set of practical  $r_c$  values, we used physical constraints on the initial grain sizes and final distances traveled. We chose a range of reasonable initial grain sizes, varying from  $D_0 = 5$  mm (e.g., from an igneous source) to  $D_0 = 20$   $\mu\text{m}$  similar to a disseminated sedimentary pyrite source. We later input conservative  $r_c$  values for  $D_0$  up to 5 mm for pyrite grains as these are often found in Archean conglomerates at 1-2 mm (England, 2002) but used a maximum of 1 mm for uraninite grains, which are commonly

observed to be smaller in conglomerates, maximally ca. 100  $\mu\text{m}$  (England et al., 2001). Dividing by  $D_{\text{cr}}$  (10  $\mu\text{m}$ ), the parameter  $D_0/D_{\text{cr}}$  therefore varies from 1 to 500. Total travel distances were set to range from 10 to 10,000 km, encompassing short-transport systems such as Malibu Creek, CA (22 km) to long continental rivers such as the Mississippi River (3734 km) and the Nile River (6650 km). When divided by an  $x_0$  of 1000 km, the  $x/x_0$  parameter has a range of 0.01 to 10. Under these transport conditions, spanning reasonable ranges in initial sizes and total travel distances,  $r_c$  values were calculated to show the ranges and relationships between these variables in equation (7) (Fig. 7A). Note that choosing a different erodibility coefficient ( $x_0$ ) simply shifts the solution space either right or left, but the range of  $r_c$  needed to fill the parameter space remains similar.

Figure 7A shows that for  $x/x_0$  less than  $\sim 0.1$  (i.e., transport distances less than 100 km with  $x_0 = 1000$  km), only the initial grain size  $D_0$  is relevant for determining the erosion rate. Chemical erosion dominates this domain:  $r_c$  is essentially constant for a given  $D_0$  and there is no relationship between amount of chemical erosion and relative travel distance or  $x/x_0$ . This solution space encompasses previous work on the chemical erosion rates of redox-sensitive detrital grains where physical erosion was neglected. Such high rates of chemical erosion consequently require higher levels of  $\text{O}_2$ .

As  $x/x_0$  increases from mid-length streams (like the Hudson River, 507 km) to transcontinental rivers (like the Mississippi River, 3734 km), physical erosion becomes more important (Fig. 7A). At these large transport distances, the initial grain size



becomes less determinate and distance traveled is a larger factor in grain survival. Lines of low  $r_c$  at large total travel distances (large  $x/x_0$ ) represent extensive river systems with grains abrading under low chemical erosion. This is likely the case for grains preserved in the proximal part of the basin during deposition of the Koegas Subgroup, which likely traversed much of the Kaapvaal craton (Sumner and Beukes, 2006; Schröder et al., 2011). For these larger river systems, Figure 7A illustrates that chemical erosion and physical abrasion are both important factors in grain survival.

To help conceptualize the factors that affect the relative chemical erosion ( $r_c$ ), we produced two plots showing  $r_c$  when one parameter (either the relative initial grain size or the relative distance) is held constant. The solution shown in Figure 7B, and in Figure 7A as a dashed line marked “(B)”, demonstrates how the portion of chemical erosion changes with increasing distance for a set grain size (in this case, a diameter of 1 mm). At short distances, a large amount of chemical erosion is required to erode the 1 mm grain to the critical diameter of 10  $\mu\text{m}$ —implying that a high level of oxygen is also required to generate this high degree of chemical erosion. At longer distances, however, physical abrasion increases and relative chemical erosion decreases, resulting in lower and lower  $r_c$  values. At around 4500 km, physical abrasion erodes nearly all of the grain, and thus no chemical erosion is needed to explain the absence of grains larger than 10  $\mu\text{m}$ . At larger distances (shaded in grey), physical abrasion is so strong that 1 mm grains would not have survived to these distances at a size above our detectable limit of 10  $\mu\text{m}$ .

Figure 7C, shown in Figure 7A as a dashed line marked “(C)”, illustrates the grain size control under a set travel distance of 1000 km. Grains beginning at diameters of  $\sim 30\ \mu\text{m}$  or smaller would no longer exist after 1000 km of travel. Particles starting at  $\sim 100\ \mu\text{m}$  or smaller would require very little chemical erosion as physical abrasion would cause most of the grain destruction, although viscous damping may reduce physical abrasion rates for these small sediment sizes depending on the transport mode. As the initial grain size increases, the relative amount of chemical erosion necessary for grain destruction also increases, and large grains several millimeters in diameter would require a large degree of chemical erosion to be destroyed by 1000 km of travel.

Because the relative amount of chemical erosion,  $r_c$ , is environmentally controlled, estimates of the ancient  $r_c$  for specific deposits can be informed by the sedimentary context of the redox-sensitive grains. Observable differences in grain sizes, chemistry, provenance, sedimentary structures, basin size, and sequence stratigraphy can be applied to inform transport conditions (distances and times) and thus  $\text{O}_2$  constraints. Armed with estimates of the transport conditions, one can estimate an appropriate range of  $r_c$  values for a given sedimentary deposit bearing detrital pyrite or uraninite grains.

As  $r_c$  is a function of the oxygen-dependent chemical erosion for both pyrite and uraninite, the dissolved oxygen (*DO*) content of weathering fluids (river water, ground water, pore fluids in soils and sediments, and seawater) can be constrained using both the uraninite and pyrite erosion equations, yielding predictions of  $\text{O}_2$  (in atm) from both

minerals, assuming gas exchange equilibrium. We input  $r_c$  values previously determined using reasonable but conservative ranges of  $D_0/D_{cr}$  and  $x/x_0$  (Fig. 7A). We used a range of 0 to 300 for pyrite, as it commonly has larger initial grain sizes, and 0 to 150 for uraninite. We solved Eqn. 8 for  $O_2$ , using the appropriate rate laws for pyrite and uraninite (Eqn. 3, Eqn. 4), inputting a typical riverine pH of 6, modern  $CO_2$  values (Fig. 8A) and a mid-range paleo- $CO_2$  estimate of 0.1 atm (see previous discussion, Fig. 8B). These functions denote oxygen concentrations required for grain erosion to 10  $\mu m$  ( $D_{cr}$ ) for a given amount of time (Fig. 8). A model calculation for current day conditions has modern oxygen levels marked, indicating where pyrite and uraninite grains would be stable under today's atmosphere (Fig. 8A). According to these estimates both pyrite and uraninite appear to be stable (as long as the initial grains are large enough) for about 10,000 years under today's atmosphere. Modeling ancient atmospheric conditions shifted the uraninite destruction field considerably but did not alter the  $O_2$  requirements for pyrite grain destruction, because of the  $CO_2$  dependence of uraninite dissolution (Fig. 8B; Eqn. 3). Changing the pH of weathering fluids to 5 causes estimates based on pyrite to vary imperceptibly while this change decreases the uraninite upper bounds by approximately an order of magnitude. At pH = 7, pyrite constraints on  $O_2$  similarly do not significantly change but uraninite  $O_2$  constraints are relaxed by a factor of ten, increasing the maximum oxygen levels that are allowed by the preservation of detrital uraninite grains.

Because the  $O_2$  estimates indicate the oxygen levels where pyrite and uraninite should be undetectable, these calculated levels can be used as the maximum oxygen levels at which pyrite and/or uraninite will still survive and be recognizable detrital components of a clastic sedimentary rock. The  $O_2$  constraint estimates are shown for a range of solutions that account for the diversity of environments and transport regimes affecting sediment supply and physical erosion (i.e., ranges of expected  $D_0$  and  $x$ ). The time allowed for grain destruction is also a corollary of different paleoenvironments and deposit types, as these relate to travel time. The ranges marked with  $r_c$  values show the influence of physical conditions, such as initial grain size and total distance traveled, with higher  $r_c$  corresponding to a higher degree of chemical erosion and lower  $r_c$  representing lower proportion of chemical erosion. Higher  $r_c$  would be anticipated for rivers with low total travel distance and larger initial grain sizes like proglacial or coastal mountain streams (left side of Fig. 8B marked “Short Rivers”). Lower  $r_c$  represents a lower proportion of chemical erosion and more physical erosion, with smaller saltating grains and larger total travel distances like in large continental river and delta systems (right side of Fig. 8B marked “Long Rivers”). Figure 7A suggests that the highest levels of chemical erosion would not allow pyrite and uraninite grains to still be present at long distances. Thus, longer continental rivers such as the Mississippi can only have  $r_c$  values up to  $\sim 5$  (Fig. 7A). Consequently, in our longer river estimates, we conservatively constrain  $r_c$  to be 50 or less.

We can also add time constraints on different river system types using recent work applying U-series disequilibrium techniques to measuring sediment transport times. Transport time starts when the grains are first excised from their source bedrock, and integrates both the time the sediments spend being transported and their temporary storage on hillslopes and in floodplains, on the riverbed and in fluvial bedforms (like bars). As U and Th have different mobility and are consequently fractionated during initial weathering from bedrock in secular equilibrium (i.e., a closed system for > 1 million years), the degree to which this isotope decay series is in disequilibrium can be inverted to calculate the time since initial removal from source bedrock (Chabaux et al., 2003; DePaolo et al., 2006; Dosseto et al., 2008). This technique has been applied to both the suspended load and bedload of several rivers. In mountain streams, cobbles and boulders are typically in bedload, and consequently they have longer transport times than the suspended and dissolved load. The <5 mm pyrite and <1 mm uraninite mineral grains would be in the suspended load in such systems. Measurements in short rivers have ranged from mountain streams in the Andes to Icelandic glacial streams, where the suspended sediment load transport time has been measured at 3 to 4 kyr in the ~200km Andes tributaries (Dosseto et al., 2006) and 1 to 10 kyr in short Icelandic rivers (~40-200 km) (Vigier et al., 2006). In a different type of measurement, Lauer and Parker (2008) modeled a tracer from mining contamination to estimate the transport of clay and silt (the suspended load) of the upper ~70 km of the Clark Fork River would take thousands of years (Lauer and Parker, 2008). We therefore posit that mountain, glacial, and shorter rivers (1000km or less) will have total transport times of 1000 to 10,000 years, and add a

label to Figure 8 for 'Short Rivers' to constrain the oxygen levels from finding detrital uraninite and pyrite from these river systems.

Larger rivers with broad floodplains have much longer grain transport times (e.g., Bradley and Tucker, 2013), and this distance-time relationship is enhanced by the transport mode. In rivers such as the Mississippi or Nile, sandy bedforms indicate that sand-sized particles travel in bedload and silt-sized grains are typically in suspension. Figure 7A indicates that at these long distances all preserved grains likely started  $>500\ \mu\text{m}$  in diameter. These grains probably started out in hillslopes, first weathering from bedrock, and then were transported in mountain streams as suspended load, and finally as bedload in larger rivers. Only a few studies have examined the bedload transport time using the U-series method. For example, Granet et al. (2010) determined that the transport time from the Himalayas to the Ganges delta in Bengal (Manihari, India) was  $>300\ \text{kyr}$  for bedload grains to move  $\sim 2200\ \text{km}$ . They also studied the bedload of Himalayan feeder streams (650-1000 km) and estimated that transport time from the source bedrock to the confluence with the main Ganges river was  $\sim 100\ \text{kyr}$  (Granet et al., 2007). These are significantly longer than estimates for the suspended sediment load, where only 20-25 kyr was measured for these shorter Himalayan feeder streams (Granet et al., 2010). Another study found a similarly short transport time (10 to 28 kyr) for the suspended sediments of the  $\sim 1700\ \text{km}$  Mackenzie River in Canada (Vigier et al., 2001); however, the authors noted that erosion in this river system was affected by recent glaciations. Dosseto et al. (2006) observed that in Amazon lowland rivers, the suspended

load took 100 to 500 kyr to travel 760 km to several thousand km. We therefore suggest that for long,  $> 1000$  km river systems, total sediment transport time ranges from 100 to 500 kyr. While the U-series approach is still being refined (e.g., see Lee et al., 2010; Handley et al., 2013), we applied these estimates of bedload transport time (i.e., 1 kyr to 10 kyr for short river systems and 100 kyr to 500 kyr for long river systems) to compare depositional environments (Fig. 8).

With these timing constraints of river sediment transport and our estimates of  $r_c$ , we can place upper boundaries on ancient oxygen levels. Short rivers, such as mountain or glacial streams, show some pyrite being stable up to  $O_2$  concentrations of 40 atm, or  $\sim 190$  times the oxygen content of the modern atmosphere. Finding detrital uraninite in ancient mountain (cobble-bedded) rivers, however, constrains the atmospheric oxygen levels to a maximum of  $10^{-2}$  atm. Longer river systems with small initial grains and long transport distances, like the Amazon or Mississippi rivers, constrain  $O_2$  to much lower levels. The presence of both pyrite and uraninite in these systems implies an upper limit of ancient  $O_2$  on the order of  $1 \cdot 10^{-5}$  or  $1 \cdot 10^{-6}$  atm, with all pyrite being destroyed before  $1 \cdot 10^{-4}$  atm and uraninite no longer preserved at  $3.2 \cdot 10^{-5}$  atm. Thus, if grain provenance and/or travel distance for an ancient river system can be determined, the presence of redox-sensitive detrital grains can provide powerful redox constraints.

For our study area, the deltaic sediments of the Koegas Subgroup, our model provides a mechanism to determine an upper bound on the paleo-oxygen levels. For a craton-scale

sediment transport system (ca. 1000 km, our best estimate for Koegas provenance), we can use the estimates at ~100,000 years to predict a maximal oxygen level of  $3.2 \times 10^{-5}$  atm at 2.415 billion years ago. This estimate is an upper limit for the largest pyrite and uraninite grains to be preserved: for all pyrite and uraninite particles to be preserved, oxygen levels can be constrained to more like  $1 \times 10^{-7}$  atm. As we do not observe reaction rims suggestive of chemical erosion, this lower estimate may be a more appropriate upper bound for Earth surface  $O_2$  levels at this time.

## DISCUSSION AND CONCLUSIONS

Detrital uraninite and pyrite have long been recognized and interpreted as a robust but qualitative measure of low  $O_2$  levels on the early Earth. In the context of our combined chemical and physical erosion framework, the preservation of these grains in Archean and early Paleoproterozoic siliciclastic sedimentary rocks (like those in the Koegas Subgroup) can be viewed through a more quantitative lens. We examined the plausible range of  $O_2$  values necessary to erode (to a critical diameter set at 10  $\mu\text{m}$ ) pyrite and uraninite grains under different environmental and transport conditions (Fig. 6). The minimum  $O_2$  levels to cause pyrite and uraninite destruction thus become maximum oxygen concentrations for these detrital grains to be preserved, and these values constrain the  $O_2$  levels of Archean and early Paleoproterozoic Earth surface environments.

Due to differences in their oxidative weathering kinetics, the erosion rates of pyrite and uraninite—and consequently the maximum  $O_2$  constraints generated from their



preservation in sedimentary successions—have different sensitivities to  $O_2$  under various physical transport scenarios. These calculations predict that in modern short-transport systems, one might find detrital pyrite and uraninite present if they began as very large grains and if both were present in the source protolith (Fig. 8A). This prediction is consistent with our modern observations: we only occasionally find detrital pyrite and uraninite, in areas with rapid erosion and transport or high aridity (Holland, 1984). Indeed, pyrite and uraninite are known from some high-gradient alpine streams (Simpson and Bowles, 1977, 1981; Maynard et al., 1991). Yet this pyrite is being actively oxidatively weathered during transport in our current atmosphere and these grains do not survive into terminal deposits. Clearly by the end of even short rivers, even the largest initial pyrite and uraninite grains do not survive (Fig. 8A).

Our model is, however, limited by the accuracy of the chemical rate laws. Ono (2001) examined the Grandstaff chemical erosion relationship and found that some of the parameters, such as the factored dependence on oxygen, proton, and bicarbonate concentrations and his use of a geometric surface area in his calculations, may not be accurate or under certain conditions appropriate (Ono, 2001). This highlights the value of further experimental studies examining the controls on the oxidation of natural uraninite by  $O_2$ . Nevertheless, the ability to observe the weathering behavior of these two different minerals in systems—particularly with independent information from observations of the sedimentary geology about transport processes, distances, and provenance (such as in Hofmann et al., 2009)—provides more precise  $O_2$  constraints. An understanding of the

ancient basin geology and process sedimentology can indicate the paleo-river parameters, enabling a determination of river length and initial grain size. Knowing these river specifications, our model framework facilitates an understanding of ancient O<sub>2</sub> levels at the time of fluvial or marine deposition. These predictions can be applied in the context of Archean or Paleoproterozoic river systems, where the presence of redox-sensitive detrital grains in deposits provides an estimate of maximal O<sub>2</sub> in the atmosphere, or for later post-rise of oxygen successions from which the absence of these grains provides a lower bound on O<sub>2</sub> concentrations. For example, observing detrital pyrite grains in short-traveled conglomerates provides a less strict constraint on ancient O<sub>2</sub> levels. For the most part, these active systems are less likely to be preserved in the geological record over long timescales. Locally-sourced fluvial deposits associated with small isolated basins (ca. 100km<sup>2</sup>) during early phases of rifting, or glacial deposits (e.g., Williford et al., 2011) with a limited amount of transport and without any knowledge of the initial grain size, would be examples of systems with short travel distances. The presence of pyrite grains in these rapid transport systems does not constrain the O<sub>2</sub> to any lower than today, while the discovery of uraninite in these systems does constrain paleo-oxygen levels to at most 0.01 atm (Fig. 8A).

Redox-sensitive detrital grains observed in sedimentary rocks deposited at the termini of larger riverine systems—including the detrital pyrite and uraninite in the 2.415 Ga Koegas Subgroup deltaic deposits described here—constrain the O<sub>2</sub> concentrations to a much better extent because they offer a greater window of time for chemical erosion to

manifest even at exceedingly low O<sub>2</sub> concentrations. In the 100,000 to 500,000 year time span of large ancient rivers similar to the Amazon lowland and Ganges rivers (Granet et al., 2007; Dosseto et al., 2008), pyrite and uraninite both constrain the maximum O<sub>2</sub> levels to be  $1 \times 10^{-4}$  and  $3.2 \times 10^{-5}$  atm, respectively (Fig. 8B). A constraint of  $3.2 \times 10^{-5}$  atm effectively means environmental fluids in contact with these pyrite and uraninite grains had dissolved oxygen concentrations less than ~40 nM—perhaps substantially less. These are upper estimates, made purposefully conservative. In addition to modeling physical and chemical erosion processes separately rather than (more realistically) coupled, we have also only considered the chemical erosion of pyrite and uraninite by O<sub>2</sub> from abiotic oxidation rates and defect-free grains. This approach provides very conservative estimates for O<sub>2</sub>, as much faster kinetics are expected by biological oxidation processes (e.g. Konhauser et al., 2011) and naturally-occurring pyrite and uraninite (Anbar et al., 2007; Reinhard et al., 2009).

The O<sub>2</sub> constraints from redox-sensitive detrital grains can be used to reflect on the interpretations made from other redox proxies. Though the nature and origin of mass anomalous sulfur isotope fractionations are not well-understood, our results support estimates from photochemical models that suggest this isotopic proxy is sensitive to very low O<sub>2</sub> levels (Pavlov and Kasting, 2002; Zahnle et al., 2006; Zerkle et al., 2012). In addition, widespread observations of redox-sensitive detrital grains provide an integrated first-order view of the lack of oxidative weathering processes across a range of environments on early Earth—from hillslopes to river channels, floodplains, and

nearshore marine environments. Though in our model framework some amounts of chemical erosion of grains can be permitted under certain transport scenarios (i.e., large initial size and low transport distance; Fig. 8), it is intriguing to wonder how much oxidative surface weathering did indeed occur during Archean and early Proterozoic time. A number of authors have proposed substantial amounts of pyrite weathering, yet the presence of well-preserved and rounded detrital pyrite grains throughout this interval without evidence for chemical erosion conflicts with these hypotheses (Anbar et al., 2007; Kaufman et al., 2007; Reinhard et al., 2009). Lastly, our observations imply the rise of oxygen is younger than 2.415 Ga, and is consistent with a wide range of results from sulfur isotope studies of Kaapvaal Craton strata (Bekker et al., 2004; Guo et al., 2009; Ono et al. 2009a; 2009b; Johnson et al. 2013).

The chemical erosion rate laws of pyrite and uraninite (equations 1 and 2) are directly responsible for differences in their weathering behavior and paleo-O<sub>2</sub> estimates from our calculations (Fig. 8). Despite the potential uncertainty with current understanding of the uraninite chemical erosion rate law (Ono, 2001), it is reasonable to think that these mineral phases will behave differently during oxidative weathering as a function of environmental O<sub>2</sub> concentrations. This forms the logic for an approach to identify intervals in Earth history wherein the atmosphere contained intermediate O<sub>2</sub> concentrations (e.g., levels that destroy uraninite but preserve pyrite in short-traveled fluvial systems). Systematic studies of the behavior of redox-sensitive detrital grains in Proterozoic-age siliciclastic successions would be valuable to test ideas of intermediate

oxygen concentrations following the initial rise of oxygen. It is important to note, however, that our current database of deposits shows uraninite and pyrite disappearing at about the same time from Canada (Pienaar, 1963; Robinson and Spooner, 1982; Krogh et al., 1984; Prasad and Roscoe, 1996), Brazil (Figueiredo, 1989), and South Africa (Johnson et al., 2013). The O<sub>2</sub> sensitivity and binary nature of the secular distribution of redox-sensitive grains in siliciclastic deposits suggests that the initial rise of oxygen was very substantial and oxygen levels never again dropped low enough to allow significant amounts of transport and preservation of either of these grains in either short- or long-traveled Earth surface weathering systems.

## **ACKNOWLEDGEMENTS**

We would like to thank Grayson Chadwick for assistance with derivations and programming, as well as Chi Ma for support on the E-probe and SEM, and we are grateful to Chris Reinhard, Joel Scheingross, and two anonymous reviewers for feedback on the manuscript. We thank the Caltech Summer Undergraduate Research Fellowships (SURF) program, which co-sponsored A.G. to work on this project. J.E.J. acknowledges support from the NSF Graduate Research Fellowship program and W.W.F. acknowledges funding from the David and Lucile Packard Foundation. M.P.L. acknowledges support from NSF grant OCE-1233685, and the donors of the America Chemical Society Petroleum Research Fund. We thank the Agouron Institute for support of the South African Drilling Project.

FIGURES AND TABLES

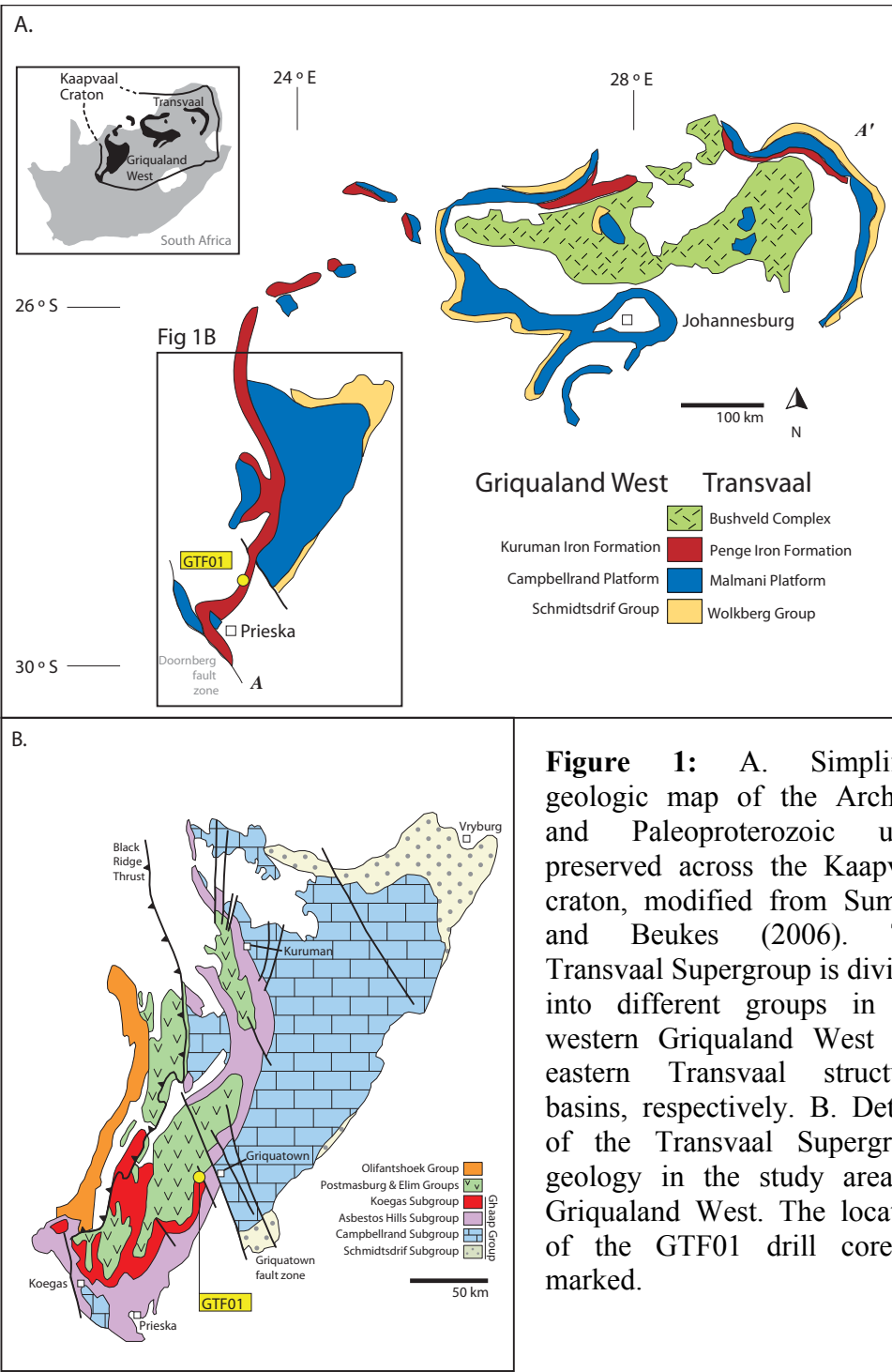


**Figure 1:** A. Simplified geologic map of the Archean and Paleoproterozoic units preserved across the Kaapvaal craton, modified from Sumner and Beukes (2006). The Transvaal Supergroup is divided into different groups in the western Griqualand West and eastern Transvaal structural basins, respectively. B. Details of the Transvaal Supergroup geology in the study area of Griqualand West. The location of the GTF01 drill core is marked.

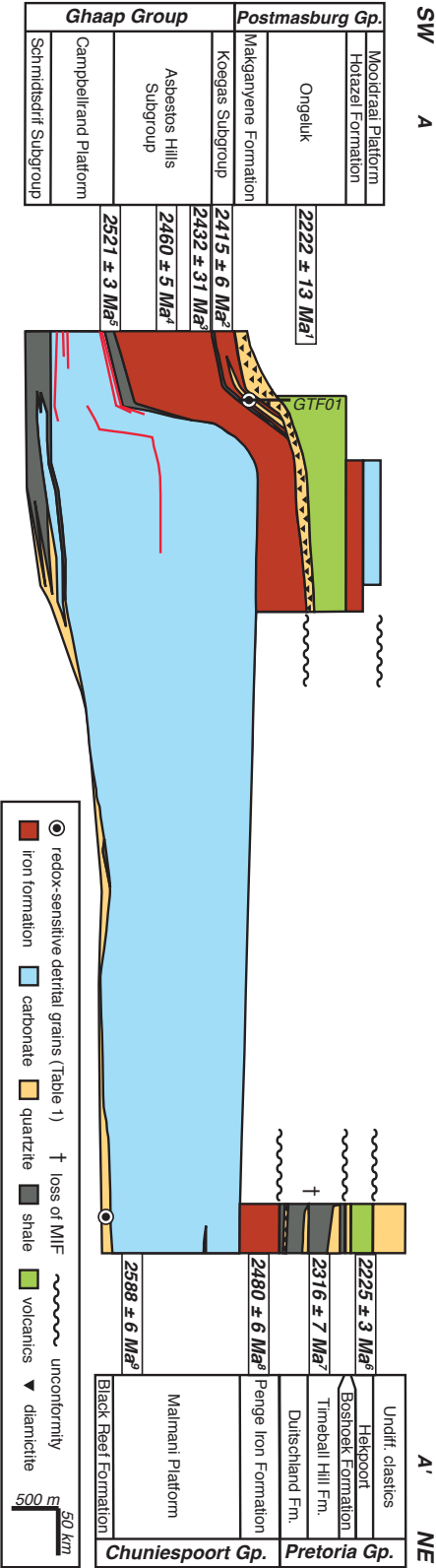


**Figure 2:** Stratigraphic cross section of the Transvaal Supergroup across the Kaapvaal craton from A to A' (see Fig. 1) based on stratigraphic data from Sumner and Beukes (2006). Key geochronologic constraints are shown from: 1. (Cornell et al., 1996) 2. (Gutzmer, Jens and Beukes, Nicolas, 1998) 3. (Trendall et al., 1990) 4. (Pickard, 2003) 5. (Sumner and Bowring, 1996) 6. (Yang and Holland, 2003) 7. (Hannah et al., 2004) 8. (Nelson et al., 1999) 9. (Martin et al., 1998). Also marked are redox constraints from mass-independent fractionation of sulfur isotopes (Bekker et al., 2004; Guo et al., 2009), detrital pyrite and uraninite (England et al., 2002; Hofmann et al., 2009; Johnson et al., 2013), and Mn deposits (Tsikos et al., 2003; Johnson et al., 2013).

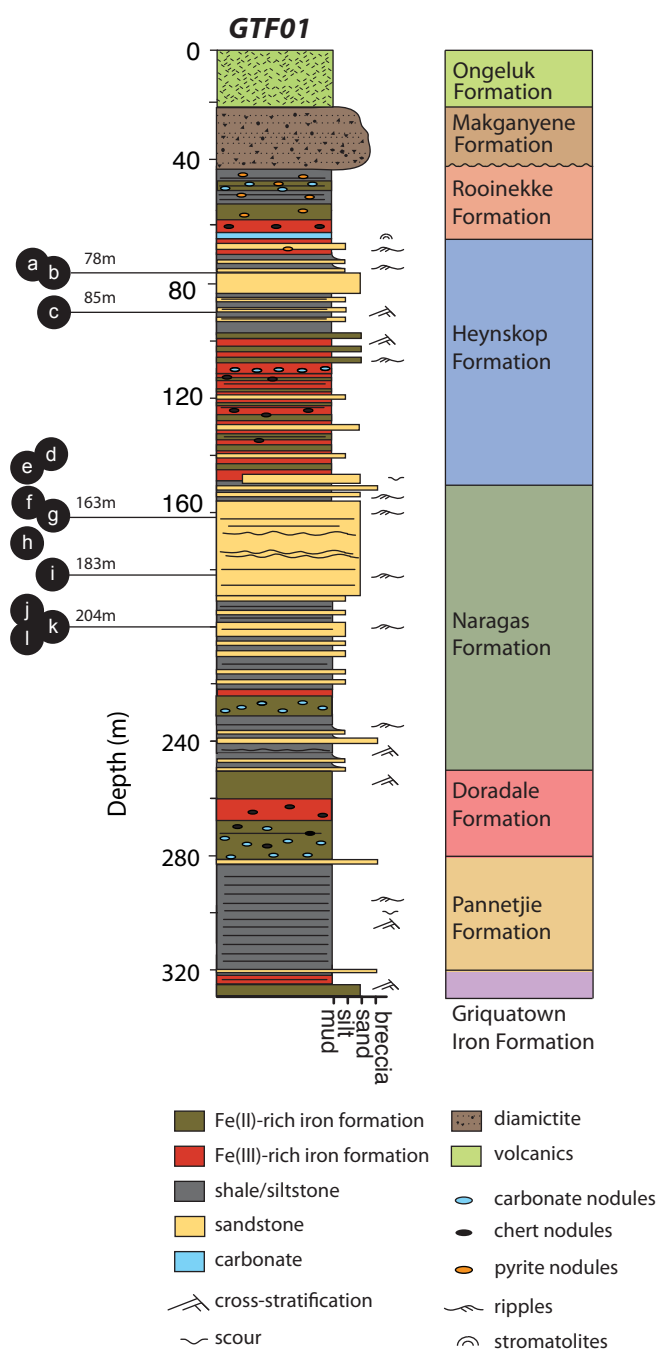


**Figure 3:** Stratigraphic section of GTF01 indicating formations and locations of redox-sensitive detrital grains photographed in Fig. 6.



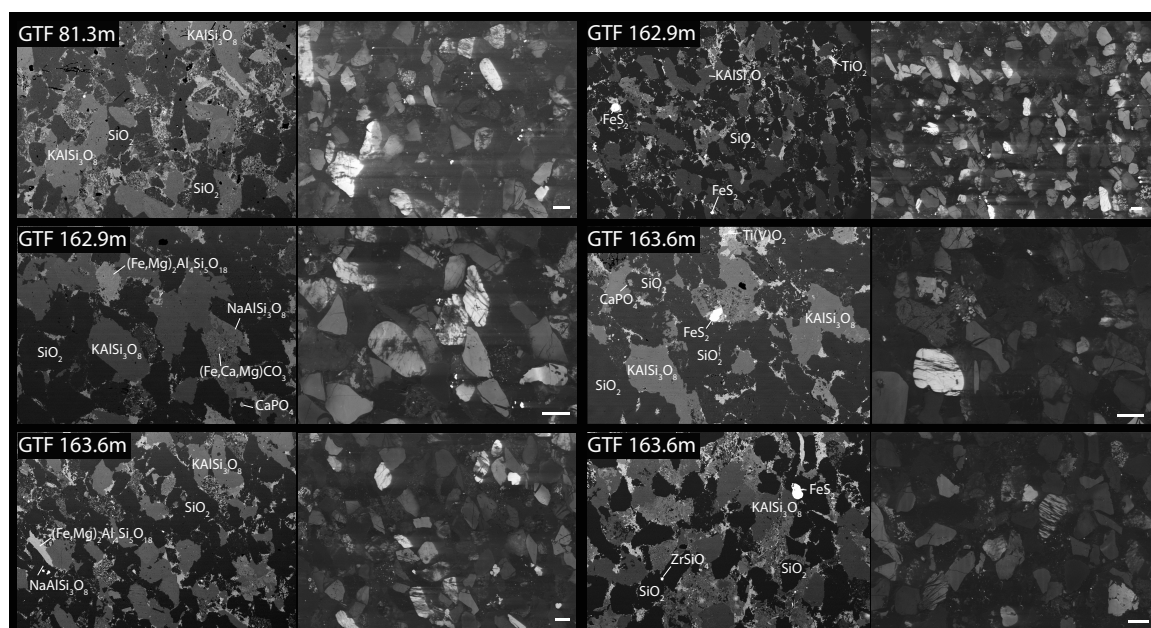


**Figure 4:** Sandstone textures from electron microscopy. Left panels show backscatter electron photomicrographs with detrital quartz, feldspar, and pyrite grains. Right panels depict the same view using variable pressure secondary electron images, highlighting via cathodoluminescence (CL) the rounding and truncation of quartz and feldspar zonation caused by physical abrasion. Scale bars are 100  $\mu\text{m}$ .

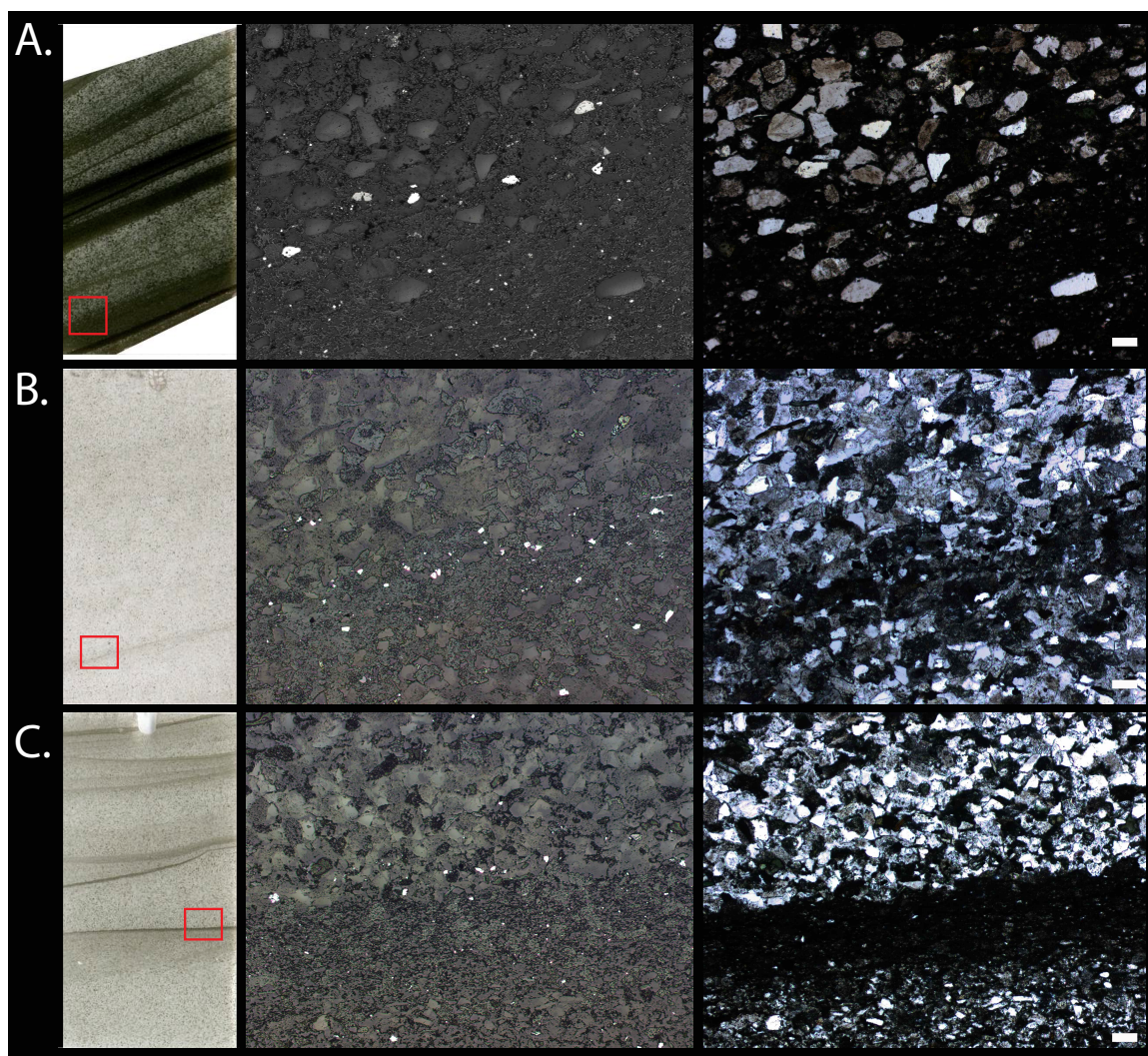


**Figure 5:** Pyrite distributions along ripple foreset laminae. A. GTF 78.75m, B. GTF 178.45m, C. GTF 182m, all showing (left to right) thin section image with target area marked in red, reflected light photograph of area indicating pyrite as bright white grains, and transmitted light photograph of same region. Scale bars are 100  $\mu\text{m}$ .

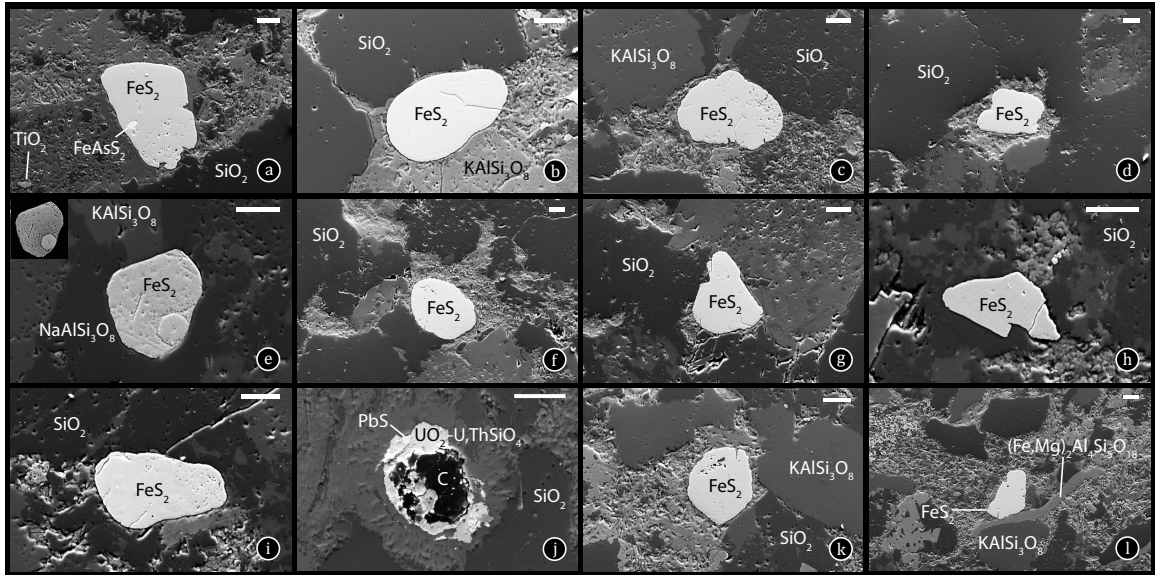
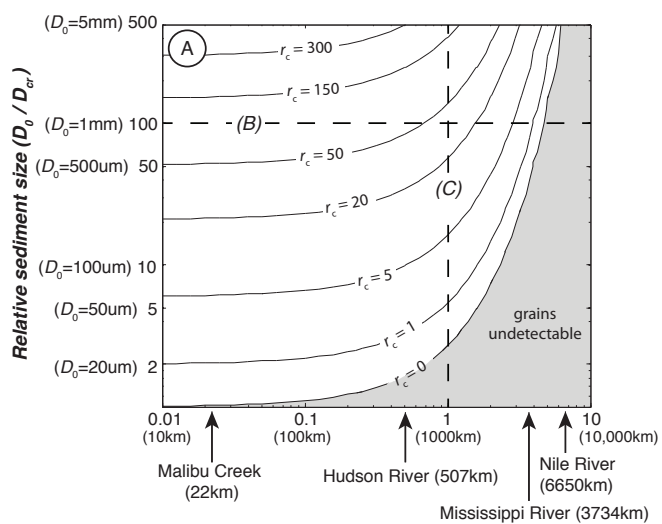


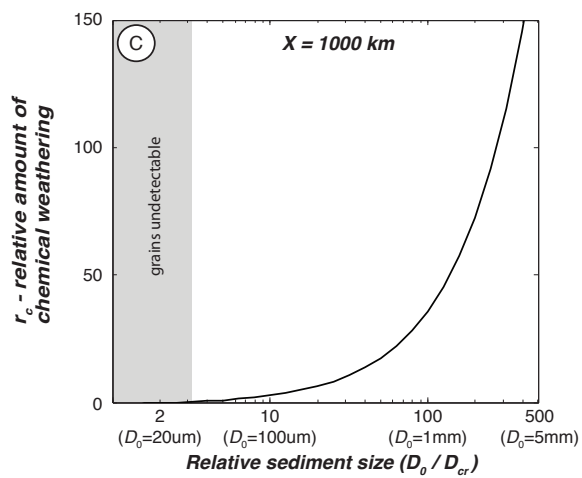
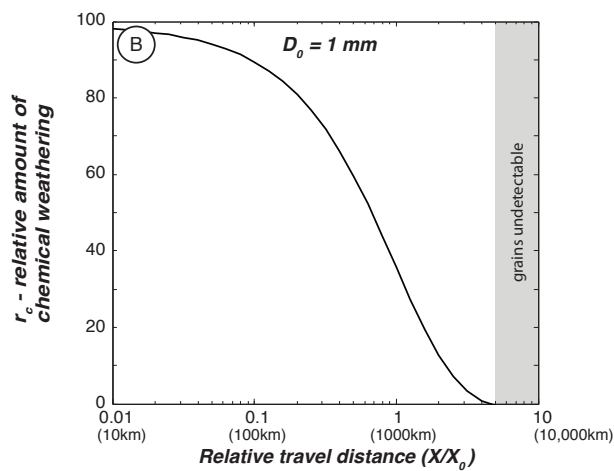
**Figure 6:** Backscatter electron photomicrographs showing examples of detrital pyrite and detrital uraninite found throughout thin sections of sandstones sampled from drill core. Letters correspond to specific stratigraphic samples shown in Fig. 3. Note inset of the pyrite grain in (e) with compositional differences and truncated internal zonation highlighted by high contrast. A detrital uraninite grain shown in (j) is now composed of uraninite-uranothorite with galena and bitumen inclusions due to radioactive decay (see text for details). Scale bars are 20  $\mu\text{m}$ .

**Figure 7 (below):** A) Contours of the relative amount of chemical weathering ( $r_c$ ) as a function of initial relative sediment diameter and relative grain travel distance for the parameter space realistic for Earth surface environments. Examples of initial sediment diameters ( $D_0$ ) and river systems (with different lengths:  $x$ ) are listed for comparison, assuming a critical sediment size for detection of  $D_{cr} = 10 \mu\text{m}$  and an erodibility coefficient of  $x_0 = 1000 \text{ km}$ . Dashed lines marked “(B)” and “(C)” denote slices through solution space plotted in panels (B) and (C). B) Relative amount of chemical weathering ( $r_c$ ) as a function of the relative distance traveled ( $x/x_0$ ) of a grain with fixed relative initial size of  $D_0 = 10 \mu\text{m}$ . C) Relative amount of chemical weathering ( $r_c$ ) as a function of relative initial sediment size ( $D_0/D_{cr}$ ) for a fixed relative travel distance ( $x = 1000 \text{ km}$ ). The shaded zones in all three panels are regions of parameter space where all grains are predicted to be smaller than the detection limit (i.e.,  $D < D_{cr}$ ).

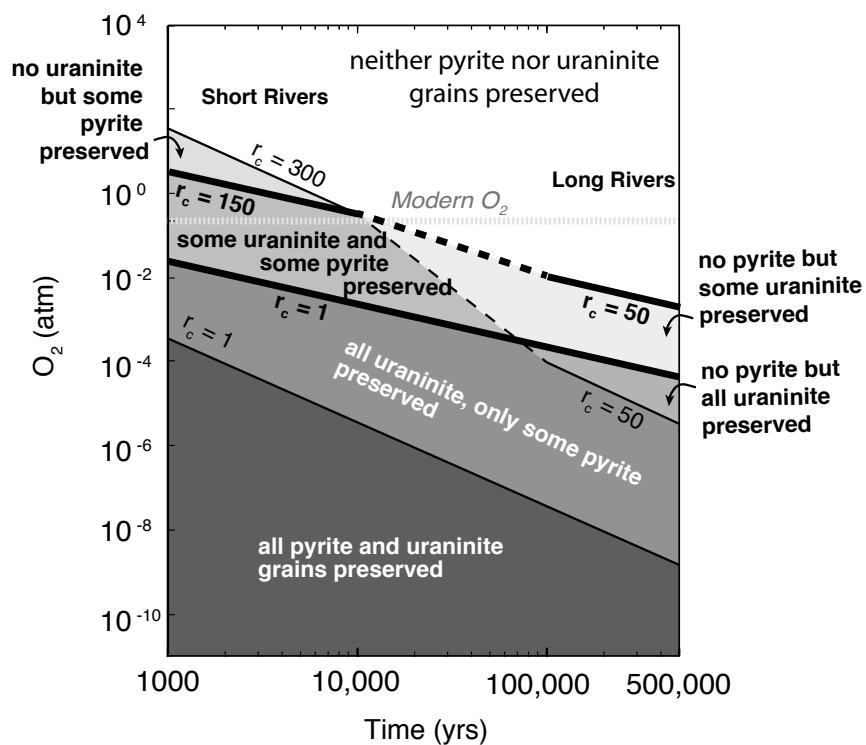




**Relative travel distance ( $X/X_0$ )**  
 increasing distance ( $x$ ),  $x_0 = 1000\text{km}$  →  
 ← increasing material strength ( $x_0$ )



A. Modern conditions;  $p\text{CO}_2 = 280 \text{ ppm}$



B. Archean and Paleoproterozoic conditions;  $p\text{CO}_2 = 0.1 \text{ atm}$

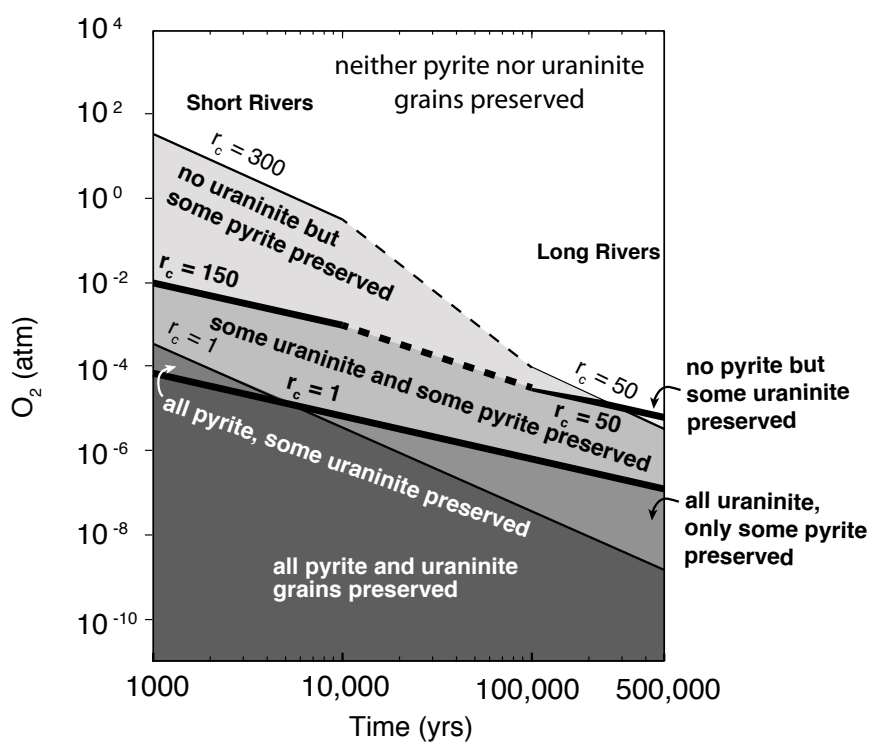


**Figure 8:** Upper bounds on environmental  $O_2$  levels calculated for pyrite and uraninite preservation and destruction for the modern and Paleoproterozoic-Archean environment. The bounding values of relative chemical weathering in short river systems for pyrite ( $1 < r_c < 300$ ; thin black lines) and uraninite ( $1 < r_c < 150$ ; thick black lines) and long river systems for pyrite ( $1 < r_c < 50$ ; thin black lines) and uraninite ( $1 < r_c < 50$ ; thick black lines) come from the full range of environmental conditions explored in Figure 7A (see text for discussion), which incorporate a wide range of reasonable physical grain erosion rates and initial grain sizes. Dashed lines between the upper  $r_c$  estimates represent uncertainty as to when it is appropriate to change upper  $r_c$  bounds. Darkest grey area represents preservation of all pyrite and uraninite grains and white region represents no grain preservation, with intermediate shades of grey representing various scenarios of either pyrite or uraninite or both types of grains being only partially preserved. Labels for “Short Rivers” and “Long Rivers” from U-series disequilibria estimates (see text). A) Predicted levels of  $O_2$  required for grain preservation and destruction as a function of transport time under modern (pre-industrial)  $CO_2$  conditions. For modern  $O_2$  levels (horizontal dotted line in pale grey), the model predicts preservation of pyrite and uraninite (shaded regions) over only relatively short timescales and relatively large  $r_c$  values, corresponding to environments with large protolith grain sizes and short transport distances. B) Calculated concentrations of  $O_2$  for grain preservation and destruction as a function of transport time for a Paleoproterozoic or Archean environment with 0.1 atm of  $CO_2$ . Upper estimates on paleo-oxygen levels can be determined if reasonable knowledge of paleo-river distance and/or initial grain sizes are known.

TABLE 1. REPORTED OCCURRENCES OF REDOX-SENSITIVE DETRITAL GRAINS

Age (Ga)	Redox-sensitive grains	Rock environment and type	Stratigraphy	Reference
ca. 3.25	Pyrite, uraninite	Fluviodeltaic sandstones and conglomerates	Mosquito Creek Formation, Australia	Rasmussen and Buick (1999)
3.2–3.0	Pyrite, uraninite	Braided stream fluvial plain conglomerate	Bababudan Group, Dharwar Craton, South India	Srinivasan and Ojakangas (1986); Janardhan and Basavalingu (1988)
ca. 3.08	Pyrite, uraninite	Fluvial pebble conglomerate	Rhenosterspruit Formation, Dominion Group, South Africa	Hofmann et al. (2009); Simpson and Bowles (1977); Hiemstra (1968)
ca. 3–2.95	Pyrite, siderite	Fluvial sandstones	Lalla Rookh Formation, Australia	Rasmussen and Buick (1999)
ca. 2.95	Pyrite	Sandstone, wackestone, diamictite	Coronation Formation, West Rand Group, South Africa	Guy et al. (2010)
ca. 2.95	Pyrite, uraninite?	Fluvial conglomerate to shallow marine sandstone	Mozaan Contact Reef, Mozaan Group, Pongola Supergroup, South Africa	Hofmann et al. (2009); Orberger et al. (2011); Hegner et al. (1994)
ca. 2.85	Pyrite, uraninite	Fluviodeltaic sandstones and conglomerates	Kimberley Reef, Central Rand Group, Witwatersrand Supergroup, South Africa	Kositcin and Krapez (2004); England et al. (2002); Hofmann et al. (2009)
2.77–2.715	Pyrite, uraninite, siderite	Braided river mature sandstones	Fortescue Group, Australia	Rasmussen and Buick (1999)
ca. 2.72	Pyrite, uraninite	Fluvial conglomerates interbedded with sandstones	Ventersport Formation, Ventersdorp Supergroup, South Africa	Krapez (1985); Hofmann et al. (2009)
ca. 2.64	Pyrite, uraninite	Fluvial fine-grained quartz and pebble conglomerate	Black Reef Quartzite Formation, South Africa	Barton and Hallbauer (1996); England et al. (2002); Walraven and Martini (1995); Gauert et al. (2011)
ca. 2.6	Pyrite	Marine turbidity current conglomerate, sandstone, shale deposits	Cheshire Formation, Belingwe greenstone belt, Zimbabwe	Hofmann et al. (2001, 2009)
2.58–2.42	Pyrite, uraninite	Fluvial conglomerates and coarse sandstones	Moeda Formation, Quadrilatero Ferrifero, Brazil	Villaca and Moura (1981); Minter et al. (1990); Hartmann et al. (2006)
2.66–2.1	Pyrite, uraninite	Fluviodeltaic conglomerates, sandstones, shales	Jacobina Group, Brazil	Figueiredo (1989)
ca. 2.45 (constrained 2.45–2.1 Ga)	Pyrite, uraninite	Conglomerates and sandstones, prograding alluvial fan(?) + deltaic deposits + fluvial cross-bedded quartz-pebble conglomerates	Rock Mountain Conglomerate, Bow Quartzite, Jack Hills Quartzite, Bridger Peak Quartzite, Sierra Madre and Medicine Bow Mountains, USA	Houston et al. (1992); Bekker et al. (2003)
2.45–2.22	Pyrite, uraninite	Fluviodeltaic conglomerates and sandstones	Matinenda Formation, Elliot Lake Group, Canada	Pienaar (1963); Robinson and Spooner (1982); Krogh et al. (1984); Prasad and Roscoe (1996)
ca. 2.415	Pyrite, uraninite	Deltaic sandstones	Naragas and Heynskop Formations, Koegas Subgroup, South Africa	Johnson et al. (2013); this study
2.42–2.22	Pyrite	Diamictite	Meteorite Bore Member, Kungarra Formation, Australia	Williford et al. (2011)

Note: Compiled from a variety of sources (see column 5). Approximate ages, redox-sensitive mineralogy, paleoenvironment and lithology, and stratigraphy from relevant reference are highlighted.

\*Questionable due to poor preservation.

**Table 1: Reported occurrences of redox-sensitive detrital grains.**

Sample	% pyrite	% zircon	% apatite + monazite	% zircon + apatite + monazite
GTF 77.53m	0.4091	0.0055	0.2297	0.2352
GTF 163.65m	0.0398	0.0055	0.17	0.1755
GTF 203.65m	0.2638	0.0083	0.2688	0.2771
GTF 243.00m	0.1341	0.00075	0.2236	0.22435

**Table 2: Abundances of detrital grains by mineralogy. Estimated using elemental abundance maps of S, Zr, and P as proxies for pyrite, zircon, and apatite+monazite from four representative sections. Note abundance of pyrite scales with abundance of combined heavy minerals (% zircon+apatite+monazite).**

## REFERENCES

- Anbar, A.D., Duan, Y., Lyons, T.W., Arnold, G.L., Kendall, B., Creaser, R.A., Kaufman, A.J., Gordon, G.W., Scott, C., Garvin, J., and Buick, R., 2007, A Whiff of Oxygen Before the Great Oxidation Event?: *Science*, v. 317, p. 1903–1906, doi: 10.1126/science.1140325.
- Barton, E.S., and Hallbauer, D.K., 1996, Trace-element and U-Pb isotope compositions of pyrite types in the Proterozoic Black Reef, Transvaal Sequence, South Africa: Implications on genesis and age: *Chemical Geology*, v. 133, p. 173–199, doi: 10.1016/S0009-2541(96)00075-7.
- Bekker, A., Holland, H.D., Wang, P.-L., Rumble, D., Stein, H.J., Hannah, J.L., Coetzee, L.L., and Beukes, N.J., 2004, Dating the rise of atmospheric oxygen: *Nature*, v. 427, p. 117–120, doi: 10.1038/nature02260.
- Bekker, A., Sial, A.N., Karhu, J.A., Ferreira, V.P., Noce, C.M., Kaufman, A.J., Romano, A.W., and Pimentel, M.M., 2003, Chemostratigraphy of Carbonates from the Minas Supergroup, Quadrilátero Ferrífero (Iron Quadrangle), Brazil: A Stratigraphic Record of Early Proterozoic Atmospheric, Biogeochemical and Climatic Change: *American Journal of Science*, v. 303, p. 865–904, doi: 10.2475/ajs.303.10.865.
- Beukes, N.J., 1987, Facies relations, depositional environments and diagenesis in a major early Proterozoic stromatolitic carbonate platform to basinal sequence, Campbellrand Subgroup, Transvaal Supergroup, Southern Africa: *Sedimentary Geology*, v. 54, p. 1–46, doi: 10.1016/0037-0738(87)90002-9.
- Beukes, N.J., Dorland, H., Gutzmer, J., Nedachi, M., and Ohmoto, H., 2002, Tropical laterites, life on land, and the history of atmospheric oxygen in the Paleoproterozoic: *Geology*, v. 30, p. 491–494, doi: 10.1130/0091-7613(2002)030<0491:TLLOLA>2.0.CO;2.
- Beukes, N.J., and Gutzmer, J., 2008, Origin and Paleoenvironmental Significance of Major Iron Formations at the Archean-Paleoproterozoic Boundary, *in* Hagemann, S., Rosiere, C., Gutzmer, J., and Beukes, N. eds., *Banded Iron Formation-Related High-Grade Ore*, p. 5–47.
- Beukes, N., and Klein, C., 1992, Models for Iron-Formation Deposition, *in* Schopf, J.W. and Klein, C. eds., *The Proterozoic Biosphere: A Multidisciplinary Study*, Cambridge University Press.
- Boggs, S., 2006, *Principles of sedimentology and stratigraphy*: Pearson Prentice Hall, 696 p.



- Le Bouteiller, C., Naaïm-Bouvet, F., Mathys, N., and Lavé, J., 2011, A new framework for modeling sediment fining during transport with fragmentation and abrasion: *Journal of Geophysical Research: Earth Surface*, v. 116, p. n/a–n/a, doi: 10.1029/2010JF001926.
- Bradley, D.N., and Tucker, G.E., 2013, The storage time, age, and erosion hazard of laterally accreted sediment on the floodplain of a simulated meandering river: *Journal of Geophysical Research: Earth Surface*, v. 118, p. 1308–1319, doi: 10.1002/jgrf.20083.
- Cameron, E.M., 1982, Sulphate and sulphate reduction in early Precambrian oceans: *Nature*, v. 296, p. 145–148, doi: 10.1038/296145a0.
- Chabaux, F., Riotte, J., and Dequincey, O., 2003, U-Th-Ra Fractionation During Weathering and River Transport: *Reviews in Mineralogy and Geochemistry*, v. 52, p. 533–576, doi: 10.2113/0520533.
- Clemmey, H., and Badham, N., 1982, Oxygen in the Precambrian atmosphere: An evaluation of the geological evidence: *Geology*, v. 10, p. 141–146, doi: 10.1130/0091-7613(1982)10<141:OITPAA>2.0.CO;2.
- Cloud, P., 1972, A working model of the primitive Earth: *American Journal of Science*, v. 272, p. 537–548, doi: 10.2475/ajs.272.6.537.
- Cloud, P.E., 1968, Atmospheric and Hydrospheric Evolution on the Primitive Earth Both secular accretion and biological and geochemical processes have affected earth's volatile envelope: *Science*, v. 160, p. 729–736, doi: 10.1126/science.160.3829.729.
- Cornell, D.H., Schütte, S.S., and Eglington, B.L., 1996, The Ongeluk basaltic andesite formation in Griqualand West, South Africa: submarine alteration in a 2222 Ma proterozoic sea: *Precambrian Research*, v. 79, p. 101–123, doi: 10.1016/0301-9268(95)00090-9.
- DePaolo, D.J., Maher, K., Christensen, J.N., and McManus, J., 2006, Sediment transport time measured with U-series isotopes: Results from ODP North Atlantic drift site 984: *Earth and Planetary Science Letters*, v. 248, p. 394–410, doi: 10.1016/j.epsl.2006.06.004.
- Dosseto, A., Bourdon, B., Gaillardet, J., Allègre, C.J., and Filizola, N., 2006, Time scale and conditions of weathering under tropical climate: Study of the Amazon basin with U-series: *Geochimica et Cosmochimica Acta*, v. 70, p. 71–89, doi: 10.1016/j.gca.2005.06.033.

- Dosseto, A., Bourdon, B., and Turner, S.P., 2008, Uranium-series isotopes in river materials: Insights into the timescales of erosion and sediment transport: *Earth and Planetary Science Letters*, v. 265, p. 1–17, doi: 10.1016/j.epsl.2007.10.023.
- England, G.L., Rasmussen, B., Krapež, B., and Groves, D.I., 2002, Palaeoenvironmental significance of rounded pyrite in siliciclastic sequences of the Late Archaean Witwatersrand Basin: oxygen-deficient atmosphere or hydrothermal alteration?: *Sedimentology*, v. 49, p. 1133–1156, doi: 10.1046/j.1365-3091.2002.00479.x.
- England, G.L., Rasmussen, B., Krapež, B., and Groves, D.I., 2001, The Origin of Uraninite, Bitumen Nodules, and Carbon Seams in Witwatersrand Gold-Uranium-Pyrite Ore Deposits, Based on a Permo-Triassic Analogue: *Economic Geology*, v. 96, p. 1907–1920, doi: 10.2113/gsecongeo.96.8.1907.
- Ferrier, K.L., and Kirchner, J.W., 2008, Effects of physical erosion on chemical denudation rates: A numerical modeling study of soil-mantled hillslopes: *Earth and Planetary Science Letters*, v. 272, p. 591–599, doi: 10.1016/j.epsl.2008.05.024.
- Figueiredo, M.C.H., 1989, Geochemical evolution of eastern Bahia, Brazil: A probable Early Proterozoic subduction-related magmatic arc: *Journal of South American Earth Sciences*, v. 2, p. 131–145, doi: 10.1016/0895-9811(89)90041-2.
- Finch, R., and Murakami, T., 1999, Systematics and paragenesis of uranium minerals: *Reviews in Mineralogy and Geochemistry*, v. 38, p. 91–179.
- Folk, R.L., 1957, *Petrology of Sedimentary Rocks*: Austin, Texas: University of Texas.
- Gauert, C.D.K., Brauns, M., Batchelor, D., and Simon, R., 2011, Gold Provenance of the Black Reef Conglomerate, West and East Rand, South Africa, *in* SGA Abs. Volumes,.
- Grandstaff, D.E., 1976, A kinetic study of the dissolution of uraninite: *Economic Geology*, v. 71, p. 1493–1506, doi: 10.2113/gsecongeo.71.8.1493.
- Grandstaff, D.E., 1980, Origin of uraniferous conglomerates at Elliot Lake, Canada and Witwatersrand, South Africa - Implications for oxygen in the Precambrian atmosphere: *Precambrian Research*, v. 13, p. 1–26.
- Granet, M., Chabaux, F., Stille, P., Dosseto, A., France-Lanord, C., and Blaes, E., 2010, U-series disequilibria in suspended river sediments and implication for sediment transfer time in alluvial plains: The case of the Himalayan rivers: *Geochimica et Cosmochimica Acta*, v. 74, p. 2851–2865, doi: 10.1016/j.gca.2010.02.016.

- Granet, M., Chabaux, F., Stille, P., France-Lanord, C., and Pelt, E., 2007, Time-scales of sedimentary transfer and weathering processes from U-series nuclides: Clues from the Himalayan rivers: *Earth and Planetary Science Letters*, v. 261, p. 389–406, doi: 10.1016/j.epsl.2007.07.012.
- Grotzinger, J.P., and Kasting, J.F., 1993, New constraints on Precambrian ocean composition: *The Journal of geology*, v. 101, p. 235–243.
- Guo, Q., Strauss, H., Kaufman, A.J., Schröder, S., Gutzmer, J., Wing, B., Baker, M.A., Bekker, A., Jin, Q., Kim, S.-T., and Farquhar, J., 2009, Reconstructing Earth's Surface Oxidation Across the Archean-Proterozoic Transition: *Geology*, v. 37, p. 399–402, doi: 10.1130/G25423A.1.
- Gutzmer, Jens, and Beukes, Nicolas, 1998, High-grade manganese ores in the Kalahari manganese field: characterisation and dating of ore forming events: Rand Afrikaans University Unpublished Report, 221 p.
- Guy, B.M., Beukes, N.J., and Gutzmer, J., 2010, Paleoenvironmental Controls on the Texture and Chemical Composition of Pyrite from Non-Conglomeratic Sedimentary Rocks of the Mesoarchean Witwatersrand Supergroup, South Africa: *South African Journal of Geology*, v. 113, p. 195–228, doi: 10.2113/gssajg.113.2.195.
- Halevy, I., Pierrehumbert, R.T., and Schrag, D.P., 2009, Radiative transfer in CO<sub>2</sub>-rich paleoatmospheres: *Journal of Geophysical Research (Atmospheres)*, v. 114, p. 18112, doi: 10.1029/2009JD011915.
- Hallbauer, D.K., and Utter, T., 1977, Geochemical and morphological characteristics of gold particles from recent river deposits and the fossil placers of the Witwatersrand: *Mineralium Deposita*, v. 12, p. 293–306.
- Handley, H.K., Turner, S., Afonso, J.C., Dosseto, A., and Cohen, T., 2013, Sediment residence times constrained by uranium-series isotopes: A critical appraisal of the comminution approach: *Geochimica et Cosmochimica Acta*, v. 103, p. 245–262, doi: 10.1016/j.gca.2012.10.047.
- Hannah, J.L., Bekker, A., Stein, H.J., Markey, R.J., and Holland, H.D., 2004, Primitive Os and 2316 Ma age for marine shale: implications for Paleoproterozoic glacial events and the rise of atmospheric oxygen: *Earth and Planetary Science Letters*, v. 225, p. 43–52, doi: 10.1016/j.epsl.2004.06.013.
- Hartmann, L.A., Endo, I., Suita, M.T.F., Santos, J.O.S., Frantz, J.C., Carneiro, M.A., McNaughton, N.J., and Barley, M.E., 2006, Provenance and age delimitation of Quadrilátero Ferrífero sandstones based on zircon U–Pb isotopes: *Journal of*

- South American Earth Sciences, v. 20, p. 273–285, doi: 10.1016/j.jsames.2005.07.015.
- Hegner, E., Kröner, A., and Hunt, P., 1994, A precise U-Pb zircon age for the Archaean Pongola Supergroup volcanics in Swaziland: *Journal of African Earth Sciences*, v. 18, p. 339–341, doi: 10.1016/0899-5362(94)90072-8.
- Hiemstra, S.A., 1968, The mineralogy and petrology of the uraniferous conglomerate of the Dominion Reefs Mine, Klerksdorp area: *Trans. Geol. Soc. S. Afr.*, v. 71, p. 1–65.
- Hofmann, A., Bekker, A., Rouxel, O., Rumble, D., and Master, S., 2009, Multiple sulphur and iron isotope composition of detrital pyrite in Archaean sedimentary rocks: A new tool for provenance analysis: *Earth and Planetary Science Letters*, v. 286, p. 436–445, doi: 10.1016/j.epsl.2009.07.008.
- Hofmann, A., Dirks, P.H.G., and Jelsma, H., 2001, Late Archaean foreland basin deposits, Belingwe greenstone belt, Zimbabwe: *Sedimentary Geology*, v. 141–142, p. 131–168, doi: 10.1016/S0037-0738(01)00072-0.
- Holland, H.D., 1984, *The Chemical Evolution of the Atmosphere and Oceans*: Princeton University Press, 598 p.
- Houston, R.S., Karlstrom, K.E., Graff, P.J., and Flurkey, A.J., 1992, New Stratigraphic Subdivisions and Redefinition of Subdivisions of Late Archean and Early Proterozoic Metasedimentary and Metavolcanic Rocks of the Sierra Madre and Medicine Bow Mountains, Southern Wyoming: U.S. Geological Survey Professional Paper, v. 1520, p. 1–50.
- Janardhan, A.S.F., and Basavalingu, B., 1988, Sedimentology, Mineralogy and Geochemistry of the Kalasapura Conglomerate: *Memoir Geological Society of India*, v. 9, p. 65–82.
- Janeczek, J., and Ewing, R.C., 1992, Dissolution and alteration of uraninite under reducing conditions: *Journal of Nuclear Materials*, v. 190, p. 157–173, doi: 10.1016/0022-3115(92)90084-X.
- Johnson, J.E., Webb, S.M., Thomas, K., Ono, S., Kirschvink, J.L., and Fischer, W.W., 2013, Manganese-oxidizing photosynthesis before the rise of cyanobacteria: *PNAS*, in press.
- Joseph, G.G., and Hunt, M.L., 2004, Oblique particle-wall collisions in a liquid: *J. Fluid Mech.*, v. 510, p. 71–93.

- Kaufman, A.J., Johnston, D.T., Farquhar, J., Masterson, A.L., Lyons, T.W., Bates, S., Anbar, A.D., Arnold, G.L., Garvin, J., and Buick, R., 2007, Late Archean Biospheric Oxygenation and Atmospheric Evolution: *Science*, v. 317, p. 1900–1903, doi: 10.1126/science.1138700.
- Kodama, Y., 1994, Experimental study of abrasion and its role in producing downstream fining in gravel-bed rivers: *Journal of Sedimentary Research*, v. 64, p. 76–85.
- Kong, M., Bhattacharya, R.N., James, C., and Basu, A., 2005, A statistical approach to estimate the 3D size distribution of spheres from 2D size distributions: *Geological Society of America Bulletin*, v. 117, p. 244–249, doi: 10.1130/B25000.1.
- Konhauser, K.O., Lalonde, S.V., Planavsky, N.J., Pecoits, E., Lyons, T.W., Mojzsis, S.J., Rouxel, O.J., Barley, M.E., Rosiere, C., Fralick, P.W., Kump, L.R., and Bekker, A., 2011, Aerobic bacterial pyrite oxidation and acid rock drainage during the Great Oxidation Event: *Nature*, v. 478, p. 369–373, doi: 10.1038/nature10511.
- Kositcin, N., and Krapez, B., 2004, Relationship between detrital zircon age-spectra and the tectonic evolution of the Late Archaean Witwatersrand Basin, South Africa: *Precambrian Research*, v. 129, p. 141–168.
- Kozhevnikov, V., Skublov, S., Marin, Y., Medvedev, P., Systra, Y., and Valencia, V., 2010, Hadean-archean detrital zircons from Jatulian quartzites and conglomerates of the Karelian craton: *Doklady Earth Sciences*, v. 431, p. 318–323, doi: 10.1134/S1028334X10030128.
- Krapez, B., 1985, The Ventersdorp Contact placer: a gold-pyrite placer of stream and debris-flow origins from the Archaean Witwatersrand Basin of South Africa: *Sedimentology*, v. 32, p. 223–234, doi: 10.1111/j.1365-3091.1985.tb00505.x.
- Krogh, T.E., Davis, D.W., and Corfu, F., 1984, Precise U-Pb zircon and baddeleyite ages for the Sudbury area, *in* The geology and ore deposits of the Sudbury Structure, Ontario, Geological Survey Special Volume 1, Energy, Mines and Resources Canada, p. 431–446.
- Lamb, M.P., Dietrich, W.E., and Sklar, L.S., 2008, A model for fluvial bedrock incision by impacting suspended and bed load sediment: *Journal of Geophysical Research: Earth Surface*, v. 113, p. n/a–n/a, doi: 10.1029/2007JF000915.
- Lauer, J.W., and Parker, G., 2008, Modeling framework for sediment deposition, storage, and evacuation in the floodplain of a meandering river: *Theory: Water Resources Research*, v. 44, p. n/a–n/a, doi: 10.1029/2006WR005528.

- Lee, V.E., DePaolo, D.J., and Christensen, J.N., 2010, Uranium-series comminution ages of continental sediments: Case study of a Pleistocene alluvial fan: *Earth and Planetary Science Letters*, v. 296, p. 244–254, doi: 10.1016/j.epsl.2010.05.005.
- Lewin, J., and Brewer, P.A., 2002, Laboratory simulation of clast abrasion: *Earth Surface Processes and Landforms*, v. 27, p. 145–164, doi: 10.1002/esp.306.
- Liebenberg, W.R., 1955, The Occurrence and Origin of Gold and Radioactive Minerals in the Witwatersrand System, the Dominion Reef, the Ventersdorp Contact Reef and the Black Reef: Geological Society of South Africa, 154 p.
- Martin, D.M., Clendenin, C.W., Krapez, B., and McNaughton, N.J., 1998, Tectonic and geochronological constraints on late Archaean and Palaeoproterozoic stratigraphic correlation within and between the Kaapvaal and Pilbara Cratons.: *Journal of the Geological Society of Australia*, v. 155, p. 311–322.
- Maynard, J.B., Ritger, S.D., and Sutton, S.J., 1991, Chemistry of sands from the modern Indus River and the Archean Witwatersrand basin: Implications for the composition of the Archean atmosphere: *Geology*, v. 19, p. 265–268, doi: 10.1130/0091-7613(1991)019<0265:CO&2.3.CO;2.
- McDowell, J.P., 1957, The Sedimentary Petrology of the Mississagi Quartzite in the Blind River Area: Baptist Johnston, 31 p.
- Mikoš, M., 1995, Fluvial abrasion; converting size reduction coefficients into weight reduction rates: *Journal of Sedimentary Research*, v. 65, p. 472–476, doi: 10.1306/D42680FE-2B26-11D7-8648000102C1865D.
- Minter, W.E.L., Renger, F.E., and Siegers, A., 1990, Early Proterozoic gold placers of the Moeda Formation within the Gandarela Syncline, Minas Gerais, Brazil: *Economic Geology*, v. 85, p. 943–951, doi: 10.2113/gsecongeo.85.5.943.
- Nelson, D.R., Trendall, A.F., and Altermann, W., 1999, Chronological correlations between the Pilbara and Kaapvaal cratons: *Precambrian Research*, v. 97, p. 165–189, doi: 10.1016/S0301-9268(99)00031-5.
- Ono, S., 2001, Detrital uraninite and the early earth's atmosphere: SIMS analyses of uraninite in the Elliot Lake District and the dissolution kinetics of natural uraninite: Pennsylvania State University.
- Orberger, B., Hoffmann, A., Hicks, N., Wirth, R., Tudryn, A., and Megneng, M., 2011, Uranium mineralization in carbonaceous chert pebbles from Mesoarchean Mozaan Group conglomerates (~3 Ga, Pongola Basin, South Africa): trap or source rock?, *in* 11th SGA Biennial Meeting “Let’s talk ore Deposits” Conference, Antofagasta, Chili.

- Papineau, D., Mojzsis, S.J., and Schmitt, A.K., 2007, Multiple sulfur isotopes from Paleoproterozoic Huronian interglacial sediments and the rise of atmospheric oxygen: *Earth and Planetary Science Letters*, v. 255, p. 188–212, doi: 10.1016/j.epsl.2006.12.015.
- Pavlov, A.A., and Kasting, J.F., 2002, Mass-Independent Fractionation of Sulfur Isotopes in Archean Sediments: Strong Evidence for an Anoxic Archean Atmosphere: *Astrobiology*, v. 2, p. 27–41, doi: 10.1089/153110702753621321.
- Pickard, A., 2003, SHRIMP U–Pb zircon ages for the Palaeoproterozoic Kuruman Iron Formation, Northern Cape Province, South Africa: evidence for simultaneous BIF deposition on Kaapvaal and Pilbara Cratons: *Precambrian Research*, v. 125, p. 275–315, doi: 10.1016/S0301-9268(03)00113-X.
- Pienaar, P.J., 1963, Stratigraphy, petrology, and genesis of the Elliot Group, Blind River, Ontario.: Including the uraniferous conglomerate.,: Dept. of Mines and Technical Surveys, Canada, 140 p.
- Prasad, N., and Roscoe, S.M., 1996, Evidence of anoxic to oxic atmospheric change during 2.45–2.22 Ga from lower and upper sub-Huronian paleosols, Canada: *CATENA*, v. 27, p. 105–121, doi: 10.1016/0341-8162(96)00003-3.
- Pufahl, P.K., and Hiatt, E.E., 2012, Oxygenation of the Earth's atmosphere–ocean system: A review of physical and chemical sedimentologic responses: *Marine and Petroleum Geology*, v. 32, p. 1–20, doi: 10.1016/j.marpetgeo.2011.12.002.
- Ramdohr, P., 1958, New observations on the ores of the Witwatersrand in South Africa and their genetic significance: *Geological Society of South Africa*, 186 p.
- Rasmussen, B., and Buick, R., 1999, Redox State of the Archean Atmosphere: Evidence from Detrital Heavy Minerals in Ca. 3250–2750 Ma Sandstones from the Pilbara Craton, Australia: *Geology*, v. 27, p. 115–118, doi: 10.1130/0091-7613(1999)027<0115:RSOTAA>2.3.CO;2.
- Reinhard, C.T., Raiswell, R., Scott, C., Anbar, A.D., and Lyons, T.W., 2009, A late Archean sulfidic sea stimulated by early oxidative weathering of the continents: *Science (New York, N.Y.)*, v. 326, p. 713–716, doi: 10.1126/science.1176711.
- Riebe, C.S., Kirchner, J.W., and Finkel, R.C., 2003, Long-term rates of chemical weathering and physical erosion from cosmogenic nuclides and geochemical mass balance: *Geochimica et Cosmochimica Acta*, v. 67, p. 4411–4427, doi: 10.1016/S0016-7037(03)00382-X.

- Robinson, A., and Spooner, E.T.C., 1982, Source of the detrital components of uraniferous conglomerates, Quirke ore zone, Elliot Lake, Ontario, Canada: *Nature*, v. 299, p. 622–624, doi: 10.1038/299622a0.
- Roscoe, S.M., 1973, The Huronian Supergroup, a Paleoaphebian succession showing evidence of atmospheric evolution, *in* Young, G.M. ed., *Huronian Stratigraphy and Sedimentation*, Geological Association of Canada, p. 31–47.
- Rye, R., and Holland, H.D., 1998, Paleosols and the evolution of atmospheric oxygen: a critical review: *American journal of science*, v. 298, p. 621–672.
- Rye, R., Kuo, P.H., and Holland, H.D., 1995, Atmospheric carbon dioxide concentrations before 2.2 billion years ago: *Nature*, v. 378, p. 603–605, doi: 10.1038/378603a0.
- Schmeeckle, M.W., Nelson, J.M., Pitlick, J., and Bennett, J.P., 2001, Interparticle collision of natural sediment grains in water: *Water Resources Research*, v. 37, p. 2377–2391, doi: 10.1029/2001WR000531.
- Schmitz, M.D., and Bowring, S.A., 2003, Ultrahigh-temperature metamorphism in the lower crust during Neoarchean Ventersdorp rifting and magmatism, Kaapvaal Craton, southern Africa: *Geological Society of America Bulletin*, v. 115, p. 533–548, doi: 10.1130/0016-7606(2003)115<0533:UMITLC>2.0.CO;2.
- Schröder, S., Bedorf, D., Beukes, N.J., and Gutzmer, J., 2011, From BIF to red beds: Sedimentology and sequence stratigraphy of the Paleoproterozoic Koegas Subgroup (South Africa): *Sedimentary Geology*, v. 236, p. 25–44, doi: 10.1016/j.sedgeo.2010.11.007.
- Shaw, J., and Kellerhals, R., 1982, The Composition of Recent Alluvial Gravels in Alberta River Beds: Alberta Research Council Alberta Geological Survey, 151 p.
- Sheldon, N.D., 2006, Precambrian paleosols and atmospheric CO<sub>2</sub> levels: *Precambrian Research*, v. 147, p. 148–155, doi: 10.1016/j.precamres.2006.02.004.
- Simonson, B.M., and Hassler, S.W., 1996, Was the Deposition of Large Precambrian Iron Formations Linked to Major Marine Transgressions?: *Journal of Geology*, v. 104, p. 665–676, doi: 10.1086/629861.
- Simpson, P.R., and Bowles, J.F., 1981, Detrital Uraninite and Pyrite: Are They Evidence for a Reducing Atmosphere?: U.S. Geological Survey, book p.
- Simpson, P.R., and Bowles, J.F.W., 1977, Uranium Mineralization of the Witwatersrand and Dominion Reef Systems: *Philosophical Transactions of the Royal Society of London. Series A, Mathematical and Physical Sciences*, v. 286, p. 527–548, doi: 10.1098/rsta.1977.0130.



- Sklar, L.S., Dietrich, W.E., Foufoula-Georgiou, E., Lashermes, B., and Bellugi, D., 2006, Do gravel bed river size distributions record channel network structure?: *Water Resources Research*, v. 42.
- Srinivasan, R., and Ojakangas, R.W., 1986, Sedimentology of Quartz-Pebble Conglomerates and Quartzites of the Archean Bababudan Group, Dharwar Craton, South India: Evidence for Early Crustal Stability: *The Journal of Geology*, v. 94, p. 199–214, doi: 10.1086/629023.
- Sternberg, H., 1875, Untersuchungen uber Langen-und Querprofil geschiebefuhrender Flusse: *Zeitschrift fur Bauwesen*, v. XXV, p. 483–506.
- Stumm, W., and Morgan, J.J., 1996, *Aquatic Chemistry: Chemical Equilibria and Rates in Natural Waters*: Wiley-Interscience, 1040 p.
- Sumner, D.Y., and Beukes, N.J., 2006, Sequence stratigraphic development of the Neoproterozoic Transvaal carbonate platform, Kaapvaal Craton, South Africa: v. 109.
- Sumner, D.Y., and Bowring, S.A., 1996, U-Pb geochronologic constraints on deposition of the Campbellrand Subgroup, Transvaal Supergroup, South Africa: *Precambrian Research*, v. 79, p. 25–35, doi: 10.1016/0301-9268(95)00086-0.
- Tabakh, M.E., Grey, K., Pirajno, F., and Schreiber, B.C., 1999, Pseudomorphs after evaporitic minerals interbedded with 2.2 Ga stromatolites of the Yerrida basin, Western Australia: Origin and significance: *Geology*, v. 27, p. 871–874, doi: 10.1130/0091-7613(1999)027<0871:PAEMIW>2.3.CO;2.
- Trendall, A.F., Compston, W., Williams, I.S., Armstrong, R.A., Arndt, N.T., McNaughton, N.J., Nelson, D.R., Barley, M.E., Beukes, N.J., De Laeter, J.R., Retief, E.A., and Thorne, A.M., 1990, Precise zircon U–Pb chronological comparison of the volcano-sedimentary sequences of the Kaapvaal and Pilbara Cratons between about 3.1 and 2.4 Ga, *in* *Proceedings of the Third International Archean Symposium*, Perth, Geological Society of Australia, p. 81–83.
- Tsikos, H., Beukes, N.J., Moore, J.M., and Harris, C., 2003, Deposition, Diagenesis, and Secondary Enrichment of Metals in the Paleoproterozoic Hotazel Iron Formation, Kalahari Manganese Field, South Africa: *Economic Geology*, v. 98, p. 1449–1462, doi: 10.2113/gsecongeo.98.7.1449.
- Utsunomiya, S., Murakami, T., Nakada, M., and Kasama, T., 2003, Iron oxidation state of a 2.45-Byr-old paleosol developed on mafic volcanics: *Geochimica et Cosmochimica Acta*, v. 67, p. 213–221, doi: 10.1016/S0016-7037(02)01083-9.

- Vigier, N., Bourdon, B., Turner, S., and Allègre, C.J., 2001, Erosion timescales derived from U-decay series measurements in rivers: *Earth and Planetary Science Letters*, v. 193, p. 549–563, doi: 10.1016/S0012-821X(01)00510-6.
- Vigier, N., Burton, K.W., Gislason, S.R., Rogers, N.W., Duchene, S., Thomas, L., Hodge, E., and Schaefer, B., 2006, The relationship between riverine U-series disequilibria and erosion rates in a basaltic terrain: *Earth and Planetary Science Letters*, v. 249, p. 258–273, doi: 10.1016/j.epsl.2006.07.001.
- Villaca, J.N., and Moura, L.A.M., 1981, Uranium in Precambrian Moeda Formation, Minas Gerais, Brazil, *in* *Genesis of Uranium- and Gold-Bearing Precambrian Quartz-Pebble Conglomerates*, Geological Survey Professional Paper, U.S. Government Printing Office.
- Walraven, F., and Martini, J., 1995, Zircon Pb-evaporation age determinations for the Oak Tree Formation, Chuniespoort Group, Transvaal Sequence; implications for Transvaal-Griqualand West basin correlations: *South African Journal of Geology*, v. 98, p. 58–67.
- Wentworth, C.K., 1922, A scale of grade and class terms for clastic sediments: *Journal of Geology*, v. 30, p. 377–392.
- Williamson, M.A., and Rimstidt, J.D., 1994, The kinetics and electrochemical rate-determining step of aqueous pyrite oxidation: *Geochimica et Cosmochimica Acta*, v. 58, p. 5443–5454, doi: 10.1016/0016-7037(94)90241-0.
- Williford, K.H., Van Kranendonk, M.J., Ushikubo, T., Kozdon, R., and Valley, J.W., 2011, Constraining atmospheric oxygen and seawater sulfate concentrations during Paleoproterozoic glaciation: In situ sulfur three-isotope microanalysis of pyrite from the Turee Creek Group, Western Australia: *Geochimica et Cosmochimica Acta*, v. 75, p. 5686–5705, doi: 10.1016/j.gca.2011.07.010.
- Yang, W., and Holland, H.D., 2003, The Hekpoort paleosol profile in Strata 1 at Gaborone, Botswana: Soil formation during the Great Oxidation Event: *American Journal of Science*, v. 303, p. 187–220, doi: 10.2475/ajs.303.3.187.
- Zahnle, K., Claire, M., and Catling, D., 2006, The loss of mass-independent fractionation in sulfur due to a Palaeoproterozoic collapse of atmospheric methane: *Geobiology*, v. 4, p. 271–283, doi: 10.1111/j.1472-4669.2006.00085.x.
- Zerle, A.L., Claire, M.W., Domagal-Goldman, S.D., Farquhar, J., and Poulton, S.W., 2012, A bistable organic-rich atmosphere on the Neoarchaeon Earth: *Nature Geoscience*, v. 5, p. 359–363, doi: 10.1038/ngeo1425.

*Chapter 4***Real-time manganese phase dynamics during abiotic and biological manganese oxide reduction**

Jena E Johnson<sup>1</sup>, Pratixa Savalia<sup>2</sup>, Ryan Davis<sup>3</sup>, Benjamin Kocar<sup>4</sup>, Samuel M Webb<sup>3</sup>,  
Kenneth Nealson<sup>2</sup>, Woodward W Fischer<sup>1</sup>

<sup>1</sup>Division of Geological and Planetary Sciences, California Institute of Technology, Pasadena, CA 91125, USA. <sup>2</sup>University of Southern California, Los Angeles, CA 90089. <sup>3</sup>Stanford Synchrotron Radiation Lightsource, Menlo Park CA 94025. <sup>4</sup>Massachusetts Institute of Technology, Cambridge MA 02139.

**ABSTRACT**

**Many toxic and bioessential trace elements are sequestered by insoluble manganese oxides, but Mn oxides are also highly reactive and easily reduced by a variety of species, abiotically and as a part of biological anaerobic respiration. The reaction pathways during these different manganese oxide reduction routes and their products have been thusfar understudied. We measured the sequence progression of live microbial manganese(IV) oxide reduction under several environmentally-relevant conditions using real-time synchrotron x-ray spectroscopic measurements and x-ray diffraction on precipitates collected throughout the reaction. These results were compared to abiotic reduction pathways using common inorganic reductants sulfide and ferrous iron. We observed formation of rhodochrosite (MnCO<sub>3</sub>) during the microbial reduction of Mn(IV) oxides with high organic carbon and negligible phosphate while high phosphate and organic carbon conditions formed Mn(II)-phosphate. Both sulfide and ferrous iron reduction of manganese oxides in the**

**absence of inorganic carbon produced only aqueous  $\text{Mn}^{2+}$ . A Mn(III) oxyhydroxide intermediate similar to feitknechtite was produced during sulfide- and ferrous iron-induced reduction and during low-phosphate experiments, which we suggest was formed during comproportionation reactions between remnant Mn(IV) oxides and produced  $\text{Mn}^{2+}$ . Our real-time measurements contribute to understanding the kinetics and mechanism of Mn(IV) oxides reduction and what the possible mineralogical intermediates and products are, and our observations should assist in interpreting the processes recorded in the geologic record of manganese on Earth and beyond.**

## **INTRODUCTION**

The cycling of manganese is critically important for the sequestration of toxins and trace metals, the neutralization of reactive oxygen species and the reactivity of major geochemical species like sulfur and iron<sup>1</sup>. Manganese is introduced to the fluid Earth as soluble  $\text{Mn}^{2+}$  by hydrothermal sources or igneous rock weathering but is oxidized in oxygenated water and air to insoluble Mn(III,IV) oxyhydroxides<sup>2–4</sup>. These manganese oxides are highly favorable electron acceptors for microbial anaerobic respiration<sup>5,6</sup>, an important process both in marine sediments and terrestrial environments<sup>7–9</sup>. But manganese can also be rapidly reduced by many inorganic species, including ferrous iron, sulfide, arsenite and uraninite<sup>10–13</sup>. These Mn(III,IV) oxides are then deposited in sediments, where they are often rapidly cycled as they undergo many reduction and re-oxidation reactions<sup>1,8</sup>.

Initial manganese precipitates can be subsequently incorporated into the sedimentary record or aqueous manganese(II) can be released to shallower sediments, groundwater, or other nearby fluids. Currently, it is unclear which reductants and what environmental conditions control the behavior of manganese and its potential to become ‘fixed’ in minerals or re-released. The geologic record of manganese is illuminating here:

while manganese is deposited primarily as Mn(IV) oxides <sup>1,14–19</sup>, ancient well-preserved sedimentary rocks host Mn in more reduced phases, mainly in Mn-bearing carbonates [rhodochrosite, MnCO<sub>3</sub>, or kutnohorite, Mn<sub>0.5</sub>Ca<sub>0.5</sub>CO<sub>3</sub>] or in Mn(II,III) silicified oxides [braunite, Mn(III)<sub>6</sub>Mn(II)SiO<sub>12</sub>] <sup>3,20–23</sup>. These Mn-carbonates have been hypothesized to be derived from Mn(IV) oxides undergoing post-depositional diagenetic reduction by organic carbon (microbially-mediated at low-temperatures) <sup>3,22–25</sup>, as in Rxn 1 and 2:



However, the high redox potential of manganese results in multiple possible Mn(IV) reduction pathways, including but not limited to microbially-mediated reactions with organic carbon. The mechanistic differences and the mineralogical products of the various Mn reduction potential pathways have been understudied. Rhodochrosite has been observed as a product of microbial respiration of Mn oxides previously<sup>5,12,26</sup> although not explored extensively for the requisite conditions of precipitation. Other

studies have measured Mn-carbonate production during microbial sulfate reduction or thiosulfate disproportionation from secondary abiotic interactions between sulfide and Mn-oxides<sup>27–30</sup>.

To our knowledge only one study has measured a partial reaction sequence of Mn(IV) oxides to Mn(II)-carbonate, using time-resolved XRD measurements<sup>31</sup>. Fischer et al. reacted total membrane extracts from *Shewanella oneidensis* with powdered birnessite (a layered Mn(III,IV) oxide) and observed the mineralogical changes that occurred, reportedly finding production of rhodochrosite and hausmannite (Mn<sub>3</sub>O<sub>4</sub>), although only rhodochrosite data is shown. However, using only XRD measurements limits the results to crystalline phases, and it is unclear how much this *in vitro* study really represents natural reaction mechanisms and mineralogical changes.

Our experiments seek to systematically address what the environmental and mechanistic controls are on mineral products of Mn oxide reduction with various reductants. Time-resolved measurements both constrain the reduction mechanism and reveal reaction intermediates during various Mn reduction pathways. These intermediates may be stabilized as products if Mn reduction is reductant-limited, introducing another set of possible products. Real-time measurements of the Mn redox state and phase throughout inorganic and organic, microbially-mediated manganese reduction reveals the reaction mechanisms for these two distinct processes. Not only do these experiments yield mechanistic insight, but we can also compare reaction intermediates and products for

different reduction pathways against observations from Earth's modern environments and ancient rock record.

## **MATERIALS AND METHODS**

Abiotic and biologically-mediated manganese reduction reactions were analyzed using a succession of X-ray spectroscopic measurements to assess what manganese phases were formed throughout the reaction. Measuring the dynamics of manganese phase changes *in situ* is highly challenging because of the complex media necessary for microbial sustenance, the amorphous intermediate phases often formed in low-temperature reactions, and (during microbial experiments) the extra complications introduced by cellular mass. These issues make real-time measurements not feasible by Raman, Fourier Transform Infrared Spectroscopy, or X-ray Diffraction (XRD) techniques, although these methods can and do help to assess crystalline products. X-ray absorption spectroscopy (XAS) is the ideal way to probe the entire reaction sequence since XAS can focus on one element (Mn) without matrix effects and measure the coordination and redox environment of all phases (contributing at least 5% to the total) regardless of crystallinity<sup>32</sup>. Thus all experiments were performed at the Stanford Synchrotron Radiation Lightsource, either on beam line 11-2 or beam line 4-1. We used high concentrations of Mn oxides and large quantities of bacteria to have strong Mn signal and rapid enough rates to measure in limited synchrotron time. This does not mimic environments directly, but reveals how these reactions progress mechanistically.

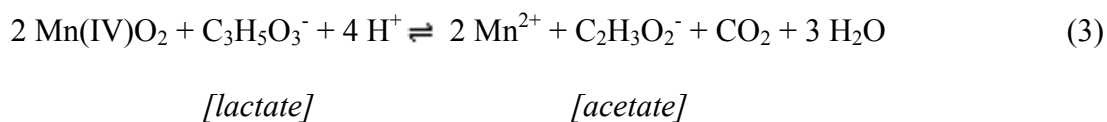
To capture the reduction reaction in real-time, we set up a flow-through system which siphoned a subsample of a stirred 1L reaction vessel into a small flow cell where the X-ray beam could evaluate the Mn valence state and coordination environment (Figure 1). Our flow-through cell was constructed from polymethacrylate polymer using a 3D printer. Fluid moved rapidly through the tubing and flow through cell and we saw no evidence of beam reduction or lactate-induced reduction in multi-hour control experiments with 20mM lactate and Mn oxides (Figure S1). New X-ray absorption spectra to detect Mn coordination and redox state (see <sup>23,33–35</sup>) were measured every 20 to 30 minutes. The reaction vessel was sealed with a rubber stopper and anaerobic conditions were maintained by nitrogen gas inflow. Solid filter samples were taken using a sampling portal through the rubber stopper and later analyzed using synchrotron-based x-ray diffraction on beam line 11-3 to characterize crystalline products and confirm XAS identifications.

Our reaction vessel contained the M1 minimal media (after Kostka and Neelson<sup>36</sup>, with phosphate eliminated unless noted) necessary for our biotic experiments, 20mM lactate except in a lactate-limiting experiment, and began with freshly-made colloidal Mn(IV)O<sub>2</sub>. For each experiment, we prepared colloidal MnO<sub>2</sub> by mixing equal weights of potassium permanganate and sodium thiosulfate (~1g each, after Perez-Benito et al, 1989) in a small volume of milliQ water (~20mL) and washed once with a dilute sodium chloride solution (.008M NaCl) to remove any adsorbed sulfur species, pipetting away as much excess solution as possible. We added this colloidal MnO<sub>2</sub> to the reaction vessel in an anaerobic



chamber. Using colloidal MnO<sub>2</sub> reduced the experimental time dramatically, since non-crystalline Mn(IV) oxides are much more reactive than crystalline Mn(IV) oxides like birnessite or pyrolusite, but this did add some variety to our initial conditions. Our media was always titrated to pH 8, but with the colloidal MnO<sub>2</sub> addition, occasionally additional pH adjustments were necessary (using sodium hydroxide or hydrochloric acid) to return the initial pH to 8.

For our microbially-mediated manganese reduction experiments, we used a wild-type bacterial system to most realistically capture the process dynamics of Mn reduction. We chose to use *Shewanella oneidensis*, a well-studied model bacteria for anaerobic metal reduction including the reduction of Mn(IV) oxides<sup>11,37–39</sup>. *S. oneidensis* employs either (or both) soluble electron carriers [flavins]<sup>40,41</sup> or direct electron transfer on the cell surface or via nanowires<sup>42–44</sup> to pass electrons from a limited number of organic compounds to a substantial diversity of electron acceptors. Regardless of the mechanism, the reduction reaction should be similar for *Shewanella* and other microbial manganese reducers:



This reaction produces reduced manganese, alkalinity, and dissolved inorganic carbon, which should promote the precipitation of manganese carbonates<sup>3,45</sup>.

We grew *S. oneidensis* in conditions to optimize cellular density so the experiments could be performed in limited time spans. *S. oneidensis* was grown aerobically in Lysogeny Broth (LB) in a 25-30°C shaking incubator until the optical density at 600nm was approximately 1.2. We then spun down the cells in 250mL tubes using a centrifuge at 3000rpm for 5 minutes and resuspended the cells in a small amount of LB. The thick cellular paste (often 10-15mL) was added to the reaction vessel through the sampling port by a syringe after acquiring an initial MnO<sub>2</sub> spectra.

We performed three variations of microbially-mediated reduction of Mn(IV) oxides. One had our ‘normal’ conditions of being lactate-replete (20mM) but no added phosphate in the media, so the bacteria only had the cellular phosphate they had accumulated while growing in LB. Another had similarly phosphate-restricted conditions but also was limiting in lactate, only starting with 0.5mM with two subsequent of 0.5mL additions of 1M sodium lactate. A third had lactate-replete conditions (20mM) and abundant phosphate in the media (the usual M1 recipe with 4.3mM phosphate<sup>36</sup>).

In abiotic experiments, we added either sodium sulfide (Na<sub>2</sub>S) or ferrous chloride (FeCl<sub>2</sub>) as a titrant to the manganese(IV) oxide in the same media conditions as the biotic experiments. In the ferrous iron-induced reduction of manganese, X-ray absorption spectral parameters were adjusted to also acquire iron near-edge x-ray absorption spectra as well as the Mn edge, increasing the total spectra time to about 30 min.

Replicates of all experiments were performed either off-line, with the precipitate centrifuged and later analyzed as a sediment monolayer on tape, or in other experiments at the synchrotron under similar conditions.

## RESULTS

We performed five distinct experiments with real-time measurements of manganese phase and redox state to understand the Mn reaction intermediates and products under diverse environmental conditions and reduction mechanisms. Manganese oxides are commonly reduced by sulfide, ferrous iron, and organic carbon, with the latter being a type of anaerobic respiration frequently utilized in anoxic sediments and soils<sup>7-9</sup>. We characterized the sequence of manganese redox state and phases which were produced during sulfide-stimulated manganese(IV) reduction, ferrous iron-induced manganese(IV) reduction, and the anaerobic respiration of manganese(IV) by the lactate-consuming bacteria *S. oneidensis*.

We observed the reduction mechanics of microbially-mediated MnO<sub>2</sub> reduction by lactate in three distinct experiments mimicing endmember conditions to understand processes that occur in various environments (Figure 2). We manufactured an environment with very high (4.3mM) phosphate and high (20mM) lactate to see how these might affect the intermediates and products of microbial respiration of manganese oxides. In this experiment (Figure 2a), we observed a direct transformation of MnO<sub>2</sub> into a Mn(II)

phosphate similar to our hureaulite  $[\text{Mn}^{2+}_5(\text{PO}_3\text{OH})_2(\text{PO}_4)_2 \cdot 4\text{H}_2\text{O}]$  standard (standard confirmed using Raman spectroscopy). Isosbestic points, where all spectra have the same absorbance, are only seen in two-phase conversions and these are clearly observed in the Figure 2a inset.

In contrast, the two experiments with negligible (and more realistic) phosphate have dramatically different reaction products. Our high (20mM) lactate experiment provides a reaction mechanism for what occurs when manganese oxides are limiting as compared to organic carbon concentrations, conditions which can be compared to highly productive coastal settings<sup>47,48</sup>. This lactate-replete experiment shows several important transitional phases with intermediates like Mn(III) oxides,  $\text{Mn}^{2+}$  in solution, and then precipitating a rhodochrosite ( $\text{MnCO}_3$ ) product (Figure 2b). Examining the pH through time plots of each of these experiments (Figure 2a&b) demonstrates the similar beginning of both, with the consumption of  $\text{MnO}_2$  consuming protons (Rxn 3), but then the two plots have very different secondary phases. Figure 2a shows that with high phosphate levels, the system is quickly stabilized as Mn(II)-phosphate forms and there is little subsequent change to the pH. With low phosphate levels, one can see a very different reaction progression in Figure 2b: pH continues to rise past the ~8.35 we saw in Figure 2a all the way up to ~8.6, and then pH rapidly drops followed by a slow decrease approximately back to its original pH of 8. This pH drop can be accounted for by the precipitation of  $\text{MnCO}_3$ :



Another minimal-phosphate experiment had an additional limitation in its organic carbon (lactate) source, comparable to an oligotrophic open-ocean marine setting without many nutrients or much primary productivity producing organic carbon<sup>47,48</sup>. This experiment shows the production of a Mn(III) oxyhydroxide and  $\text{Mn}^{2+}$  (Figure 2c). The media began with just 0.5mL of 1M lactate, which upon addition of *S. oneidensis* was used by the bacteria to convert Mn(IV) to  $\text{Mn}^{2+}$ . This yielded approximately 11%  $\text{Mn}^{2+}$ , which we calculated by fitting the spectra to a birnessite and a  $\text{Mn}^{2+}$  standard using the Linear Fit function in Sixpack (Webb et al, 2005). We added two more aliquots of 0.5mL 1M lactate, which led to growth of a Mn(III) phase similar to what we saw as a transient phase in the high-lactate experiments. The second aliquot (dubbed t2, Figure 2c) made a stable mixture of aqueous  $\text{Mn}^{2+}$  (33%), feitknechtite [ $\text{MnOOH}$ , chosen by fitting routine over  $\text{Mn}_2\text{O}_3$ ] (15%), and remnant birnessite (51%). The third aliquot (t3) temporarily made up to ~34% feitknechtite (with 26% remnant  $\text{MnO}_2$  and 40%  $\text{Mn}^{2+}$ ) but then stabilized into a system with 18% remnant birnessite, 60%  $\text{Mn}^{2+}$ , and 22% feitknechtite. Our spectral measurements indicate that this combination was stable for at least ~1 hr, but it would likely remain even longer as no redox changes could occur without addition of a reductant (Figure 2c). The development of three distinct redox equilibria can be observed in the unchanging pH plateaus (Figure 2c).

Abiotic experiments also formed a Mn(III) phase intermediate, but the Mn(II) product was highly distinct. Both sulfide (Figure 3a) and ferrous iron (Figure 3b,c) titration experiments have Mn(III) intermediates, although the sulfide spectral sequence is clearer. With sufficient reductant, however, both abiotic experiments form aqueous  $\text{Mn}^{2+}$  without any mineral product. This result is artificial in the case of sulfide-induced Mn(IV) reduction, since the increase in pH and alkalinity indicate that Mn-carbonate may have formed if enough dissolved inorganic carbon was present (an experiment for future work). In ferrous iron-induced Mn(IV) reduction, the decrease in pH indicates that this reaction should not promote carbonate precipitation but should always make  $\text{Mn}^{2+}$ , which can then be lost to the environment<sup>19</sup>. In these experiments, iron appears to be rapidly oxidized as it reduces Mn(IV) (Figure 3b), closely matching our FeOOH (goethite) standard and even more similar to the lepidocrocite spectra shown in O'day et al<sup>49</sup>.

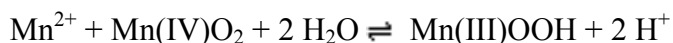
## DISCUSSION

We present observations from a suite of manganese oxide reduction experiments representing diverse environmental conditions and reductants from the anaerobic respiration of Mn(IV) in soil, coastal marine, and oligotrophic ocean-like conditions to abiotic iron and sulfide titrations. There were distinct differences in each biotic experiment, where phosphate-rich conditions led to the direct formation of a Mn(II)-phosphate product, and phosphate-poor conditions formed Mn(III) oxides and eventually Mn(II)-carbonates (rhodochrosite) if given sufficient organic carbon. These all contrasted

with abiotic experiments, with both ferrous iron- and sulfide-induced reductions of Mn(IV) forming Mn(III) intermediates and then aqueous  $\text{Mn}^{2+}$ .

Each experiment we performed provides insight into how manganese(IV) oxides are reduced and how the environment impacts this reduction. If Mn(IV) is reduced abiotically, especially if the reductant is ferrous iron, then  $\text{Mn}^{2+}$  is formed and, in the environment, would likely diffuse away and not enter the sediments as potential storage of manganese (or a geologically-observable deposit of manganese). The dropping pH in the ferrous iron-induced reduction signifies that aqueous  $\text{Mn}^{2+}$  will be more and more soluble and Mn(II) hydroxide and Mn(II) carbonate phase precipitation will not be promoted (Figure 3b,c).

One exception here is the Mn(III) intermediate in both abiotic experiments (Figure 3). It appears first as an extension of the Mn(IV) peak, probably as a mixed Mn(III,IV) oxide, and later as a flattened shoulder (see t8-12 in Fig3a), but only arising after a Mn(II) shoulder is present. Because of this relative timing, we believe that this Mn(III) is forming from comproportionation reactions between produced  $\text{Mn}^{2+}$  and still-present Mn(IV) oxides, as in Reaction 4:



If this Mn(III) intermediate is indeed a Mn(III) oxyhydroxide precipitate, then it would retain manganese as a solid and be a stable product to potentially enter the sedimentary record, as long as there was limiting sulfide or ferrous iron (like product in Figure 3c). As we observed in other experiments, if there is a surplus of reductant, then all the manganese is converted to  $\text{Mn}^{2+}$  and, in the case of sulfide and ferrous iron, does not form a mineralogical product in our experiments.

There is a caveat in the case of the sulfide-induced reduction experiment: our data contrasts with previous work that has noted reactions between sulfide and Mn(IV) oxides producing rhodochrosite<sup>27–30</sup>. These other reports were all in natural sediments with active microbial cycling and respiration<sup>28</sup>, or in experiments with microbes performing thiosulfate or sulfur disproportionation in the presence of Mn(IV) oxides<sup>27</sup>, or with concomitant manganese oxide reduction and either sulfate or thiosulfate reduction<sup>29,30</sup>. All of these circumstances would have high dissolved inorganic carbon, as well as elevated alkalinity, and these conditions would promote the precipitation of carbonates including rhodochrosite. We note that our experiments began with essentially no dissolved inorganic carbon, and so even though we measured increasing pHs in our sulfide-induced manganese reduction experiment, no Mn(II)-carbonate could form. Exploring how much dissolved inorganic carbon is required for rhodochrosite precipitation associated with sulfide- $\text{MnO}_2$  reactions is beyond the scope of this project, but should be investigated in further work.



**Kinetic Controls on Microbially-Mediated Reaction Sequences** The microbial reduction of Mn(IV) oxides also shows a Mn(III) oxyhydroxide secondary phase, but only when phosphate is deficient. This observation yields important insights into the kinetics of Mn-phosphates and Mn-carbonates: Mn-phosphates must form significantly more rapidly than Mn-carbonates. This inference is supported by what is known about these two minerals, where Mn-phosphates have been observed to dominate over rhodochrosite in a phosphate-rich meromictic lake (Hongve, 1997) and experiments that show rhodochrosite has even slower precipitation rates than calcite<sup>50,51</sup>. We clearly see in the high-phosphate experiments that there is a two-phase system: directly after Mn(II) is produced, Mn(II)-phosphate is precipitated because we don't see any aqueous Mn<sup>2+</sup> build up in solution and contribute to the spectra (Figure 2a). The lack of Mn(III) oxyhydroxide in the phosphate-rich experiments reveals the speedy precipitation kinetics of Mn(II)-phosphate, and also indicates that *S. oneidensis* produces Mn<sup>2+</sup> directly (or at least in two very rapid one-electron transfers) as we cannot resolve a Mn(III) step in the high-phosphate experiments (Figure 4). Some studies have shown a Mn(III) step during the reduction of Mn(IV)<sup>38</sup>, but this is likely a very fast intermediate, and may have been promoted by their experimental conditions (with the high concentrations of pyrophosphate).

The major differences between the phosphate and low-phosphate experiments can be solely explained by a combination of precipitation kinetics and environmental controls (Figure 4). Our low-phosphate experiments show a Mn(II) shoulder grow while Mn(IV)

oxides become more and more enriched in Mn(III), much more similar to the abiotic reduction experiments (Figure 2b,c). This Mn(III) phase with varying amounts of Mn(IV) and  $\text{Mn}^{2+}$  can be stabilized if more organic carbon is not added, as we show in our lactate-limiting experiment (Figure 2c). With lactate-replete conditions, this trend continues until aqueous  $\text{Mn}^{2+}$  dominates the entire system. Then slowly, the Mn(II) peak position shifts and the 6563 second peak of rhodochrosite forms and the system transitions to being completely Mn-carbonate (Figure 2b). The formation of Mn(III) oxyhydroxides, suggesting that there is sufficient  $\text{Mn}^{2+}$  accumulation to react with Mn(IV) oxides, and the long presence of aqueous  $\text{Mn}^{2+}$  (>1.5 hrs), indicate that the formation of Mn(II)-carbonate is highly kinetically-impaired as expected (Figure 4). The lack of  $\text{Mn}^{2+}$  in the high-phosphate experiments establishes that the kinetics of Mn(II)-phosphate precipitation is much faster than  $\text{Mn}^{2+}$  generation, Mn(III)OOH formation, or Mn(II)-carbonate precipitation in general (Figure 4). The build-up of aqueous  $\text{Mn}^{2+}$  in the low-phosphate experiments reveals that the kinetics of Mn(IV) reduction must also be faster than rhodochrosite precipitation (Figure 4). The rate of Mn(III) oxyhydroxide formation seems to be faster than the reduction of that Mn(III) phase by *S. oneidensis* since we do see this phase spectrally (although not for very long), but Mn(III) oxyhydroxide formation must be slower than Mn(II)-phosphate precipitation as we do not see it appear in the phosphate-replete experiments (Figure 4).

Our diverse manganese reduction experiments not only yield insights into the kinetic controls on intermediates (which can be products with incomplete reactions), but we also

present preliminary evidence that reaction products can potentially be diagnostic for reaction pathway and environmental conditions. Mn(II)-phosphates only formed when there were very high (mM) concentrations of phosphate in the media. Mn(II)-carbonates (rhodochrosite) precipitated with high lactate and limiting phosphate, suggesting that this mineral should form in similar natural conditions when organic carbon is in excess of Mn(IV) oxides. In simple systems free of dissolved inorganic carbon, sulfide- and ferrous iron-induced reduction of Mn(IV) oxides produced only soluble  $\text{Mn}^{2+}$ , but further experiments are necessary to examine whether Mn(II)-carbonates can form abiotically under more realistic conditions with inorganic carbon present. When  $\text{Mn}^{2+}$  is formed, this soluble product will be able to migrate away from the reaction locus. If surrounding conditions are anoxic, this could result in a Mn loss to the system. If these reactions are occurring in sediments near the oxic-anoxic boundary, then this may simply recycle Mn back to where there is oxygen and  $\text{Mn}^{2+}$  can be re-oxidized and re-precipitated.

Mn(III) oxyhydroxides are intriguing yet complex: they appear to form in both abiotic and biotic reduction reactions, and thus are not distinctive for reduction pathway, but they also present as an appealing precursor to the Mn(III) phase in the rock record, braunite. One of the proposed pathways of braunite formation involves reacting a Mn(III) oxide,  $\text{Mn}_2\text{O}_3$ , with silica ( $\text{SiO}_2$ )<sup>52</sup>, and this Mn(III) oxyhydroxide may be an attractive phase to begin this reaction with. In the rock record, braunite is always present with Mn(II)-carbonates (Johnson et al, Chapter 1), which, according to our experiments, is consistent with microbial Mn(IV) reduction since that reaction does make a Mn(III) oxyhydroxide

and (eventually) Mn(II)-carbonate and the reaction extent could be separated in pore spaces to have access to different levels of organic carbon. A mixture of Mn(III) oxides and Mn(II) carbonate could also be formed in any system with manganese oxides, a reductant that does not lower the pH (i.e., not ferrous iron), and sufficient dissolved inorganic carbon, so this assemblage does not necessarily imply a microbial presence.

Time-resolved measurements throughout the reduction sequences of microbial manganese oxide reduction harnessing lactate and abiotic manganese oxide reduction with sulfide and ferrous iron reveal the importance of kinetics and geochemical environment to understand reaction pathways and products. We observe  $\text{MnCO}_3$  (rhodochrosite) precipitation upon microbial  $\text{MnO}_2$  reduction with deficient phosphate and high organic carbon conditions, but a Mn(II)-phosphate product when phosphate is abundant. The kinetics of Mn(II)-phosphate precipitation are so rapid that the high-phosphate experiments show that Mn(IV) reduction by *S. oneidensis* is effectively a 2-electron reduction. Mn(III) oxyhydroxides are formed during other reduction conditions, and reductant availability predominantly controls whether Mn(III) oxyhydroxides are formed as an intermediate or a product. Abiotic  $\text{MnO}_2$  reduction using ferrous iron and sulfide terminally produced  $\text{Mn}^{2+}$  in solution, but  $\text{MnO}_2$ -sulfide reactions could produce  $\text{MnCO}_3$  with available dissolved inorganic carbon. By recognizing unique products from different  $\text{MnO}_2$  reduction pathways, we can now begin to more accurately link the geologic record on Earth with a process-based understanding of mineral genesis.

## **ACKNOWLEDGEMENTS**

We would like to express our gratitude to Cynthia Patty, John Bargar, Courtney Roach, and Cathy Knotts for going above and beyond so that it was possible for us to run these experiments at the synchrotron; to Jeffrey Gralnick, Annie Rowe and Jim Hemp for experimental assistance and advice; and to George Rossman for assistance and frequent access to his RAMAN and Fourier Transform Infrared Spectrometer. We acknowledge a Packard Foundation grant to W.W.F., which funded much of this research, and an NSF Graduate Research Fellowship to J.E.J. Portions of this research were carried out at the Stanford Synchrotron Radiation Lightsource, a Directorate of SLAC National Accelerator Laboratory and an Office of Science User Facility operated for the US Department of Energy Office of Science by Stanford University.

## FIGURES

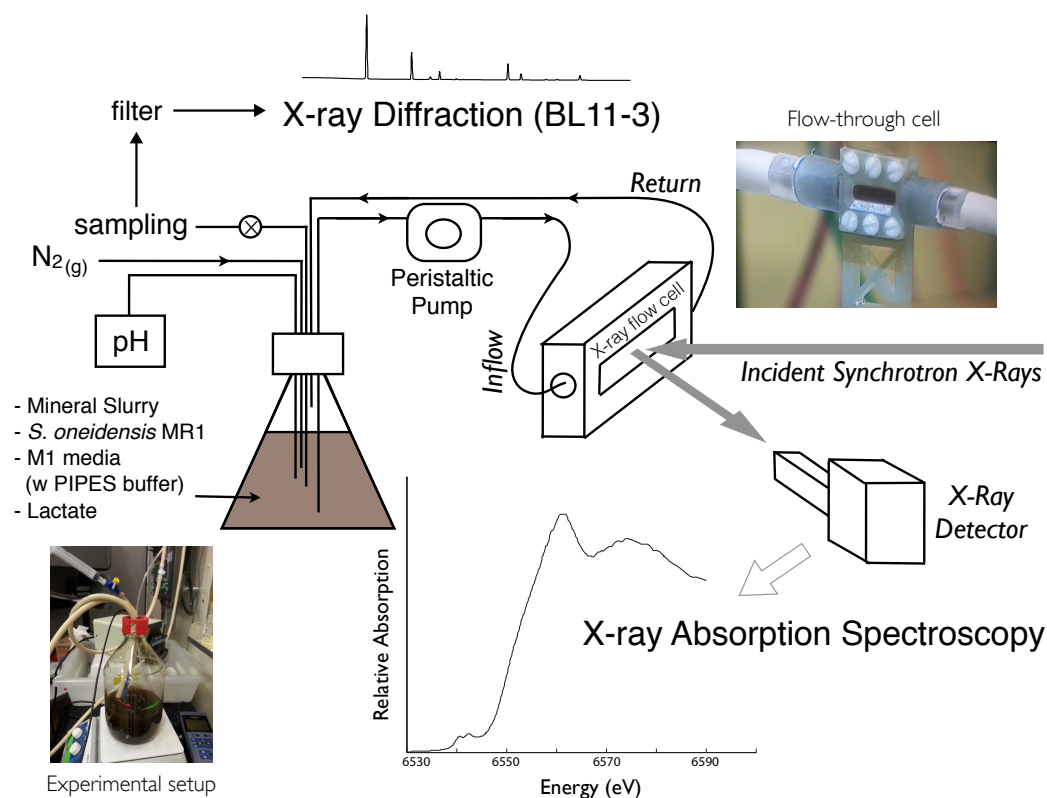
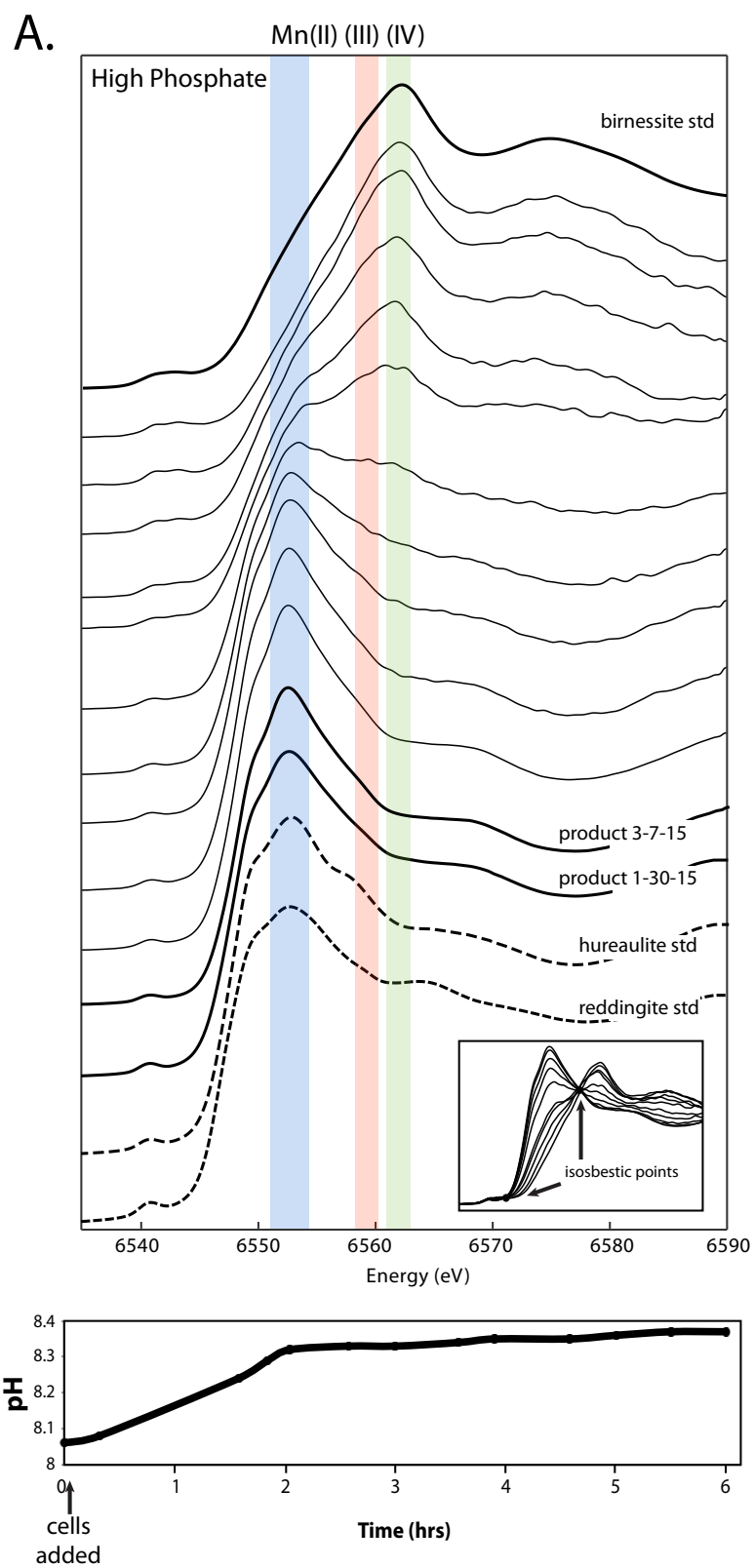
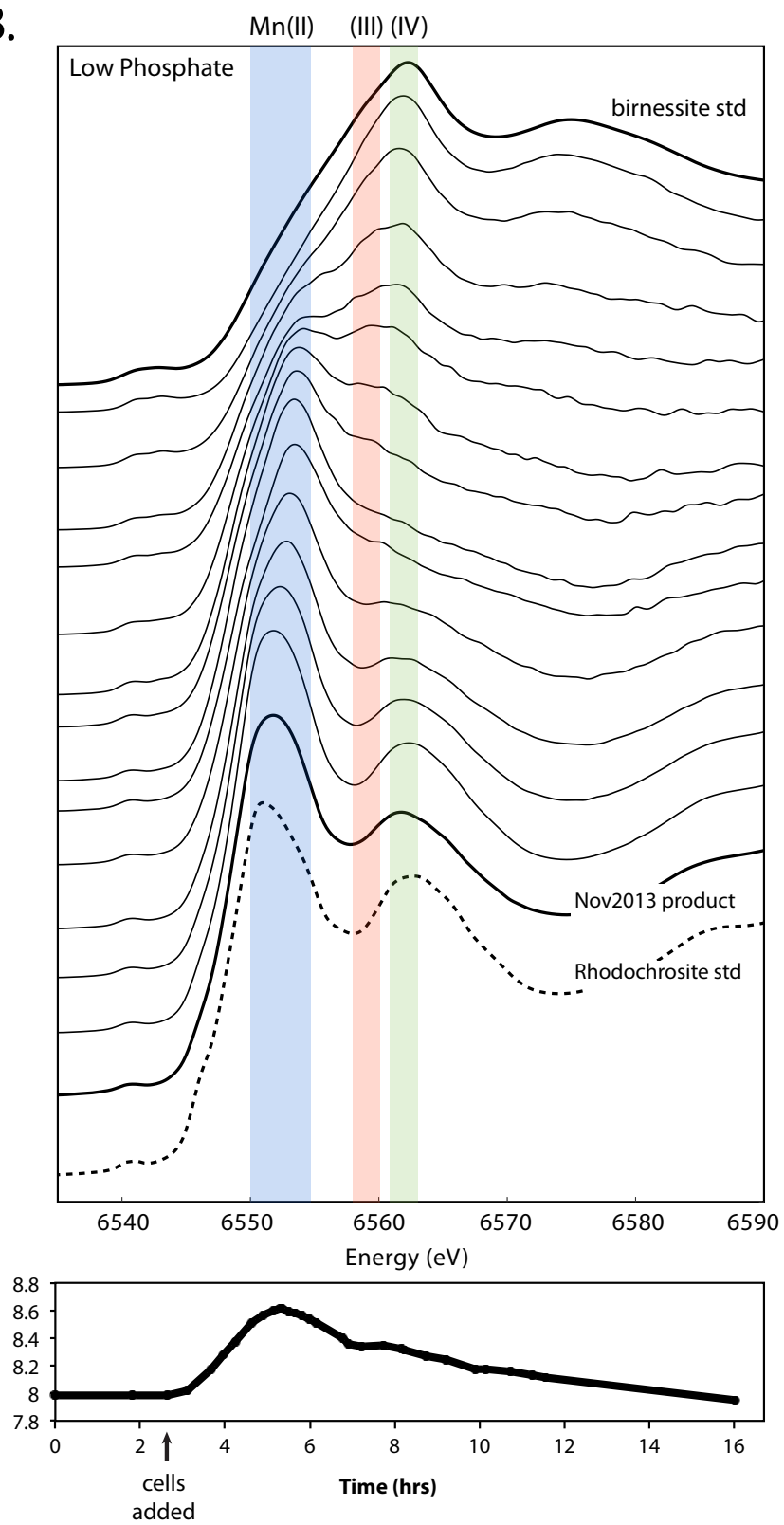


**Figure 1** – Schematic of flow-through system showing reaction vessel with colloidal manganese oxide mineral slurry, M1 media with PIPES buffer, and (depending on experiment) lactate and *S. oneidensis*. The reaction vessel was kept anoxic with  $N_2$  and pH was measured via an environmental pH probe. A sampling portal enabled acquisition of hourly filter samples to be later measured on a synchrotron X-ray diffraction beam line. A peristaltic pump brought a representative portion of the flow-through cell through anaerobic tubing into the beam line hutch, where the X-ray beam could sample the Mn mineralogy, coordination environment and redox state through a window on an X-ray flow through cell. The resultant X-ray absorption spectra was measured on a X-ray detector. Photos of the reaction vessel and flow-through cell are shown alongside the schematic drawing.

Figure 2



B.





C.

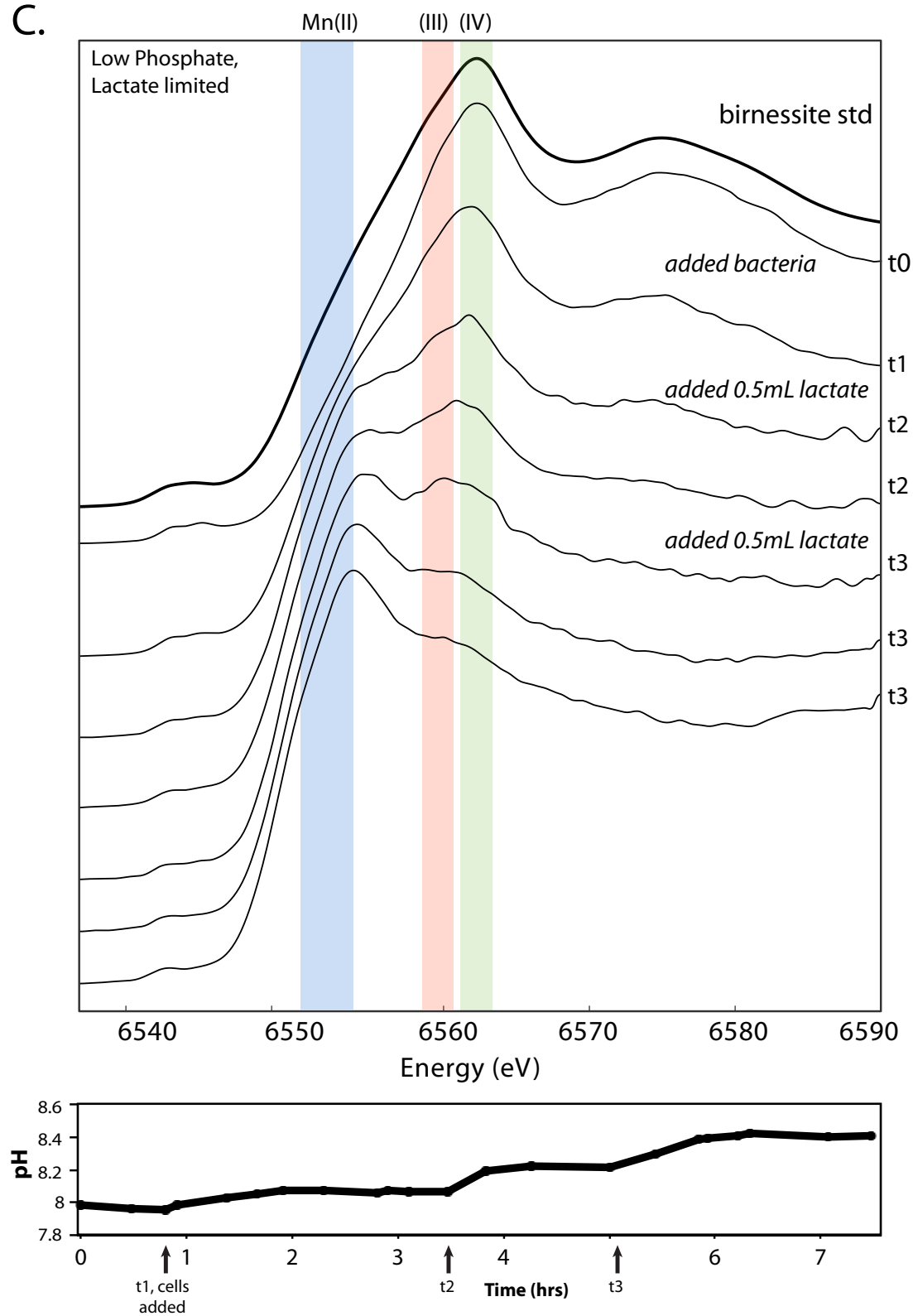
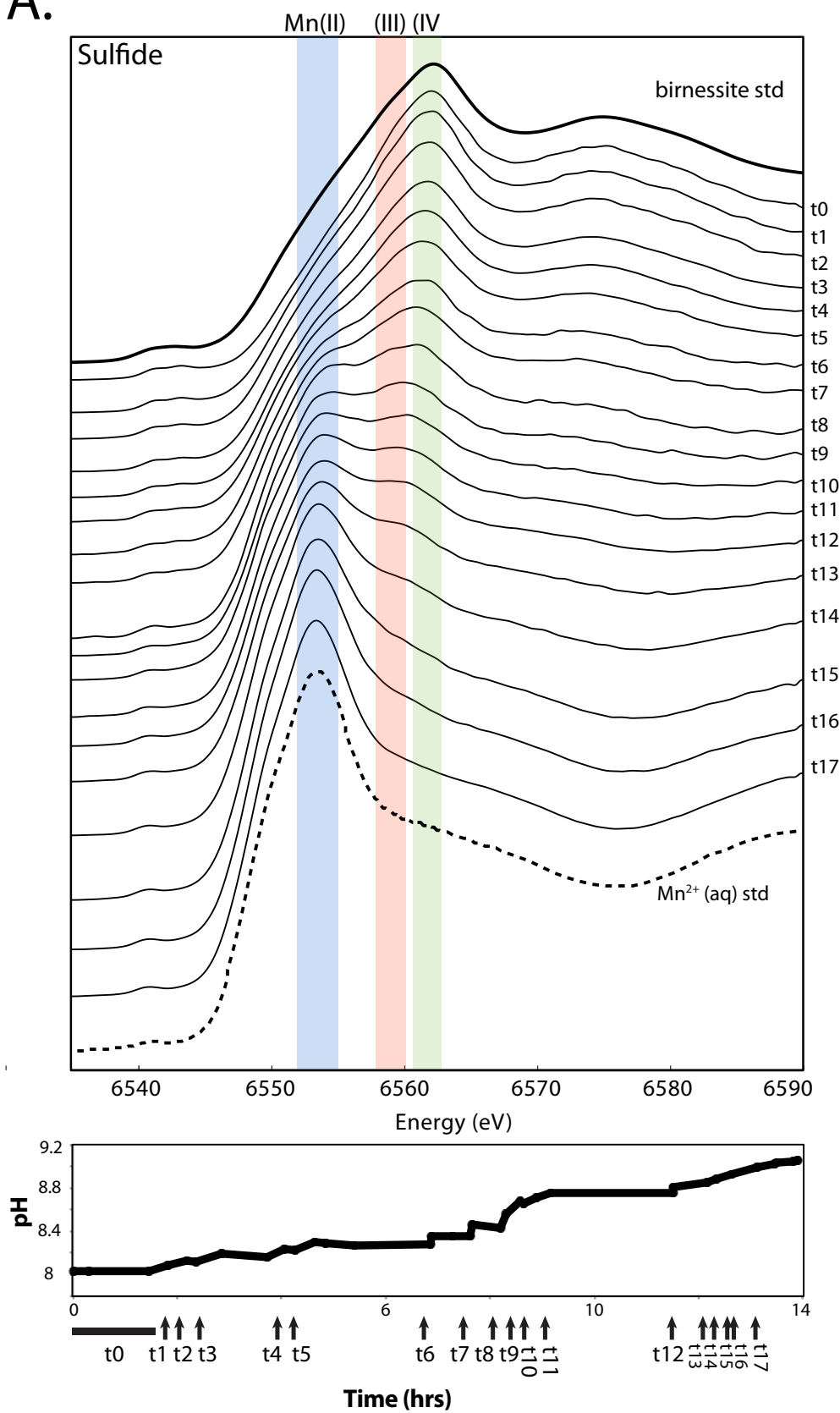


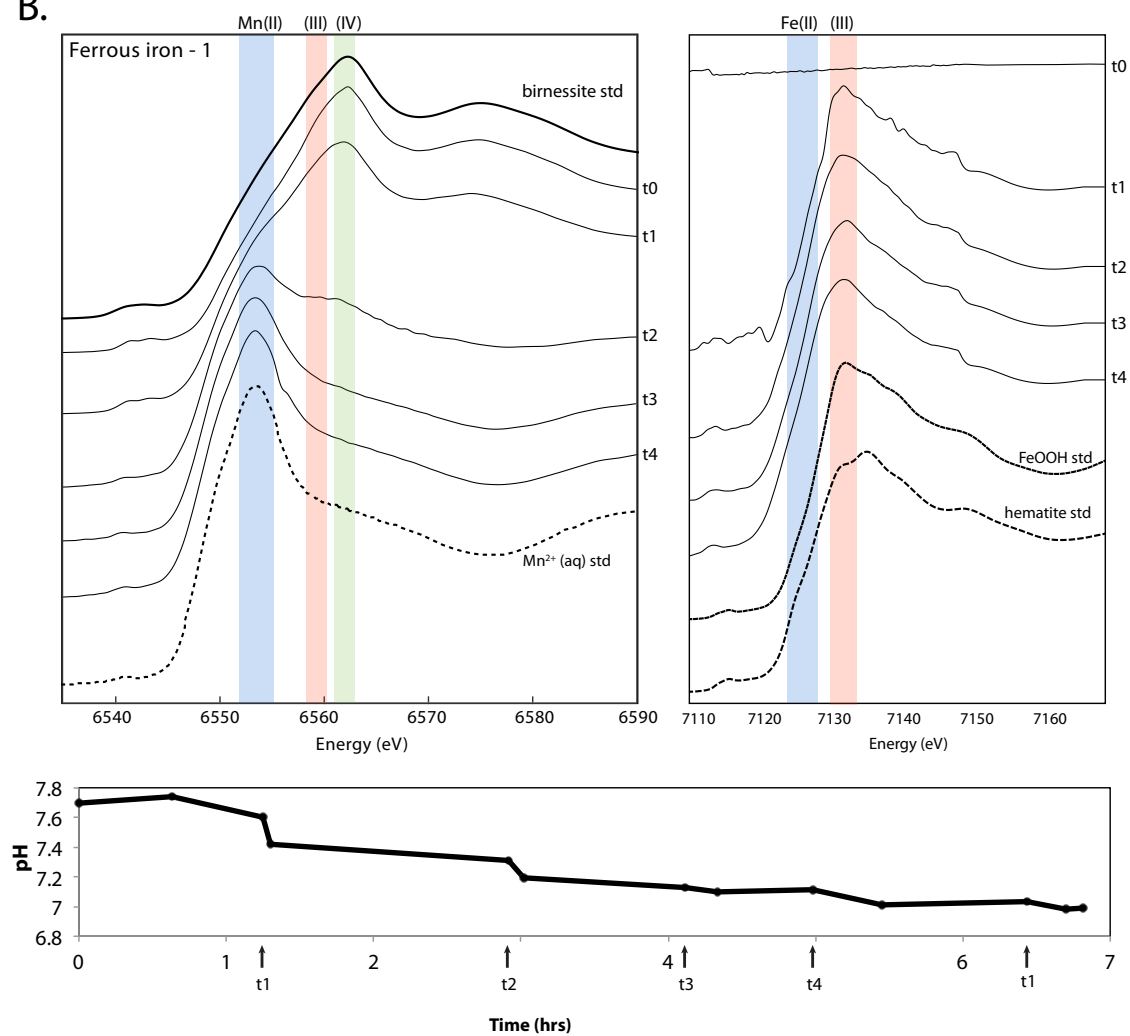
**Figure 2** – Three representative microbial reduction experiments observing the reduction sequence induced by *S. oneidensis* are depicted via a waterfall, with the initial colloidal MnO<sub>2</sub> (MnIV, similar to a birnessite) at the top and the progression of spectra shown descending to a final product at the bottom. When appropriate, relevant standard spectra are shown below the product spectra. A time course of pH measurements is plotted below each experiment. A. High (4.3mM) phosphate experiment, proceeding from MnO<sub>2</sub> to a Mn(II) phosphate similar to hureaulite (Mn<sup>2+</sup><sub>5</sub>(PO<sub>3</sub>OH)<sub>2</sub>(PO<sub>4</sub>)<sub>2</sub>\*4H<sub>2</sub>O). B. High (20mM) lactate experiment, evolving colloidal MnO<sub>2</sub> to rhodochrosite (MnCO<sub>3</sub>). A product from an earlier experiment and a rhodochrosite standard are shown for comparison. C. Lactate-limited experiment, beginning at 0.5mM lactate with two additions of 0.5mM lactate. See text for further details.

**Figure 3 (below)** – Three representative abiotic reduction experiments observing the reduction sequence induced by various species are depicted via a waterfall, with the initial colloidal MnO<sub>2</sub> (similar to a MnIV birnessite) at the top and the progression of spectra shown descending to a final product at the bottom. When appropriate, relevant standard spectra are shown below the product spectra. pH measurements are plotted below each experiment. A. Sulfide-induced manganese oxide reduction, evolving to a Mn<sup>2+</sup> solution. B. Ferrous iron titration of manganese oxides, with both manganese and iron X-ray absorption spectra shown. Mn(IV) proceeds to Mn<sup>2+</sup> while iron added all appears to be rapidly oxidized to Fe(III) oxides. pH drops with each iron addition. C. Another representative experiment showing how ferrous iron reduces manganese. Only manganese spectra are shown. This is an incomplete reduction and a Mn(III) phase can be observed.

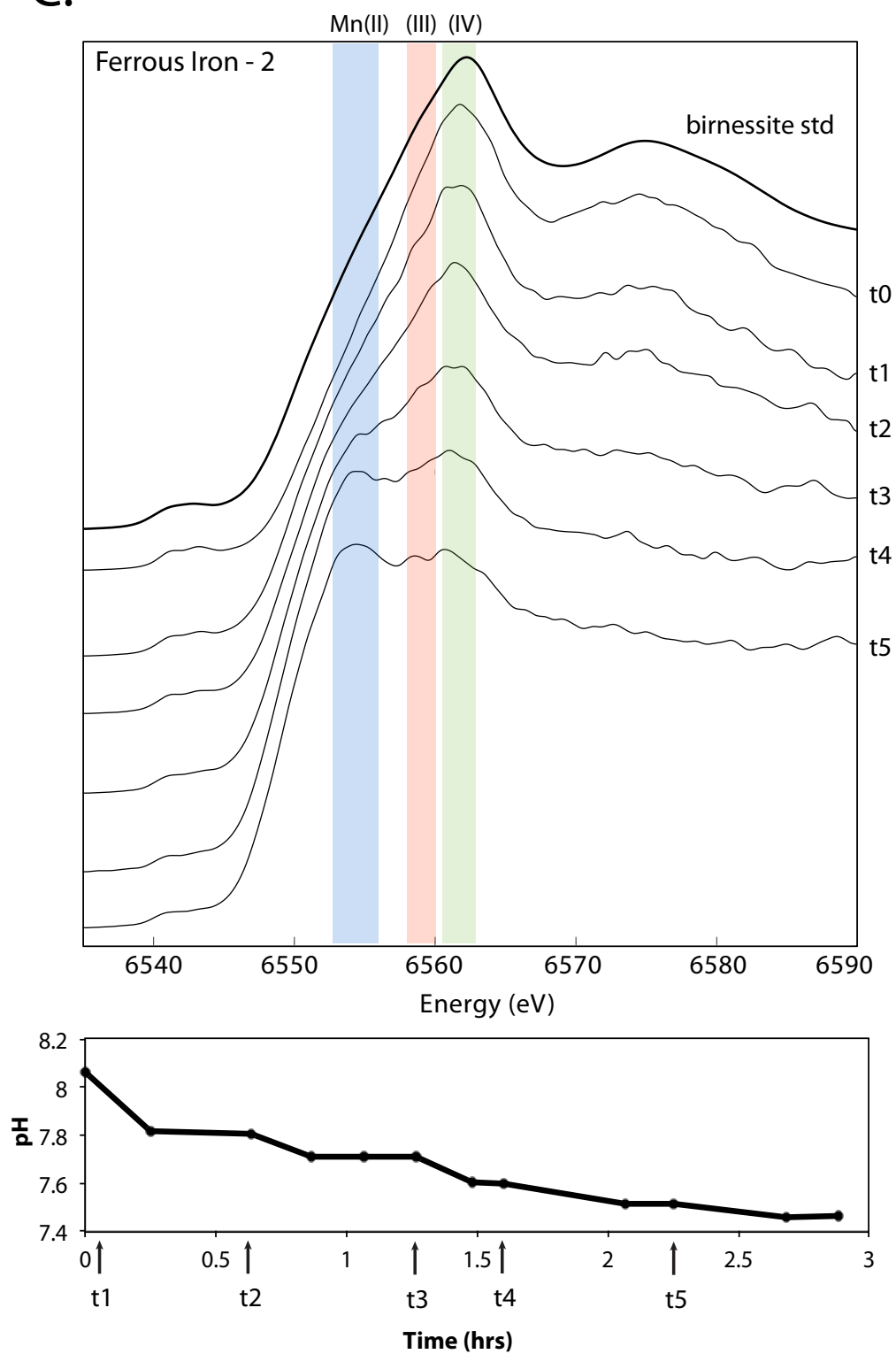
A.



B.



C.



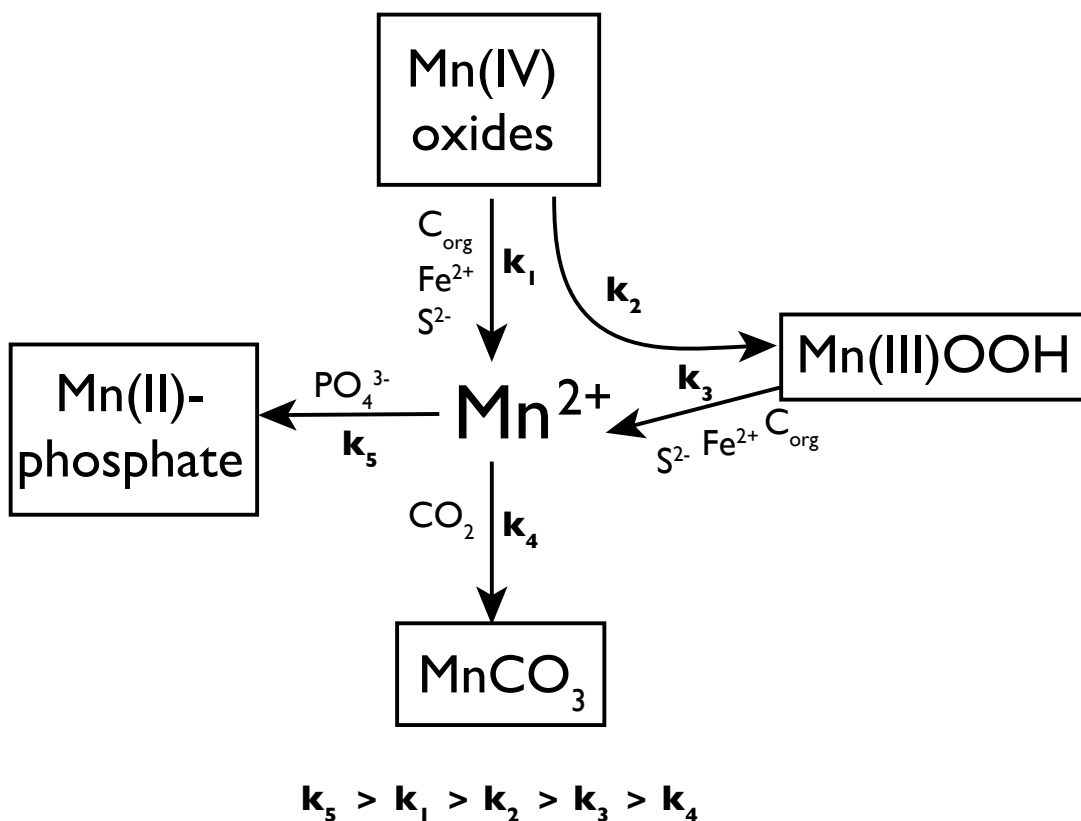


**Figure 4** – Our model of how various manganese reduction pathways lead to  $\text{Mn}^{2+}$ , which then can react with Mn(IV) oxides to produce Mn(III) oxyhydroxides or precipitate as Mn(II) phosphates or  $\text{MnCO}_3$ .

$\mathbf{k_1}$ : kinetic rate constant for reduction of Mn(IV) to  $\text{Mn}^{2+}$

$\mathbf{k_2}$ : kinetic rate constant for comproportionation reaction between Mn(IV) and  $\text{Mn}^{2+}$  to Mn(III) oxyhydroxides

$\mathbf{k_3}$ : kinetic rate constant for reduction of Mn(III) to  $\text{Mn}^{2+}$

$\mathbf{k_4}$ : kinetic rate constant for precipitation of  $\text{MnCO}_3$  from  $\text{Mn}^{2+}$  and  $\text{CO}_3^{2-}$

$\mathbf{k_5}$ : kinetic rate constant for precipitation of  $\text{MnCO}_3$  from  $\text{Mn}^{2+}$  and  $\text{PO}_4^{3-}$

## REFERENCES

- (1) Tebo, B. M.; Johnson, H. A.; McCarthy, J. K.; Templeton, A. S. Geomicrobiology of manganese(II) oxidation. *Trends Microbiol.* **2005**, *13* (9), 421–428.
- (2) Post, J. E. Manganese oxide minerals: Crystal structures and economic and environmental significance. *Proc. Natl. Acad. Sci.* **1999**, *96* (7), 3447–3454.
- (3) Calvert, S. E.; Pedersen, T. F. Sedimentary geochemistry of manganese; implications for the environment of formation of manganiferous black shales. *Econ. Geol.* **1996**, *91* (1), 36–47.
- (4) Armstrong, F. A. Why Did Nature Choose Manganese to Make Oxygen? *Philos. Trans. R. Soc. B Biol. Sci.* **2008**, *363* (1494), 1263–1270.
- (5) Lovley, D. R.; Phillips, E. J. P. Novel Mode of Microbial Energy Metabolism: Organic Carbon Oxidation Coupled to Dissimilatory Reduction of Iron or Manganese. *Appl. Environ. Microbiol.* **1988**, *54* (6), 1472–1480.
- (6) Myers, C. R.; Nealson, K. H. Bacterial manganese reduction and growth with manganese oxide as the sole electron acceptor. *Science* **1988**, *240* (4857), 1319–1321.
- (7) Van Cappellen, P.; Viollier, E.; Roychoudhury, A.; Clark, L.; Ingali, E.; Lowe, K.; Dichristina, T. Cycling of iron and manganese in surface sediments; a general theory for the coupled transport and reaction of carbon, oxygen, nitrogen, sulfur, iron, and manganese. *Environ. Sci. Technol.* **1998**, *32*, 2931–2939.
- (8) Canfield, D. E.; Thamdrup, B.; Hansen, J. W. The anaerobic degradation of organic matter in Danish coastal sediments: Iron reduction, manganese reduction, and sulfate reduction. *Geochim. Cosmochim. Acta* **1993**, *57* (16), 3867–3883.
- (9) Thamdrup, B.; Rosselló-Mora, R.; Amann, R. Microbial Manganese and Sulfate Reduction in Black Sea Shelf Sediments. *Appl. Environ. Microbiol.* **2000**, *66* (7), 2888–2897.
- (10) Burdige, D. J.; Nealson, K. H. Chemical and microbiological studies of sulfide-mediated manganese reduction. *Geomicrobiol. J.* **1986**, *4* (4), 361–387.
- (11) Myers, C. R.; Nealson, K. H. Microbial reduction of manganese oxides: Interactions with iron and sulfur. *Geochim. Cosmochim. Acta* **1988**, *52* (11), 2727–2732.
- (12) Ying, S. C.; Kocar, B. D.; Griffis, S. D.; Fendorf, S. Competitive Microbially and Mn Oxide Mediated Redox Processes Controlling Arsenic Speciation and Partitioning. *Environ. Sci. Technol.* **2011**, *45* (13), 5572–5579.
- (13) Fredrickson, J. K.; Zachara, J. M.; Kennedy, D. W.; Liu, C.; Duff, M. C.; Hunter, D. B.; Dohnalkova, A. Influence of Mn oxides on the reduction of uranium(VI) by the metal-reducing bacterium *Shewanella putrefaciens*. *Geochim. Cosmochim. Acta* **2002**, *66* (18), 3247–3262.
- (14) Webb, S. M.; Tebo, B. M.; Bargar, J. R. Structural characterization of biogenic Mn oxides produced in seawater by the marine bacillus sp. strain SG-1. *Am. Mineral.* **2005**, *90* (8-9), 1342–1357.

- (15) Bargar, J. R.; Tebo, B. M.; Villinski, J. E. In situ characterization of Mn(II) oxidation by spores of the marine *Bacillus* sp. strain SG-1. *Geochim. Cosmochim. Acta* **2000**, *64*, 2775–2778.
- (16) Murray, J. W.; Dillard, J. G.; Giovanoli, R.; Moers, H.; Stumm, W. Oxidation of Mn(II): Initial mineralogy, oxidation state and ageing. *Geochim. Cosmochim. Acta* **1985**, *49* (2), 463–470.
- (17) Wehrli, B.; Friedl, G.; Manceau, A. Reaction Rates and Products of Manganese Oxidation at the Sediment-Water Interface. In *Aquatic Chemistry*; Advances in Chemistry; American Chemical Society, 1995; Vol. 244, pp 111–134.
- (18) McKeown, D. A.; Post, J. E. Characterization of manganese oxide mineralogy in rock varnish and dendrites using X-ray absorption spectroscopy. *Am. Mineral.* **2001**, *86* (5-6), 701–713.
- (19) Tebo, B. M.; Bargar, J. R.; Clement, B. G.; Dick, G. J.; Murray, K. J.; Parker, D.; Verity, R.; Webb, S. M. BIOGENIC MANGANESE OXIDES: Properties and Mechanisms of Formation. *Annu. Rev. Earth Planet. Sci.* **2004**, *32* (1), 287–328.
- (20) Roy, S. Sedimentary manganese metallogenesis in response to the evolution of the Earth system. *Earth-Sci. Rev.* **2006**, *77* (4), 273–305.
- (21) Maynard, J. B. The Chemistry of Manganese Ores through Time: A Signal of Increasing Diversity of Earth-Surface Environments. *Econ. Geol.* **2010**, *105* (3), 535–552.
- (22) Okita, P. M.; Maynard, J. B.; Spiker, E. C.; Force, E. R. Isotopic evidence for organic matter oxidation by manganese reduction in the formation of stratiform manganese carbonate ore. *Geochim. Cosmochim. Acta* **1988**, *52* (11), 2679–2685.
- (23) Johnson, J. E.; Webb, S. M.; Ma, C.; Fischer, W. W. Manganese mineralogy and diagenesis in the sedimentary rock record. *Geochim. Cosmochim. Acta* **in review**.
- (24) Coleman, M. L.; Fleet, A.; Donson, P. *Preliminary studies of manganese-rich carbonate nodules from Leg 68, Site 503, eastern equatorial Pacific*; Init. Repts. DSDP 68; 1982; pp 481–489.
- (25) Johnson, J. E.; Webb, S. M.; Thomas, K.; Ono, S.; Kirschvink, J. L.; Fischer, W. W. Manganese-oxidizing photosynthesis before the rise of cyanobacteria. *Proc. Natl. Acad. Sci.* **2013**, *110* (28), 11238–11243.
- (26) Nealson, K. H.; Saffarini, D. Iron and Manganese in Anaerobic Respiration: Environmental Significance, Physiology, and Regulation. *Annu. Rev. Microbiol.* **1994**, *48* (1), 311–343.
- (27) Böttcher, M. E.; Thamdrup, B. Anaerobic sulfide oxidation and stable isotope fractionation associated with bacterial sulfur disproportionation in the presence of MnO<sub>2</sub>. *Geochim. Cosmochim. Acta* **2001**, *65* (10), 1573–1581.
- (28) Meister, P.; Bernasconi, S. M.; Aiello, I. W.; Vasconcelos, C.; McKenzie, J. A. Depth and controls of Ca-rhodochrosite precipitation in bioturbated sediments of the Eastern Equatorial Pacific, ODP Leg 201, Site 1226 and DSDP Leg 68, Site 503. *Sedimentology* **2009**, *56* (5), 1552–1568.
- (29) Huckriede, H.; Meischner, D. Origin and environment of manganese-rich sediments within black-shale basins. *Geochim. Cosmochim. Acta* **1996**, *60* (8), 1399–1413.



- (30) Lee, J.-H.; Kennedy, D. W.; Dohnalkova, A.; Moore, D. A.; Nachimuthu, P.; Reed, S. B.; Fredrickson, J. K. Manganese sulfide formation via concomitant microbial manganese oxide and thiosulfate reduction. *Environ. Microbiol.* **2011**, *13* (12), 3275–3288.
- (31) Fischer, T. B.; Heaney, P. J.; Jang, J.-H.; Ross, D. E.; Brantley, S. L.; Post, J. E.; Tien, M. Continuous time-resolved X-ray diffraction of the biocatalyzed reduction of Mn oxide. *Am. Mineral.* **2008**, *93* (11-12), 1929–1932.
- (32) Brown, G. E.; Sturchio, N. C. An Overview of Synchrotron Radiation Applications to Low Temperature Geochemistry and Environmental Science. *Rev. Mineral. Geochem.* **2002**, *49* (1), 1–115.
- (33) Manceau, A.; Marcus, M. A.; Grangeon, S. Determination of Mn valence states in mixed-valent manganates by XANES spectroscopy. *Am. Mineral.* **2012**, *97*, 816–827.
- (34) Bargar, J. R.; Webb, S. M.; Synchrotron, S. Structural Determination of Marine Bacteriogenic Manganese Oxides. *Sci. York* **2005**, No. August, 1–4.
- (35) Webb, S. M.; Dick, G. J.; Bargar, J. R.; Tebo, B. M. Evidence for the presence of Mn(III) intermediates in the bacterial oxidation of Mn(II). *Proc. Natl. Acad. Sci. U. S. A.* **2005**, *102* (15), 5558–5563.
- (36) Kostka, J.; Nealson, K. H. Isolation, Cultivation and Characterization of Iron- and Manganese-Reducing Bacteria. In *Techniques in Microbial Ecology*; Burlage, R. S., Atlas, R., Stahl, D., Geesey, G., Sayler, G., Eds.; Oxford University Press: Oxford, 1998; p 468.
- (37) Richardson, D. J.; Butt, J. N.; Fredrickson, J. K.; Zachara, J. M.; Shi, L.; Edwards, M. J.; White, G.; Baiden, N.; Gates, A. J.; Marritt, S. J.; et al. The “porin-cytochrome” model for microbe-to-mineral electron transfer. *Mol. Microbiol.* **2012**, *85* (2), 201–212.
- (38) Lin, H.; Szeinbaum, N. H.; DiChristina, T. J.; Taillefert, M. Microbial Mn(IV) reduction requires an initial one-electron reductive solubilization step. *Geochim. Cosmochim. Acta* **2012**, *99*, 179–192.
- (39) Harris, H. W.; El-Naggar, M. Y.; Bretschger, O.; Ward, M. J.; Romine, M. F.; Obraztsova, A. Y.; Nealson, K. H. Electrokinesis is a microbial behavior that requires extracellular electron transport. *Proc. Natl. Acad. Sci.* **2010**, *107* (1), 326–331.
- (40) Marsili, E.; Baron, D. B.; Shikhare, I. D.; Coursolle, D.; Gralnick, J. A.; Bond, D. R. *Shewanella* secretes flavins that mediate extracellular electron transfer. *Proc. Natl. Acad. Sci.* **2008**, *105* (10), 3968–3973.
- (41) Kotloski, N. J.; Gralnick, J. A. Flavin electron shuttles dominate extracellular electron transfer by *Shewanella oneidensis*. *mBio* **2013**, *4* (1).
- (42) Gorby, Y. A.; Yanina, S.; McLean, J. S.; Rosso, K. M.; Moyles, D.; Dohnalkova, A.; Beveridge, T. J.; Chang, I. S.; Kim, B. H.; Kim, K. S.; et al. Electrically conductive bacterial nanowires produced by *Shewanella oneidensis* strain MR-1 and other microorganisms. *Proc. Natl. Acad. Sci.* **2006**, *103* (30), 11358–11363.

- (43) Myers, C. R.; Myers, J. M. Localization of cytochromes to the outer membrane of anaerobically grown *Shewanella putrefaciens* MR-1. *J. Bacteriol.* **1992**, *174* (11), 3429–3438.
- (44) Okamoto, A.; Hashimoto, K.; Nealson, K. H.; Nakamura, R. Rate enhancement of bacterial extracellular electron transport involves bound flavin semiquinones. *Proc. Natl. Acad. Sci. U. S. A.* **2013**, *110* (19), 7856–7861.
- (45) Bergmann, K. D.; Grotzinger, J. P.; Fischer, W. W. Biological Influences on Seafloor Carbonate Precipitation. *PALAIOS* **2013**, *28* (2), 99–115.
- (46) Conkright, M. E.; Garcia, H. E.; O'Brien, T. D.; Locarnini, R. A.; Boyer, T. P.; Antonov, C. S. *World Ocean Atlas 2001*; Levitus, E., Ed.; NOAA Atlas NESDIS 52; U.S. Gov. Printing Office: Wash., D.C., 2002; Vol. 4: Nutrients.
- (47) Williams, R. G.; Follows, M. J. *Ocean Dynamics and the Carbon Cycle: Principles and Mechanisms*; Cambridge University Press: New York City, 2011.
- (48) O'Day, P. A.; Rivera, N.; Root, R.; Carroll, S. A. X-ray absorption spectroscopic study of Fe reference compounds for the analysis of natural sediments. *Am. Mineral.* **2004**, *89* (4), 572–585.
- (49) Sternbeck, J. Kinetics of rhodochrosite crystal growth at 25°C: The role of surface speciation. *Geochim. Cosmochim. Acta* **1997**, *61* (4), 785–793.
- (50) Jensen, D. L.; Boddum, J. K.; Tjell, J. C.; Christensen, T. H. The solubility of rhodochrosite (MnCO<sub>3</sub>) and siderite (FeCO<sub>3</sub>) in anaerobic aquatic environments. *Appl. Geochem.* **2002**, *17* (4), 503–511.
- (51) Robie, R. A.; Huebner, J. S.; Hemingway, B. S. Heat capacities and thermodynamic properties of braunite (Mn<sub>7</sub>SiO<sub>12</sub>) and rhodonite (MnSiO<sub>3</sub>). *Am. Mineral.* **1995**, *80*, 560–575.

## SUPPORTING FIGURES

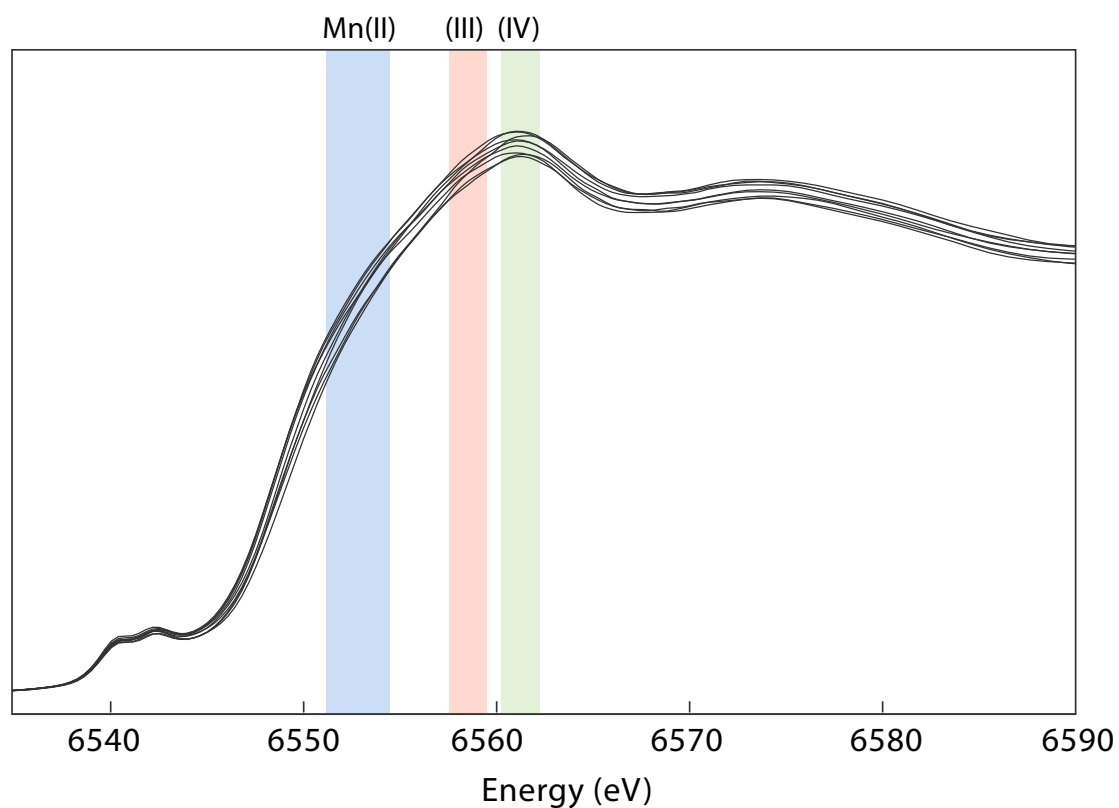


**Figure S1** – Control reaction, showing > 5 hours of Mn X-ray absorption spectra with colloidal  $\text{MnO}_2$  and 20mM lactate are in solution. Unchanging spectra indicate that there is no perceptible abiotic reaction between colloidal  $\text{MnO}_2$  and lactate in a multi-hour time frame and no clear X-ray beam reduction of manganese.

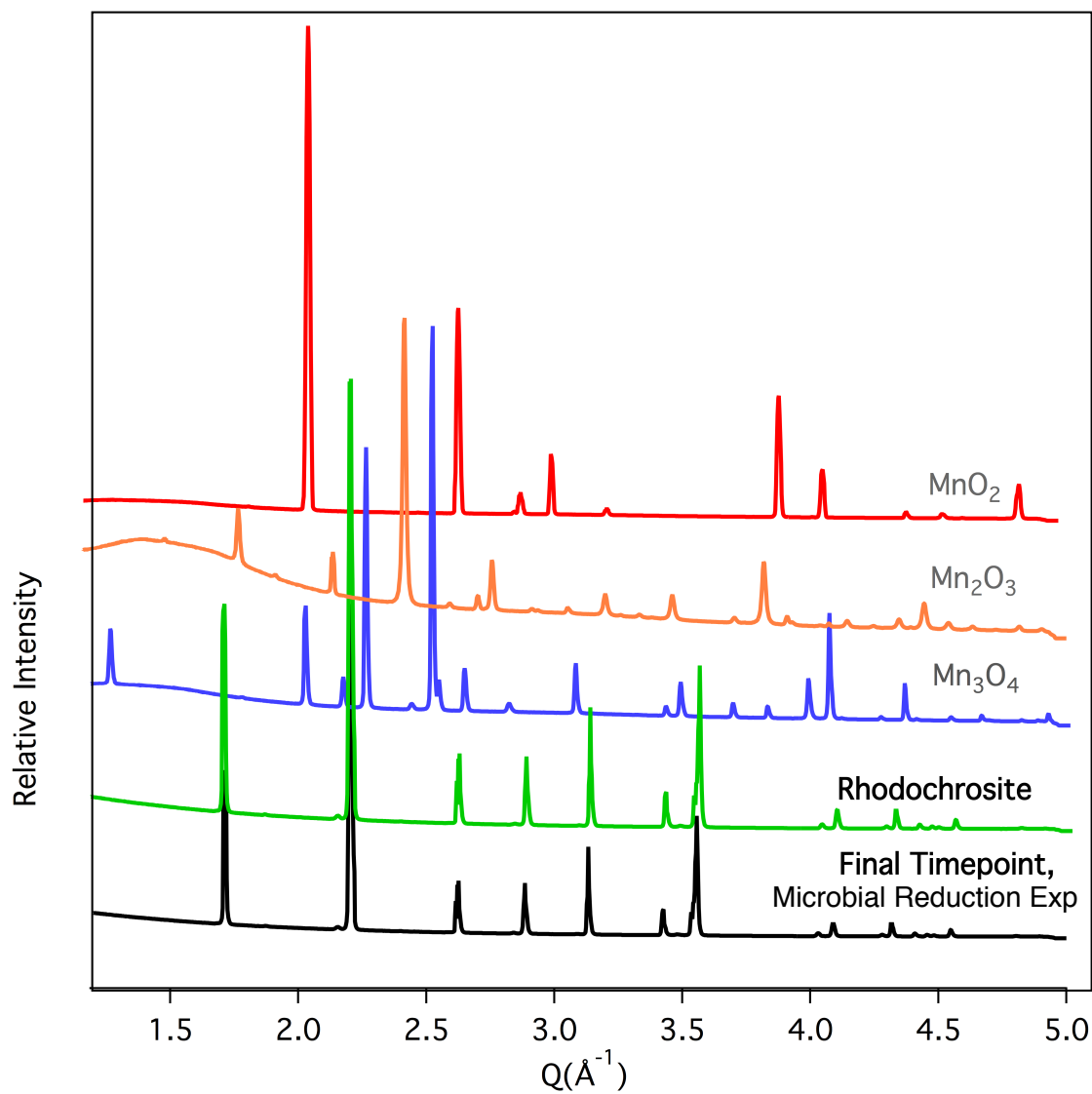


**Figure S2** – X-ray diffraction data comparing manganese standards to the final crystalline product of manganese oxide reduction by *S. oneidensis* using lactate (20mM).

*Chapter 5***Manganese mobility during metamorphism: An example from the 2.5 Ga Kuruman-Penge Formation**

Jena E Johnson<sup>1</sup>, Samuel M. Webb<sup>2</sup>, Nic J. Beukes<sup>3</sup>, Woodward W. Fischer<sup>1</sup>

<sup>1</sup>Division of Geological and Planetary Sciences, California Institute of Technology, Pasadena, CA 91125, USA. <sup>2</sup>Stanford Synchrotron Radiation Lightsource, Menlo Park CA 94025. <sup>3</sup>University of Johannesburg, Auckland Park, South Africa

**ABSTRACT**

**Manganese-enriched sedimentary rocks from the geologic record are often used as evidence of an oxygenated water column. This inference stems from two important attributes of manganese: 1) manganese concentration in sedimentary rocks requires oxidation and 2) thermodynamics dictates that manganese oxidation demands high redox potential species like oxygen. For massive deposits of manganese dating to after the great rise in oxygen at ca. 2.3 billion years ago, this logic likely holds true. However, there are several ancient examples of manganese-enriched rocks before the emergence of free oxygen, conflicting with the classical proxies for oxygen like redox-sensitive detrital grains and the behavior of iron in paleosols. We probed one such reported manganese enrichment in a highly metamorphosed succession in the Transvaal Supergroup from the South African Kaapvaal Craton (Miyano and Beukes, 1997). These sedimentary rocks date to ca. 2.5 billion years ago, well before the great rise of oxygen, and comprise a craton-wide sequence that has established metamorphic gradients due to contact metamorphism from the 2.05 Ga Bushveld Igneous Complex in the eastern Transvaal basin. We collected core samples across a transect of correlative rocks through a metamorphic gradient from lower**

greenschist facies in the west up to amphibolite facies in the east. Examining these samples with whole-rock ICP-MS, X-ray fluorescence and spectroscopic imaging, and electron microscopic analyses including energy dispersive spectrometry and backscatter diffraction, we determined that manganese was primarily in trace levels in authigenic and detrital carbonates, but at higher metamorphic grades manganese had been enriched in and precipitated as manganoan garnets, amphiboles, and a variety of carbonates. Both texture and mineralogical assemblages yield clues to the source, whether depositional or metasomatic, of the manganese. Our results indicate that manganese can and does become enriched in minerals and, occasionally, in whole-rock concentrations during contact metamorphism. However, we cannot distinguish between more local mobilization and Mn concentration from nearby sediments and/or the underlying Archean carbonates, or Mn sourcing from hydrothermal fluids enriched in manganese. Regardless, our well-preserved samples suggest that manganese was not being significantly oxidized and concentrated in western Kaapvaal Craton sediments at 2.5 Ga.

## INTRODUCTION

Manganese is a powerful redox proxy to understand ancient environmental redox conditions. Unlike various other redox proxies, manganese has a very high reduction-oxidation potential and thus only certain common environmental oxidants like O<sub>2</sub> or species derived from O<sub>2</sub> like superoxide can chemically oxidize manganese (Stumm and Morgan, 1996; Luther, 2010). When manganese is oxidized, it is deposited in the

sediments and therefore concentrated in the rock record. However, reduced manganese ( $\text{Mn}^{2+}$ ) is soluble and manganese will remain as a reduced cation in anoxic water with its primary sink being a low degree ( $\leq 1\%$ ) of substitution for Ca in carbonates (Veizer, 1978; Wallmann et al., 2008). Archean carbonates from before the rise of oxygen consequently have high Mn levels of approximately 1% MnO while Phanerozoic carbonates record a very different Mn cycle, averaging 30ppm MnO (Veizer, 1978; Holland, 1984; Komiya et al., 2008). Manganese has the further advantage of being a major component of the environmental system: as the third most abundant transition metal in Earth's crust, the behavior of manganese and in-depth examinations of its mineral hosts are relatively easy to determine by X-ray spectroscopy. These overall abundance, redox, and solubility attributes of manganese make the rock record of Mn especially illuminating to understand paleo-redox constraints.

Indeed, manganese enrichments have been used as evidence for oxygen during the Precambrian Era time and time again. The largest manganese ore deposit, the giant Kalahari manganese field in the 2.2 Ga Hotazel Formation (Gutzmer, 1996), has been linked to the oxygenation of Earth's surface oceans (Kirschvink et al., 2000). Other major manganese ore deposits appear only after the rise of oxygen (Johnson et al., Chapter 1), consistent with oxygen being required to concentrate manganese in sediments, such as the Neoproterozoic Urucum deposit (Urban et al., 1992), the Jurassic Molango deposit (Okita et al., 1988), and the Oligocene Baltic Sea deposits (Varentsov and Grasselly, 1976).

Manganese-enriched rocks from Archean strata before the rise of oxygen have also been noted in India, Brazil, and South Africa, suggesting small amounts of oxygen may be present prior to the rise of oxygen (Roy, 2000; Smith et al., 2010; Planavsky et al., 2014). These manganese-bearing strata include Mn oxides in shale from the ca. 3.1 Ga Iron Ore Group in the Singhbhum Craton in India, Mn oxides and silicate-carbonates in the ca. 2.8-2.6 Ga Khondalite Group in the Indian Eastern Ghats Belt, Mn oxide ore in stromatolitic chert-carbonate of the ca. 2.7-2.6 Ga Chitradurga Group in the Dharwar Craton, Mn oxide beds in limestone in the >2.65Ga Sandur Group of South India, the ca. 2.9-2.7 Ga Jequie Complex in Brazil with Mn silicate-carbonate protolith, and Mn carbonate and garnet in the ca. 2.9 Ga Witwatersrand-Mozaan succession in South Africa (Roy, 2000; Roy, 2006; Smith et al., 2010; Planavsky et al., 2014). All of these rocks are metamorphosed, with some even categorized in the granulite facies (>700degC and 2-15kbar) (Roy, 2000). This metamorphism creates difficulties in assessing what the primary minerals were in some of these deposits. Furthermore, several of these deposits are highly weathered, and may be formed or enriched in Mn from supergene processes in carbonates during dissolution and oxidative weathering (Varentsov, 1996; Roy, 2006). Traditionally, these Indian, Brazilian, and South African deposits have been interpreted as evidence for manganese oxidation by oxygen and thus oxygenic photosynthesis being present far earlier than the rise of oxygen would suggest (Roy, 2006; Smith et al., 2010; Maynard, 2010; Planavsky et al., 2014).

In this study, we investigated less well-known manganese-enriched minerals from the Transvaal Supergroup in the Kaapvaal Craton of South Africa to understand whether they



were environmental signals of manganese oxidation (and by inference, indicating the presence of oxygen or manganese-oxidizing photosynthesis (Johnson et al., 2013)) prior to the major rise of oxygen. Manganese-enriched garnets from ca. 2.5 billion year old sediments were reported from drill cores obtained near the Bushveld Complex, a massive layered suite that intruded into the Transvaal Supergroup (Eriksson et al., 1995; Miyano and Beukes, 1997). The Kaapvaal craton has well-known metamorphic gradients caused by contact metamorphism associated with the Bushveld Complex in the east, and this enabled us to compare manganese concentrations and mineralogical properties in metamorphosed samples from the eastern Kaapvaal to better-preserved samples from the western Kaapvaal (Kaufman, 1996; Miyano and Beukes, 1997; de Kock et al., 2009). This metamorphic gradient also presents an ideal field laboratory to explore the behavior of manganese under different levels of metamorphism. The western strata in the Griqualand West basin is relatively unaffected and categorized as lower greenschist facies (Miyano and Beukes, 1984) but the eastern portion of the Kaapvaal craton (the Transvaal basin) was strongly impacted by the Bushveld intrusion and is greenschist facies reaching amphibolite facies in places (Buick et al., 2001).

## **GEOLOGIC SETTING**

The Neoproterozoic to Paleoproterozoic lower Transvaal Supergroup in South Africa comprises a well-exposed and well-preserved sequence encompassing the stratigraphy before and after the great rise in oxygen. The Transvaal is recorded in two major basins of the Kaapvaal Craton: the Transvaal basin in the east and the western Griqualand West basin. The Transvaal Supergroup begins with the clastic Wolkberg-Schmidtsdrif

sediments, which are unconformably overlain by the Black Reef Quartzite grading into the Campbellrand-Malmani carbonate platform rocks (Sumner and Beukes, 2006). This platform was 1.5 to 2 km thick, deepening to the south and west, and then it was drowned around 2.5 billion years ago, recorded in the transitional shales and large iron formation deposition hosted by the contemporaneous Kuruman Formation (Griqualand West) and Penge Formation (Transvaal) (Beukes, 1987; Sumner and Beukes, 2006). Subsequent shoaling is indicated by the shallower-water granular iron formation in the Griquatown Formation overlying the Kuruman Formation in Griqualand West, followed by the mixed siliclastic and iron formation-rich Koegas Subgroup (Beukes and Klein, 1992; Johnson et al., 2014). In the Transvaal basin, the Penge Formation is overlain by the carbonates of the Tongwane Formation prior to an unconformity (Guo et al., 2009).

The strata with reported manganese-enriched garnets lie near the boundary between the Campbellrand-Malmani carbonate platform and the Kuruman-Penge iron formation (Miyano and Beukes, 1997), and thus they are constrained across the craton by several important zircon ages. The Gamohaani formation has been dated at  $2521 \pm 3$  Mya (Sumner and Bowring, 1996) and at  $2516 \pm 4$  Mya (Altermann and Nelson, 1998), and the Riries Member of the Kuruman overlying the Groenwater member is constrained by a U-Pb age of  $2460 \pm 5$  Mya (Pickard, 2003). The 2521 Mya age is from a volcanic ash 40-50m below the contact between the Campbellrand-Malmani Subgroup and the Kuruman-Penge Iron Formation of the Transvaal supergroup (Sumner and Bowring, 1996), which is approximately the beginning of our sampling interval.

The Bushveld Complex of southern Africa introduced a massive layered mafic intrusion into the sediments of the Transvaal Supergroup (Harris et al., 2010). The intrusion occurred at approximately 2.05 Ga (Walraven et al., 1990; Buick et al., 2001). Temperatures of  $>700^{\circ}\text{C}$  have been implied by the mineral assemblage in the inner-most zone, which has migmatites, schists, and sillimanite-bearing hornfels (Kaneko and Miyano, 1990). The Bushveld Complex also introduced hydrothermal fluids resulting in major deposits of platinum-group elements, base-metal sulfides, chromites, and vanadium ores (Eriksson et al., 1995; Lee, 1996). Other geochemical and textural studies of the migmatite zone in the Bushveld aureole concluded that there was localized fluid infiltration-driven melting of sandstones, and fluid fluxing caused open-system behavior of at least Ba and Sr during and after melting (Harris et al., 2003). Fluid inclusions from Bushveld Complex granite had daughter crystals with high iron, manganese, chlorine, calcium, sodium, and potassium, suggesting the late Bushveld fluids were enriched in manganese among other elements (Ollila, 1984).

The shales which mark the transition between the carbonate platform and iron formation have been previously reported to host Mn-enriched garnets near the Bushveld complex (Miyano and Beukes, 1997), and this provided a target for our comparison of the manganese phases and abundance throughout the craton. We sampled the same lithologies in cores from the transition between the Campbellrand-Malmani carbonate platform strata and the development of the overlying Kuruman-Penge iron formation, carefully selecting cores adjacent to the Bushveld complex and from the well-preserved rocks to the west (Figure1). The metamorphism-affected cores chosen were drilled at

Penge and Mafefe, where mineralogical assemblages constrain metamorphic pressure at  $2.6 \pm 0.8$  kbar and temperatures of 420-460°C and 340-420°C, respectively (Miyano and Beukes, 1997). This contrasts with mineralogical constraints on the temperatures reached by better-preserved strata in Griqualand West, which are only 110-170°C (Miyano and Beukes, 1984).

## **MATERIALS AND METHODS**

We acquired drill core samples and one sample from a mining pit to assess manganese abundance and mineralogy. We sampled six drill cores, GKP-01, GKF-01, DI-1, WB-98, MF-2, and PA-13, at the South African Council for Geosciences, obtaining several representative carbonate, shale, and iron formation samples from each core across the transition between the carbonate platform strata and the Kuruman-Penge iron formation (Figure 1). Photos of these samples can be found in Figure 2. The majority of the samples were shale and iron formation, but a few representative carbonate and Bushveld-associated sill samples were chosen as well (Figure 2). These strata include the top of the Gamohaam formation, where a clastic shale is developed, to the Kliphuis and lower Groenwater members of the Kuruman Iron Formation (Figure1b) (Beukes, 1984). We also sampled at the Kumba Iron Ore Mine in Thabazimbi (TH, Figure1a), obtaining a ferruginous shale mining pit sample from near the carbonate-iron formation boundary (Figure 2).

Additional data was obtained on well-preserved core samples from the Kuruman and Griquatown Iron Formations. These samples were examined for comparative purposes by

N. Beukes and are derived from the PAN21 core (Griquatown Formation) and the P4010 core (Kuruman Iron Formation). Bulk Mn wt. % data from these samples were included in Table 1 and Kuruman data was used for comparison purposes as a well-preserved endmember example, in conjunction with results from Schroder et al (2006).

We chose representative shale, iron formation, and carbonate samples to measure manganese concentration, in both a bulk-powder form and by mapping manganese abundance across a thick section. Bulk powders from all cores were evaluated at the Activation Labs in Ancaster, Ontario. Using a lithium metaborate/tetraborate fusion-ICP method, approximately 0.5g of rock were pulverized and mixed with lithium metaborate and lithium tetraborate. A 5% nitric acid solution with an internal standard was added to the molten sample melt, and this was mixed approximately 30 min until completely dissolved. Manganese concentration was determined using a combination/simultaneous Thermo Jarrell-Ash ENVIRO II ICP or a sequential Varian Vista 735 ICP. The samples were run with replicates, a method reagent blank and certified reference material, and the instrument is calibrated using seven certified reference materials. The detection limit is 0.001% and accuracy determined from standards is 2.3% or better for MnO > 0.1 wt. % and about 12% for MnO < 0.1 wt. %.

Manganese concentration maps across thick sections of core and mine samples were produced using a mesoprobe X-ray beam rastered across the sections at the Stanford Synchrotron Radiation Lightsource using beam line 10-2. The beam was ~30µm, pixels were designated at ~50µm x 50µm, and we used a Vortex SII International Silicon drift

detector to collect manganese X-ray fluorescence. The incoming beam energy was set at 13,500 eV to excite and measure the fluorescence of other elements in addition to manganese including nickel, iron, and calcium. Iron was often extremely enriched in the ferruginous shales and iron formations, causing iron photons to enter the manganese fluorescence window. We removed most of the iron contribution and isolated the manganese signal using a best-fit polynomial in a Mn v. Fe plot, which usually was  $Mn = 5 \times 10^{-6}(Fe)^2 + 0.0159(Fe)$ . The resultant manganese fluorescence maps enabled us to choose areas from each core to make into thin sections. Some sections were chosen to be representative shales from each location, choosing regions that looked typical of the shale thick section(s) available from an individual core. Other samples were made into thin sections with notably higher localizations of manganese, like the manganese-enriched portion of MF402 and a sample of the higher-manganese particles that appeared in PA1470. These samples were made into microprobe quality thin sections by High Mesa Petrographics and observed optically on a Leica polarizing microscope.

We examined these sample targets using X-ray spectroscopic imaging, a technique that pairs microscale X-ray spectroscopy with microscale X-ray fluorescence mapping to create speciation maps of a designated element (Johnson et al., in review; Mayhew et al., 2011; Johnson et al., 2013). We used beam line 2-3 at the Stanford Synchrotron Radiation Lightsource to measure the manganese X-ray fluorescence at 2-10 $\mu$ m pixels at four specified incoming X-ray energies. A high beam resolution of  $\sim 2\mu$ m beam size was accomplished using Kirkpatrick Baez focusing mirrors, and a Vortex SII International Silicon drift detector collected the fluorescence signal. We chose energies using

differences in X-ray spectra to best distinguish between various manganese(II),(III), and (IV) phases: 6551eV, 6556eV, 6562eV, and 6590eV. Principal component analyses (PCA) of these four energy maps highlighted areas with differing manganese signals, and helped guide where we measured X-ray absorption near edge structure (XANES) spectra to confirm phase differences. These internal XANES spectra became sample endmembers employed to perform a linear fit using the normalized fluorescence at each energy for every pixel. This best-fitting created manganese speciation maps for each sample. A 2-point averaging was applied to smooth the spectra so noise in the spectra did not affect XANES multiple energy fitting.

The regions of interest chosen for each representative sample were then further investigated on a nano-scale using electron microscopy. We probed textural relationships between minerals using carbon-coated samples (coated with 7-15nm of graphite using a Cressington Carbon Coater) on the scanning electron microscope (SEM) housed in the Caltech GPS Analytical Facility. This SEM is a Zeiss 1550VP Field Emission SEM equipped with an Oxford INCA Energy 300 X-ray Energy Dispersive Spectrometer (EDS) system and an Electron Backscatter Diffraction (EBSD) system. We captured high-resolution images in backscatter mode, enhancing compositional contrast, and identified minerals using elemental and diffraction analyses. Samples for EBSD measurements were additionally polished using a Vibromet 2 vibratory polisher. Quantitative elemental analyses of points have a relative accuracy of better than 5%.

## RESULTS

Whole-rock measurements of manganese concentration by fusion-ICP indicated that manganese was not enriched in well-preserved samples from Griqualand West, and only became significantly enriched in one metamorphosed sample. Rock powders relatively unaffected by the Bushveld intrusion-related metamorphism had MnO weight percents ranging from 0.03 to 0.48% in shales and 0.84 to 1% in carbonates (Table 1). A previous study had measured MnO weight percent in the Kuruman iron formation in the well-preserved cores GKF-01 and GKP-01 and the data ranged from 0.07 to 0.33%, averaging 0.18% (Schröder, 2006). Our measurements of whole-rock samples from metamorphosed cores and one mining pit sample reached up to 1.5% MnO in one shale sample, although other shale samples had 0.04 to 0.17% (Table 1). Only the PA2014m sample has significantly enriched manganese, distinguished from the average well-preserved shales with a z-score of 7.16 and a p value of  $1 \times 10^{-12}$  ( $p \ll 0.05$ , the usual cut-off for significant difference in population). Metamorphosed iron formation showed a very slight enrichment in Mn, with MF402m at 0.68 % Mn having a statistically significant Mn enrichment but close to being within the well-preserved population ( $p = 0.035$ ) and PA1470m 0.57% falling within the normal distribution of the well-preserved iron formation samples ( $p = 0.12$ ). Two carbonates forming the base of the PA-13 core were relatively depleted in Mn, having only 0.025 and 0.039 wt% MnO (Table 1). This is low compared to our measurements of Mn in carbonates (0.8 to 1%), but according to previous measurements of the Campbellrand carbonates in GKP-01 and GKF-01, all of these values do fall within the normal population of these carbonates ( $p > 0.05$ ), which average to 0.19 wt % (Schröder, 2006).



Spatially, our X-ray mesoprobe results revealed that manganese in metamorphosed samples have interesting differences from their well-preserved counterparts (Figure 3). Metamorphosed samples from the Bushveld complex region have abundant grunerite, a fibrous iron amphibole (Miyano and Beukes, 1997). Grunerite seems to have grown during metamorphism with a small but significant amount of manganese, which maps as long fibers or fibrous rosettes in thick section fluorescence maps (Figure3, MF402, PA1355). We could also see discrete Mn-rich areas in some of the metamorphosed sections (Figure3, PA1470, PA2014) that warranted further investigation, and a strong correlation between Ca and Mn. One Bushveld-affected section, MF493, had clear Mn-enriched veins cutting across lamination and that section was also chosen for further analyses. Lower-grade metamorphic sections unaffected by the Bushveld complex were all internally quite similar: Mn was generally very low and associated with Ca in carbonates if enriched at all.

We chose shale samples from each core, targeting areas shown by our mesoprobe to have at least a small amount of Mn in representative samples and those with especially interesting manganese trends, to perform microscale analyses on using X-ray spectroscopic imaging methods and electron microscopy techniques. Initial imaging was performed on an optical microscope, using reflected, transmitted, and polarized light (Figure 4). These paired approaches yielded illuminating results. Many metamorphosed samples had fibrous or blocky Mn-bearing grunerite, an iron silicate in the amphibole group. This identification was confirmed using EBSD, which confirmed that the iron-rich silicate was in the cummingtonite-grunerite family. Manganese and magnesium, and

occasionally calcium, appeared to substitute for iron in grunerite [grunerite formula:  $\text{Fe}_7\text{Si}_8\text{O}_{22}(\text{OH}_2)$ ]. Since there is no color-based optical evidence of Fe(II)-(III) intervalence transfer or Mn(III) presence (the grunerite is white, Figure4), we agree with Klein, who also asserted that the grunerite was all Fe(II) (Klein, 1968). The likelihood of Mn(III) being present is very low if there is no Fe(III). This is pertinent to the XANES spectra produced from these grunerite samples. Despite having very similar EDS and EBSD spectra, the grunerite has very variable X-ray absorption spectra, including some peaks shifted to higher energy suggestive of an Mn(III) presence (Figure5). We instead propose that these X-ray spectral variations are due to Mn site occupancy differences and/or crystal orientation differences.

Intriguingly, the manganese contents of the grunerite were fairly different sample-to-sample, although intra-sample variations were minor. The widest range of MnO content was found in the most manganese-enriched sample, PA 2014m. Here Mn varied from 1.49 to 6.44 wt. % MnO, although most samples were ~1.9% MnO (Supp Table 1). MF402 had fairly consistent MnO content of its grunerites, ranging from 0.94 to 1.28 and averaging 1.12 wt %. One other sample we examined in depth was PA1470m, and this had only trace levels of Mn, ranging 0.5 to 0.84%, and averaging 0.65 wt. % MnO (Supp Table 1).

Another common manganese mineral host was carbonate phases, from manganoan calcites and dolomites to manganese-enriched siderites and rhodochrosites. Well-preserved shales and carbonates had low levels of manganese (up to ~1 atomic % Mn,

averaging 0.5%) as well as iron (~2.6% Fe) incorporated into calcites and dolomites. These carbonates were either ~10-30um euhedral crystals or detrital carbonate grains, except for a highly recrystallized section from D1-1 (218m) which exhibits exsolution of a mixed cation carbonate into calcite and manganoan and ferruginous pseudo-dolomite (~30% of cations were Mg). The temperatures predicted by the Mg content of the calcites range from 250-330°C (Goldsmith and Newton, 1969) (Supp Table 1), considerably higher than the regional diagenesis predicted by other methods (Miyano and Beukes, 1984). Therefore, the exsolution into two endmember phases was likely incomplete and had not yet reached equilibrium. Metamorphosed thin sections from PA-13 and MF-2 also had manganoan carbonates: samples MF402, PA1470 and PA2014 had ferruginous (~7-20 atomic % Fe) carbonates with ~0.5-2.5 atomic % Mn and MF493 had manganoan siderites and even rhodochrosite in veins with 6-17 atomic % Mn. Other than the higher iron content (~7-20 atomic % Fe), the textures of the carbonates also contrasted with the well-preserved samples.

The presence and distribution of manganoan grunerite, carbonate, and other minerals were distinct for each sample we explored in-depth. Figure 5 shows PA2014, a black shale that now has abundant porphyroblasts of manganoan almandine garnet, with about 9% Fe, 4.5% Mn, and 2.8% Ca (Supp Table1). It also has iron sulfides, likely pyrite, and manganese-bearing and fibrous grunerite veins with a small amount of grunerite dispersed throughout the matrix that cross-cuts lamination (Figure 5). In a background of iron ( $\pm$  K, Mg) aluminosilicates and silica, our X-ray spectroscopic imaging picked out four phases hosting manganese (Figure 5). Two of these were ascertained to both be

grunerite, from identical EBSD and EDS signatures. Here we hypothesize that these different grunerite signatures are correlated to the stark crystal orientation differences in the late-stage veins: the grunerite spectral signature corresponds to where SEM imaging shows a clear difference in fiber orientation (Figure 5). This is consistent with other studies which have found dramatic differences in Fe XANES spectra from different crystal orientations (Dyar et al., 2002). The other two manganese-containing minerals were from carbonates and garnets. Carbonates in PA2014 had relatively high manganese, ranging from 1.7 to 2.7% Mn. These were also distinct from well-preserved samples by being highly iron-enriched, averaging 7% iron with ~17% Ca and ~3.5% Mg. Carbonates in PA 2014m were also relatively coarse-grained, comprising crystallites from 30um to >60um (Figure 5).

Aside from the garnets, PA 2014 is similar to two other metamorphosed samples, PA 1470 and MF 402. Both of these sections also had abundant grunerite and manganoan carbonates. MF 402 appears to be almost entirely replaced by grunerite fibers and blocky crystals, although it also has a vein of microcrystalline quartz cemented by large equant carbonate crystals which are manganese-bearing (Figure 6). The carbonate cement has ~1-1.5% Mn and, like PA 2014, very high iron content in the range of 8-9%. PA1470 had large euhedral magnetites rather than garnets, and a matrix of fine manganoan grunerite fibers and silica with aggregates of manganoan carbonate crystals (Figure 7). The grunerite appears to have grown over pre-existing quartz with a few later coarse grunerite fibers, with the coarse magnetite crystals and manganoan calcite cross-cutting the grunerite (Figure 7). The carbonates from PA1470 were, like other metamorphic

carbonates, between calcites and ankerites with ~10% Fe and 16% Ca with minor Mn (~1.2%) and Mg (~3.1%). Small domains appear darker in backscatter images (Figure-) and these were much more Ca-enriched than the majority of the carbonates. The carbonate crystals formed large aggregates often hundreds of microns in both dimensions (Figure 7).

Another metamorphosed shale sample has manganese-enriched mineralized veins, which are often a good sampling of the fluid composition that percolated through the rocks during late diagenesis and metamorphism. MF493 is mostly composed of fine-grained iron, sodium, and potassium aluminosilicates, but it has several large veins cutting through this matrix with high enrichments of sulfides, manganoan siderites, and ferrous rhodochrosites (Figure 8). These carbonates have 6-17 atomic % manganese, the highest Mn concentrations we observed in any sample. The veins also have abundant zinc and iron sulfides, which is consistent with the Zn-Pb mineralization associated with the Bushveld intrusion (de Kock et al., 2009). The co-occurrence of manganese-iron carbonates with zinc sulfides suggests manganese-enriched fluids were sourced from the Bushveld Complex into these rocks. Other nickel-rich iron sulfides (with 3-4 atomic % Ni) are scattered throughout the matrix.

PA 886m does not have nearly as high of manganese content, but its manganese is in an unusual form: large manganese-bearing ilmenite grains that appear detrital in a matrix of iron and magnesium aluminosilicates, quartz, and potassium feldspar (Supp Figure1).

While not a significant source of manganese to the bulk rock (which had only 0.05% MnO), these grains individually reach up to 1.1 atomic % Mn.

Well-preserved shale and carbonate examples were more consistent and only had manganese in trace amounts occurring in carbonates. DI-218 has calcites and ferruginous pseudo-dolomites with small amounts of Mn, with these two phases separated by what appears to be severe recrystallization and exsolution (Figure 9). It also has scattered small iron sulfides. WB 830m has scattered blocky crystals of calcites that have up to ~0.5% Mn in a matrix of potassium aluminosilicates, quartz, and bright block of iron and magnesium aluminosilicates (Figure 10). Some of these carbonates are cored by Mg-rich calcites without much iron or manganese, suggesting that much of the carbonate are overgrowths and cements precipitating during early diagenesis (Figure 10). GKF 338m has abundant calcite as euhedral Mg-enriched cements with small amounts of Fe and trace Mn, alongside potassium aluminosilicates, iron clays, and quartz (Figure 11). GKP 242m is mainly extremely fine-grained K aluminosilicates with rarer iron aluminosilicates and rounded detrital carbonate grains with trace Mn in coarser-grained bands (Figure 12).

## DISCUSSION

We examined an array of shale, carbonate, and iron formation samples from the Campbellrand-Malmani carbonate platform to Kuruman-Penge iron formation boundary

to try to understand if manganese was enriched in these sediments through environmental reactions or mobilization and/or introduction during metamorphism. We used the Kaapvaal craton as a natural laboratory with its well-known metamorphic gradients and focused on shales from the Transvaal Supergroup, which had reported manganese enrichments near a large igneous intrusion [the Bushveld Complex] (Miyano and Beukes, 1997). Examining core samples on a micro- and nano-scale, we determined that manganese was moderately enriched in carbonates, garnets, and amphiboles in samples from the Transvaal close to the Bushveld Complex but manganese was only a trace component of carbonates in cores from the better-preserved Griqualand West region. Thus manganese was mobilized, enriched, and altered mineralogically, probably related to the contact metamorphism and hydrothermal fluid fluxes associated with the Bushveld Complex.

Manganese enrichment and remineralization implies that manganese was mobilized during the high heat and pressure conditions imposed during metamorphism, but the source of manganese is unclear. We hypothesize three possible explanations for the behavior of manganese that we observe: 1) Manganese was present in the original sediments but locally re-mobilized and concentrated into new minerals during metamorphism; 2) hydrothermal fluids related to the Bushveld Complex were enriched in manganese and thus introduced Mn to the nearby rocks; and 3) the underlying sediments was a source of manganese, potentially the underlying Malmani carbonate undergoing decarboxylation or dissolution, and fluids then brought this Mn up to overlying rocks. Hypothesis #1 we can address with our measurements from the well-preserved correlated

sediments from the other side of the basin. Our observations indicate that manganese was originally in trace amounts in authigenic or detrital carbonates. Many of our metamorphosed sections show manganese in different minerals, like in fibrous grunerite, or in more manganese-enriched carbonates, but the bulk Mn content is similar to their well-preserved counterparts. A couple samples, especially PA2014m but also MF 402m, have higher Mn than we would expect from their better-preserved equivalents. Furthermore, we observed Mn in veins alongside Bushveld-associated minerals like lead sulfides. Both of these observations suggest to us that there was an additional Mn source besides the Mn that could be derived from local sediments, and this source may have been associated with Bushveld fluids.

The other two possible explanations for Mn introduction during metamorphism seem to be both feasible. Late-stage magmatic fluids may contain large quantities of Fe, Mg, and Mn (Burnham, 1979; Kontak and Corey, 1988). In a similar study of manganese-enriched garnet-bearing rocks affected by contact metamorphism by the South Mountain Batholith, magmatic fluids were considered a likely source of Mn (Kontak and Corey, 1988). However, the Mn, Mg, and Fe in hydrothermal fluids were also attributed partially to sourcing from surrounding metasedimentary rocks; it was suggested that some late-magmatic or post-magmatic fluids interacted with the surrounding rocks and extracted and mobilized these elements (Kontak and Corey, 1988). This may have also been true in the Bushveld-associated magmatic fluids. In support of this idea, our measurements of the underlying carbonate in the metamorphosed PA-13 core (Table 1) showed a large (40x) Mn depletion from the better-preserved carbonate examples. However, a more



extensive dataset from well-preserved carbonate samples shows that the metamorphosed carbonates still fall into a normal range for Mn in these carbonates, so this is not necessarily evidence that Mn has been stripped from the underlying rocks.

Regardless of the mobilization mechanism, we can now propose some guidelines for identifying whether manganese in an ancient sedimentary rock was primary or introduced later. Assessing manganese minerals on a micron- to nano-scale greatly helps to show whether manganese-bearing minerals cross-cut other minerals or whether manganese hosts appear to be in expected early phases that do not interrupt other grain boundaries. That said, it is quite difficult to untangle the complexities of ancient rocks, especially metamorphosed strata from Archean time. Ideally, manganese-enriched strata would show expected manganese minerals consistently appearing across kilometers of distance, with trends following expected stratigraphic relationships and unrelated to regional metamorphism.

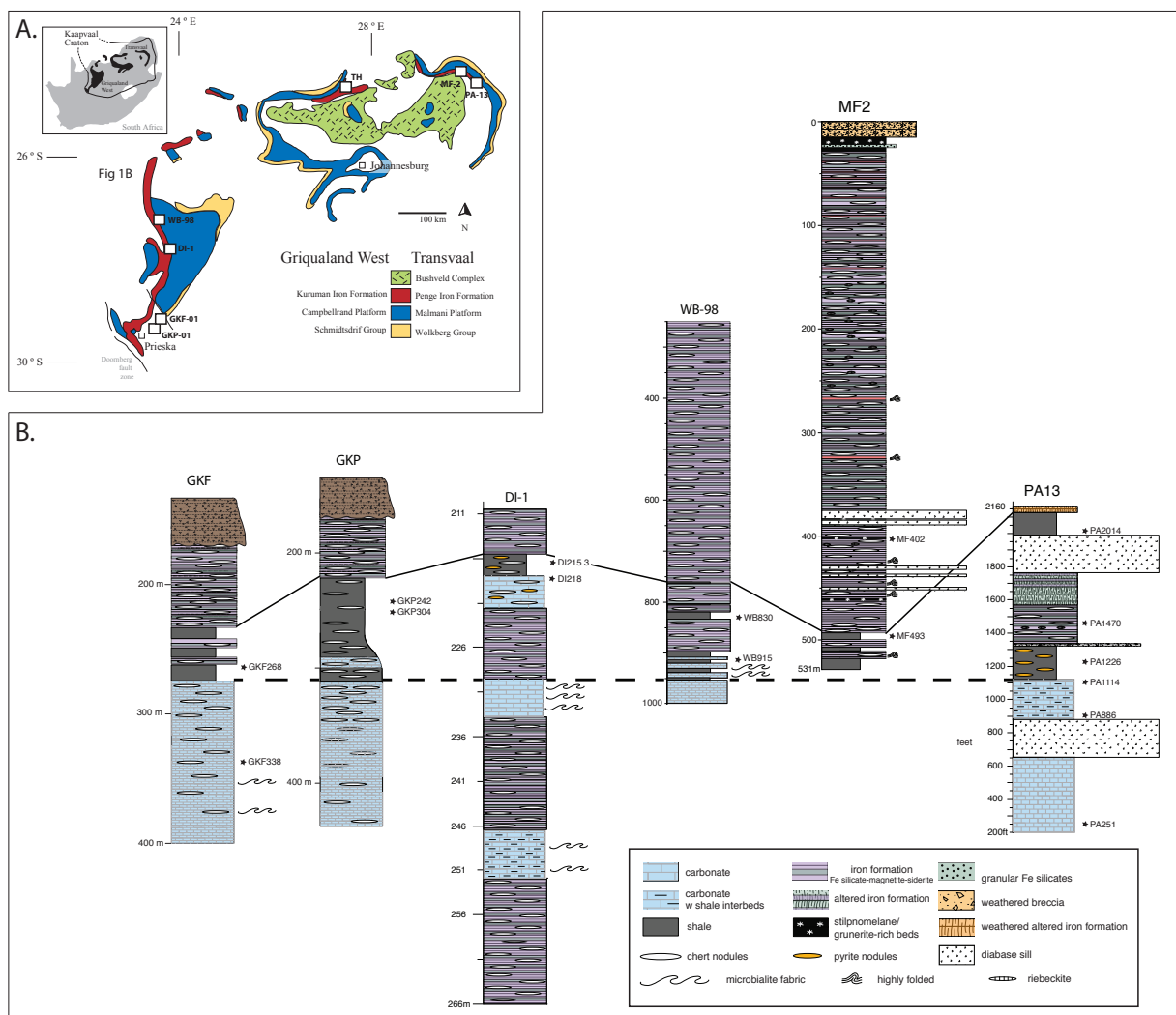
We can gain from these samples two discrete conclusions: 1) manganese mobility and introduction is a potential problem especially near intrusive igneous complexes, and 2) well-preserved strata at ~2.5 Ga from Griqualand West show no sign of manganese oxidation. Mn-enriched carbonate crystals and mineralized veins, Mn-enriched amphiboles (grunerite), and Mn-enriched garnets from contemporaneous metamorphosed sections and the significance enrichment of at least two samples close to the Bushveld Complex demonstrate that manganese can and does become mobile during metamorphic processes, either by extraction from surrounding strata or from Mn-enriched

hydrothermal fluids. While manganese enrichments were found in 2.5 Ga metamorphosed strata from the Bushveld-affected Transvaal basin, we examined 15 sections (including 4 sections in-depth) from the Griqualand West basin and found no evidence of primary manganese enrichment. This result suggests that manganese was not being oxidized and concentrated in Griqualand West during the ~2.5 Ga transition from carbonate platform to iron formation.

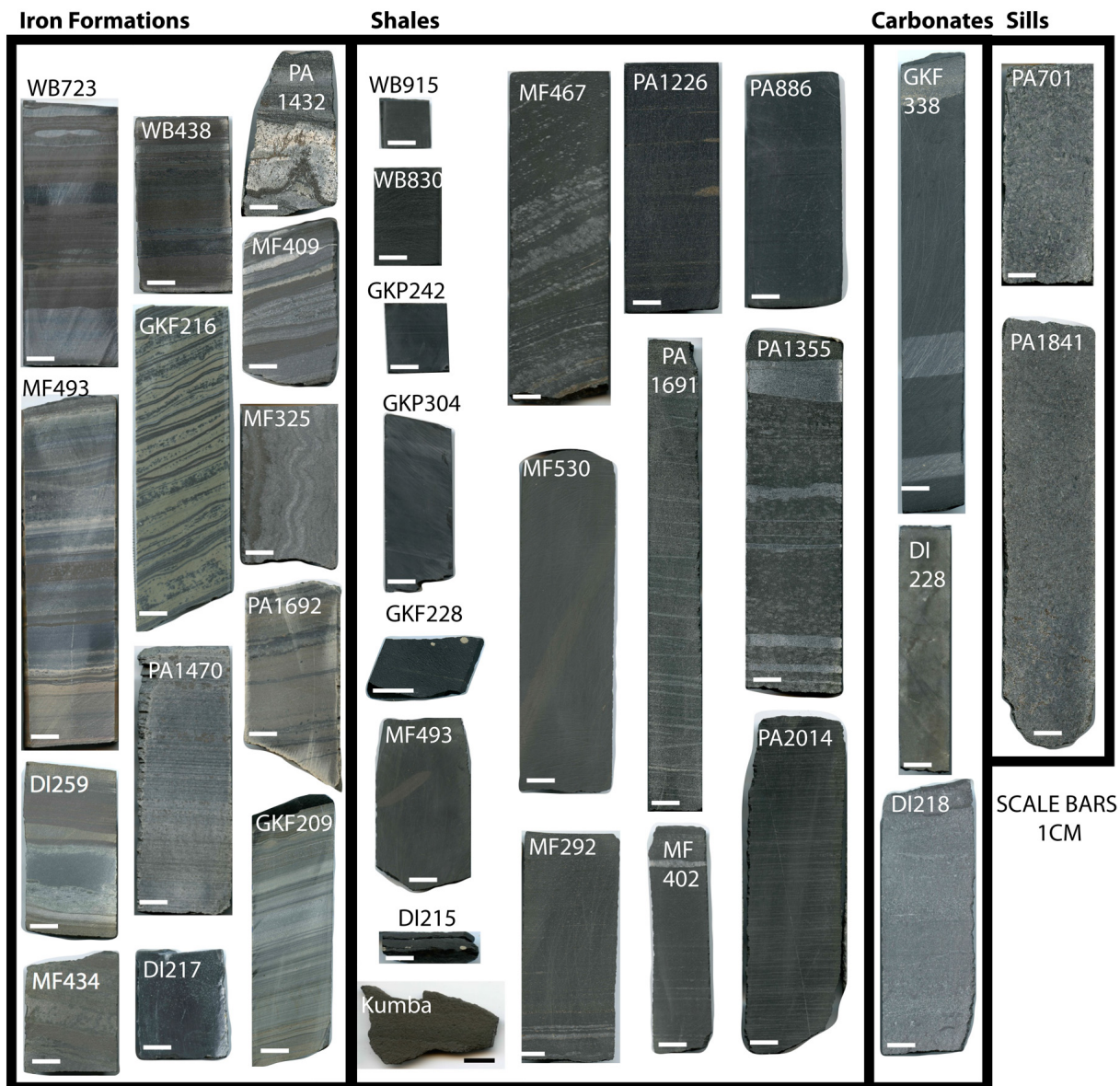
## **ACKNOWLEDGEMENTS**

We would like to thank Bertus Smith for all his time and help with field work in South Africa, Courtney Roach for X-ray microprobe assistance and trouble-shooting, Chi Ma for help with EBSD measurements, and George Rossman for valuable mineralogical consultations and assistance with Raman spectral data collection and interpretation. We also thank John Eiler and Max Lloyd for helpful input. We are also grateful to the Lewis and Clark Foundation for funding field research in South Africa, the Agouron Drilling Project for obtaining GKF and GKP cores, and a Packard Foundation grant to W.W.F. for funding sample analyses. Portions of this research were carried out at the Stanford Synchrotron Radiation Lightsource, a Directorate of SLAC National Accelerator Laboratory and an Office of Science User Facility operated for the US Department of Energy Office of Science by Stanford University.

## FIGURES AND TABLES



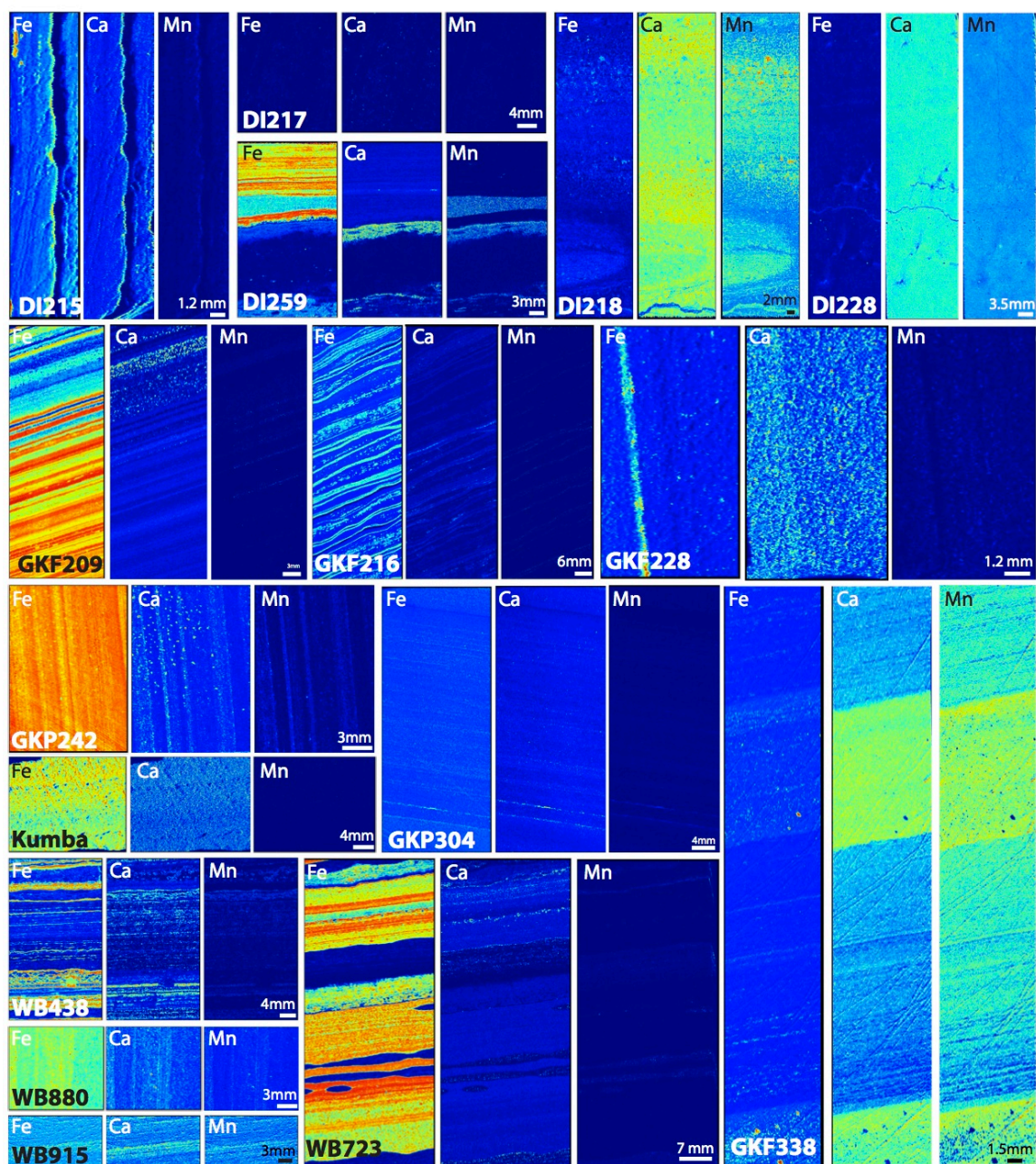
**Figure 1** – A. Core locations shown on map of Kaapvaal craton. Inset indicates the location of the Kaapvaal relative to the Republic of South Africa. Well-preserved cores [GKP-01, GKF-01, DI-1, WB-98] are located in the Griqualand West basin. Metamorphosed cores and mining pit sample from Thabazimbi [TH] are derived from the Transvaal basin on the east surrounding the Bushveld Complex (green). B. Core stratigraphy drawn with respect to the legend shown in the lower right. Cores correlated using a lithostratigraphic pseudo datum but could be time-transgressive across platform (Sumner and Beukes, 2006).



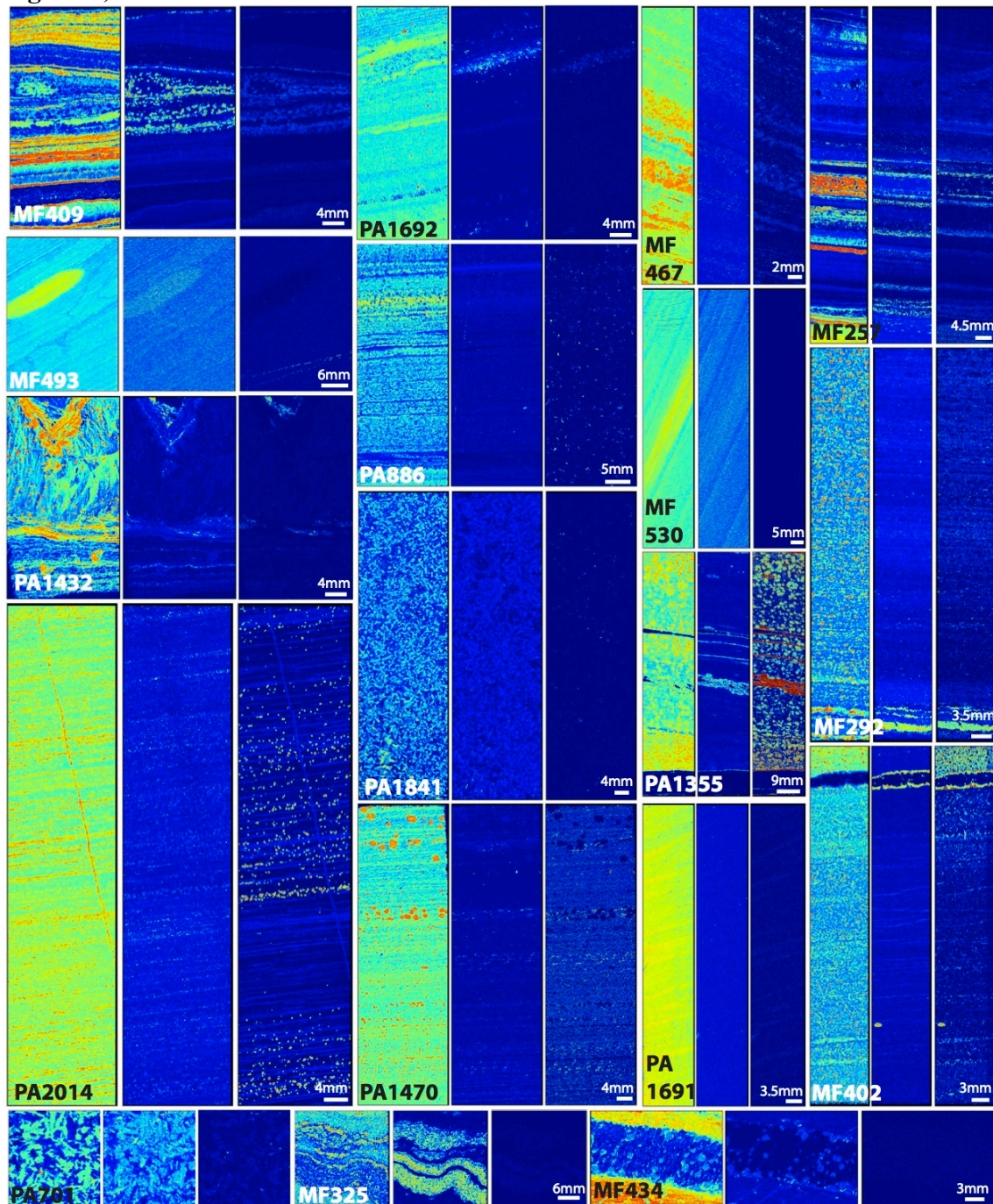
**Figure 2** – Photographs of core samples analyzed for Mn content, categorized into shale, iron formation, carbonate, and diabase sill samples as schematically represented in Figure 1.



Figure 3, Panel 1:

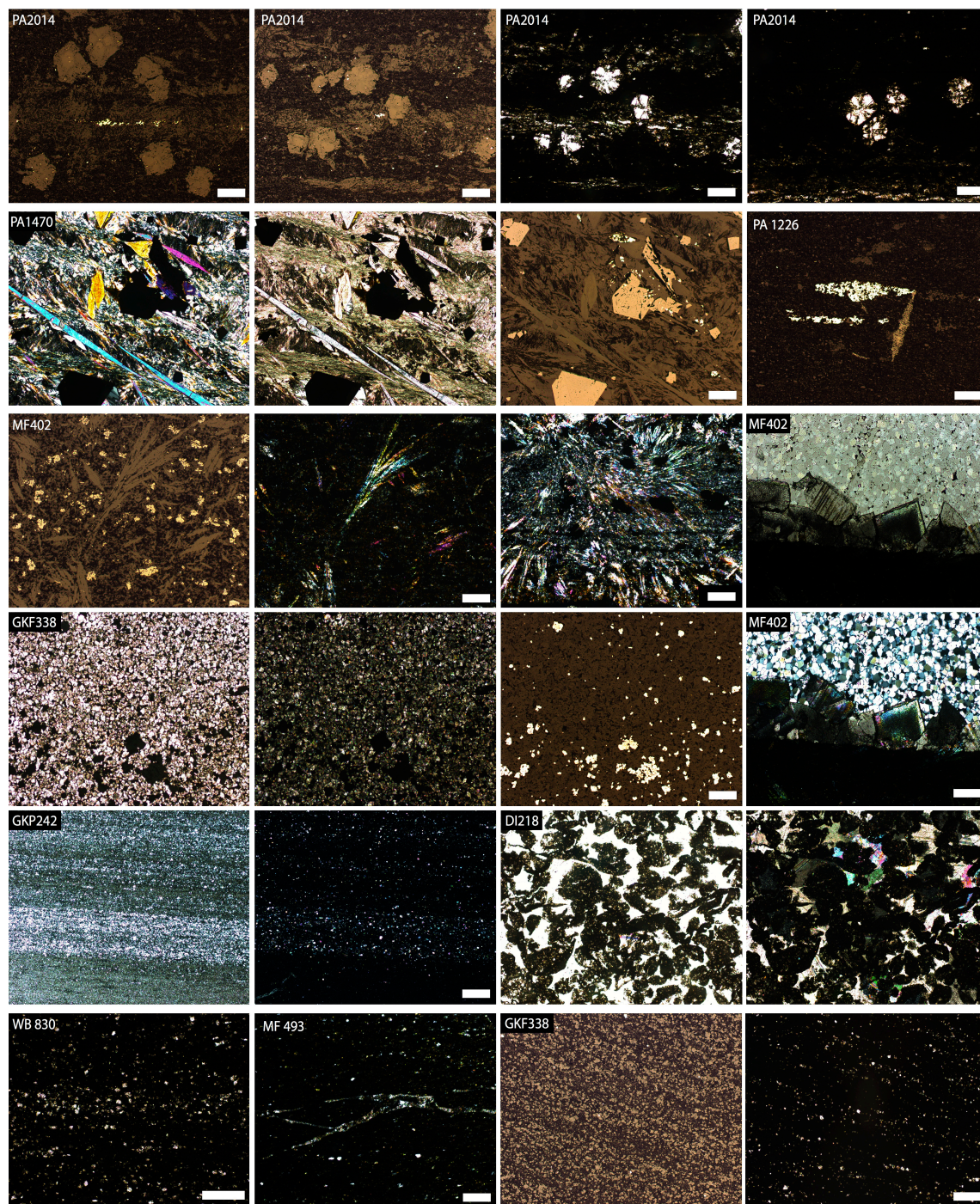




**Figure 3, Panel 2:**

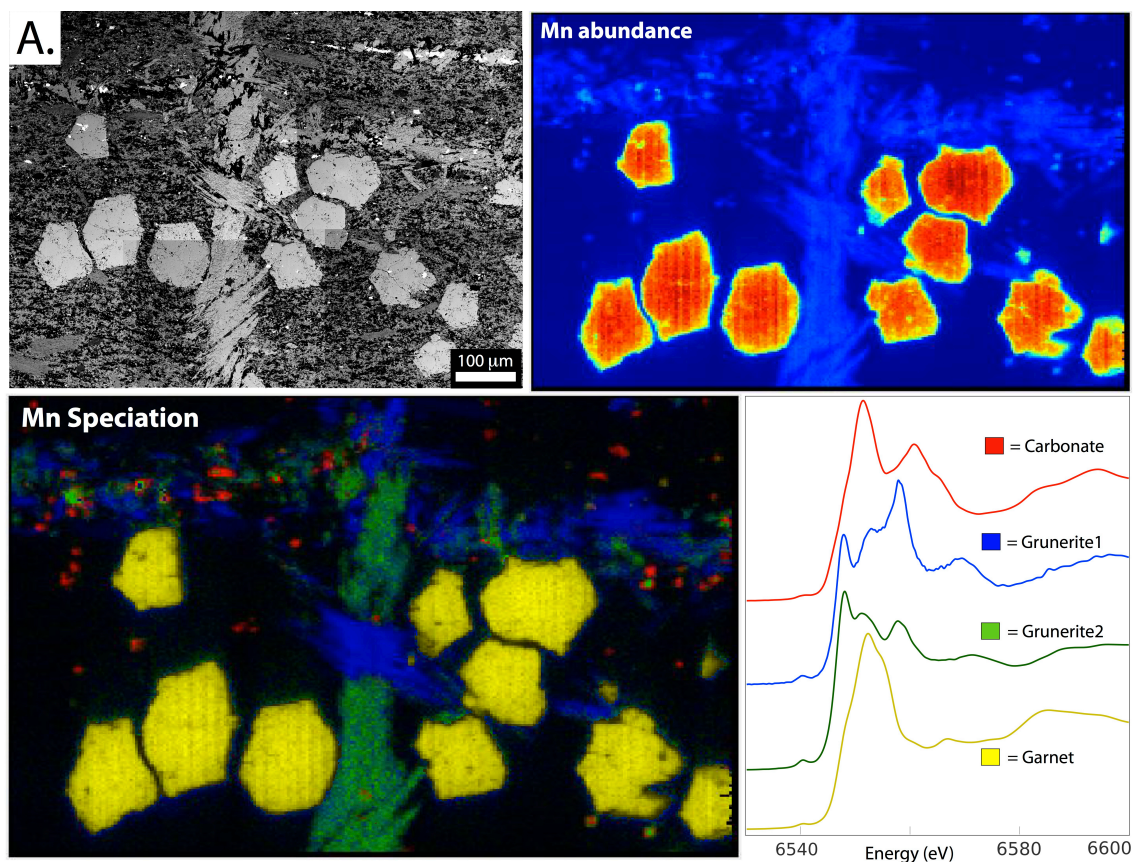
**Figure 3 (above)** – X-ray fluorescence imaging of iron, calcium and manganese abundance, with all Mn scales set to  $100 \mu\text{g}/\text{cm}^2$  and Fe and Ca set to internal maximums. Manganese data was corrected for iron overlap into the manganese fluorescence window by subtracting the iron contribution into the manganese signal using a best-fit polynomial, fitting the majority of points in a Mn v. Fe plot.





**Figure 4** – Microscopic photographs under transmitted, polarized, and reflected light of representative thin section samples from each core. All scale bars are 50 $\mu$ m.

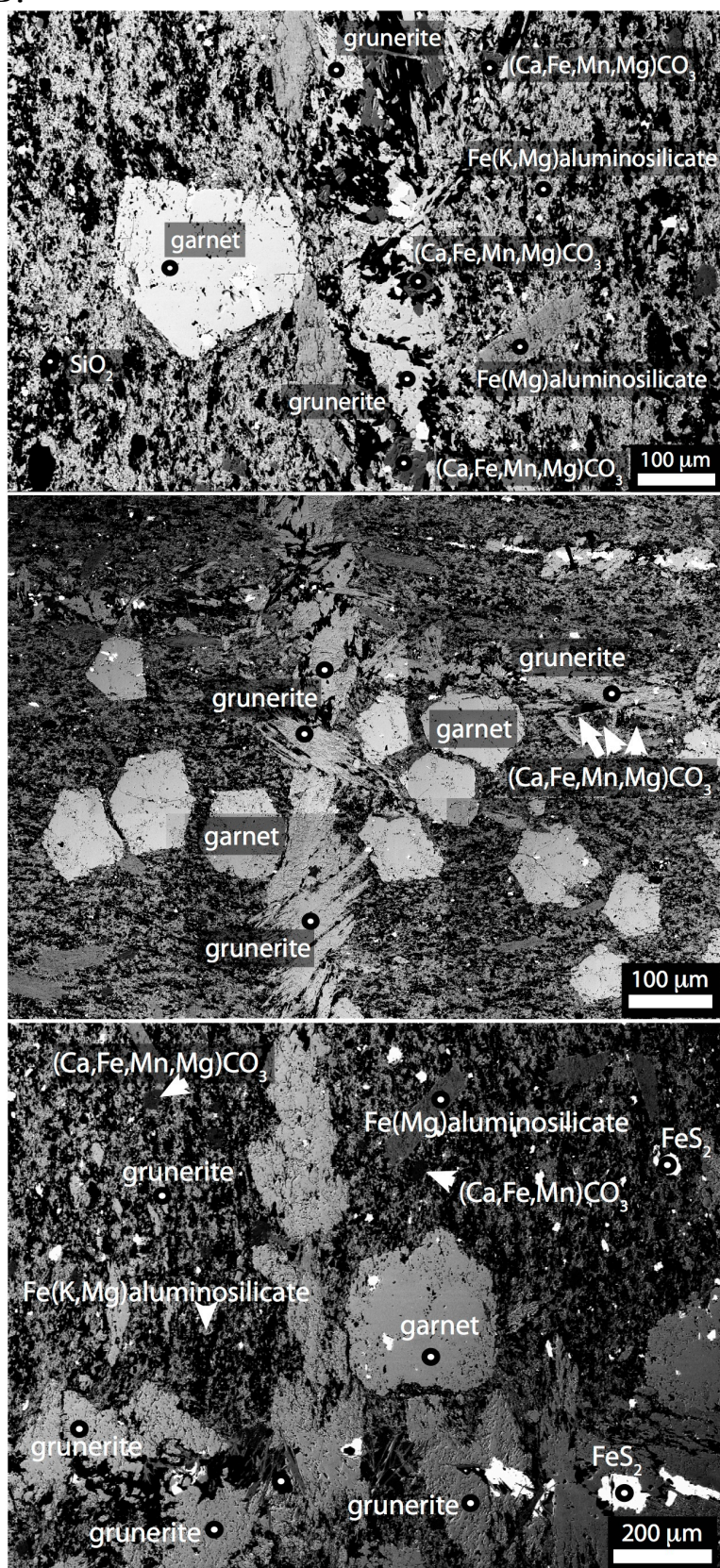




**Figure 5** – A. Target region of PA 2014m thin section that had cross-cutting grunerite veins, large garnets, and scattered carbonates. X-ray spectroscopic imaging and spectra are shown on top, imaging garnets (yellow), two types of grunerite (green and blue, see discussion in text), and carbonates (red). B. Scanning electron microscopy images, with mineral identifications made using energy dispersive spectrometry (see Supplementary Table 1).



B.





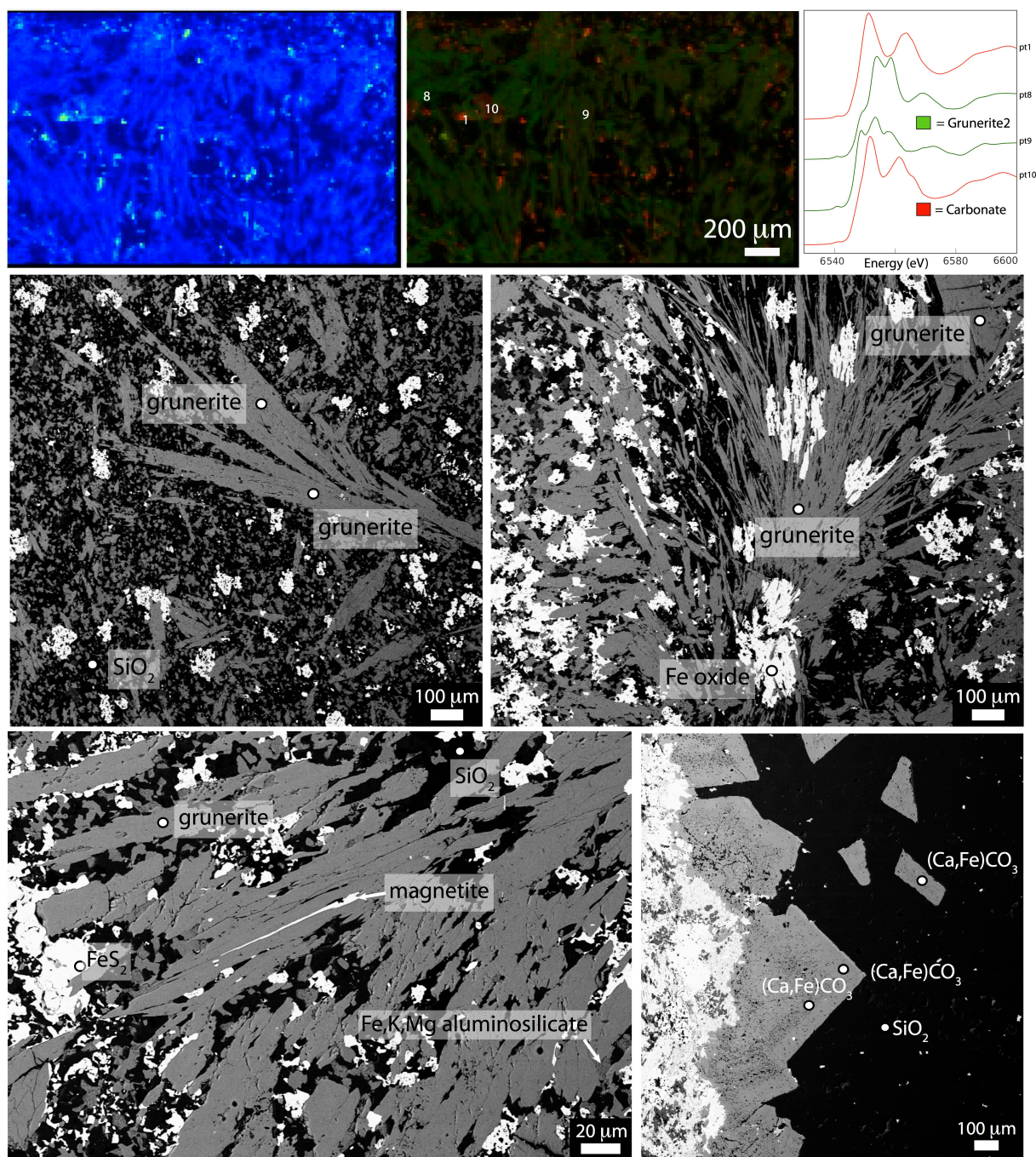


**Figure 6** – Representative region of MF 402m with abundant grunerite fibers. Top shows manganese speciation map indicating grunerite (green) and carbonate (red) produced from multiple energy maps and X-ray absorption spectra (top right). SEM photos with mineral identifications shown below for comparison.



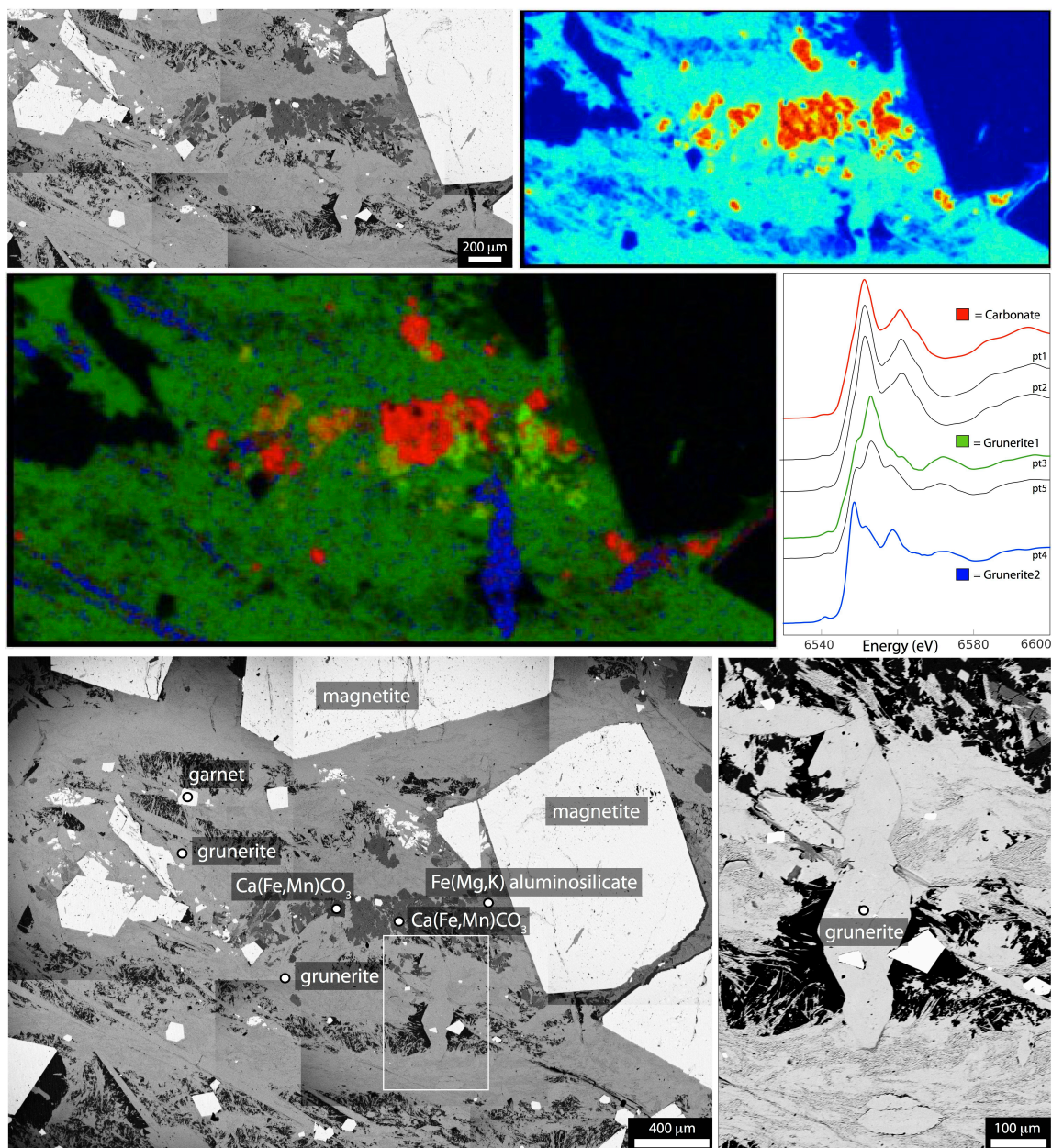


**Figure 7** – PA 1470m section focusing on one of the Mn hot spots identified by X-ray fluorescence imaging. The manganese was determined to be hosted by manganoan mixed-cation carbonates, both by X-ray spectroscopic imaging and SEM-EDS analyses.



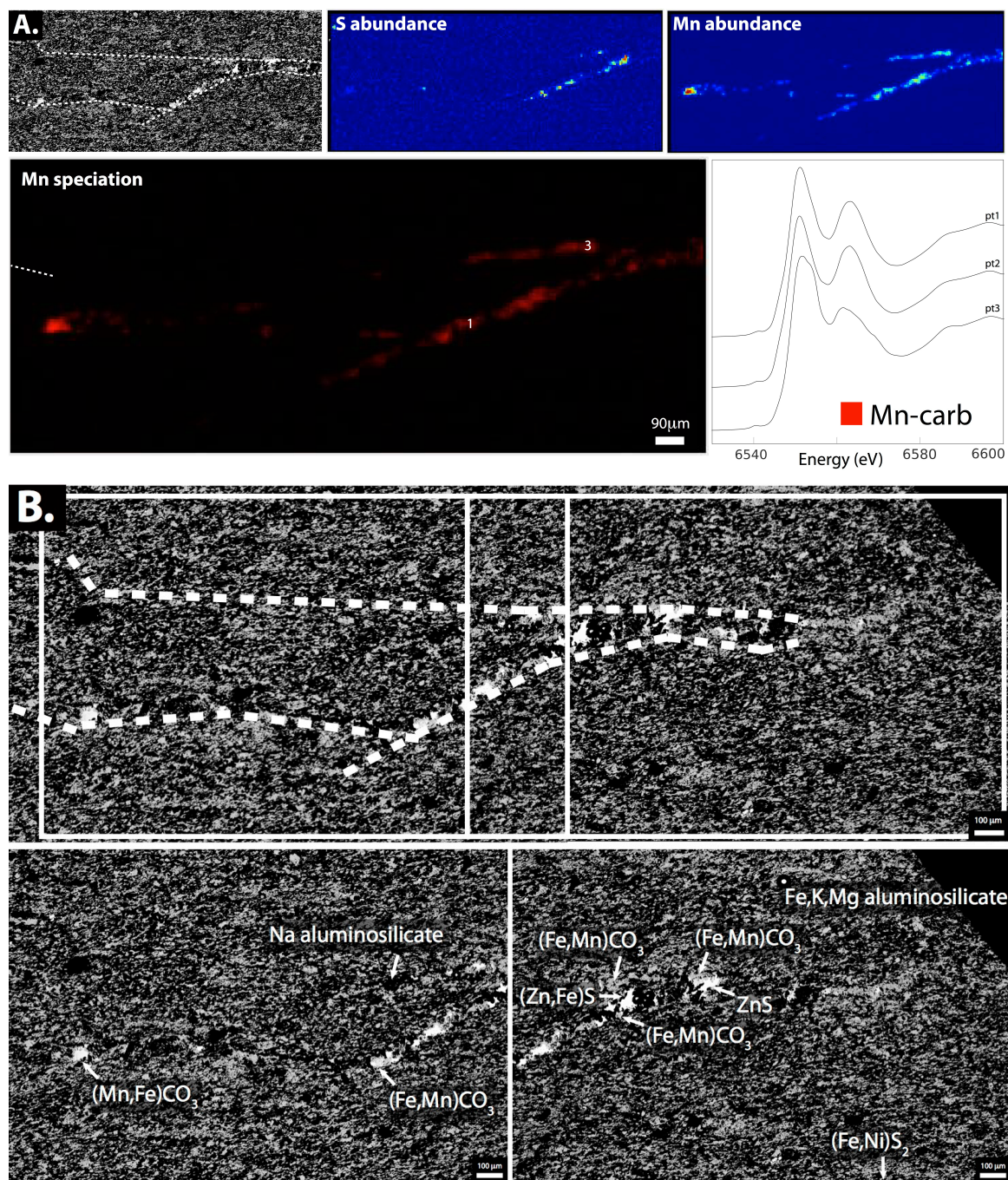


**Figure 8** – A. Cross-cutting veins in MF 493m which are enriched in manganese and sulfide phases (see S and Mn X-ray fluorescence maps). Speciation mapping from multiple energy maps of the same region indicates that all manganese is in carbonate. B. Further electron microscopy images and EDS-assisted mineral identifications shown below. Note consistency between Mn-carbonate and sulfide phase locations between SEM and X-ray imaging.

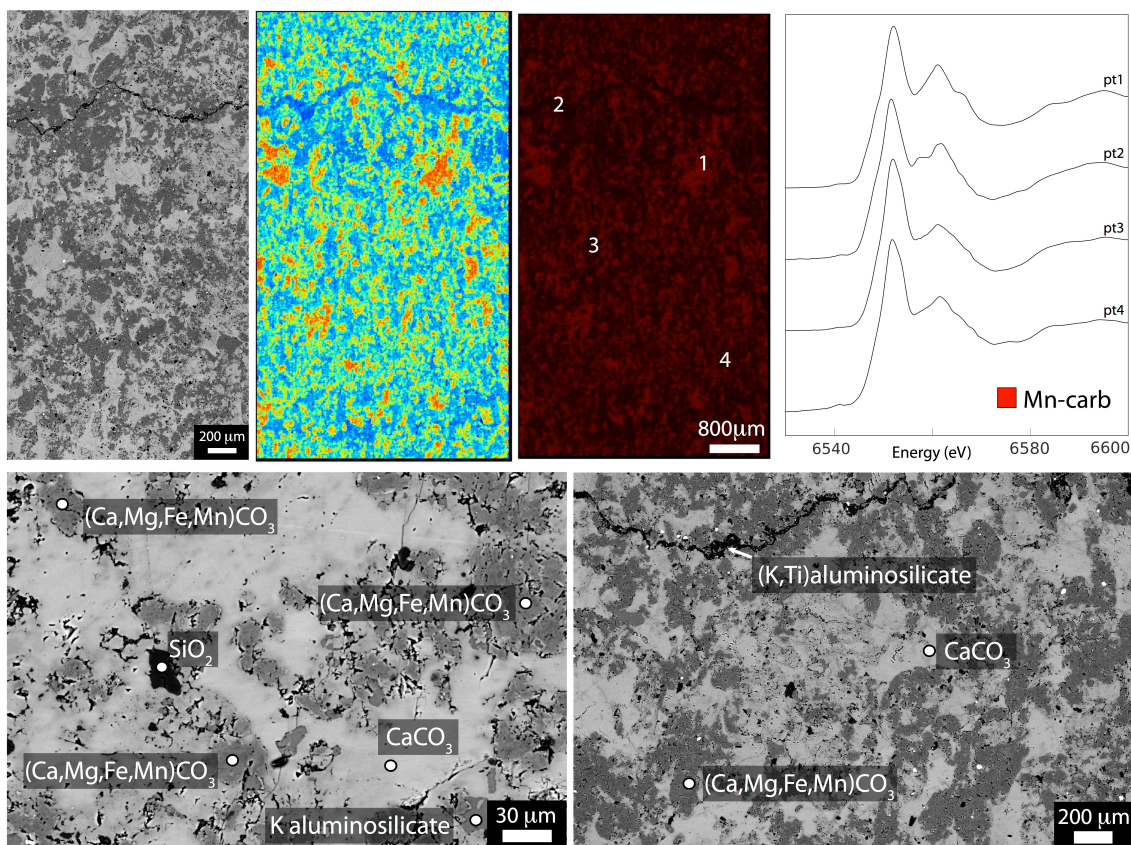


**Figure 9** – Representative region from DI 218m, showing heavily recrystallization and incomplete exsolution of calcites and ferrous-magnesian carbonates. All manganese is in low levels in the mixed-cation carbonates and in trace levels in calcites (see Supplementary Table 1). X-ray region shown above with SEM images and identifications shown below.



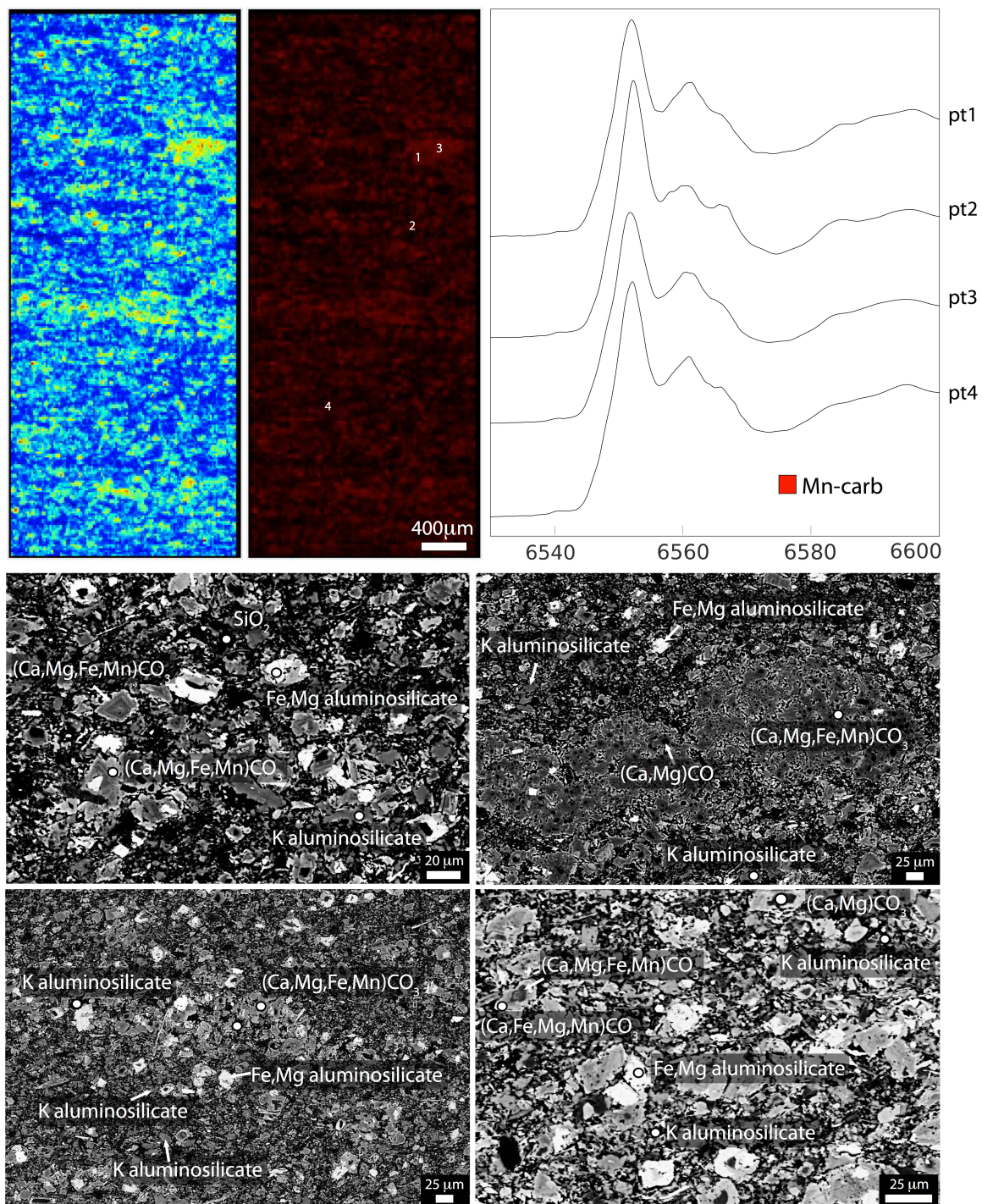


**Figure 10** – A representative region from WB 830m, with X-ray spectroscopic imaging and X-ray absorption spectra indicating all manganese is in carbonates. Four SEM image plates of various small-scale textures observed in WB 830 shown below. Carbonates are mainly in euhedral crystals or pore-filling cements, suggesting an early diagenetic origin.



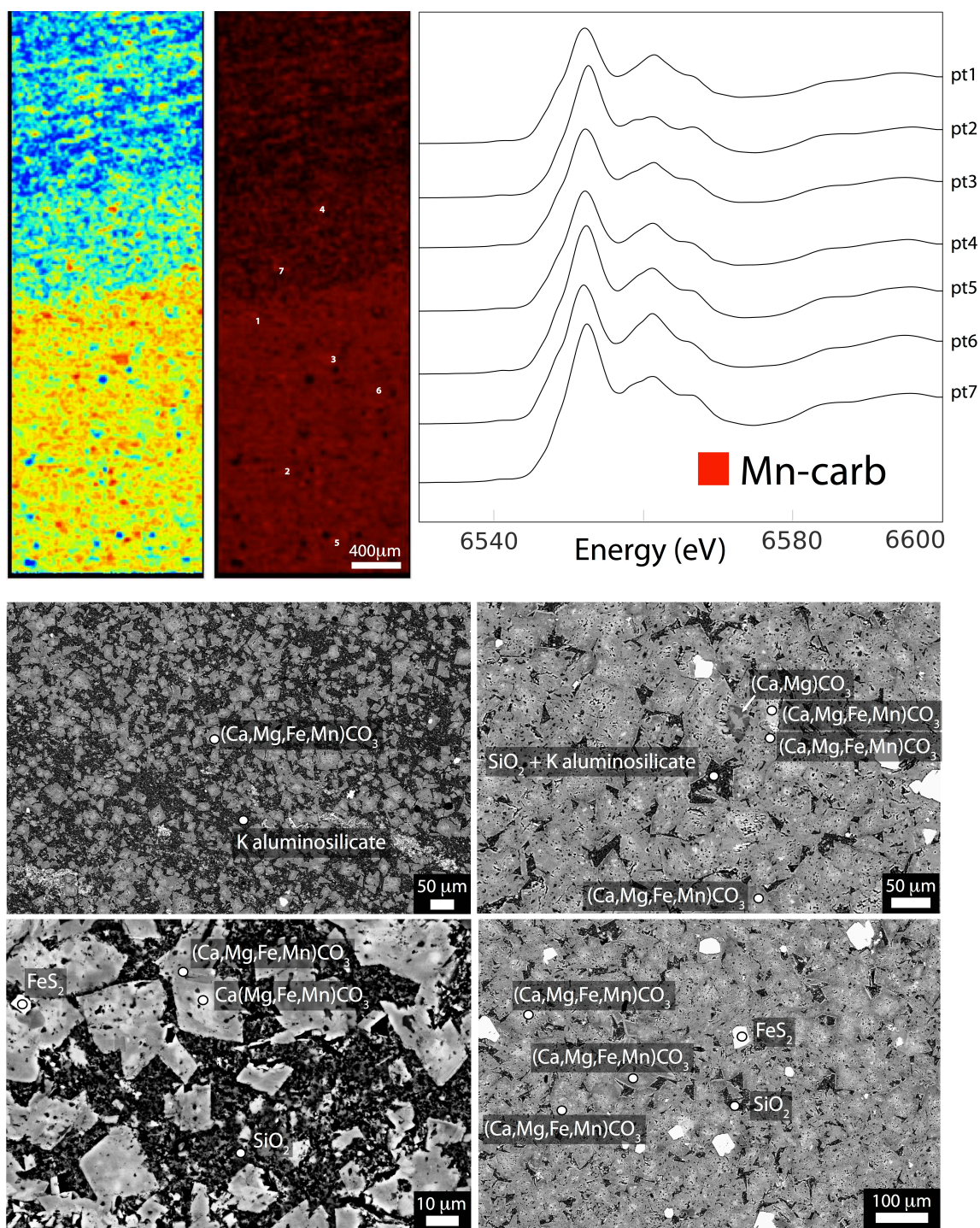


**Figure 11** – GKF 338 shown in a representative X-ray spectroscopic image of both the calcium-and-manganese-enriched band and the more clay-rich band. All manganese appears to be in carbonates. SEM images from both regions are shown below, with mineral identifications made using energy dispersive spectrometry (EDS).



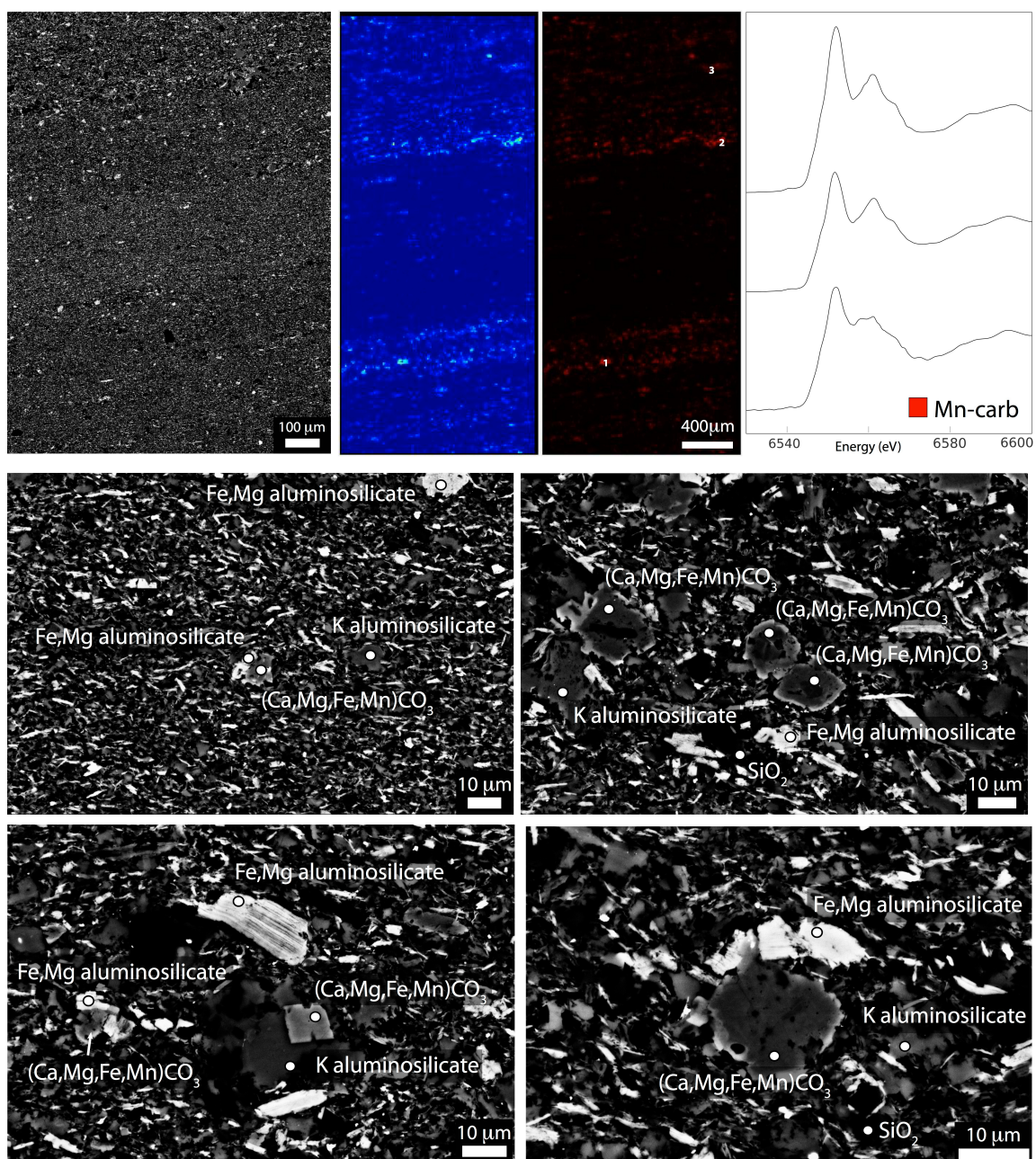


**Figure 12** – A representative region of GKP 242, which is dominantly a silica and K-aluminosilicate shale. Coarser bands have more manganese-enriched particles, which are all Mn-bearing carbonates according to X-ray spectroscopic imaging and X-ray absorption spectra. Bottom panels show typical Mn hosts observed on the SEM: all mixed-cation carbonates with low levels of manganese and mainly in rounded carbonate grains, although the image on bottom left is far more euhedral and has higher levels of Fe and Mn.



**Table 1 – Whole-rock manganese concentration results from a survey of well-preserved and metamorphosed samples from the Transvaal Supergroup.**

<b>Sample</b>	<b>Facies</b>	<b>History</b>	<b>MnO (wt. %)</b>	<b>± error</b>
WB 830m	shale	well-preserved	0.348	0.017
WB 915m	shale	well-preserved	0.478	0.024
GKF 268m	shale	well-preserved	0.109	0.005
GKP 242m	shale	well-preserved	0.086	0.013
GKP 304m	shale	well-preserved	0.034	0.005
DI 215.3m	shale	well-preserved	0.118	0.006
PA 2014m	shale	metamorphosed	1.455	0.073
PA 1226m	shale	metamorphosed	0.034	0.005
PA 886m	shale	metamorphosed	0.051	0.008
MF 493m	ferruginous shale	metamorphosed	0.173	0.009
Kumba Mine	ferruginous shale	metamorphosed	0.044	0.007
P40 155.55m	iron formation (Kur)	well-preserved	0.035	0.005
PAN 158.8m	iron formation (Griq)	well-preserved	0.395	0.020
PAN 163.9m	iron formation (Griq)	well-preserved	0.228	0.011
PAN 188.5m	iron formation (Griq)	well-preserved	0.082	0.012
PAN 196.6m	iron formation (Griq)	well-preserved	0.504	0.025
PAN 206m	iron formation (Griq)	well-preserved	0.422	0.021
MF 402m	iron formation (Penge)	metamorphosed	0.684	0.034
PA 1470m	iron formation (Penge)	metamorphosed	0.57	0.029
DI 218m	carbonate	well-preserved	0.838	0.042
GKF 338m	carbonate	well-preserved	1.005	0.050
PA 1114m	carbonate	metamorphosed	0.039	0.006
PA 251m	carbonate	metamorphosed	0.025	0.004

## SUPPORTING TABLES

Supporting Table 1 – Point measurements of elemental abundance obtained by energy dispersive spectrometry measurements.

MF402				
carbonates	Mg	Ca	Mn	Fe
12	5.66	14.86	0.66	8.4
14	5.93	14.89	0.43	8.68
15	6.1	15.12	0.42	8.6
16	5.13	15.24	0.64	9.08
21	5.72	14.6	0.64	8.55
23	5.52	14.68	1.91	8.19
29	5.23	14.59	1.69	8.42

grunerites	O	Mg	Si	Mn	Fe
1	59.39	4.78	22.18	0.45	13.14
2	58.98	5.08	21.89	0.42	13.62
7	58.94	5.08	21.86	0.54	13.58
8	59.57	4.75	21.65	0.54	13.48
9	59.06	4.86	22.22	0.48	13.39
19	58.96	5.23	21.84	0.52	13.45
26	58.35	5.07	22.24	0.42	13.91
27	59.23	5	21.72	0.52	13.53
31	59.46	4.98	21.46	0.58	13.28
32	59.03	4.73	21.92	0.51	13.8
35	59.27	4.66	21.65	0.49	13.93

PA2014				
carbonates	Mg	Ca	Mn	Fe
2	4.3	16.02	2.36	8.04
7	4.09	17.65	2.65	7.93
65	4.85	16.01	2.43	8.47
66	3.65	16.38	2.67	7.55
67	3.87	16.76	2.52	7.81
68	3.77	16.14	2.5	7.93
58	3.88	13.99	2.2	6.61
32	1.41	21.53	1.74	3.62
33	3.79	15.73	2.5	7.11
59	3.7	16.2	2.41	7.3
60	3.79	16.19	2.52	7.57
61	3.97	16.08	2.5	7.6
62	2.66	18.73	2.15	6.33
63	3.58	15.77	2.42	7.35
64	3.61	15.4	2.41	7.39

<b>grunerite</b>	<b>O</b>	<b>Mg</b>	<b>Si</b>	<b>Mn</b>	<b>Fe</b>
5	54.22	5.14	24.32	1.05	15.27
6	57.85	5.15	21.7	0.9	13.65
8	57.59	4.9	22.45	0.86	13.97
16	58.15	5.06	22.07	0.85	13.44
36	58.03	5	22.19	0.78	13.53
41	58.33	5.23	21.89	0.83	13.51
44	57.6	5.05	21.92	0.82	14.09
46	58.22	4.93	22.06	0.8	13.84
21	58.22	5.01	22.11	0.87	13.78
22	58.64	4.94	21.95	0.88	13.46
26	58.46	5.01	21.78	0.79	13.5
27	57.59	5.15	22.24	1.05	13.97
28	58.41	5.06	22.06	0.89	13.58
30	57.91	5.02	22.08	0.98	13.82
31	57.93	5.05	22.07	0.99	13.72
47	58.16	5.06	22.17	0.83	13.67
54	58.06	5.05	21.99	0.86	13.65
73	58.52	5.02	21.96	0.87	13.53
74	58.56	5.2	21.92	0.76	13.41
75	57.54	4.99	22.59	0.94	13.93
78	58.29	5.06	21.75	0.81	13.52
79	59.45	4.86	21.55	0.72	12.89
80	57.63	5.32	22.56	0.96	13.43
81	58.26	4.99	22	0.73	13.53
82	58.15	5.22	22	0.87	13.6
83	59.44	4.73	18.58	2.97	13.49
84	57.49	5.01	22.19	0.95	14.35
85	60.78	5.07	20.89	0.65	12.1
86	59.54	4.9	21.66	0.74	13.16
87	58.95	5.06	21.53	0.78	13.29

<b>garnet</b>	<b>O</b>	<b>Al</b>	<b>Si</b>	<b>Ca</b>	<b>Mn</b>	<b>Fe</b>
3	56.16	10.69	16.05	2.77	4.98	9.36
18	56.72	10.51	15.82	2.77	4.63	9.22
19	56.44	10.63	16.07	2.82	4.63	9.41
40	56.73	10.42	15.88	2.79	4.92	8.86
43	56.77	10.61	15.89	2.77	4.15	9.82
49	56.46	10.49	15.89	2.8	4.59	9.42
50	57.05	10.77	15.8	2.73	4.65	8.99
51	57.42	10.25	15.81	2.92	4.6	9

PA1470				
grunerite	O	Mg	Si	Ca
3	57.74	3.5	22.4	0.12
2	58.72	3.65	22.11	
5	57.96	3.66	22.36	
6	59.07	3.76	21.89	0.07
7	58.11	3.61	22.17	
8	58.05	3.5	22.36	
14	58.25	3.44	22.26	0.07
18	57.59	3.71	22.47	
19	57.25	3.69	22.81	
20	57.9	3.66	22.43	
21	57.9	3.49	22.48	
22	58.45	3.31	21.68	0.12
23	58.17	3.6	22.22	
24	58.22	3.41	22.29	0.06
25	57.75	3.72	22.42	

carbonates	Mg	Ca	Mn	Fe
10	0.31	28.09	0.65	1.79
11	2.92	15.96	1.23	9.51
12	2.93	15.84	1.18	9.44
15	3.13	16.11	1.19	9.9
16	3.18	16.1	1.2	10.06
17	3.27	15.66	1.24	9.89

MF 493				
carbonates	Mg	Ca	Mn	Fe
53	1.92	1.12	12.49	19.67
54	2.52	0.87	14.27	15.26
56	2.12	1.01	11.76	18.58
57	5.15	0.87	6.05	19
58	1.25	2.51	17.44	12.86

PA 886				
ilmenite	O	Ti	Mn	Fe
17	62.09	24.61	1.04	11.83
9	60.17	18.72	0.95	17.09
2	57.34	21.48	1.12	20.06



DI-1					
carbonates	Mg	Ca	Mn	Fe	total
29	8.29	16.75	0.65	4.18	29.87
30	9.38	15.53	0.54	3.87	29.32
31	10.72	17.68	0.82	4.48	33.7
32	9.21	15.42	0.67	3.78	29.08
33	10.92	16.73	0.64	3.91	32.2
34	0.23	42.84	0.61	0.36	44.04
35		33.69	0.29	0.28	34.26
24	0.19	38.42	0.23	0.31	39.15
25	11.2	17.87	0.71	4.35	34.13
28	10.42	17.33	0.79	4.27	32.81
10	0.34	31.74	0.46	0.35	32.89
11		37.29	0.61	0.37	38.27
12		30.9	0.34	0.37	31.61
13	0.39	33.49	0.44	0.42	34.74
14	10.11	16.53	0.69	4.24	31.57
15	9.42	15.07	0.66	3.91	29.06
16	9.15	15.32	0.63	3.63	28.73
18	9.92	15.8	0.68	3.64	30.04
1	0.27	32.7	0.43	0.38	33.78
2	10.24	16.25	0.67	3.82	30.98
6	9.16	15.8	0.7	3.98	29.64
7	9.78	15.55	0.64	3.42	29.39
8	10.22	15.79	0.53	3.58	30.12

proportionMg	Ca	Mn	Fe	Temperatures predicted	
0.277535989	0.56076331	0.02176096	0.13993974		
0.319918145	0.52967258	0.01841746	0.13199181		
0.31810089	0.52462908	0.02433234	0.13293769		
0.316712517	0.53026135	0.02303989	0.12998624		
0.339130435	0.51956522	0.01987578	0.12142857		
0.005222525	0.97275204	0.01385104	0.00817439	<b>255.1062447</b>	
0	0.98336252	0.00846468	0.0081728	<b>[NA]</b>	
0.004853129	0.98135377	0.00587484	0.00791826	<b>249.1389068</b>	
0.328157047	0.52358629	0.02080281	0.12745385		
0.317586102	0.52819262	0.02407802	0.13014325		
0.010337489	0.96503497	0.01398601	0.01064153	<b>317.9687819</b>	
0	0.97439247	0.01593938	0.00966815	<b>[NA]</b>	
0	0.97753875	0.01075609	0.01170516	<b>[NA]</b>	
0.011226252	0.96401842	0.01266552	0.01208981	<b>326.5897772</b>	
0.320240735	0.52359835	0.02185619	0.13430472		
0.324156917	0.51858224	0.02271163	0.13454921		
0.318482423	0.53324052	0.0219283	0.12634876		
0.330226365	0.52596538	0.02263648	0.12117177		
0.007992895	0.96802842	0.01272943	0.01124926	<b>292.6060033</b>	
0.33053583	0.52453196	0.02162686	0.12330536		
0.309041835	0.53306343	0.02361673	0.134278		
0.332766247	0.52909153	0.02177611	0.11636611		
0.339309429	0.52423639	0.01759628	0.1188579	average Mg	Temp
				of all calcite	predicted
				<b>0.00495404</b>	<b>250.79928</b>

WB 830				
carbonates	Mg	Ca	Mn	Fe
1	6.22	13.8	0.35	3.43
3	9.08	13.36	0.21	2.07
4	5.64	10.83	0.3	3.92
7	11.39	15.09	0.15	0.64
9	6.84	14.97	0.62	2.52
10	8.14	12.55	0.43	2
17	6.51	16.53	0.97	3.15
18	6.62	13.95	0.42	3.17
19	5.26	11.65	0.24	3.04
21	6.03	12.01	0.34	3.14
25	4.7	9.48	0.39	4.15
26	5	10.32	0.53	3.59
27	4.56	8.98	0.45	4
30	4.19	9.51	0.13	2.67
33	4.56	9.01	0.35	4.08
34	4.47	9.24	0.37	4.22
43	9.79	10.9	0.14	0.61
44	4.64	10.57	0.17	3.04
45	6.1	10.03	0.27	2.85
46	5.11	9.11	0.27	3
47	8.23	11.05	0.1	0.38
48	10.38	13.13	0.13	0.19
50	5.66	11.55	0.31	2.49
52	5.93	11.52	0.74	2.39
53	5.84	11.17	0.39	1.71

GKF 338				
carbonates	Mg	Ca	Mn	Fe
61	8.29	15.13	0.63	2.51
62	8.93	24.32	0.62	1.98
69	9.22	18.08	0.75	2.08
70	6.55	10.81	0.73	2.5
71	7.24	11.71	0.67	1.87
74	5.43	9.45	0.73	2.44
72	10.82	12.14	0.46	0.64

<b>73</b>	7.77	13.1	0.52	1.44
<b>74</b>	5.43	9.45	0.73	2.44
<b>75</b>	8.02	13.21	0.48	1.76
<b>76</b>	6.39	10.6	0.42	1.47
<b>77</b>	8.99	11.91	0.4	1.33
<b>88</b>	1.65	24.77	0.7	1.85
<b>89</b>	6.6	9.72	0.41	1.63
<b>79</b>	5.65	9.13	0.54	2.5
<b>80</b>	5.03	7.8	0.5	2.24
<b>81</b>	6.59	9.99	0.41	1.55
<b>86</b>	6.36	11.72	0.65	2.07

GKP 242m				
carbonates	Mg	Ca	Mn	Fe
<b>95</b>	4.99	8.07	0.31	2.98
<b>103</b>	6.93	12.15	0.49	3.65
<b>113</b>	5.22	11.17	1.29	4.82
<b>117</b>	4.64	8.1	0.38	3.6
<b>130</b>	6.52	11	0.45	3.09
<b>131</b>	6.49	9.34	0.45	1.99
<b>132</b>	5.73	9.05	0.42	1.88
<b>133</b>	5.33	8.91	0.29	2.35

[euohedral crystal]

## REFERENCES

- Altermann W. and Nelson D. R. (1998) Sedimentation rates, basin analysis and regional correlations of three Neoarchaeon and Palaeoproterozoic sub-basins of the Kaapvaal craton as inferred from precise U–Pb zircon ages from volcanoclastic sediments. *Sediment. Geol.* **120**, 225–256.
- Beukes N. J. (1987) Facies relations, depositional environments and diagenesis in a major early Proterozoic stromatolitic carbonate platform to basinal sequence, Campbellrand Subgroup, Transvaal Supergroup, Southern Africa. *Sediment. Geol.* **54**, 1–46.
- Beukes N. J. (1984) Sedimentology of the Kuruman and Griquatown Iron-formations, Transvaal Supergroup, Griqualand West, South Africa. *Precambrian Res.* **24**, 47–84.
- Beukes N. and Klein C. (1992) Models for Iron-Formation Deposition. In *The Proterozoic Biosphere: A Multidisciplinary Study* (eds. J. W. Schopf and C. Klein). Cambridge University Press.
- Buick I. S., Maas R. and Gibson R. (2001) Precise U–Pb titanite age constraints on the emplacement of the Bushveld Complex, South Africa. *J. Geol. Soc.* **158**, 3–6.
- Burnham C. W. (1979) Magmas and hydrothermal fluids. In *Geochemistry of Hydrothermal Ore Deposits* (ed. H. L. Barnes). John Wiley & Sons, New York. pp. 71–136.
- Dyar M. D., Gunter M. E., Delaney J. S., Lanzarotti A. and Sutton S. R. (2002) Systematics in the structure and XANES spectra of pyroenes, amphiboles, and micas as derived from oriented single crystals. *Can. Mineral.* **40**, 1375–1393.
- Eriksson P. G., Hattingh P. J. and Altermann W. (1995) An overview of the geology of the Transvaal Sequence and Bushveld Complex, South Africa. *Miner. Deposita* **30**, 98–111.
- Goldsmith J. R. and Newton R. C. (1969) P–T–X relations in the system CaCO<sub>3</sub>–MgCO<sub>3</sub> at high temperatures and pressures. *Am. J. Sci.* **267-A**, 160–190.
- Guo Q., Strauss H., Kaufman A. J., Schröder S., Gutzmer J., Wing B., Baker M. A., Bekker A., Jin Q., Kim S.-T. and Farquhar J. (2009) Reconstructing Earth's Surface Oxidation Across the Archean-Proterozoic Transition. *Geology* **37**, 399–402.
- Gutzmer J. (1996) Genesis and alteration of the Kalahari and Postmasburg manganese deposits, Griqualand West, South Africa. Rand Afrikaans University.



- Harris H. W., El-Naggar M. Y., Bretschger O., Ward M. J., Romine M. F., Obraztsova A. Y. and Nealson K. H. (2010) Electrokinesis is a microbial behavior that requires extracellular electron transport. *Proc. Natl. Acad. Sci.* **107**, 326–331.
- Harris N., McMillan A., Holness M., Uken R., Watkeys M., Rogers N. and Fallick A. (2003) Melt generation and fluid flow in the thermal aureole of the Bushveld Complex. *J. Petrol.* **44**, 1031–1054.
- Holland H. D. (1984) *The Chemical Evolution of the Atmosphere and Oceans.*, Princeton University Press.
- Johnson J. E., Gerpheide A., Lamb M. P. and Fischer W. W. (2014) O<sub>2</sub> constraints from Paleoproterozoic detrital pyrite and uraninite. *Geol. Soc. Am. Bull.* **126**, 813–830.
- Johnson J. E., Webb S. M., Ma C. and Fischer W. W. (in review) Manganese mineralogy and diagenesis in the sedimentary rock record. *Geochim. Cosmochim. Acta*.
- Johnson J. E., Webb S. M., Thomas K., Ono S., Kirschvink J. L. and Fischer W. W. (2013) Manganese-oxidizing photosynthesis before the rise of cyanobacteria. *Proc. Natl. Acad. Sci.* **110**, 11238–11243.
- Kaneko Y. and Miyano T. (1990) Contact metamorphism of the Bushveld Complex in the northeastern Transvaal, South Africa. *J. Mineral. Petrol. Econ. Geol.* **85**, 66–81.
- Kaufman A. J. (1996) Geochemical and mineralogic effects of contact metamorphism on banded iron-formation: an example from the Transvaal Basin, South Africa. *Precambrian Res.* **79**, 171–194.
- Kirschvink J. L., Gaidos E. J., Bertani L. E., Beukes N. J., Gutzmer J., Maepa L. N. and Steinberger R. E. (2000) Paleoproterozoic snowball Earth: Extreme climatic and geochemical global change and its biological consequences. *Proc. Natl. Acad. Sci.* **97**, 1400–1405.
- Klein C. (1968) Coexisting Amphiboles. *J. Petrol.* **9**, 281–330.
- De Kock M. O., Evans D. A. D., Kirschvink J. L., Beukes N. J., Rose E. and Hilburn I. (2009) Paleomagnetism of a Neoarchean-Paleoproterozoic carbonate ramp and carbonate platform succession (Transvaal Supergroup) from surface outcrop and drill core, Griqualand West region, South Africa. *Precambrian Res.* **169**, 80–99.
- Komiya T., Hirata T., Kitajima K., Yamamoto S., Shibuya T., Sawaki Y., Ishikawa T., Shu D., Li Y. and Han J. (2008) Evolution of the composition of seawater through geologic time, and its influence on the evolution of life. *Gondwana Res.* **14**, 159–174.
- Kontak D. J. and Corey M. (1988) Metasomatic origin of spessartine-rich garnet in the South Mountain Batholith, Nova Scotia. *Can. Mineral.* **26**, 315–334.

- Lee C. A. (1996) A Review of Mineralization in the Bushveld Complex and some other Layered Intrusions. In *Developments in Petrology* (ed. R. G. Cawthorn). Layered Intrusions. Elsevier. pp. 103–145. Available at: <http://www.sciencedirect.com/science/article/pii/S0167289496800066> [Accessed April 14, 2015].
- Luther G. W. I. (2010) The Role of One- and Two-Electron Transfer Reactions in Forming Thermodynamically Unstable Intermediates as Barriers in Multi-Electron Redox Reactions. *Aquat. Geochem.* **16**, 395–420.
- Mayhew L. E., Webb S. M. and Templeton A. S. (2011) Microscale imaging and identification of Fe speciation and distribution during fluid-mineral reactions under highly reducing conditions. *Environ. Sci. Technol.* **45**, 4468–4474.
- Maynard J. B. (2010) The Chemistry of Manganese Ores through Time: A Signal of Increasing Diversity of Earth-Surface Environments. *Econ. Geol.* **105**, 535–552.
- Miyano T. and Beukes N. J. (1997) Mineralogy and Petrology of the Contact Metamorphosed Amphibole Asbestos-bearing Penge Iron Formation, Eastern Transvaal, South Africa. *J. Petrol.* **38**, 651–676.
- Miyano T. and Beukes N. J. (1984) Phase relations of stilpnomelane, ferri-annite, and riebeckite in very low-grade metamorphosed iron-formations. *South Afr. J. Geol.* **87**, 111–124.
- Okita P. M., Maynard J. B., Spiker E. C. and Force E. R. (1988) Isotopic evidence for organic matter oxidation by manganese reduction in the formation of stratiform manganese carbonate ore. *Geochim. Cosmochim. Acta* **52**, 2679–2685.
- Ollila J. T. (1984) Fluid inclusion and tin deposition at Zaaipplaats, South Africa. *Bull. Geol. Soc. Finl.* **56**, 59–73.
- Pickard A. . (2003) SHRIMP U–Pb zircon ages for the Palaeoproterozoic Kuruman Iron Formation, Northern Cape Province, South Africa: evidence for simultaneous BIF deposition on Kaapvaal and Pilbara Cratons. *Precambrian Res.* **125**, 275–315.
- Planavsky N. J., Asael D., Hofmann A., Reinhard C. T., Lalonde S. V., Knudsen A., Wang X., Ossa Ossa F., Pecoits E., Smith A. J. B., Beukes N. J., Bekker A., Johnson T. M., Konhauser K. O., Lyons T. W. and Rouxel O. J. (2014) Evidence for oxygenic photosynthesis half a billion years before the Great Oxidation Event. *Nat. Geosci.* **7**, 283–286.
- Roy S. (2000) Late Archean initiation of manganese metallogenesis: its significance and environmental controls. *Ore Geol. Rev.* **17**, 179–198.
- Roy S. (2006) Sedimentary manganese metallogenesis in response to the evolution of the Earth system. *Earth-Sci. Rev.* **77**, 273–305.

- Schröder S. (2006) Stratigraphic and geochemical framework of the Agouron drill cores, Transvaal Supergroup (Neoarchean-Paleoproterozoic, South Africa). *South Afr. J. Geol.* **109**, 23–54.
- Smith A. J. B., Beukes N. J., Gutzmer J. and Cochrane J. M. (2010) Evidence for dissimilatory manganese reduction and availability of free molecular oxygen during deposition of Mesoarchean Witwatersrand-Mozaan strata. *Mineral. Mag.* **74**, A973.
- Stumm W. and Morgan J. J. (1996) *Aquatic Chemistry: Chemical Equilibria and Rates in Natural Waters*. 3rd ed., Wiley-Interscience, New York.
- Sumner D. Y. and Beukes N. J. (2006) Sequence stratigraphic development of the Neoarchean Transvaal carbonate platform, Kaapvaal Craton, South Africa. **109**, 11–22.
- Sumner D. Y. and Bowring S. A. (1996) U-Pb geochronologic constraints on deposition of the Campbellrand Subgroup, Transvaal Supergroup, South Africa. *Precambrian Res.* **79**, 25–35.
- Urban H., Stribny B. and Lippolt H. J. (1992) Iron and manganese deposits of the Urucum District, Mato Grosso do Sul, Brazil. *Econ. Geol.* **87**, 1375–1392.
- Varentsov I. M. (1996) *Manganese Ores of Supergene Zone: Geochemistry of Formation.*, Kluwer Academic Publishers, Dordrecht, The Netherlands.
- Varentsov I. M. and Grasselly G. eds. (1976) *Geology and geochemistry of manganese: proceedings of the 2nd International Symposium on Geology and Geochemistry of Manganese.*, International Symposium on Geology and Geochemistry of Manganese, Sydney.
- Veizer J. (1978) Secular variations in the composition of sedimentary carbonate rocks, II. Fe, Mn, Ca, Mg, Si and minor constituents. *Precambrian Res.* **6**, 381–413.
- Wallmann K., Aloisi G., Haeckel M., Tishchenko P., Pavlova G., Greinert J., Kutterolf S. and Eisenhauer A. (2008) Silicate weathering in anoxic marine sediments. *Geochim. Cosmochim. Acta* **72**, 3067–3090.
- Walraven F., Armstrong R. . and Kruger F. . (1990) A chronostratigraphic framework for the north-central Kaapvaal craton, the Bushveld Complex and the Vredefort structure. *Tectonophysics* **171**, 23–48.

*Concluding Remarks and Future Directions*

This thesis centers on the redox cycling of manganese and how the redox state of manganese can reveal environmental conditions and biological processes. Chapter 1 presents the current knowledge of manganese oxidation and reduction reactions and analyses of a series of representative manganese-enriched sedimentary rocks ('manganese deposits') throughout geologic time. This mineralogical survey of manganese deposits concluded that manganese is generally stabilized in the geologic record in a different and more reduced form (like in Mn(II) carbonates or Mn(III) oxides) than the primary precipitate (which is usually Mn(IV) oxides).

Chapter 2 focuses on the origin of the earliest significant manganese deposit, from the 2.415 billion-year-old Koegas Subgroup in South Africa. Here we investigated whether this deposit, which appeared to occur prior to the oxygenation of Earth's atmosphere and ocean, could be evidence for a biological hypothesis that predicted manganese-oxidizing photosynthesis was a precursor to water-oxidizing photosynthesis. Two proxies for oxygen in two cores through the Koegas Subgroup indicated very low levels of oxygen, but a micro-scale study of the manganese deposits showed these were originally manganese oxides – now stabilized as manganese-enriched carbonates. Finding manganese oxidation before oxygen production strongly supports the presence of manganese-oxidizing photosynthesis, and this study marks the first strong geologic evidence for an evolutionary hypothesis.

As a follow-up report, Chapter 3 probes deeper into one of the proxies for oxygen used in Chapter 2: the oxygen-sensitive detrital grains. In this study, we presented a second redox-sensitive detrital grain, uraninite, in addition to expanding on the abundant detrital pyrite described earlier. We also developed a mathematical model combining physical erosion and chemical weathering processes to constrain ancient oxygen concentrations. For the Koegas Subgroup, the model limits the atmosphere to less than  $\sim 10^{-5}$  atm of  $O_2$ —not enough to support Mn oxidation as we understand it today.

Chapter 4 returns to manganese cycling, exploring how such a wide variety of manganese deposits become reduced post-deposition using real-time measurements of common manganese reduction pathways. We used a flow-through system to measure redox state and coordination environment of manganese throughout abiotic reduction by sulfide and ferrous iron and biologically-mediated reduction using a model metal-reducing bacteria, *Shewanella oneidensis*, in several end-member conditions. We found that the most common manganese phase in the geologic record, Mn(II)-carbonates, was produced by microbially-mediated manganese oxide reduction, while abiotic reduction pathways (without inorganic carbon present) made Mn(II) in solution. Mn(III) oxyhydroxides were produced as an intermediate in almost all reaction pathways, and these could serve as precursors to the Mn(III) oxides found in ancient manganese deposits.

Chapter 5 is a final investigation into ancient manganese deposits, but this time focusing on the minor Mn deposits reported from prior to the Koegas Subgroup. Manganese oxidation (and therefore  $O_2$ ) has long since been inferred from manganese enrichment of sedimentary rocks, but another possibility exists: manganese could be enriched from magmatic or hydrothermal fluids associated with alteration occurring at high temperatures and pressures (i.e., during metamorphism). We tested whether metamorphism could mobilize and enrich manganese in ancient rocks harnessing well-understood metamorphic gradients across South Africa. We performed micro-scale and nano-scale analyses of 2.5 billion-year-old correlated strata from the highly metamorphosed eastern basin and the unperturbed western basin and determined that manganese was mobilized during metamorphism and enriched in garnets, amphiboles, and carbonates from metamorphosed samples, and occasionally enriched in bulk concentrations. These results are limited to these specific strata, but they suggest that other small deposits from before the rise of oxygen need to be carefully examined.

There are countless ways in which these chapters could be expanded and developed in future work. There are major manganese deposits from the Oligocene in the Baltic Sea area – for example, a reported deposit in Ukraine and Georgia with over a billion tons of manganese noted in Chapter 1 – which we were unable to acquire samples of. Since these are only approximately 30 million years old, it would be quite interesting to see what redox state(s) and minerals the manganese is in and determine to what extent it has post-depositional alteration. Similarly, this thesis has not explored the processes behind

supergene manganese deposits. Somehow, oxic weathering has dissolved carbonate and surrounding material and produced a highly manganese-enriched deposit (like in the 1 billion-year-old Woodie-Woodie deposit in Australia or the 2 billion-year-old Postmasburg deposit in South Africa) but does that have microbial involvement? Recent work has shown that microbes can oxidize manganese from solids including manganese carbonates (e.g., Tang et al, 2013) and it would be interesting to do a microbial enrichment from some of these supergene deposits and explore the interactions between microbes and rocks in these deposits. Furthermore, the mineralogy of supergene deposits are necessarily different from other manganese deposits due to their formation, and preliminary work indicates they are Mn(III,IV) oxides with a large proportion of Mn(III) (see Appendix A). Pre-oxygen deposits could also be interrogated in more detail using methods established in this thesis: paired micro-scale X-ray spectroscopic imaging and X-ray absorption spectroscopy with optical microscopy and nano-scale electron microscopic analyses supplemented by Raman and X-ray diffraction methods. These in-depth analyses seem to be required for such ancient (and therefore necessarily corrupted by heat, pressure, and time) rocks which may or may not have primary manganese enrichments.

The Koegas Subgroup evidence for manganese-oxidizing photosynthesis also has several follow-up avenues. On the geological side, the manganese in this deposit is relatively unquantified and it would be illuminating to see how a better estimate of manganese volume compared with other post-oxygen manganese deposits. More investigations could

be made into contemporaneous strata from Australia and Canada to see whether similar manganese-enriched sedimentary rocks could be found and compared to the Koegas Subgroup. Biological possibilities also abound: our lab has already begun to see whether we can produce a manganese-oxidizing cyanobacterium which cannot oxidize water and lives anaerobically, and that would be an exciting biological parallel to the geological data. And we are currently examining deep-branching cyanobacteria to see whether they might hold signs of manganese-oxidizing photosynthesis.

The calculations we made for quantifying oxygen from the presence and circumstances of oxygen-sensitive pyrite and uraninite grains were an improvement upon the existing models, which only used chemical weathering and did not incorporate physical erosion, but the chemical weathering equations also require refinement. The reaction rate for uraninite oxidation was developed in 1976 by Grandstaff, and there has been no published updates since this article. The commonly used pyrite oxidation law is also from one paper, now over ten years old, from Williamson and Rimstidt. Neither oxidation rate law explores the effects of microbial enhancement upon chemical weathering, which is highly unrealistic. With better chemical and biological constraints on pyrite and uraninite chemical weathering, our model for chemical dissolution and physical erosion could be much more accurate. Another improvement would be producing a model where physical erosion had a positive feedback on chemical weathering, as this is more similar to what occurs in natural environments.



The experiments we present measuring manganese phase through abiotic and biotic manganese reduction are just the beginning of an entire avenue of potential research. Ancient manganese deposits are often associated with iron deposits, like the Neoproterozoic Santa Cruz Formation in Brazil or the Koegas Subgroup in South Africa. Thus understanding the dynamics that occur with dual-oxide systems may be key to developing a realistic understanding of the processes that occurred in these formations. Experiments addressing this problem may involve biological reduction experiments with both iron oxides and manganese oxides, and varying levels of lactate to see if organic carbon abundance can control the amount of iron and manganese carbonate precipitation versus iron oxide products. Another exciting avenue to explore is the interactions that occur between sulfur and manganese, another combination commonly seen in nature (see Chapter 4). While we observed only manganese(II) cations produced from sulfide-induced manganese oxide reduction, others have noted manganese carbonate formation. This is likely due to the dissolved inorganic carbon controls and alkalinity influences on carbonate saturation. Future experiments to constrain when and how manganese carbonate may form in mixed manganese-sulfate/thiosulfate/sulfide systems might include *S. oneidensis* performing thiosulfate and sulfate reduction with  $\text{Mn}^{2+}$  present to measure whether manganese carbonate is formed, and sulfide-induced Mn(IV) reduction with a bicarbonate buffer and  $\text{N}_2/\text{CO}_2$  gas mixture to see whether that stimulates manganese carbonate production (as I would predict) rather than the aqueous manganese(II) ions produced with PIPES buffer that we used. A third direction may be to test whether other electron donors like molecular hydrogen or fumarate affect

mineralogy: this will help to constrain the requisite conditions for manganese carbonate and manganese(III) oxide formation. With manganese-enriched sedimentary rocks newly discovered on Mars, relating manganese minerals to environmental processes, and especially establishing whether any minerals are unique to biological processes, becomes even more important and stimulating.

The experiments suggested above have mainly addressed the astrobiological potential of understanding manganese mineralogy during various types of manganese reduction processes; however, another equally fascinating approach is exploring the mechanism of biological manganese reduction using the same flow-through real-time system we developed. One of the experiments we performed in Chapter 4, microbial manganese oxide reduction using *Shewanella oneidensis* under high phosphate, revealed that *S. oneidensis* effectively reduces manganese(IV) oxides in a two-electron process because Mn(II)-phosphate was immediately formed from Mn(IV) oxides. The mechanism of another common manganese-reducing microbe, *Geobacter sulfurreducens*, is thought to be different but is at present unclear. Using similar phosphate levels to ligate any Mn(II) produced, our flow-through system could be used to determine whether *G. sulfurreducens* also performs manganese reduction in a two-electron process or whether it has two one-electron steps. Pyrophosphate is a doubly-bound phosphate anion that is well-known for ligating to Mn(III) and pyoverdine is a siderophore with strong Mn(III) binding capacity. With both *S. oneidensis* and *G. sulfurreducens*, it would be interesting to add pyrophosphate and/or pyoverdine to the media rather than phosphate and see if a

Mn(III) phase is produced. It may be that there is Mn(III) produced by *S. oneidensis* but it is quickly reduced to Mn(II), and pyrophosphate or pyoverdine may be a way to halt the reaction at Mn(III). As discussed briefly in Chapter 4, there are two suggestions as to how *S. oneidensis* reduces solid oxides: either direct electron transfer by approaching the metal, which would suggest that the process has one-electron steps, or by using secreted soluble electron carriers called flavins. The exact mechanism that *S. oneidensis* uses could be tested with our flow-through real-time system by using a flavin mutant (developed in the Gralnick lab, U. Minnesota): does the mutant produce a Mn(III) intermediate before an Mn(II) shoulder appears? Performing this experiment in a phosphate-rich media might be especially illuminating, since with the non-mutant strain, no Mn(III) appears at all in phosphate-rich media. Additional experiments using pyrophosphate and/or pyoverdine may prove revealing as well if there are differences between the mutant and wild-type strains in the Mn(III) production and capture by these ligands.

There are a multitude of trajectories through which one can explore manganese cycling and manganese microbe-mineral-rock dynamics, and I wish every current and future adventurer the best of luck!

*Appendix A*

## Supergene Manganese Preliminary Results

At the Kumba Iron Ore Mine, we sampled a small Mn deposit to understand the chemistry of the underlying sediments and the highly weathered supergene deposit, which may also be produced from hydrothermal fluid influences. These Mn deposits are known as ‘wad’ in mining jargon. We found that manganese was enriched over ten times more in the ‘wad’ deposit than the underlying carbonate (which was also quite weathered), and iron was enriched over fifteen times in the ‘wad’ material (Table A1). The manganese oxide in the ‘wad’ material was a mixture of MnIII and MnIV (Figure A1), which contrasts with our findings in Chapter 1 of modern manganese on the ocean.

### TABLES AND FIGURES

**Table A1:** Comparing supergene deposit and underlying carbonate.

Analyte Symbol		MnO	SiO <sub>2</sub>	Al <sub>2</sub> O <sub>3</sub>	Fe <sub>2</sub> O <sub>3</sub> (T)
Unit Symbol		%	%	%	%
Detection Limit		0.001	0.01	0.01	0.01
Analysis Method		FUS-ICP	FUS-ICP	FUS-ICP	FUS-ICP
KUMBA_WAD		8.686	18.22	9.1	40.8
KUMBA_CARB		0.818	0.35	0.17	2.51
MgO	CaO	Na <sub>2</sub> O	K <sub>2</sub> O	TiO <sub>2</sub>	P <sub>2</sub> O <sub>5</sub>
%	%	%	%	%	%
0.01	0.01	0.01	0.01	0.001	0.01
FUS-ICP	FUS-ICP	FUS-ICP	FUS-ICP	FUS-ICP	FUS-ICP
5.16	1.98	0.07	0.08	0.371	0.51
18.89	29.82	0.02	0.01	0.004	0.01

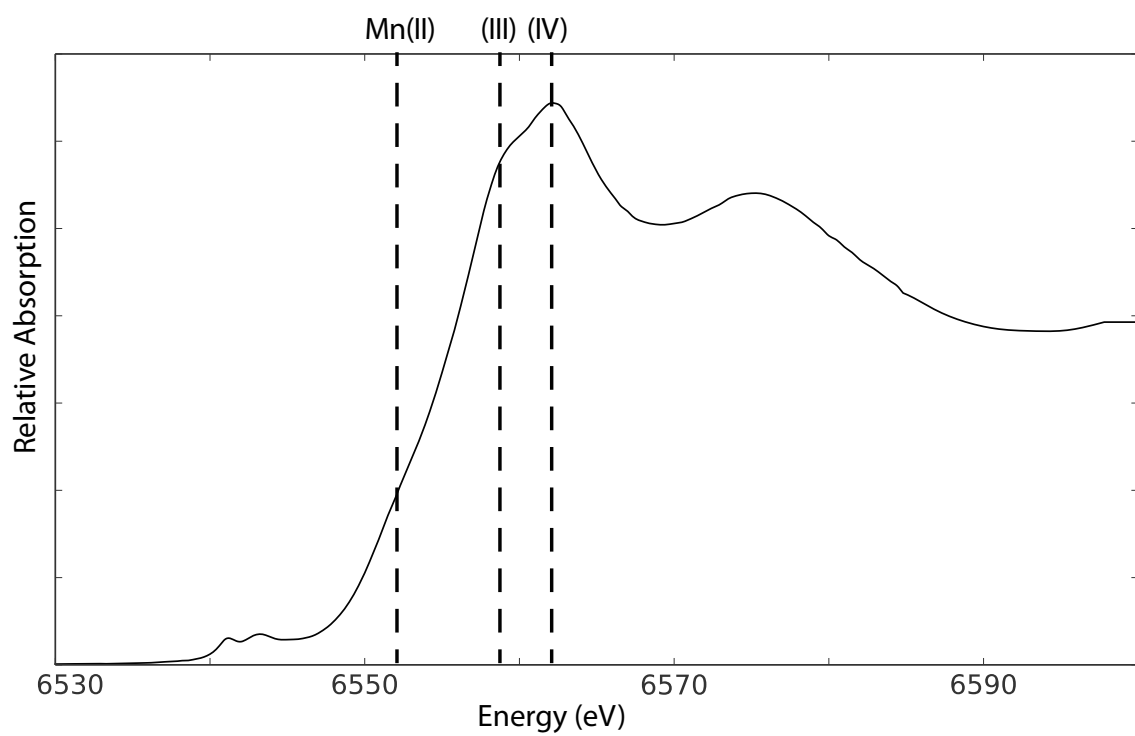


**Figure A1:** X-ray absorption spectra of Mn deposit.

*Appendix B***Pongola-Witwatersrand examples of Mn enrichments**

Manganese enrichments in Mozaan-Witwatersrand shales and iron formations have been used as evidence for environmental molecular oxygen (Smith et al., 2010; Planavsky et al., 2014). We used drill core sample chips provided to us by B. Smith (U Johannesburg) and prepared ultrathin (~15  $\mu\text{m}$ ) sections. We performed light and electron microscopy to document the textures and find regions where X-ray analysis would be the most valuable. We then obtained XAS spectra and images using two different synchrotron beam lines, beam line 10-2 and 2-3. Below are some of the salient details of each sample to accompany the figures.

**Sample DDN-1 (Figure B1)**

DDN-1 is a sandstone with abundant quartz grains, but it is also very rich in hematite and rhodochrosite, both as cements and veins. Hematite occurs as large well-crystalline needles largely as cements concentrated along laminae with larger grains sizes, and a very notable subhorizontal vein cross-cutting laminae. The carbonates are present also as cements and veins. There are small crystals of Mn-rich siderite as cement and thick veins composed of Mn-siderite, and/or Fe-rhodochrosite. There are also very large ( $> 100 \mu\text{m}$ ) euhedral pyrites that cross cut the veins and other textures. Scattered Fe-aluminosilicates (that do not contain Mn) are present in cements. The XAS data show strong abundances of Mn confined largely to Mn-siderite and Fe-rhodochrosite in the cracks with lesser

amounts in laminae with coarser sand. There are no high-valent Mn oxide phases present, only Mn(II). The high abundance of Mn in veins strongly implies a metasomatic origin in this sample. An image looking at the covariance of Mn and Fe shows that the Mn-Fe carbonate in the veins predates the hematite in the veins. The petrogenesis of this sample is complicated. The sample appears to have once been a quartz-dominated sandstone. Original cement is unclear but could have been clay minerals. Then fluids rich in Mn and Fe mineralized Mn-siderite and Fe-rhodochrosite in veins and cements in coarser laminae. This occurred either post- or syn-fracturing. The unusual and varied redox states of the vein mineralogy suggests several episodes of fluids. Oxidizing fluids mineralized hematite next. Then another generation of (more reducing and S bearing) fluids mineralized pyrites. Despite the complex petrogenesis of this sample, clear cross-cutting relationships help highlight instances of Mn and Fe mineralization tied to the migration of several generations of late fluids through the region.

### **Sample DBK-1 (Figure B2)**

DBK-1 is a more complex sample with a much higher apparent metamorphic grade. The textures show a fine-grained matrix composed of magnetite, Fe/K clays, and quartz (cements) forming an incipient metamorphic foliation/lineation in a matrix around a large (cm-scale) nodule with a concentric chemical zonation defined by differing amounts of Fe and Mn, including very large euhedral pyrites (very clear in the Mn vs. Fe XAS plot). There is Ca- and Fe-rich, Al-poor spessartine throughout the sample, both in the nodule and in the dark iron-rich matrix. The garnets (low-Al spessartine and andradite) cross-cut

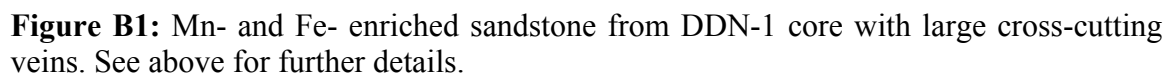
all other grain boundaries. The most Mn-rich phases occur in the nodule as two coexisting very crystalline carbonate phases: a pseudo-kutnohorite ( $\text{Mn}_{0.46}\text{Ca}_{0.41}\text{Fe}_{0.08}\text{Mg}_{0.04}\text{CO}_3$ , labelled 'ku') and in an almost pure rhodochrosite ( $\text{Mn}_{0.94}(\text{Ca,Fe,Mg})_{0.06}\text{CO}_3$ , labelled 'rh'). The carbonate phases are very coarsely crystalline and do not contain any inclusions of oxide phases. It is surprising that there is so little Fe in these carbonates: in Koegas Mn-enriched iron formations, the early diagenetic carbonate crystals are often highly enriched in iron as well as manganese and calcium (and a small amount of magnesium depending on dolomitization/ankeritization). And in the Hotazel, Fe is also present in trace domains of oxides throughout the kutnohorite and braunite. From grain boundaries here, it is difficult to constrain whether kutnohorite or rhodochrosite is earlier, with both appearing highly recrystallized. There is also a small amount of Mn in the Fe/K aluminosilicate minerals (1-2 wt. %), which is unusual. The SEM and X-ray absorption measurements produce independent and consistent mineralogy and redox state measurements, and no high valent Mn phases are present. The nodule here is a singularity: what appear to be additional small carbonate concretions throughout the sample under hand lens and light microscopy are highly-crystalline ellipsoid lenses of Fe/K aluminosilicates. Due to the high metamorphic grade, the petrogenesis is a bit tricky. The hypothesis that the nodule was composed of kutnohorite and precipitated during early diagenesis of Mn-oxide rich muds is attractive, but difficult to confirm with confidence. Because the primary lamination doesn't remain, it's not possible to assess differential compaction around the nodule. The lack of oxide inclusions and the coarse-grained nature of the carbonates could be the result of intense

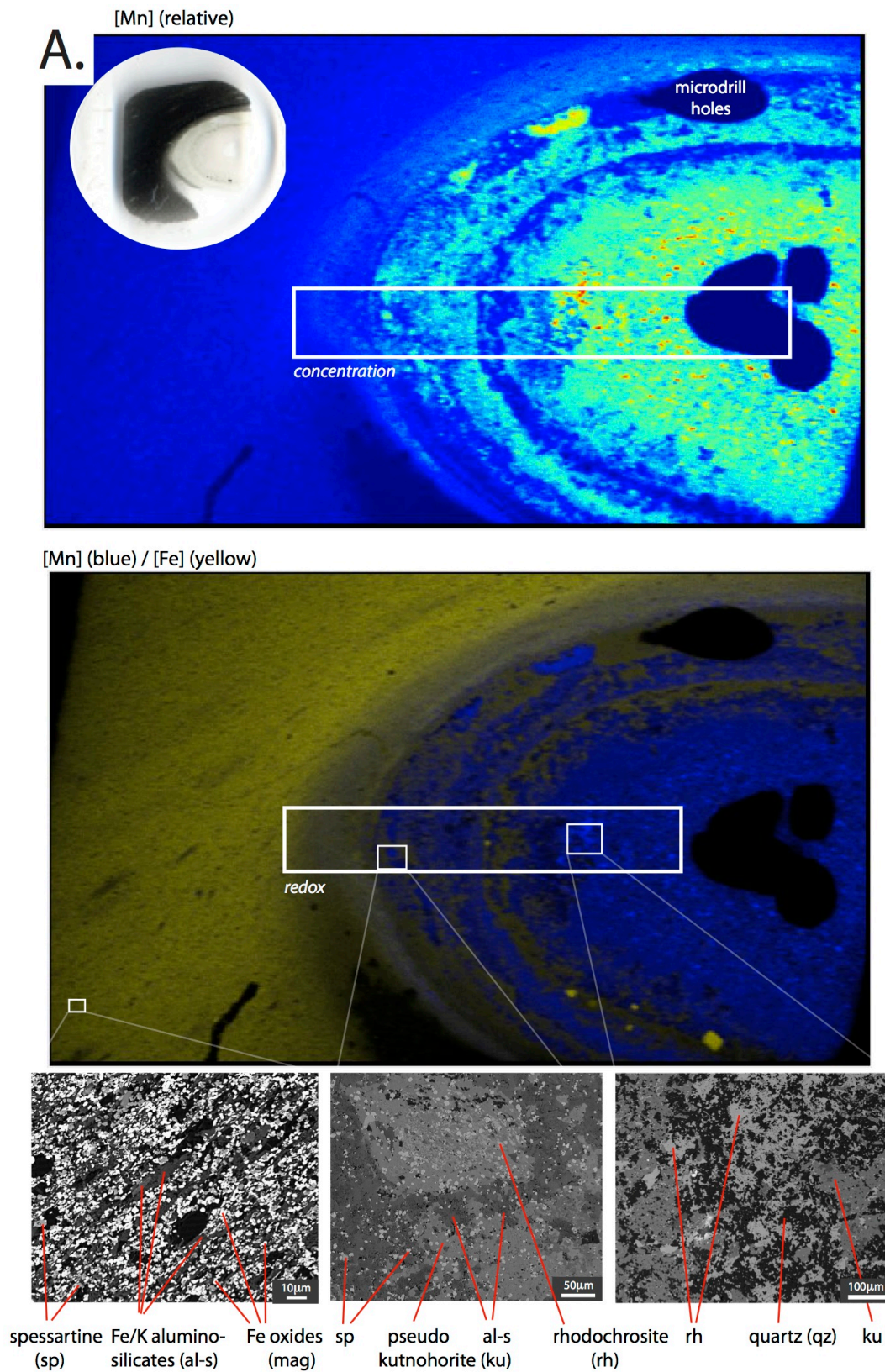


recrystallization of fine-grained pre-existing carbonates, and the garnets could result from decarboxylation of the carbonates at very high T, but can't be purely isochemical. The distinct chemical fronts associated with the growing front of the nodule are emphasized by the large trace metal-rich pyrites also give some pause. There are some potential metamorphic monazites present in there that could be used to date some of the alterations using the ion microprobe.

### **Sample PNG-3 (Figure B3)**

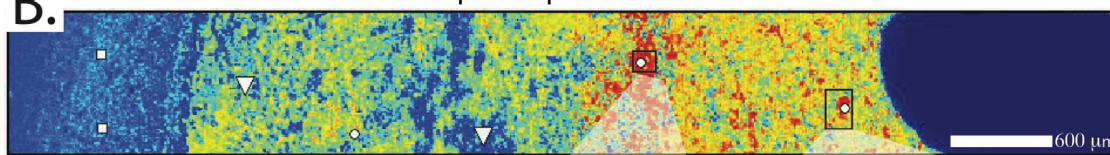
Preliminary analyses indicate that PNG-3 is very similar to DBK-1. It too bears spessartine, rhodochrosite, and kutnohorite, but it additionally has another interesting Mn-bearing phase: a very Mn-rich chromite. Galena is also common. Rhodochrosite, which dominates the Mn composition of the sample, appears highly crystalline and does not contain any oxides. The spessartines are also much larger in diameter, around 20 microns rather than <10 microns in DBK-1. Garnets in this sample also have a surprising amount of Cr. At this metamorphic grade, it's difficult to interpret primary mineralogy, but would be great to examine material from the same horizon better preserved elsewhere.



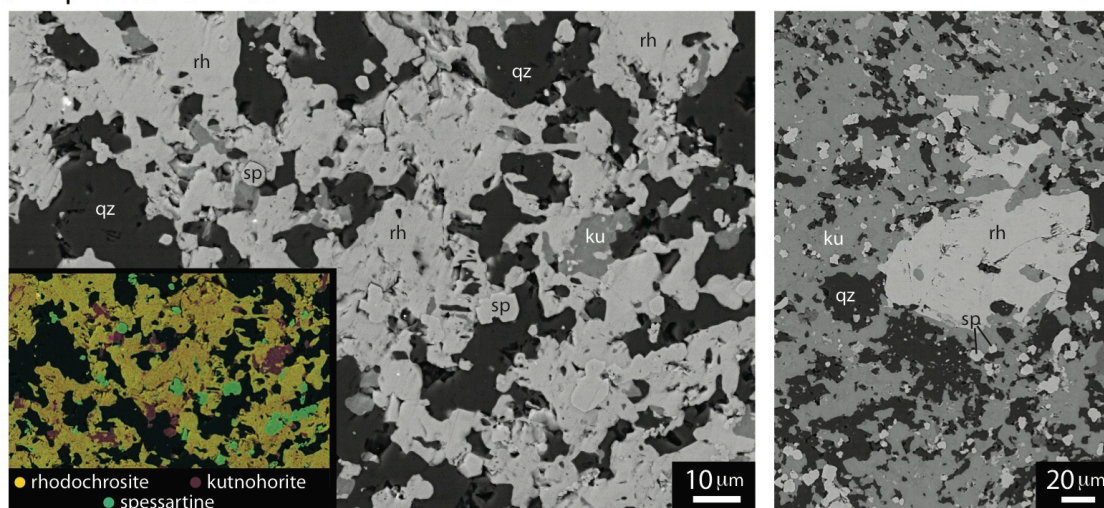




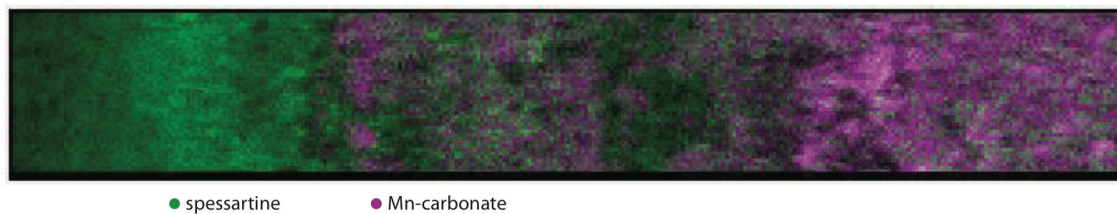
## B. Mn concentration zoom with point spectra labelled



### SEM photos from zoom



### Manganese Redox Map



### Point spectra from synchrotron

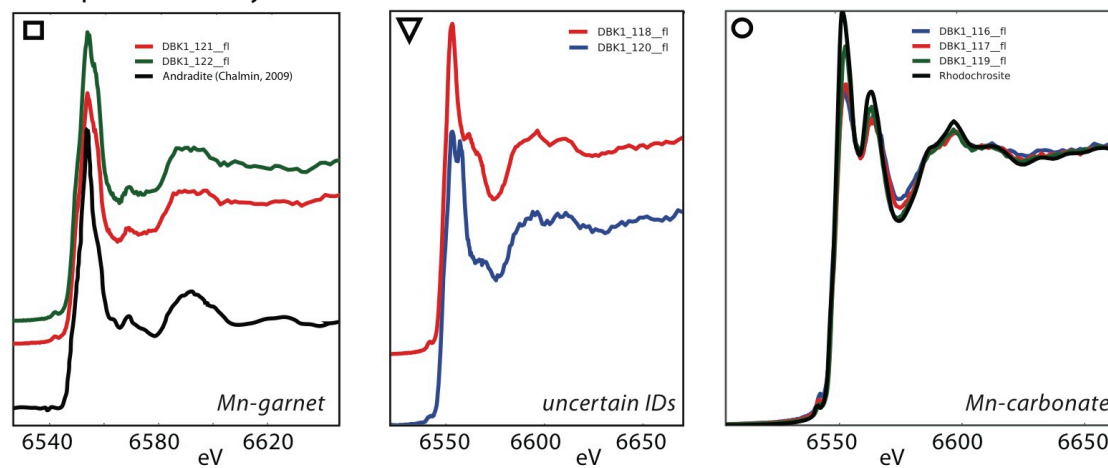
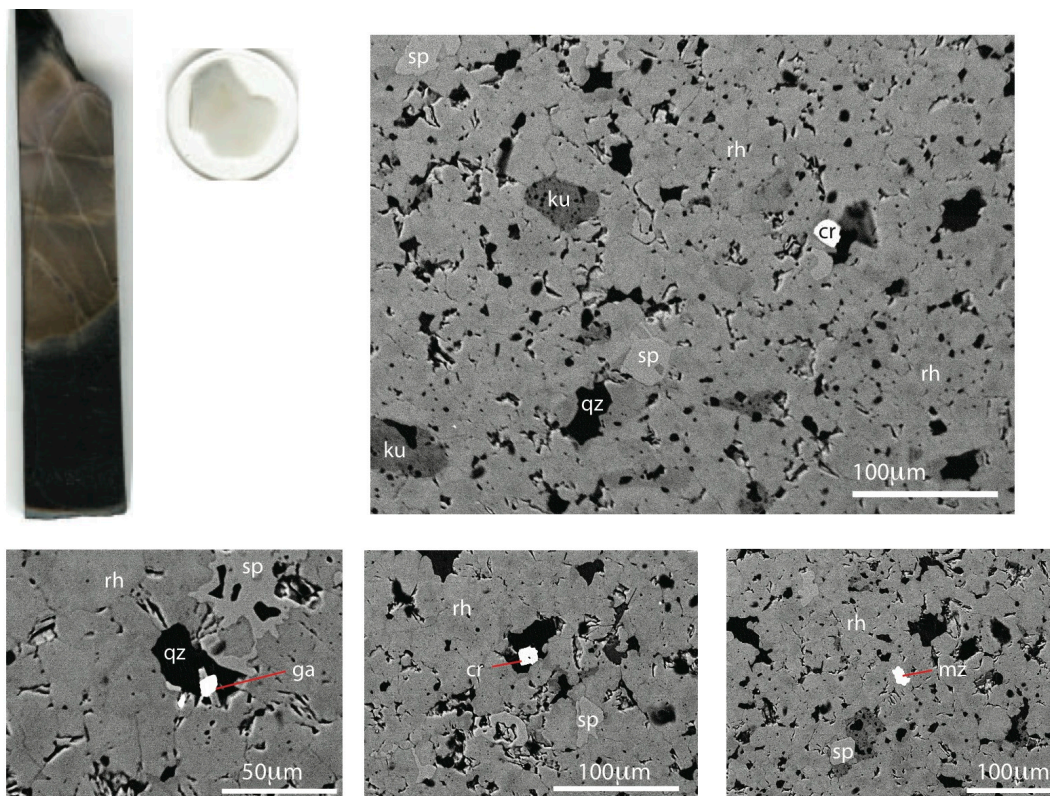


**Figure B2 (above):** Manganese-enriched concretion from DBK-1 core. A. Large-scale observations using synchrotron X-ray fluorescence and spectroscopic mapping and SEM-EDS identifications. B. Microscale analyses using synchrotron X-ray spectroscopic mapping and SEM-EDS identifications.

**Figure B3 (below):** Manganese analyses on PNG-3 core sample, showing Mn-enriched garnet (spessartine), rhodochrosite, kutnohorite, and Mn-rich chromite.



sp = Ca-enriched spessartine (Mn-garnet),

rh (here) =  $\text{Mn}_{0.96}\text{Ca}_{0.03}\text{CO}_3$ ,

ga = galena

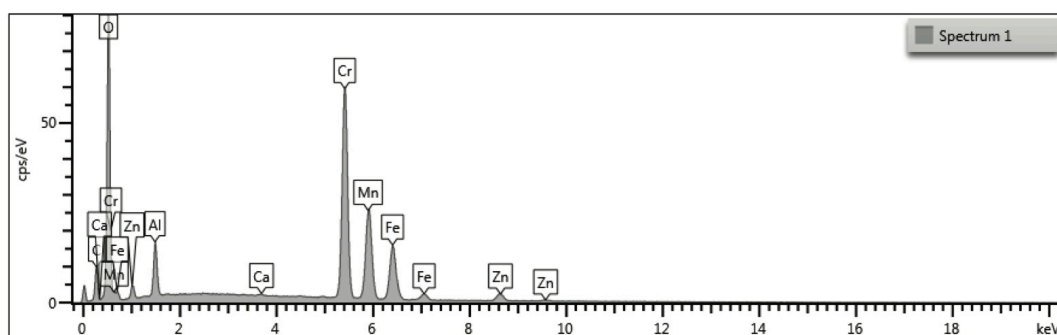
ku (here) =  $\text{Mn}_{0.67}\text{Ca}_{0.39}\text{Fe}_{0.04}\text{Mg}_{0.02}\text{CO}_3$ ,

qz = quartz

mz = monazite

cr = chromite-like min

#### Cr-enriched bright mineral with Mn: EDS Spectra



**REFERENCES CITED**

- Planavsky N. J., Asael D., Hofmann A., Reinhard C. T., Lalonde S. V., Knudsen A., Wang X., Ossa Ossa F., Pecoits E., Smith A. J. B., Beukes N. J., Bekker A., Johnson T. M., Konhauser K. O., Lyons T. W. and Rouxel O. J. (2014) Evidence for oxygenic photosynthesis half a billion years before the Great Oxidation Event. *Nat. Geosci.* **7**, 283–286.
- Smith A. J. B., Beukes N. J., Gutzmer J. and Cochrane J. M. (2010) Evidence for dissimilatory manganese reduction and availability of free molecular oxygen during deposition of Mesoarchean Witwatersrand-Mozaan strata. *Mineral. Mag.* **74**, A973.

*Appendix C*

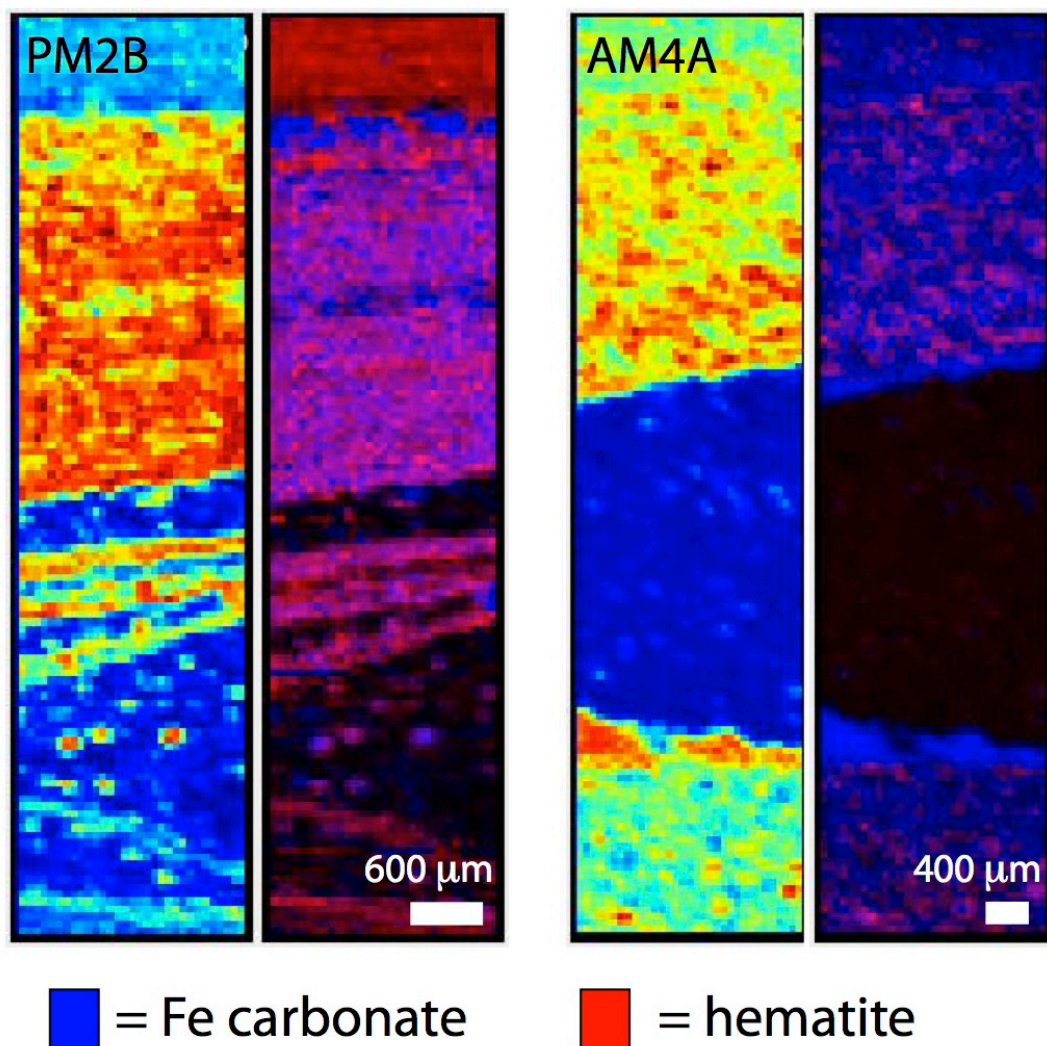
## Changing redox states in iron formations across the GOE

We have examined the redox state(s) in a number of samples from iron formations before and after the Great Oxidation Event (GOE) using synchrotron X-ray absorption spectroscopy. These analyses included both X-ray fluorescence of iron and X-ray spectroscopic mapping, and, when possible, supplementary X-ray absorption spectra. Our results were consistent with previous observations made by Klein and indicate that a major change occurred in how iron was stabilized (and possibly originally deposited) before and after the GOE and in Neoproterozoic iron formations (Klein, 2005).

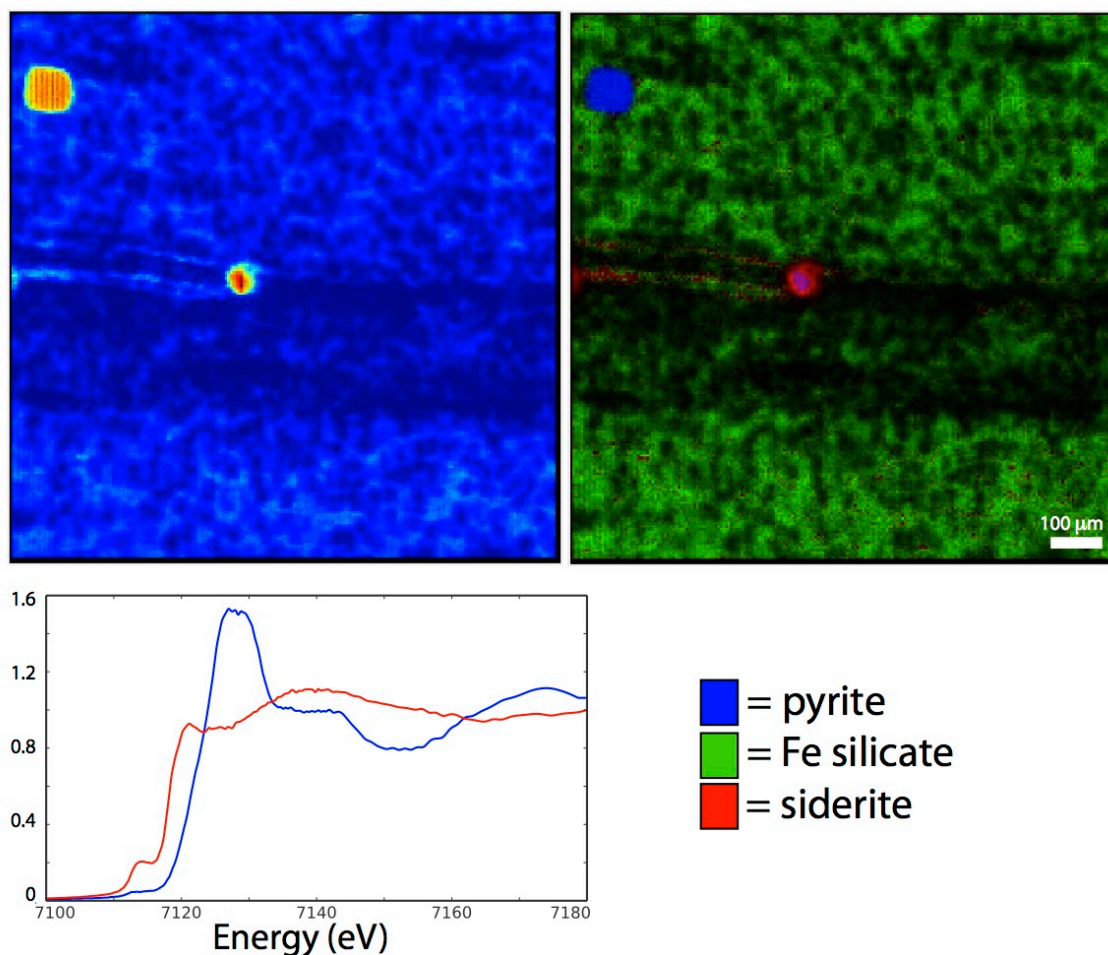
The ca. 3.2 Ga Moodies Group earlier in the Archean has both oxidized and reduced iron, probably in hematite and iron carbonate phases, but there are mainly reduced iron phases like Fe(II,III) silicates, magnetite, carbonate, and pyrite in the late Archean to early Paleoproterozoic Kuruman Formation, Mt. Sylvia Formation and Koegas Subgroup (Figure C2,C3,C4). If this is a real iron redox transition, it is interesting to speculate whether this change may relate to the advent of iron-reducing metabolisms or increase in organic carbon and productivity. After the GOE, iron oxides return again (Figure C5, C6) – suggesting that with oxygen present, iron was no longer completely reduced in the sediments. Later in the glaciation-associated iron formations of the Neoproterozoic, the iron mineralogy changed completely to all hematite (Figure C7, C8). The lack of reduced iron minerals including iron carbonate demonstrates that the iron and carbon cycles were

not linked at this time (suggesting little organic carbon was reaching the sedimentary floor) and that iron-reducing metabolisms were not reducing these iron oxides.

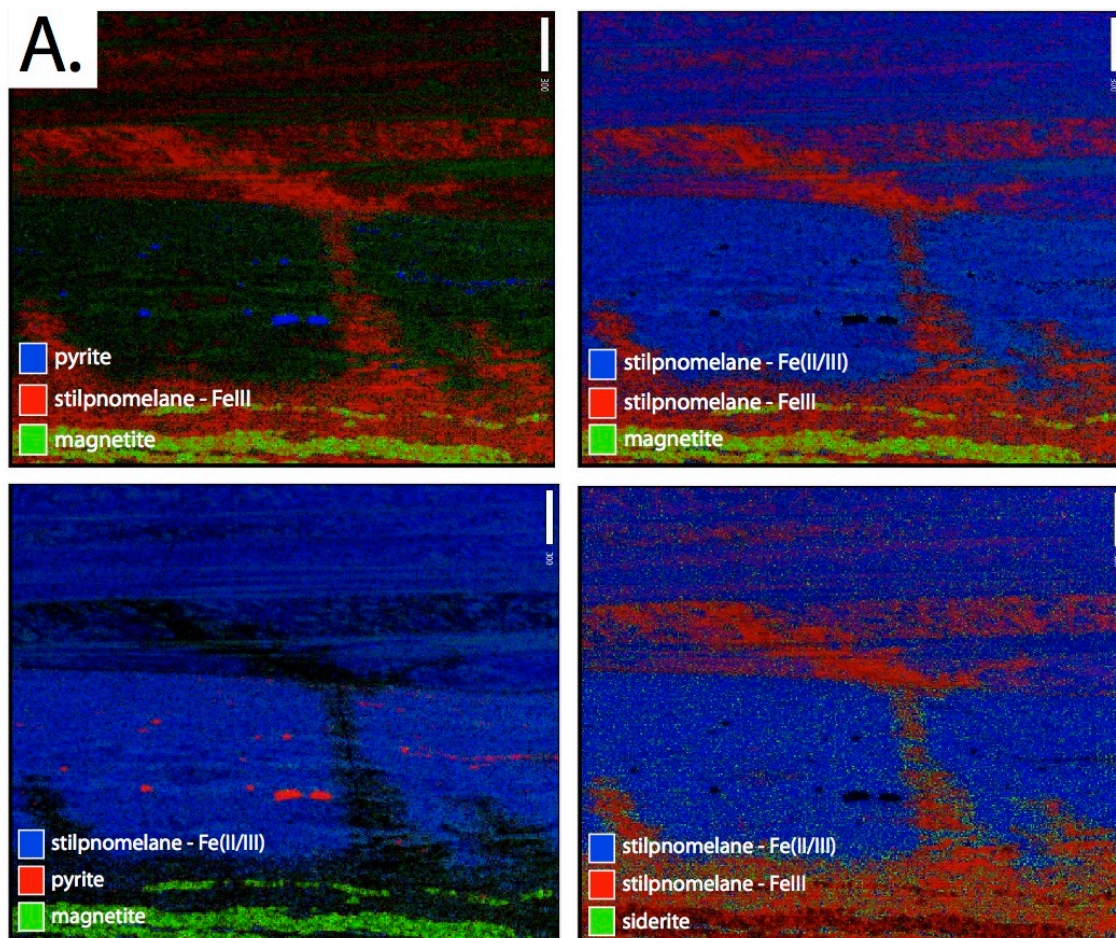


**FIGURES**

**Figure C1** – Representative samples from the ca. 3.2 Ga Moodies Group, S Africa, showing best-fitting to Fe-carbonate and hematite.



**Figure C2** – Representative sample from the ca. 2.5 Ga Kuruman Formation, S Africa, showing abundant iron silicates and less common pyrite and siderite particles. Iron silicate spectra shown in blue and pyrite spectra shown in red. Speciation maps have iron silicates shown in green, siderite in red, and pyrite in blue.





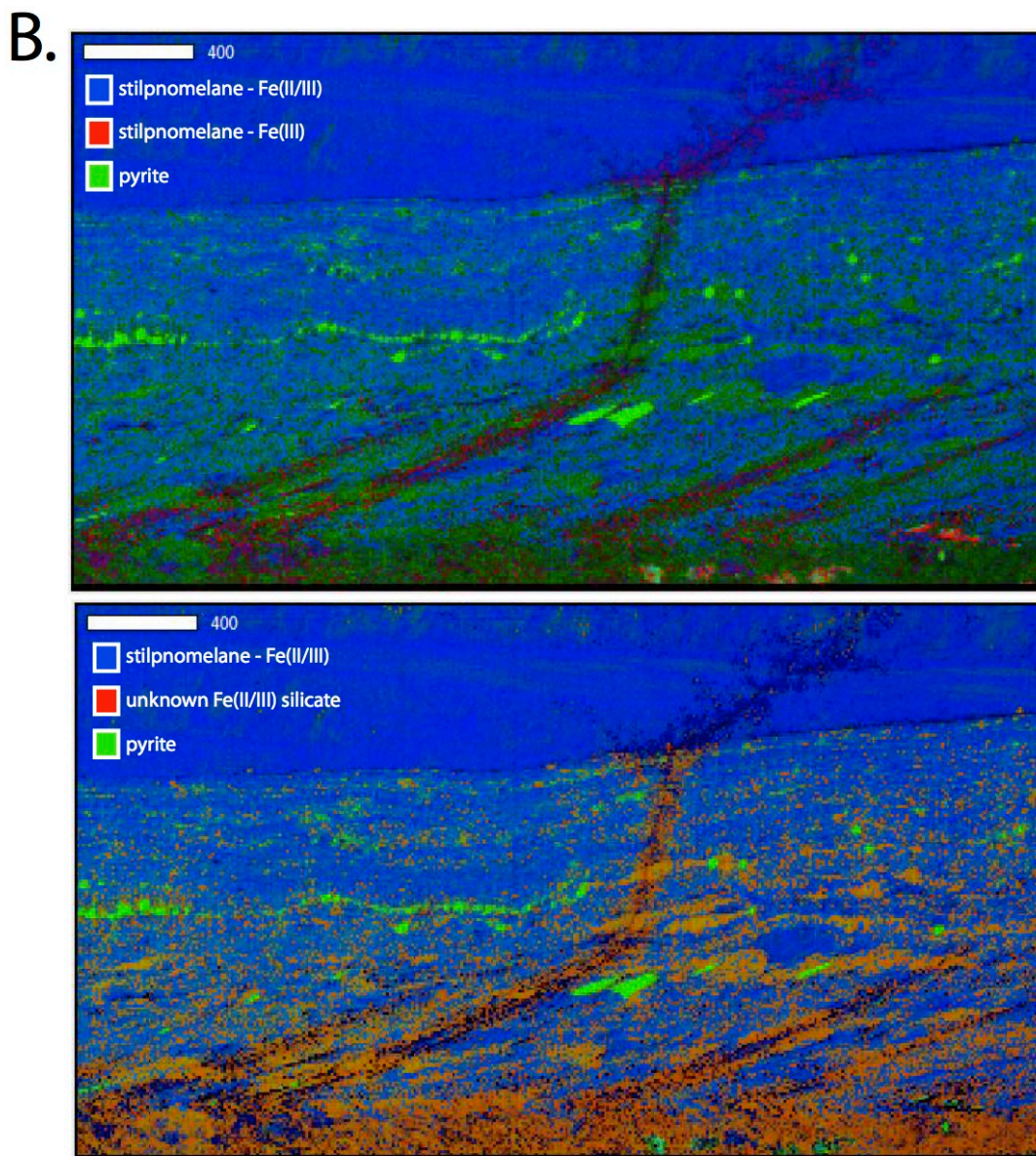


**Figure C3** – Representative regions from the ca. 2.5 Ga Mt. Sylvia Formation, Australia, showing many iron silicates, seams and crystalline pyrite, and bands of magnetite.

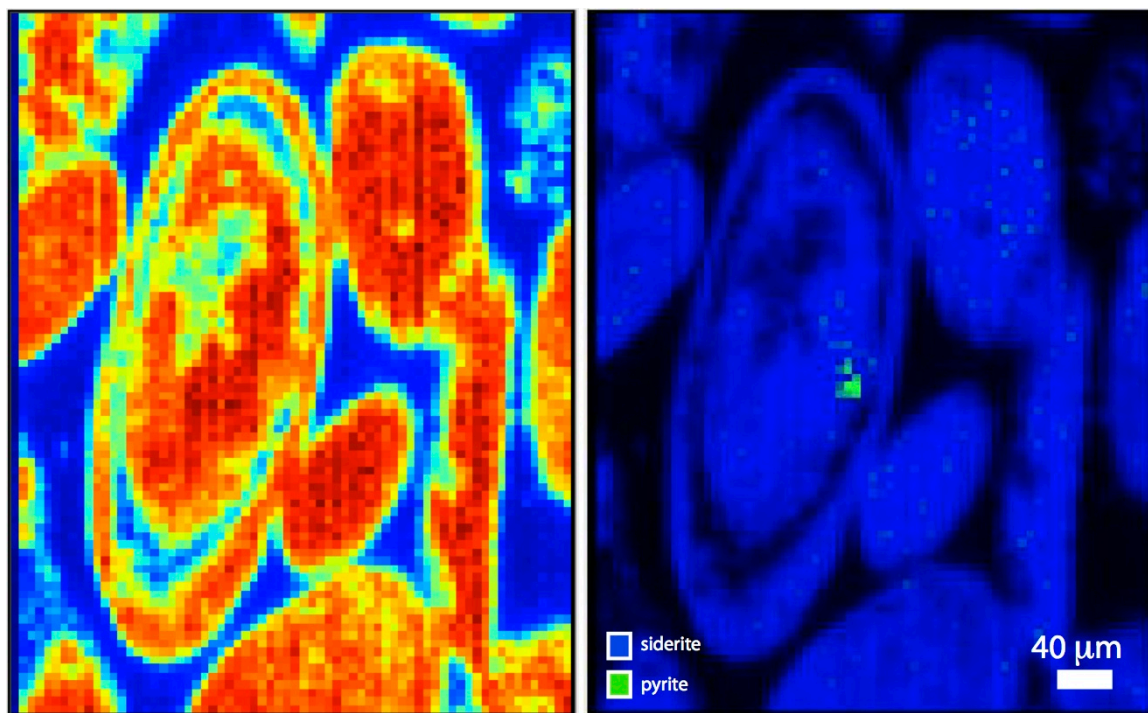


**Figure C4** – Representative area from the ca. 2.4 Ga Koegas Subgroup, S Africa, showing Fe-carbonate ooids and siderite.



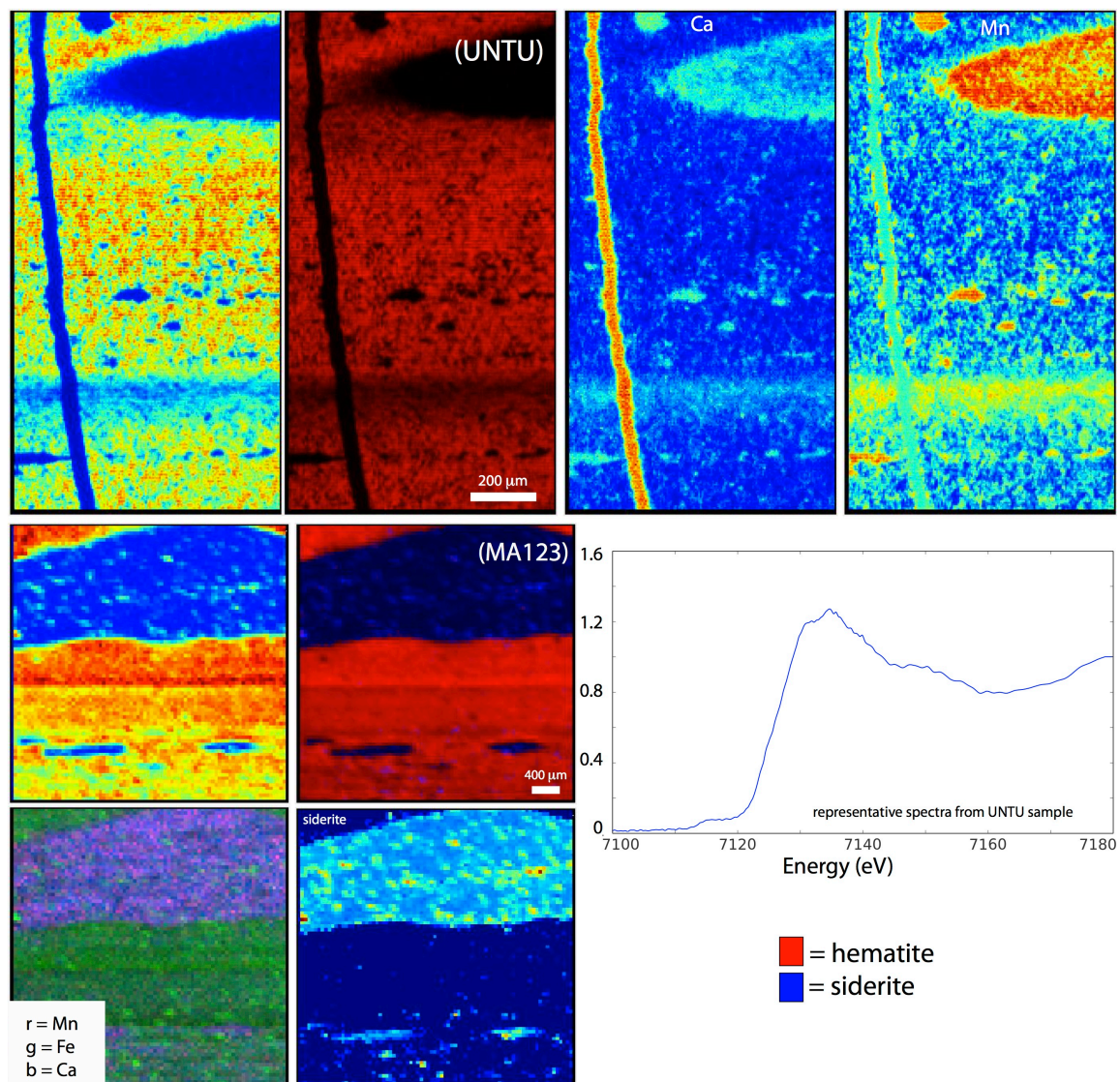


**Figure C5** – Representative samples from the ca. 2.2 Ga Hotazel Formation, S Africa, showing hematite with chert and siderite nodules.

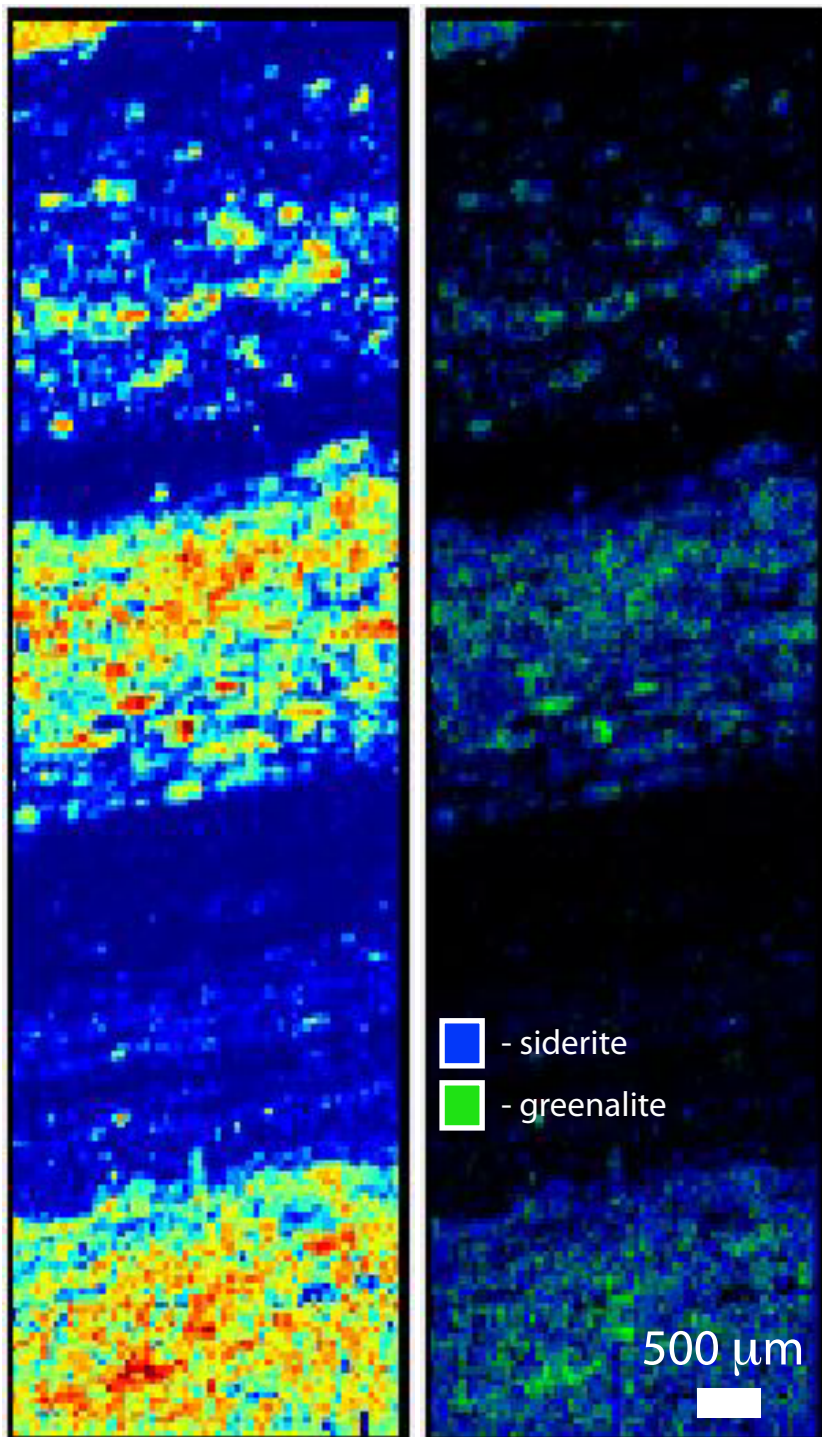


**Figure C6** – Representative sample from the ca. 1.8 Ga Gunflint Formation, Canada, best fitting iron carbonate and greenalite. Others have observed additional minerals at this time, including hematite, magnetite, berthierine, and glauconite (Wilson et al., 2010).

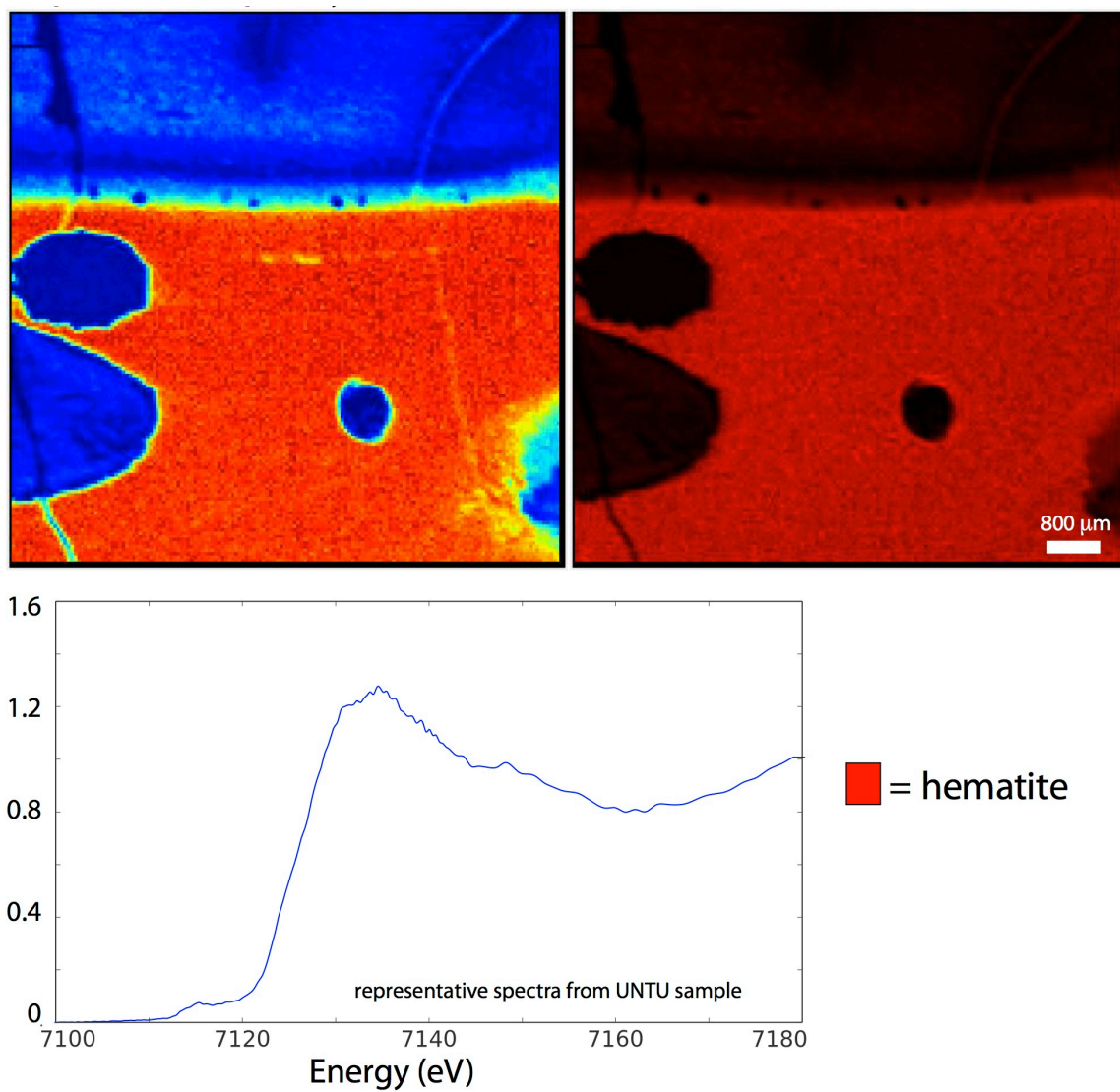


**Figure C7** – Representative sample from the ca. 730 Ma Rapitan Group, Canada, showing only hematite.



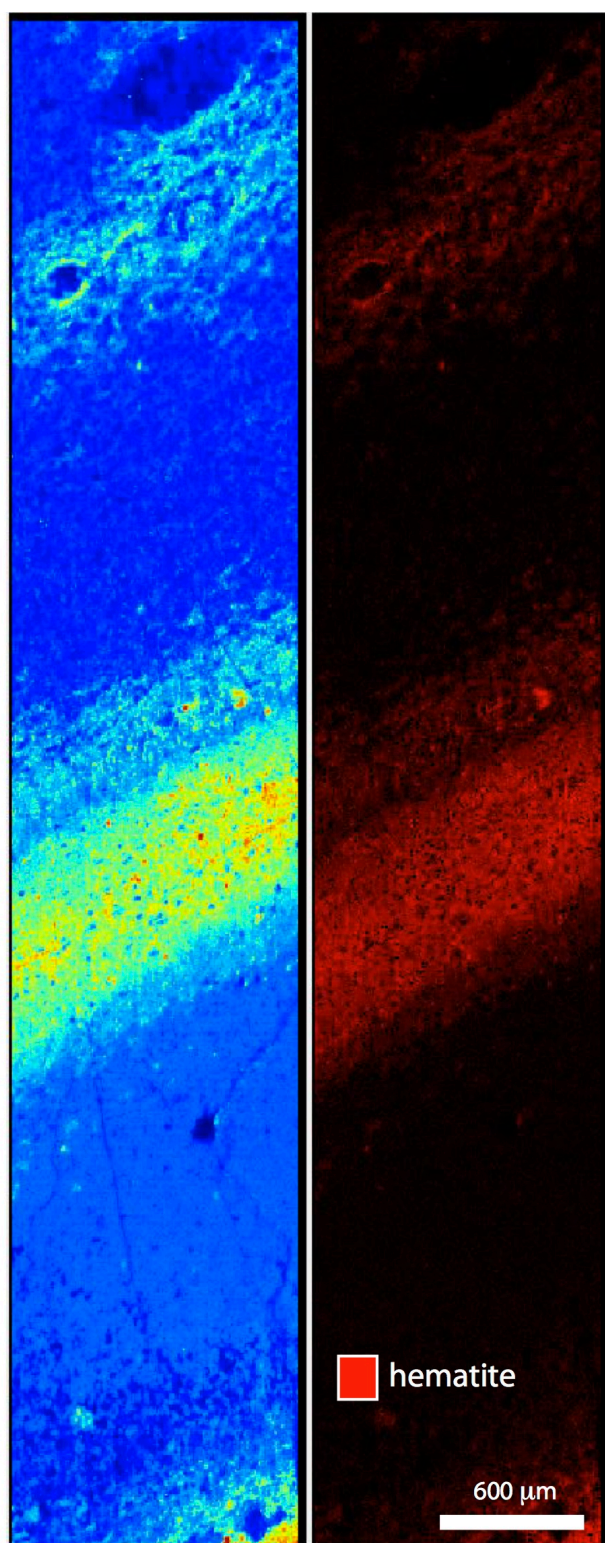


**Figure C8** – Representative sample from the ca. 630 Ma Santa Cruz Formation, Brazil, showing best-fitting to hematite.

## REFERENCES

- Klein C. (2005) Some Precambrian Banded Iron-Formations (BIFs) from Around the World: Their Age, Geologic Setting, Mineralogy, Metamorphism, Geochemistry, and Origins. *Am. Mineral.* **90**, 1473–1499.
- Wilson J. P., Fischer W. W., Johnston D. T., Knoll A. H., Grotzinger J. P., Walter M. R., McNaughton N. J., Simon M., Abelson J., Schrag D. P., Summons R., Allwood A., Andres M., Gammon C., Garvin J., Rashby S., Schweizer M. and Watters W. A. (2010) Geobiology of the Late Paleoproterozoic Duck Creek Formation, Western Australia. *Precambrian Res.* **179**, 135–149.